QUANTUM CRITICALITY AND EMERGENT SYMMETRY IN COUPLED QUANTUM DOTS

Oliver James Curtin

Submitted to

Department of Physics

Imperial College London

in

July 2016

for the degrees of

Doctor of Philosophy (PhD)

and

Diploma of the Imperial College London (DIC)

Declaration of Originality

I confirm that, to the best of my knowledge, all the content of this thesis that is not my own is properly referenced.

Declaration of Copyright

Abstract

We consider strongly correlated regimes which emerge at low temperature in coupled quantum dot (or magnetic impurity) systems. In strongly correlated systems a single particle description fails to explain the observed behaviour, so we resort to many-body methods. We describe our system using a 2-impurity Anderson model and develop a numerical renormalisation group procedure which provides non-perturbative insight into the low energy behaviour, through calculation of dynamic quantities. We combine this approach with renormalised perturbation theory, thus acquiring a picture of how the Hamiltonian and interactions change at low energies.

These approaches are first used to study the emergence of a Kondo effect with an SU(4) symmetry in capacitively-coupled double quantum dot systems. We classify the 'types' of SU(4) symmetry which can emerge and show how an experimentalist might achieve such emergence through tuning their system. We provide a way of distinguishing between the SU(2) and SU(4) Kondo regimes by considering the conductance.

We also study a quantum critical point which occurs in the Heisenberg coupled quantum dot/impurity model. There is an anomalous entropy contributed by the impurities in this regime which is indicative of an uncoupled Majorana Fermion. We calculate dynamic quantities in regimes with different symmetries and establish correspondence with the 2-channel Kondo model. We formulate possible pictures of the underlying mechanisms of the critical point and construct a Majorana fermion model for the case with particle-hole symmetry, which explains the non-Fermi liquid energy levels and degeneracies obtained. We conjecture that a Majorana zero mode is present, and that this is responsible for the anomalous entropy.

Contents

List of Figures

List of Tables

List of Abbreviations

1IAM	One-Impurity Anderson Model
2CKM	Two-Channel Kondo Model
2IAM	Two-Impurity Anderson Model
2IKM	Two-Impurity Kondo Model
BCFT	Boundary Conformal Field Theory
DQD	Double Quantum Dot
FL	Fermi Liquid
FP	Fixed Point (of the renormalisation group)
MF	Majorana Fermion
NFL	Non-Fermi Liquid
NRG	Numerical Renormalisation Group
QCP	Quantum Critical Point
QD	Quantum Dot
RG	Renormalisation Group
RPT	Renormalised Perturbation Theory

Publications

The work undertaken during the course of the PhD programme pertains to two distinct areas of research. Initially, the research was aimed towards the design and fabrication of a multiband semiconductor heterostructure solar cell. The designed devices are undergoing experimental analysis, but have been published:

- Oliver J. Curtin, Megumi Yoshida, Andreas Pusch, Nicholas P. Hylton, Ned J. Ekins-Daukes, Chris C. Phillips, Ortwin Hess, *Quantum Cascade Photon Ratchets for Intermediate-Band Solar Cells*, Journal of Photovoltaics, Vol. 6, No. 3 (2016)

After the theoretical component of this work was complete, the PhD focus shifted towards renormalisation group methods for studying quantum criticality and emergent symmetry in quantum dot/impurity systems. The prior work will not be discussed during this thesis. The presented work pertains to the following publications:

- Yunori Nishikawa, Oliver J. Curtin, Alex C. Hewson, Daniel J. G. Crow, Johannes Bauer, *Conditions for Observing Emergent* SU(4) *Symmetry in a Double Quantum Dot*, Physical Review B, Vol. 93, No. 23 (2016)
- Oliver J. Curtin, Yunori Nishikawa, Alex C. Hewson, Daniel J. G. Crow, *Interpretation of the Quantum Critical Point in a Two Impurity/Two Channel Kondo Model* [in preparation]

Introduction and Brief History

Quantum impurity physics has been at the forefront of condensed matter physics since its inception. Originally restricted to describe static local spins, quantum impurity models have been adapted to include a variety of interactions, such as hybridisation with a conduction bath, Coulombic interactions and Heisenberg exchange, with many artificially included symmetries. In essence, all of these models simply embody the interaction of a small number of degrees of freedom with a continuum and as a result of the small number of coupling constants, many of these systems may be studied experimentally. The freedom we have over the interactions and symmetries in quantum impurity models signifies that they may be applied to many different physical scenarios. These include heavy Fermion systems [1, 2], quantum dots [3], carbon nanotubes [4] and systems with free half-degrees of freedom (Majorana bound states) [5]. Majorana bound states are 2-dimensional particles with non-Abelian statistics (known as non-Abelian anyons), which are a prime candidate for the realisation of topological quantum computers [6]. Almost all of these systems can be represented by the Anderson model, which is used extensively throughout our work.

The field of quantum impurities illustrates the importance of strong electronic interactions in describing some observed quantum phenomena. An important such phenomenon is the resistivity minima with respect to temperature T occurring in metals with magnetic impurities [7, 8, 9, 10, 11, 12]. This puzzled theorists and experimentalists for decades, and led to the proposal of one of the earliest quantum impurity models, the s-d model [13, 14]. This model accounts for magnetic interactions between a spinful (usually $S = {}^{1}\!/_{2}$) impurity and a bath of non-interacting electrons, and has the Hamiltonian

$$H_{\mathrm{sd}} = \sum_{\boldsymbol{k}} \epsilon_{\boldsymbol{k}} c^{\dagger}_{\boldsymbol{k}\sigma} c_{\boldsymbol{k}\sigma} + 2J\boldsymbol{S}(0) \cdot \boldsymbol{S}$$

where the operators $c^{\dagger}_{\boldsymbol{k}\sigma}$ create non-interacting Dirac electrons of wavevector $\boldsymbol{k}$, spin σ and energy $\epsilon_{\boldsymbol{k}}$. We implicitly sum over the SU(2) index σ. The operator $\boldsymbol{S}$ describes the total static spin, which is chosen to exist at the origin such that $\boldsymbol{S}(0)$ denotes the total local spin of the non-interacting bath at the same position as the fixed static spin, which shall henceforth be referred to as the impurity or dot. The Heisenberg coupling J sets the strength of the magnetic interaction between the impurity and the conduction bath. This model correctly encapsulates the relevant physics to describe the resistivity minima, but how to make the effect manifest posed a problem.

A number of approaches were developed with this aim in mind. Originally, Kondo [15] took the magnetic interaction between the impurity and the bath as a perturbation. The bath, of non-interacting electrons, is quadratic and hence solvable. By application of perturbation theory (to third order) Kondo showed that the resistivity due to spin scattering ρ_{spin} exhibits a logarithmic divergence, $\rho_{\text{spin}} \sim J \ln(T)$ such that the total resistivity is given by

$$\rho(T) = a_0 + a_1 T^2 + a_2 T^5 + a_3 J \ln(T)$$

where the a_i are constants satisfying $a_1, a_2 > 0$ and $a_3 < 0$. The T^2 term represents the contribution from the Fermi liquid properties of the non-interacting electron bath, whilst the T^5 term accounts for the contribution to the resistivity from phonons. We thus see that the s-d model provides a solution to the Kondo effect, since $\rho(T)$ has a minimum provided $J > 0$ (antiferromagnetic coupling). However, the problem with Kondo's perturbative approach was that the experimental results did not suggest a divergence as $T \to 0$. Further studies [16] of this model concluded that below the Kondo temperature T_{K}, the perturbative approach was unreliable. A non-perturbative method, which did not assume the electrons could be modelled as being free, hence had to be developed. The quest to understand the behaviour of the system at temperatures below T_{K} became known as the Kondo problem.

One milestone in solving the Kondo problem was Anderson's Poor Man's Scaling approach [17]; this was a precursor to the application of Renormalisation Group (RG) transformations in quantum impurity problems. Anderson's idea was that if one were to integrate out the high-energy states of the system lying above some cut-off Γ, such that the Hamiltonian is valid for energies ϵ satisfying $\epsilon < \Gamma$, then the

Heisenberg coupling J acquires dependence on the energy scale associated with Γ. In the language of the RG, J becomes a running coupling constant $J(\Gamma)$ as the cut-off Γ is brought arbitrarily close to the Fermi surface, ϵ_{F}. By using this approach, Anderson showed that $\lim_{\Gamma\to\epsilon_{\mathrm{F}}} J(\Gamma) = \infty$. The impurity therefore forms a tightly bound singlet with the surrounding electrons as T is decreased. Conversely, as the temperature increases $T \to \infty$, $J(\Gamma) \to 0$, implying that the local magnetic moment becomes free in this limit. This is exactly analogous to the behaviour of quarks in QCD [18, 19], where at high energy scales the interaction between quarks and gluons is much weaker than at lower energy scales, and illustrates that the magnetic moments exhibit asymptotic freedom ($T \to \infty$) and confinement ($T \to 0$) [20].

Anderson's approach does not provide a full solution to the Kondo problem. He perturbs the system by eliminating the high-energy states in the conduction band and expands in powers of J. The result of his approach is a scaling equation. However, in the antiferromagnetic case, where $J \to \infty$ as the energy scale decreases, expressions obtained in terms of J become unreliable. That said, this approach does provide important insight into the applicability of scaling arguments to the Kondo problem. These were adopted by Wilson [21], who developed a numerical non-perturbative RG method capable of reliably solving for the low-energy eigenvalues of the s-d Hamiltonian. This method, which has become known as Wilson's Numerical Renormalisation Group (NRG) is credited with solving the Kondo problem; despite making a few approximations regarding the conduction band, it produced results which were remarkably consistent with experiment.

Wilson's NRG [22, 21] is a numerical procedure to iteratively probe the lowest energy states of certain types of Hamiltonians. We give a detailed description of our NRG calculations in chapter 2, but provide a very brief summary here. Wilson's key idea was the logarithmic discretisation of the conduction band; he assumes a flat band and splits it into very fine intervals close to the Fermi level, but for energies away from the Fermi level the sampling is more coarse. Each interval of the conduction band is expanded into a Fourier series, and Wilson notes that the first term of each series is the most significant. He approximates by retaining only these terms, and the resultant Hamiltonian is mapped exactly to a linear chain of 2-body states (a Wilson Chain). His NRG is simply iterative addition of a 2-body state by means of an RG transformation which emerges from his analysis. After a number of iterations, which depends on the logarithmic discretisation, the energy eigenvalues become invariant under the RG transformation and the system is described by an RG Fixed Point (FP). The length of the Wilson chain N denotes the number of RG transformations that the algorithm must perform and is synonymous with the energy scale reached by the approach. N can therefore be mapped directly to a temperature[1] $T \sim \mathrm{e}^{-N/2}$. There are many quantities, such as entropy, spin susceptibility and specific heat, which can be calculated at each N from the energy levels obtained with the NRG, and thus one may calculate these quantities as a function of T.

By applying his method, Wilson showed that the s-d model has two FPs; one where $J \to \infty$ which corresponds to the low temperature behaviour of the model and demonstrates that the ground state is a singlet. The other FP has $J \to 0$ where the static spins are decoupled from the bath and become asymptotically free, in agreement with Anderson's picture. In addition to calculating the lowest energy levels, Wilson was able to compute the spin susceptibility and specific heat as a function of T which were consistent with other calculations and provided further support to the NRG.

Although originally applied to solve the Kondo problem, the NRG has been extended to many other scenarios [23]. The first extension was to the Anderson impurity model [24, 25], which is the focus of our present work, where the impurity subsystem is hybridised to the conduction bath through a hopping term. This model is significant because on low-energy scales it becomes equal to the s-d model, explaining why one obtains an antiferromagnetic coupling in the first place. In much the same way as the Kondo model, the low-energy eigenvalues of the Anderson model can be obtained. The NRG has now been extensively used in multi-impurity [26, 27] and multi-channel [28, 29, 30] systems to calculate a variety of physical properties, including dynamic [31, 32, 33, 34, 35, 36, 37] and thermodynamic quantities [24, 25, 38, 39], as well as the RG flow of coupling constants [40]. It shines light on the bare-scale physics and the low-energy quasiparticle picture.

Since the advent of the NRG and the establishment of the RG as a requirement

---

[1] Note that we use the units $\hbar = k_{\mathrm{B}} = 1$, so that temperature and frequency are interpreted as energies.

for the study of quantum impurities, there has been much attention directed towards the Kondo effect and similar/more exotic low-temperature effects. These are classed as 'emergent' phenomena; those which can only be observed on certain scales, and whose mathematical treatment requires a non-perturbative RG approach. Many methods have been developed to uncover and explain emergent phenomena, such as Bethe ansatz, Boundary Conformal Field Theory (BCFT) and Renormalised Perturbation Theory (RPT).

In this thesis we are concerned with emergent phenomena, and we employ the NRG and RPT approaches. We first consider two capacitively coupled impurities, and seek to understand whether an exotic SU(4) Kondo effect can arise. We use the NRG, combined with the RPT, to understand how the interactions and symmetries change between scales and whether symmetry can be restored on the low-energy scale. We are also concerned with 'strange-metals' whose mathematical description cannot be based upon a bath of non-interacting electrons. These metals may pave the way towards superconductivity [41] and quantum computing [42]. We identify a quantum critical point with such strange properties and combine the NRG, BCFT and RPT approaches to understand the symmetry and anomalous thermodynamic quantities which arise. Throughout our work we use the 2-Impurity Anderson Model (2IAM) to represent the coupled quantum dots/impurities.

Structure of this Thesis

The thesis is structured as follows.

- In chapter 1, we introduce and formalise the RG, before discussing the Anderson impurity model. We provide some key properties of the model and explain how it can be realised in experiment.
- In chapter 2, we introduce the NRG and explain how it is applied to the 2IAM. We then discuss in detail how it can be used to calculate static quantities, such as entropy, and dynamic quantities such as the 1- and 2-particle spectral densities.
- In chapter 3, we apply RPT to the 2IAM. We show how we can obtain renormalised parameters from the NRG, and go on to apply diagrammatic perturbation theory to derive various dynamic quantities and relations (such as our

definition of strong correlation and Wilson ratios).

- Chapter 4 is devoted to the study of emergent SU(4) symmetry in double quantum dot systems. We first establish correspondence between a double quantum dot model and the 2IAM, then go on to derive the conditions for this symmetry to emerge on the low energy scale. We investigate whether such emergence is possible in experimental setups and suggest a distinguishing feature of an SU(4) Kondo regime.

- In chapter 5, we study a quantum critical point that appears in the 2IAM, due to the Heisenberg coupling. We contrast the cases of particle-hole symmetry and asymmetry, and build a physical picture of the competing regimes, providing dynamic quantities as evidence. We move on to establish a correspondence to the two-channel Kondo model, which we exploit to build a Majorana Fermion description of the quantum critical point.

Chapter 1

Impurity Physics and the Anderson Model

We begin by introducing the RG, which is arguably the most important concept regarding emergent phenomena, and proceed to the definition of the Anderson model. We list some important properties of the model, such as the Friedel sum rule, and go on to describe how experiments are performed on these systems.

1.1 The Renormalisation Group

The RG provides a framework to investigate the behaviour of models on many energy scales. It is a set of transformations to be applied to the system Hamiltonian (or Lagrangian/Partition Function), which irreversibly map the 'bare' Hamiltonian to a new 'renormalised' Hamiltonian with modified coupling constants [43, 44, 45, 46]. Denoting the Hamiltonian $H(\boldsymbol{K})$, where $\boldsymbol{K}$ is an array containing all the coupling constants, and $\mathcal{R}$ as the RG transformation, we have

$$\mathcal{R} : H(\boldsymbol{K}) \mapsto H(\boldsymbol{K}'). \tag{1.1.1}$$

Under the RG, new coupling constants can emerge such that $|\boldsymbol{K}| \neq |\boldsymbol{K}'|$, reflecting the fact that at different energy scales one can obtain new types of interactions. Throughout this work, we will adopt the picture that $\boldsymbol{K}$ contains all possible coupling constants, and in the bare Hamiltonian most elements of $\boldsymbol{K}$ are zero. We hence formulate our discussions by assuming that the Hamiltonian contains an infinite number of different types of interactions, and all those not shown simply have zero coupling; we will see in chapter 2 that this picture motivates accurate calculation of dynamic quantities.

The transformations $\mathcal{R}$ involve two key steps [47]. Firstly, we introduce a cut-off as in Poor Man's scaling and integrate out the higher energy states of the system [48]; these tend to be short-range degrees of freedom with relatively fast dynamics, such that the new system contains longer-ranged and typically slower dynamics. The second stage of an RG transformation is to ensure that the density of degrees of freedom is preserved. This is accomplished by rescaling the system such that the original energy scale is restored.

If the transformation $\mathcal{R}_\Gamma$ belonging to the RG depends on a continuous parameter Γ which is not explicitly present in the Hamiltonian, such as energy cut-off, then we may investigate changes in the renormalised systems with respect to Γ; since the coupling constants $\boldsymbol{K}$ acquire Γ-dependence. We specialise to the case where Γ is the cut-off as this is most relevant to the work presented. The trajectories generated in this way are examples of RG flow, and yield insight into how a system approaches different regimes as some scale changes. In our work we obtain the RG flow by sequential application of $\mathcal{R}_\Gamma$ on a bare Hamiltonian $H(\boldsymbol{K})$. This produces a set of Hamiltonians $S = \left\{H^N(\boldsymbol{K}^N) \ \forall \ N \in \mathbb{N}\right\}$, where

$$H^N(\boldsymbol{K}^N) = \mathcal{R}_\Gamma^N \left[H(\boldsymbol{K})\right], \tag{1.1.2}$$

and each $\mathcal{R}_\Gamma^N$ imposes a cut-off of Γ^N. We thus see that S contains Hamiltonians whose energy scale decreases as a power law, and we can plot this scale against the renormalised couplings $\boldsymbol{K}^N$ to obtain the RG flow. Generally, below some energy scale Γ^M, the Hamiltonian $H^*(\boldsymbol{K}^*) := H^M(\boldsymbol{K}^M)$ will become invariant under $\mathcal{R}_\Gamma$ and is said to describe a RG FP. Since the $\mathcal{R}_\Gamma$ integrates out short-range and higher energy degrees of freedom, the RG FP is invariant under scale transformations and describes the system on all energy scales below Γ^M, including $T = 0$. The second order quantum critical points of the system also exhibit scale invariance at $T = 0$ [49], as well as the divergence of some susceptibility [50]. In this work we identify quantum critical points as RG FPs with a susceptibility which diverges on successively lower energy scales.

The RG provides a very powerful mathematical apparatus which is used extensively in studies of quantum impurities, allowing us to ‘discern the transmundane’ by understanding how our models behave far below the bare scale. Additionally, it provides quantitative insight into the new types of interaction vertices which emerge at different scales. The RG is central to our methods of understanding coupled Anderson impurities, and allows us to build a picture of the interactions and Hamiltonian structure at the low-energy FPs we encounter.

1.2 The Anderson Impurity Model

Although very successful in describing the Kondo effect, the s-d model assumes the presence of static spins which magnetically interact with a bath; this implies that the model does not permit the possibility of 2 electrons forming a local spinless state, and hence that the electron-electron repulsion is large. Furthermore, the s-d model does not permit the static spin (which is due to an electron) to be exchanged with the bath. In a real metal, both of these mechanisms should be permitted. The Anderson model [51] aims to incorporate these by tunnel-coupling electrons on an impurity site to the conduction bath, and also includes a Coulomb interaction local to the impurity. Unlike the s-d model, the Single Impurity Anderson Model (1IAM) is expressed entirely in terms of Dirac electron operators, and has the Hamiltonian[1]

$$H_{\text{1IAM}} = \sum_{\boldsymbol{k}} \epsilon_{\boldsymbol{k}} c^{\dagger}_{\boldsymbol{k}\sigma} c_{\boldsymbol{k}\sigma} + \sum_{\boldsymbol{k}} V_{\boldsymbol{k}} \left[c^{\dagger}_{\boldsymbol{k}\sigma} d_{\sigma} + d^{\dagger}_{\sigma} c_{\boldsymbol{k}\sigma} \right] + \sum_{\sigma} \epsilon_{\sigma} d^{\dagger}_{\sigma} d_{\sigma} + U n_{\uparrow} n_{\downarrow} \tag{1.2.1}$$

where $d^{\dagger}_{\sigma}$ creates an electron of spin σ on the impurity site and $n_{\sigma} = d^{\dagger}_{\sigma} d_{\sigma}$ is the local number operator. The impurity levels ϵ_{σ} denote the amount of energy required to populate the impurity with a single electron of spin σ whilst the onsite Coulomb interaction U denotes the amount of energy which must be supplied in addition to ϵ_{σ} to create a second electron on the impurity site. The hybridisation $V_{\boldsymbol{k}}$ denotes the strength of the tunnel coupling between the impurity and the conduction band, whilst the hybridisation function

$$\Delta(\omega) = \pi \sum_{\boldsymbol{k}} \left| V_{\boldsymbol{k}} \right|^2 \delta(\omega - \epsilon_{\boldsymbol{k}}) \tag{1.2.2}$$

entirely governs how the impurity system and bath interact. The 1IAM successfully reproduces the s-d model as in the low energy limit (for certain parameter regimes)

---

[1] We express all Hamiltonians throughout this work in units of the bandwidth D so that a given Hamiltonian H should be read as H/D. For convenience we set $D = 1$.

a local spin is formed, which is responsible for a Kondo effect. The relationship between these models is formalised by the Schrieffer–Wolff transformation [52], which shows that in the regime of small hybridisation and large on-site Coulomb repulsion, a localised magnetic moment is formed. This magnetic moment is Heisenberg-coupled to the bulk with strength $J = 4V^2/U$, and hence gives rise to the Kondo effect described by the s-d model.

We shall assume throughout this thesis that the model is isotropic, so that $\epsilon_{\boldsymbol{k}}$ and $V_{\boldsymbol{k}}$ depend only on $k = |\boldsymbol{k}|$, and also that the conduction band spanned by k ranges from $-D$ to D, where D is termed the (half)bandwidth. This is motivated from Wilson's NRG approach and ensures that the impurity system only couples to spherical s-waves. We further assume that all bulk electrons are equally likely to hop onto the impurity, so that $V_{\boldsymbol{k}} = V$. Under these assumptions, the dispersion and hybridisation functions are constrained [53]. We take the hybridisation function to be constant,

$$\Delta(\omega) = \Delta = \frac{1}{2}\pi V^2, \tag{1.2.3}$$

which implies linear dispersion [23, 53]. We will frequently refer to Δ throughout our work, as this sets the energy scale at which transitions between the RG FPs occur.

The behaviour of the 1IAM is well understood and easily accessible through many different formalisms [24, 25, 54, 55, 56]. The basic model behind our work in this thesis is the Two-Impurity Anderson Model (2IAM). We take two 1IAMs, labelled by $\alpha \in \{1, 2\}$, to have Hamiltonians

$$H_\alpha = \sum_{\boldsymbol{k}} \epsilon_{\alpha\boldsymbol{k}} c^\dagger_{\alpha\boldsymbol{k}\sigma} c_{\alpha\boldsymbol{k}\sigma} + \sum_{\boldsymbol{k}} V_\alpha \left[c^\dagger_{\alpha\boldsymbol{k}\sigma} d_{\alpha\sigma} + d^\dagger_{\alpha\sigma} c_{\alpha\boldsymbol{k}\sigma} \right] + \sum_\sigma \epsilon_{\alpha\sigma} d^\dagger_{\alpha\sigma} d_{\alpha\sigma} + U_\alpha n_{\alpha\uparrow} n_{\alpha\downarrow}, \tag{1.2.4}$$

where we have promoted the coupling constants to depend explicitly on α, and introduce local inter-impurity interactions. The Coulomb interaction between each impurity is governed by the coupling constant U_{12} and the corresponding Hamiltonian is given by

$$H_{\mathrm{C}} = U_{12} \sum_{\sigma\sigma'} n_{1\sigma}\, n_{2\sigma'}. \tag{1.2.5}$$

Additionally, we define a local Heisenberg magnetic coupling J between the impurities by

$$H_{\mathrm{M}} = 2J\boldsymbol{S}_1 \cdot \boldsymbol{S}_2, \tag{1.2.6}$$

where $\boldsymbol{S}_\alpha$ denotes the total local spin of each impurity. We use the convention that $J > 0$ implies an antiferromagnetic coupling. Our Hamiltonian is thus given by

$$H = H_1 + H_2 + H_{\mathrm{C}} + H_{\mathrm{M}}. \tag{1.2.7}$$

The two interactions preserve the number of electrons in each conduction bath, and as a result we have symmetry under two distinct U(1) transformations;

$$\begin{cases} c_{1\boldsymbol{k}\sigma} & \rightarrow & \mathrm{e}^{i\theta_1} c_{1\boldsymbol{k}\sigma} \\ d_{1\sigma} & \rightarrow & \mathrm{e}^{-i\theta_1} d_{1\sigma} \end{cases} \tag{1.2.8}$$

and

$$\begin{cases} c_{2\boldsymbol{k}\sigma} & \rightarrow & \mathrm{e}^{i\theta_2} c_{2\boldsymbol{k}\sigma} \\ d_{2\sigma} & \rightarrow & \mathrm{e}^{-i\theta_2} d_{2\sigma} \end{cases}, \tag{1.2.9}$$

resulting in a charge symmetry of U(1)×U(1). Throughout our work, we will make the assumption (unless specified otherwise) that there is no local magnetic field present on either impurity, so that the impurity levels $\epsilon_{\alpha\sigma} = \epsilon_\alpha$ are independent of spin. Therefore we also have symmetry under the spin group SU(2), so that we have a total symmetry of U(1)×U(1)×SU(2).

1.3 Local Density of States and the Friedel Sum Rule

We will often calculate the local density of states of the Anderson models, and relate its value at the Fermi level to the impurity occupation. This relationship follows from the Friedel sum rule [57, 58], and the Green functions corresponding to the model. The Friedel sum rule is derived by considering the impurity system as a perturbation to the non-interacting system, and proceeds by defining a phase shift $\eta_\alpha(\omega)$ at energy ω, associated to impurity α, which is due to the switching on of interactions. The definition of the phase relies on the scattering T-matrix, which maps the non-interacting Green function $G^{(0)}_\alpha(z)$ to the interacting Green function $G_\alpha(z)$ via

$$G_\alpha(z) = G^{(0)}_\alpha(z)\left[\mathbb{I} + T_\alpha(z) G^{(0)}_\alpha(z)\right], \tag{1.3.1}$$

where $T_\alpha(z)$ is the T-matrix. The phase is subsequently defined as

$$\eta_\alpha(\omega) = \arg\left[\det T_\alpha(\omega + i\delta^+)\right], \tag{1.3.2}$$

for $\delta^+ \to 0^+$. Using this definition of the phase, the Friedel sum rule derived in detail in [59], states that $\eta_\alpha(\omega)$ is related to the local density of states $\rho_\alpha(\omega)$ by

$$\rho_\alpha(\omega) = \frac{1}{\pi}\partial_\omega \eta_\alpha(\omega). \tag{1.3.3}$$

Integrating up to the Fermi level, we obtain a relationship between the impurity occupation n_α and phase;

$$n_\alpha = \int_{-\infty}^{\epsilon_{\mathrm{F}}} \mathrm{d}\omega\ \rho_\alpha(\omega) = \frac{\eta_\alpha(\epsilon_{\mathrm{F}})}{\pi}. \tag{1.3.4}$$

We provide formal definitions of the density of states in chapter 2, but from (1.3.4) we see the importance of phase; a phase shift has a neat physical interpretation as the change in local occupation. The Friedel sum rule is highly general; it simply assumes that one has a conduction bath which interacts with some impurity system. We are able to obtain a more specialised case of the Friedel sum rule, which is of direct relevance to our work, by calculating the phase shift corresponding to an Anderson impurity [60]. To pre-empt our discussion on RPT in chapter 3, we set the coupling constants of the quartic terms to zero. In this model the phase is given by

$$\eta_\alpha(\omega) = \frac{\pi}{2} - \arctan\left(\frac{\epsilon_\alpha - \omega}{\Delta_\alpha}\right) \tag{1.3.5}$$

per spin, and the local density of states at $T = 0$ is then

$$\rho_\alpha(\omega) = \frac{1}{\pi}\frac{\Delta_\alpha}{(\epsilon_\alpha - \omega)^2 + \Delta_\alpha^2}. \tag{1.3.6}$$

These results are derived in [59]. The Friedel sum rule then implies

$$n_\alpha = \frac{1}{2} - \frac{1}{\pi}\arctan\left(\frac{\epsilon_\alpha}{\Delta_\alpha}\right) \tag{1.3.7}$$

per spin, or equivalently

$$\rho_\alpha(0) = \frac{1}{\pi\Delta_\alpha}\sin^2\left(\frac{\pi}{2}n_\alpha\right). \tag{1.3.8}$$

This relation allows prediction of the value of the spectral density at the Fermi level given local occupation, which can be calculated from the renormalised parameters. It therefore provides a useful check for our results. Note that (1.3.8) is only valid if $U = J = U_{12} = 0$, but we shall see in chapter 3 that when interactions are present, and the low energy FP is a Fermi Liquid (FL), these relations generalise.

1.4 Particle-Hole Symmetry in the 2IAM

We adopt the conventional notation that particle states have an energy above the Fermi level (hole states vice versa) and seek to develop a model where particle and hole states are degenerate. Apart from the numerical gain due to the extra symmetry, the model in this regime is interesting because it permits a description in terms of only spin groups which map to a Majorana Fermion model. If H, given in (1.2.7), is particle-hole (p-h) symmetric, then it is invariant under the transformation[2]

$$\left\{ \begin{array}{lcl} c_{\alpha \boldsymbol{k} \sigma} & \to & c^{\dagger}_{\alpha - \boldsymbol{k} \sigma} \\ d_{\alpha\sigma} & \to & -d^{\dagger}_{\alpha\sigma} \end{array} \right. . \tag{1.4.1}$$

We see that the quantity $n_{\alpha\sigma}$ is not invariant under this transformation. However, one can show that the term $(n_\alpha - 1)^2$ is invariant, where we denote $n_\alpha = n_{\alpha\uparrow} + n_{\alpha\downarrow}$. This term can be made explicit in the Hamiltonian by 'completing-the-square' in terms of the n_α operators. Noting our assumption of isotropy, we see that when $U_{12} = 0$, H is p-h symmetric if $\epsilon_\alpha = -U_\alpha/2$. When $U_{12} \neq 0$, we propose and easily check that the quantity $(n_1 - 1)(n_2 - 1)$ is invariant under (1.4.1). We rewrite H_{C} as

$$H_{\mathrm{C}} = U_{12}(n_1 - 1)(n_2 - 1) + U_{12}(n_1 + n_2) - U_{12}. \tag{1.4.2}$$

The atomic Hamiltonian (which doesn't include the trivially p-h symmetric bath electrons) now takes the form

$$\begin{aligned} H_{\mathrm{imp}} = \sum_\alpha & \left[\left(\epsilon_\alpha + \frac{U_\alpha}{2} + U_{12} \right) n_\alpha + \frac{U_\alpha}{2}(n_\alpha - 1)^2 - \frac{U_\alpha}{2} \right] \\ & + U_{12}(n_1 - 1)(n_2 - 1) - U_{12}. \end{aligned} \tag{1.4.3}$$

We have suppressed H_{M}, since it interacts only in the spin channel, so does not play a role here. We see immediately that a new condition for p-h symmetry is obtained;

$$\epsilon_\alpha = -\frac{U_\alpha}{2} - U_{12}. \tag{1.4.4}$$

The p-h symmetric Hamiltonian maps to the same low energy FP for all U_α and Δ_α, in which there is a single (quasi)particle localised at each impurity site [59], such that $\pi\Delta_\alpha\rho_\alpha(0) = 1$. The symmetry of the charge degrees of freedom in the

---

[2] Note that we take $\epsilon_{\alpha-k} = -\epsilon_{\alpha k}$, ensuring that energy remains positive when k, which we will take as 1-dimensional, goes negative. Such assumptions are common in systems which can be reduced to 1 spatial dimension [61], and this is required by the conformal field theory approach to impurity problems, which requires linear dispersion [62].

p-h symmetric 2IAM is enhanced from U(1) to SU(2) in each channel, so that the uncoupled model is invariant under SO(4)⊗SO(4), where SO(4) ≅ SU(2)⊗SU(2). This suggests that the model can be considered entirely in terms of spin and isospin; and provides a neat connection to a Majorana Fermion model which we discuss in chapter 5. Away from p-h symmetry, the low-energy behaviour is governed by a line of FPs (which are mapped back to the bare parameters). The spectral densities then develop a quasiparticle peak away from the Fermi level.

In our detailed discussion on SU(4) symmetry in chapter 4 we will make use of p-h symmetry, particularly for the half filled $n = n_1 + n_2 = 2$ model. The fact that the spectral density close to the Fermi level is fixed by p-h symmetry will be exploited by comparison to the p-h assymetric SU(4) case which occurs in the quarter-filled model $n = 1$. Our comparison shines light on recent experimental and theoretical investigations of emergent SU(4) behaviour in the 2IAM. Meanwhile, in chapter 5, p-h symmetry is responsible for the emergence of 2-impurity Kondo physics from the 2IAM, which we compare to Majorana Fermion models and a BCFT approach. The notion that p-h symmetry restricts our low-energy FPs is used extensively throughout our work.

1.5 Anderson Systems in Experiment: Magnetic Impurities and Quantum Nanostructures

Over the last 6 decades, there have been many experiments on magnetic impurities embedded in metallic hosts. These experiments have yielded great insight into the single-spin Kondo effect, and also the multi-channel Kondo effect [63]. However, it has been experimentally difficult to study systems involving coupled impurities and impurities on a lattice. In the 1990s, with the advent of precise quantum dot engineering and quantum metamaterials, it became possible to exploit the Coulomb blockade and contain a controllable number of electrons in a quantum dot, whilst tunnel coupling them to an electron bath [64, 65, 66, 67, 68]. Such a system is a tunable implementation of the 1IAM. The subsequent experiments observed the Kondo effect [69, 3] and renewed interest in the field, particularly with regard to ‘exotic’ Kondo states and critical behaviour.

Conventional Quantum Dots (QDs) are crystalline semiconductor heterostructures

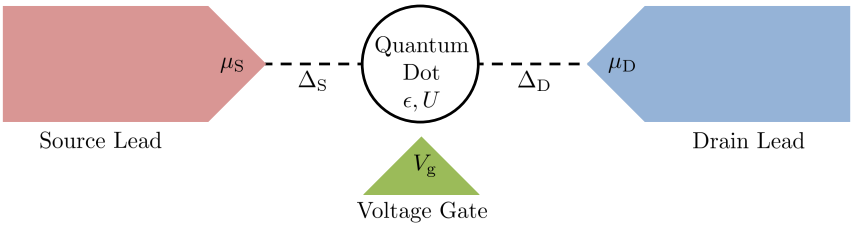

FIGURE 1.1: Gated QD Schema. The QD system is coupled, via tunnelling mechanisms to two baths of electrons, a source and a drain, with coefficients Δ_S and Δ_D. The source and drain respectively have chemical potentials μ_S and μ_D. The gate voltage is responsible for the application of a local electric field to the QD, and can continuously vary the local electrostatic energy, allowing one to vary ϵ with respect to μ_S and μ_D.

where the dot material, with a lower bandedge than the bulk material, is constrained in all dimensions and permits the presence of a few isolated electrons [70]. Due to the quasi-zero-dimensional structure, electrons in the dot are localised (there is no dispersion). The use of QDs to design devices with precisely engineered properties is now widespread, and has been applied to laser [71, 72, 73], solar cell [74, 75], spintronic [76] and transistor [77] devices. The QD systems relevant to us are gated. Such structures are designed by creating a quasi-two-dimensional electron gas in a heterostructure consisting of semiconductor and metal layers, where confinement is achieved by means of electrodes.

To demonstrate the Kondo effect, a QD system where the localised dot states are tunnel-coupled to a bath is necessary [78, 79]. An experimentally accessible model is illustrated in figure 1.1, where the QD is tunnel-coupled to a source and drain bath of electrons, with respective chemical potentials of μ_S and μ_D. The hybridisation widths are respectively denoted by Δ_S and Δ_D. The current through the dot system (or its conductance) may be measured, and used to determine the properties of the many-body states present in the system [80]. At this point it is important to note that despite the presence of an electric field, and a current flowing through the dot, the local occupation can be very finely controlled thanks to the Coulomb blockade and applied gate voltage V_g. The potential for the system, shown in figure 1.2, illustrates that bulk electrons close to the QD are unlikely (at low temperatures) to be able to tunnel through unless they do so one at a time. This is the Coulomb blockade, due to the local Coulomb repulsion U and the Pauli exclusion

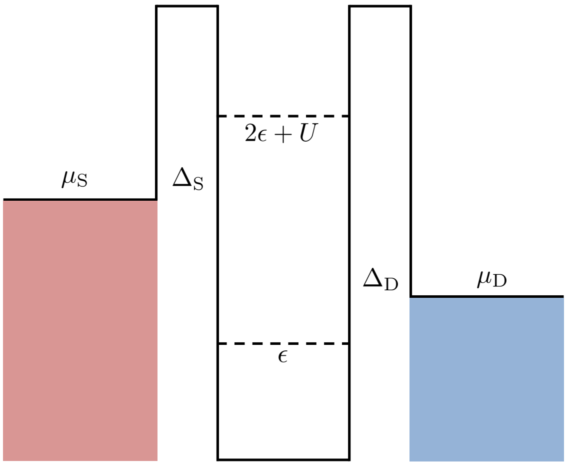

Figure 1.2: A QD representation of the 1IAM. The black solid line represents the chemical potential, whilst the red and blue sections respectively illustrate the source and drain bulk. The dot is sufficiently small that it permits only 2 states, whose energies are represented by the dotted lines. The lowest allowed energy in the quantum dot is ϵ, and the next highest (localised) state has energy $2\epsilon + U$.

principle. However, bulk electrons with higher energies could occupy the higher energy localised states in the QD, which is problematic if one wants to use a large source-drain voltage - this is where V_g becomes important. Let us suppose that the voltage gate has a capacitance C_g. By varying V_g one can induce a 'continuous charge' $q = C_\mathrm{g}V_\mathrm{g}$, which the QD seeks to cancel. Hence one can tune, very precisely, the number of electrons which are energetically favourable to remain in the QD [81]. In this way, unintentional processes involving undesired local occupancy in the QD can be eliminated.

Although this setup can restrict the number of electrons localised in the QD, it does not place any conditions on the spin. As a result, if there is a single electron local to the QD, the usual twofold spin degeneracy arises. The local spin is therefore able to undergo spin-flip processes, via virtual states such as that shown in figure 1.3, with no energy cost. These spin-flip processes are responsible for the development of a strongly correlated many-body state which leads to a narrow resonance in the local density of states at the Fermi level (the Kondo or Abrikosov-Suhl resonance) and gives rise to the Kondo effect [59]. To realise the Kondo effect in a QD system, we require equilibrium, such that $\mu_\mathrm{S} = \mu_\mathrm{D}$, and that there is a single,

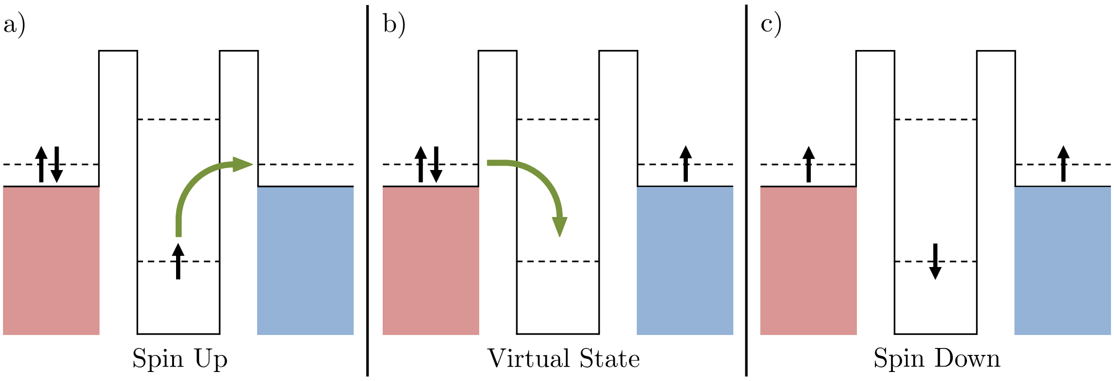

Figure 1.3: Example of a spin-flip process, by means of a virtual state, for the $S = 1/2$ Kondo effect occurring in a QD. Repeated spin-flip processes are responsible for screening the local moment, giving rise to the formation of a Kondo many-body singlet state.

well defined Fermi level around which the resonance forms. Away from equilibrium, the resonance splits into two, with a peak at the Fermi level of each bath [3]. The usual $S = 1/2$ single-channel[3] Kondo effect has been unambiguously observed in such QD systems [3, 69]. Furthermore, we see that the equilibrium QD system provides a simple realisation of the 1IAM; one has local dot electrons which are exchanged with a bath by means of tunnelling, and there is a local Coulomb interaction. It is therefore not surprising that on low energy scales, one observes the Kondo effect.

Double QD (DQD) systems can also be grown [82, 83], and these can be used to construct realisations of two-impurity Anderson systems, as depicted in figure 1.4. In this setup, each impurity is represented by a 2-level dot system as in figure 1.2 and tunnel-coupled to a source and drain lead. The material system must be engineered so that the desired interdot interactions are present. For example, to prevent interdot hopping, the material separating the dots should have a very high chemical potential, so that electron tunnelling is prohibited; the dot systems can be brought spatially close together to permit a Coulomb. We note that there are limitations on the extent to which one may choose the interdot interactions. The presence of a Heisenberg exchange is often accompanied by a hopping, as in [84]. If each source and drain is in equilibrium, so that $\mu_{S\alpha} = \mu_{D\alpha}$, then the system is well represented by the usual 2IAM (we prove this in section 4.2). For our discussions we restrict

---

[3] The condition of equilibrium introduces a degeneracy between the source and drain leads, and this can be exploited to obtain the 1IAM.

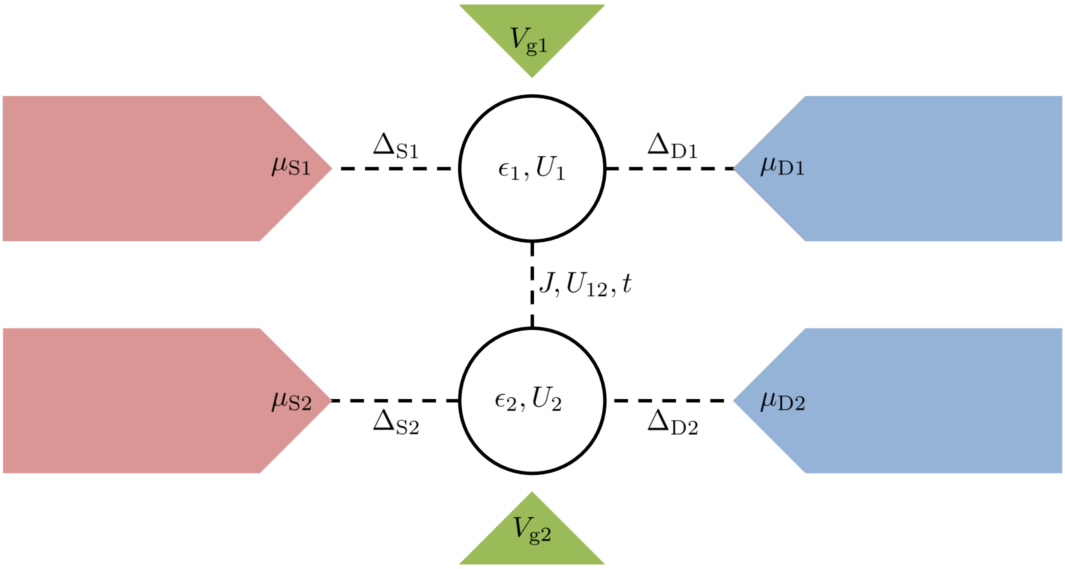

FIGURE 1.4: Schema of a DQD. Two QDs are grown close to each other, and coupled to their own source and drain baths. The material between the local QDs, and the distance between them, determines any interdot interactions which might take place.

the system to be in equilibrium, since there are numerical difficulties in extending this approach to the non-equilibrium case (4 channels are required). Similar setups have been used to investigate quantum phase transitions [85] and emergent exotic Kondo states, such as the SU(4) Kondo effect [85, 86]. In chapter 4 we discuss recent developments in the experimental observation of the SU(4) Kondo effect which have taken place for this kind of DQD system.

Chapter 2

Numerical Renormalisation Group Calculations

The NRG provides non-perturbative insight into the behaviour of quantum impurity systems over all energy scales below the bare. The use of the NRG to solve the Kondo problem marked a milestone in condensed matter physics; Wilson had introduced the RG to the field, and his numerical method could, at least in principle, be applied to any interacting system hybridised to a non-interacting electron bath. Initially it was used just to calculate static thermodynamic quantities, but it has been generalised to calculate dynamic quantities and renormalised parameters. We formulate the NRG for the 2IAM and explain in detail our calculations of static and dynamic quantities.

2.1 Construction of the NRG for the 2IAM

Our model of interest is the 2IAM where there is a capacitive coupling U_{12} and magnetic Heisenberg coupled J between the impurities,

$$\begin{aligned} H = &\sum_{\alpha \boldsymbol{k}} \epsilon_{\alpha \boldsymbol{k}} c^{\dagger}_{\alpha \boldsymbol{k} \sigma} c_{\alpha \boldsymbol{k} \sigma} + \sum_{\alpha \boldsymbol{k}} V_{\alpha} \left[c^{\dagger}_{\alpha \boldsymbol{k} \sigma} d_{\alpha \sigma} + d^{\dagger}_{\alpha \sigma} c_{\alpha \boldsymbol{k} \sigma} \right] + \sum_{\alpha} \epsilon_{\alpha} d^{\dagger}_{\alpha \sigma} d_{\alpha \sigma} \\ &+ \sum_{\alpha} U_{\alpha} n_{\alpha \uparrow} n_{\alpha \downarrow} + U_{12} \sum_{\sigma \sigma'} n_{1\sigma}\, n_{2\sigma'} + 2J \boldsymbol{S}_1 \cdot \boldsymbol{S}_2 \end{aligned} \tag{2.1.1}$$

where U_{α}, ϵ_{α} and V_{α} are respectively the local Coulomb, level and hybridisation coupling constants for the impurity/channel labelled by $\alpha \in \{1, 2\}$. Each impurity system in the 2IAM may be mapped to an interacting 2-body site coupled to a semi-infinite chain of non-interacting 2-body sites. The interacting site contains a local Coulomb interaction, but electrons on the chain may only hop between adjacent sites. We provide an outline of this prolonged mapping, with a pictorial representation in figure 2.1, but the details are widely available (for example, see [23] or [24]). The crucial starting point of the NRG is to perform a logarithmic discretisation of k-space, which spans $[-1, 1]$. The wavevector k is defined by $k = \epsilon/D$. We take a parameter $\Lambda > 1$, and let the n^{th} interval of k-space span $\left[\Lambda^{-(n+1)}, \Lambda^{-n}\right]$ as in figure 2.1a. In each region of k-space we build, by means of a Fourier expansion, a complete set of orthonormal functions $\psi^{\pm}_{np}(k)$ where $p \geq 0$ and $n = 0, 1, 2 \ldots p$. We then expand the original electron operators $c_{\alpha\mathbf{k}\sigma}$ in the basis spanned by these functions (as a Bogoliubov transformation) to obtain two new species of independent electron operators; $a_{\alpha np\sigma}$ and $b_{\alpha np\sigma}$. The impurity α is manifestly coupled only to $a_{\alpha n0\sigma}$ and $b_{\alpha n0\sigma}$, but these themselves are coupled to higher p operators. However, for $\Lambda \approx 1$ this coupling is weak, and we neglect higher p contributions to our Hamiltonian. Under this approximation, only interactions between the impurity and bulk s-waves are considered, as in figure 2.1b. Finally, using a unitary transformation, we construct new Fermionic operators $c_{\alpha n\sigma}$ from $a_{\alpha np\sigma}$ and $b_{\alpha np\sigma}$ such that our discrete approximation to (2.1.1) is

$$
\begin{aligned}
H = &\sum_{\alpha}\sum_{n=0}^{\infty} \xi_n \Lambda^{-n/2}\left[c^{\dagger}_{\alpha n\sigma} c_{\alpha(n+1)\sigma} + c^{\dagger}_{\alpha(n+1)\sigma} c_{\alpha n\sigma}\right] + \sum_{\alpha} V_{\alpha}\left[c^{\dagger}_{\alpha 0\sigma} d_{\alpha\sigma} + d^{\dagger}_{\alpha\sigma} c_{\alpha 0\sigma}\right] \\
&+ \sum_{\alpha} \epsilon_{\alpha} d^{\dagger}_{\alpha\sigma} d_{\alpha\sigma} + \sum_{\alpha} U_{\alpha} n_{\alpha\uparrow} n_{\alpha\downarrow} + U_{12}\sum_{\sigma\sigma'} n_{1\sigma}\, n_{2\sigma'} + 2J\boldsymbol{S}_1 \cdot \boldsymbol{S}_2
\end{aligned}
\tag{2.1.2}
$$

where the Wilson coefficients ξ_n are defined by

$$
\xi_n = \frac{\left(1 + \Lambda^{-1}\right)\left(1 - \Lambda^{-n-1}\right)}{2\sqrt{\left(1 - \Lambda^{-2n-1}\right)\left(1 - \Lambda^{-2n-3}\right)}}, \tag{2.1.3}
$$

and the index $n \geq 0$ label sites on a tight-binding chain of non-interacting electrons. This representation is illustrated in figure 2.2. $n = 0$ corresponds to the non-interacting conduction site adjacent to the impurity. Although seemingly abstract, there is a physical interpretation of this non-exact mapping. The many-body states represented by $c^{\dagger}_{\alpha n\sigma}$ can be thought of as being somewhat localised to the impurity. In this picture, the state $c^{\dagger}_{\alpha 0\sigma}$ is formed of conduction electrons which are the most localised to the impurity, and the 'degree of localisation' decreases (as a power law) down the chain. This chain representation allows us to simply build a basis in which to solve the Hamiltonian. It is also important to note that the hopping amplitude between sequential sites on the linear chain falls off as a power law for large n. Consequently, a good approximation for the Hamiltonian is to solve the system for

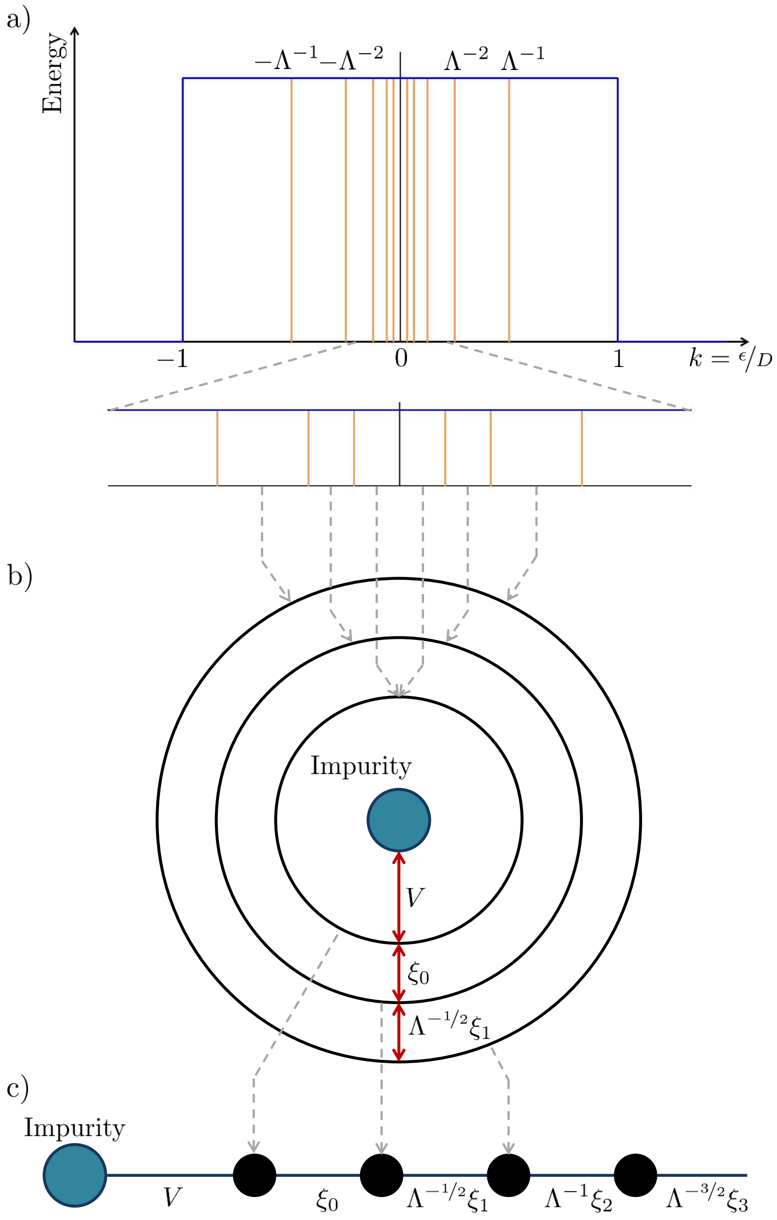

FIGURE 2.1: Representation of the mapping from the continuous Anderson model to the discrete linear chain. For simplicity, we illustrate the mapping for the 1IAM, but the same arguments apply to the 2IAM. In a) we discretise the conduction band into logarithmic intervals centered on the Fermi level. These intervals are each expanded into Fermionic S, P, D etc. Fourier modes and in b) we claim that only the S waves interact with the impurity. In c) we represent this picture as a linear chain.

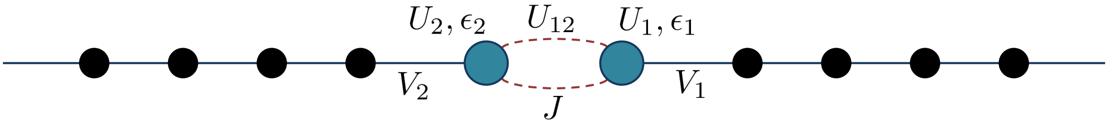

FIGURE 2.2: Linear chain representation of the 2IAM.

a finite number of sites on the chain [24]. To formulate an RG treatment of this model, we define

$$\begin{aligned} H_0 = \Lambda^{-1/2} \sum_{\alpha} \Big[\epsilon_\alpha d^\dagger_{\alpha\sigma} d_{\alpha\sigma} + V_\alpha \left[c^\dagger_{\alpha 0\sigma} d_{\alpha\sigma} + d^\dagger_{\alpha\sigma} c_{\alpha 0\sigma} \right] + U_\alpha n_{\alpha\uparrow} n_{\alpha\downarrow} \Big] \\ + \Lambda^{-1/2} U_{12} \sum_{\sigma\sigma'} n_{1\sigma}\, n_{2\sigma'} + 2\Lambda^{-1/2} \boldsymbol{J} \boldsymbol{S}_1 \cdot \boldsymbol{S}_2 \end{aligned} \tag{2.1.4}$$

and set up the iteration scheme

$$H_{N+1} = \Lambda^{1/2} H_N + \sum_{\alpha} \xi_N \left[c^\dagger_{\alpha N\sigma} c_{\alpha(N+1)\sigma} + c^\dagger_{\alpha(N+1)\sigma} c_{\alpha N\sigma} \right]. \tag{2.1.5}$$

With the imposition of an energy cutoff, the mapping $\mathcal{R} : H_N \mapsto H_{N+1}$ defined by (2.1.5) belongs to the RG. We see that

$$H = \lim_{N\to\infty} \Lambda^{-(N-1)/2} H_N, \tag{2.1.6}$$

implying that if our bare energy scale is D, then after N iterations the remaining energy levels exist on a scale $\Lambda^{-(N-1)/2} D$. The setup of the iteration scheme and the scaling of the energy levels is depicted in figure 2.3. The NRG therefore consists of iterating transformation (2.1.5) until a stable FP, describing the $T = 0$ behaviour of the model, is reached (when $H_{N+2} = H_N$)[1]. The transformation is implemented by supposing we have two N site Wilson chains forming a system denoted by H_N; we then couple the ends of the chain to two new sites and calculate the resulting Hilbert space.

---

[1] An important point is that $\mathcal{R}$ adds a single site to each chain. When the chain length is odd, the vacuum (half-filled chain) will consist of an odd number of electrons and is thus degenerate due to spin. The even N vacuum is usually not degenerate. This leads to even-odd oscillations in the RG flow. The useful transformation is in fact $\mathcal{R}^2 : H_N \mapsto H_{N+2}$, and we generally calculate our quantities using only even N. There are a number of approaches to averaging over the oscillations, and for a more detailed discussion see [23].

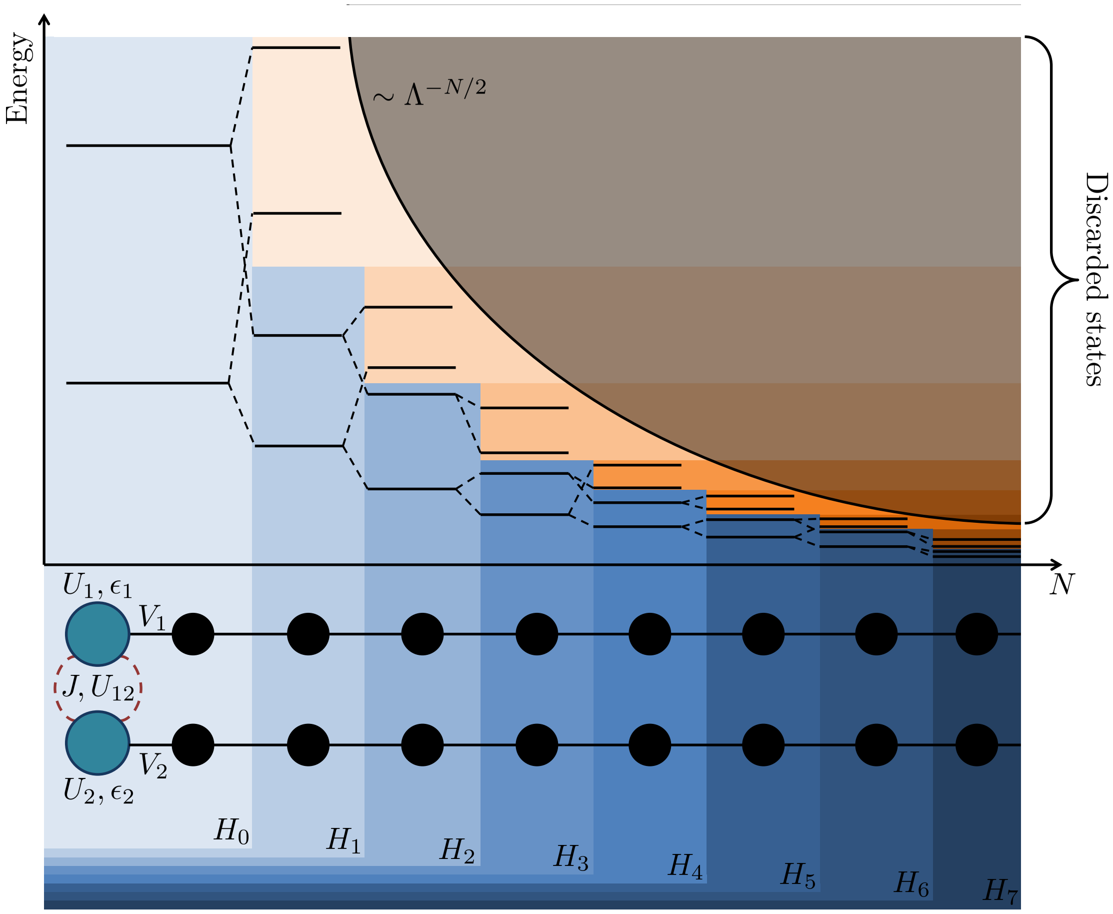

FIGURE 2.3: Schema of the NRG as applied to the 2IAM. The bare Hamiltonian is approximated by $\Lambda^{-(N-1)/2} H_N$ as N is increased. The transformation $\mathcal{R} : H_N \mapsto H_{N+1}$ generates new levels in the Hilbert space, the successive truncation of which leads to a power law reduction in the NRG levels as N increases. The initial Hamiltonian H_0 describes the local impurity system and the hybridisation to the conduction sites, whilst the Hamiltonians H_1, H_2 etc successively add a single site to each chain.

2.2 Iterative Diagonalisation

The process of building the new eigenspace H_{N+1} from an old eigenspace H_N is termed iterative diagonalisation. The first stage is to define a new basis which spans H_{N+1}. It is most convenient to use the eigenstates of H_N in these definitions so that iteration is permitted. For computational efficiency, the states must be labelled by as many quantum numbers as possible. Our Hamiltonian (2.1.2) does not permit the transfer of charge between the impurities or channels, and therefore is invariant under U(1)⊗U(1). Additionally, the absence of a magnetic field implies an SU(2) spin degeneracy. We thus denote the eigenstates of H_N by $|Q_1, Q_2, S, S_z, r; N\rangle$, where Q_α labels the charge in channel α (with respect to the half-filled chain), S is the total spin, S_z is the spin projection onto the z-axis, and r labels the states contained in the $\{Q_1, Q_2, S, S_z\}$ sector. Each new site, labelled by N, on the chain α permits four states: $|0; N\rangle_\alpha, |\uparrow; N\rangle_\alpha, |\downarrow; N\rangle_\alpha$ and $|\uparrow\downarrow; N\rangle_\alpha$. H_{N+1} is thus spanned by

$$\Big\{ |Q_1, Q_2, S, S_z, r; N\rangle \Big\} \bigotimes_\alpha \Big\{ |0; N+1\rangle_\alpha, |\uparrow; N+1\rangle_\alpha, |\downarrow; N+1\rangle_\alpha, |\uparrow\downarrow; N+1\rangle_\alpha \Big\}. \tag{2.2.1}$$

The states for the sites being added and those of H_N are spinful, so we must combine the angular momenta according to the usual rules. For combining three angular momentum vectors, we are free to first combine any two, and then combine the result with the third angular momentum [87, 88]. We choose to first combine the previous eigenstates to the channel 2 new site basis states. We define the basis states, labelled as $|Q_1, Q_2, S, S_z, r, i; N\rangle$, for the intermediate system as

$$|Q_1, Q_2, S, S_z, r, 0; N\rangle = |0; N+1\rangle_2 \, |Q_1, Q_2+1, S, S_z, r; N\rangle$$

$$\begin{aligned} &|Q_1, Q_2, S, S_z, r, 1; N\rangle \\ &\qquad = |{\uparrow}; N+1\rangle_2 \, |Q_1, Q_2, S-{}^1\!/_2, S_z-{}^1\!/_2, r; N\rangle \, \langle S-{}^1\!/_2, S_z-{}^1\!/_2; {}^1\!/_2, {}^1\!/_2 | S, S_z\rangle \\ &\qquad + |{\downarrow}; N+1\rangle_2 \, |Q_1, Q_2, S-{}^1\!/_2, S_z+{}^1\!/_2, r; N\rangle \, \langle S-{}^1\!/_2, S_z+{}^1\!/_2; {}^1\!/_2, -{}^1\!/_2 | S, S_z\rangle \end{aligned}$$

$$\begin{aligned} &|Q_1, Q_2, S, S_z, r, 2; N\rangle \\ &\qquad = |{\uparrow}; N+1\rangle_2 \, |Q_1, Q_2, S+{}^1\!/_2, S_z-{}^1\!/_2, r; N\rangle \, \langle S+{}^1\!/_2, S_z-{}^1\!/_2; {}^1\!/_2, {}^1\!/_2 | S, S_z\rangle \\ &\qquad + |{\downarrow}; N+1\rangle_2 \, |Q_1, Q_2, S+{}^1\!/_2, S_z+{}^1\!/_2, r; N\rangle \, \langle S+{}^1\!/_2, S_z+{}^1\!/_2; {}^1\!/_2, -{}^1\!/_2 | S, S_z\rangle \end{aligned}$$

$$|Q_1, Q_2, S, S_z, r, 3; N\rangle = |{\uparrow\downarrow}; N+1\rangle_2 \, |Q_1, Q_2-1, S, S_z, r; N\rangle \tag{2.2.2}$$

where we introduce an index $i \in \{0, 1, 2, 3\}$ which labels the basis states. We go on to couple the intermediate system basis state-space with the channel 1 single site states to obtain a full basis space for H_{N+1}. The basis states are labelled by $|Q_1, Q_2, S, S_z, r, i, j; N\rangle$ and are calculated as

$$|Q_1, Q_2, S, S_z, r, i, 0; N\rangle = |0; N+1\rangle_1 \, |Q_1+1, Q_2, S, S_z, r, i; N\rangle$$

$$\begin{aligned} &|Q_1, Q_2, S, S_z, r, i, 1; N\rangle \\ &\qquad = |{\uparrow}; N+1\rangle_1 \, |Q_1, Q_2, S-{}^1\!/_2, S_z-{}^1\!/_2, r, i; N\rangle \, \langle S-{}^1\!/_2, S_z-{}^1\!/_2; {}^1\!/_2, {}^1\!/_2 | S, S_z\rangle \\ &\qquad + |{\downarrow}; N+1\rangle_1 \, |Q_1, Q_2, S-{}^1\!/_2, S_z+{}^1\!/_2, r, i; N\rangle \, \langle S-{}^1\!/_2, S_z+{}^1\!/_2; {}^1\!/_2, -{}^1\!/_2 | S, S_z\rangle \end{aligned}$$

$$\begin{aligned} &|Q_1, Q_2, S, S_z, r, i, 2; N\rangle \\ &\qquad = |{\uparrow}; N+1\rangle_1 \, |Q_1, Q_2, S+{}^1\!/_2, S_z-{}^1\!/_2, r, i; N\rangle \, \langle S+{}^1\!/_2, S_z-{}^1\!/_2; {}^1\!/_2, {}^1\!/_2 | S, S_z\rangle \\ &\qquad + |{\downarrow}; N+1\rangle_1 \, |Q_1, Q_2, S+{}^1\!/_2, S_z+{}^1\!/_2, r, i; N\rangle \, \langle S+{}^1\!/_2, S_z+{}^1\!/_2; {}^1\!/_2, -{}^1\!/_2 | S, S_z\rangle \end{aligned}$$

$$|Q_1, Q_2, S, S_z, r, i, 3; N\rangle = |{\uparrow\downarrow}; N+1\rangle_1 \, |Q_1-1, Q_2, S, S_z, r, i; N\rangle \tag{2.2.3}$$

with $j \in \{0, 1, 2, 3\}$. These basis states are abbreviated as $|i, j\rangle$ below, unless the suppressed quantum numbers are required. It is important to note that the basis state

$|2,1\rangle$ does not exist if $S=0$, since the Clebsch-Gordan coefficients disallow it. To compute the eigenspace of H_{N+1}, we require the matrix elements $\langle i',j'|\,H_{N+1}\,|i,j\rangle$. We note that

$$H_N\,|Q_1,Q_2,S,S_z,r,i,j;N\rangle = E_{Q_1,Q_2,S,S_z,r}(N)\,|Q_1,Q_2,S,S_z,r,i,j;N\rangle \tag{2.2.4}$$

where the scaled energies $E_{Q_1,Q_2,S,S_z,r}(N)$ are defined by[2]

$$H_N\,|Q_1,Q_2,S,S_z,r;N\rangle = E_{Q_1,Q_2,S,S_z,r}(N)\,|Q_1,Q_2,S,S_z,r;N\rangle\,. \tag{2.2.5}$$

It follows that, in our defined basis, the diagonal elements of H_{N+1} are simply given by

$$\langle Q_1,Q_2,S,S_z,r,i,j;N|\,H_{N+1}\,|Q_1,Q_2,S,S_z,r,i,j;N\rangle = \Lambda^{1/2}E_{Q_1,Q_2,S,S_z,r}(N). \tag{2.2.6}$$

The off-diagonal matrix elements are more complicated; they are given by $\langle i',j'|\,H'\,|i,j\rangle$ where

$$H' = \xi_N \sum_{\alpha} c^{\dagger}_{\alpha N\sigma} c_{\alpha(N+1)\sigma} \tag{2.2.7}$$

and we compute only half the elements of the Hamiltonian, and then symmetrise it, for the sake of efficiency. It thus follows that the off-diagonal components depend on the matrix elements

$$\langle Q_1',Q_2',S',S_z',r';N|\,c^{\dagger}_{\alpha N\sigma}\,|Q_1,Q_2,S\,,S_z,r\,;N\rangle\,. \tag{2.2.8}$$

At this point, we make use of the S_z degeneracy (due to the SU(2) symmetry) to write the matrix elements as 'reduced' matrix elements, which carry only an S label. This substantially reduces the number of matrices which require diagonalisation and is achieved through application of the Wigner-Eckart theorem;

$$\begin{aligned}\langle Q_1',Q_2',S',S_z',r';N|\,c^{\dagger}_{\alpha N\sigma}\,|Q_1,Q_2,S,S_z,r;N\rangle \\ = \langle S,S_z;1/2,\sigma|S',S_z'\rangle\,\langle Q_1',Q_2',S',r';N||c^{\dagger}_{\alpha N}||Q_1,Q_2,S,r;N\rangle\,.\end{aligned} \tag{2.2.9}$$

The reduced eigenstates are simply a sum over a reduced basis,

$$|Q_1,Q_2,S,r;N\rangle = \sum_{p,i,j} U_{Q_1Q_2S}\,(r;p,i,j;N)\,|Q_1,Q_2,S,p,i,j;N-1\rangle \tag{2.2.10}$$

---

[2] Although notationally clunky, we write the scaled energies as a function of N to make explicit that these energies form an RG flow.

where the label p is summed over all states in the H_{N-1} system. The entries in the eigenvectors, given by $U_{Q_1Q_2S}\left(r;p,i,j;N\right)$ are used to compute the off-diagonal matrix elements. Each matrix element $\langle i',j'|\, H' \,|i,j\rangle$ can be written as a Clebsch-Gordon coefficient multiplied by a reduced matrix element. The allowed reduced matrix elements, which are

$$\begin{aligned}
&\langle Q_1+1, Q_2+1, S, r'; N||c^{\dagger}_{1N}||Q_1, Q_2+1, S-{}^1\!/_2, r; N\rangle\,,\\
&\langle Q_1+1, Q_2+1, S, r'; N||c^{\dagger}_{1N}||Q_1, Q_2+1, S+{}^1\!/_2, r; N\rangle\,,\\
&\langle Q_1+1, Q_2+1, S, r'; N||c^{\dagger}_{2N}||Q_1+1, Q_2, S-{}^1\!/_2, r; N\rangle\,,\\
&\langle Q_1+1, Q_2+1, S, r'; N||c^{\dagger}_{2N}||Q_1+1, Q_2, S+{}^1\!/_2, r; N\rangle\,,
\end{aligned}$$

may be calculated using the values of $U_{Q_1Q_2S}\left(r;p,i,j;N\right)$. We discuss the details of our approach to iterative diagonalisation in appendix B. We efficiently construct the Hamiltonians in a method that scales as $O(N^3)$. When the reduced matrix elements are expanded in terms of $U_{Q_1Q_2S}\left(r;p,i,j;N\right)$, the resultant expression is representable as the sum of matrix products.

It is important to exploit this fact, as there are multiple available algorithms which use cache locality to multiply matrices; this results in very significantly improved calculation speeds. The basic premise is that when the CPU loads its cache from the RAM, the loaded data will all be used in the following series of calculations. This means that the total number of times the CPU cache needs to be refreshed is reduced. By arranging the matrix data in the RAM in a particular order corresponding to the multiplication algorithm, so that the algorithm requires data from the RAM which is adjacent to each other (spatial locality), we can ensure that the cache loads only useful data for the calculations the CPU is being instructed to complete. This dramatically increases the rate of execution.

The Hamiltonians are diagonalised using an open-source library (Eigen) and for efficiency we exploit the fact that they are self-adjoint. The eigenvectors for a Hamiltonian block labelled by Q_1, Q_2 and S replace the values of $U_{Q_1Q_2S}\left(r;p,i,j;N\right)$, which are stored from the previous iteration.

The truncation routine then sorts all of the energies and determines the cut-off (if the algorithm retains N_{S} states at each iteration, then the cut-off is the ${N_{\mathrm{S}}}^{\mathrm{th}}$ highest energy). The states below the cut-off are used to compute the basis in the next iteration, but the states above are used to compute the matrix elements in that iteration; hence they are not completely discarded until then.

This procedure forms our NRG program for the 2IAM. It has been found empirically that in order to obtain a good approximation to the FP, one must use a larger value of Λ (typically $\Lambda \sim 6$) and retain many more states at each iteration compared to the single channel model [28, 89, 23]. It is surprising that the NRG approach works for these large values of Λ, but it does appear to, and good agreement with lower Λ NRG and BCFT results has been found. We take $\Lambda = 6$ and retain $N_{\mathrm{S}} = 4000$ for all our 2IAM NRG calculations, unless otherwise specified.

Our NRG is validated by setting $U_{12} = J = 0$ and enforcing channel symmetry. In this case the RG flow should converge on a stable FP whose levels are described by the single impurity Anderson model[3], and this is shown in figure 2.4.

2.3 Calculation of Static Thermodynamic Quantities

The NRG as presented offers only the low-lying energy levels of the system. The levels themselves show the FL (or more unusual) nature of the FPs of the 2IAM, but offer little insight into how physical quantities such as the spin susceptibility and entropy vary with respect to T. As we increase N, we explore energies of H on a decreasing energy scale (see figure 2.3). We can therefore think of an increase in N as a decrease in T. We explain this as follows. The Hamiltonian H_N defined by (2.1.5) typically has eigenvalues of the order $\lim_{N\to\infty} \xi_N = (1 + \Lambda^{-1})/2$, and contributes unscaled eigenvalues of the order $\Lambda^{-(N-1)/2}$ to the spectrum of H (one can see this from (2.1.6)). For an iteration N, we thus rewrite the Boltzmann factor $\exp(-\beta H)$, where $\beta = 1/T$, as $\exp\left(-\bar{\beta} H_N\right)$ in which $\bar{\beta}$ encapsulates a temperature scaled by the aforementioned factors. When we compute the trace of $\exp\left(-\bar{\beta} H_N\right)$, the only significant terms are those for which $\bar{\beta} E_{Q_1,Q_2,S,r}(N)$ is of order 1 (or below). This is the case for a characteristic temperature T_N, defined by

$$T_N = \frac{1}{2}\left(1 + \frac{1}{\Lambda}\right)\Lambda^{-(N-1)/2}\bar{\beta}^{-1} \tag{2.3.1}$$

---

[3] If the single impurity Anderson model has a Hilbert space $\mathcal{H}_1$ then the 2IAM with these properties will have the Hilbert space $\mathcal{H}_2 = \mathcal{H}_1 \otimes \mathcal{H}_1$.

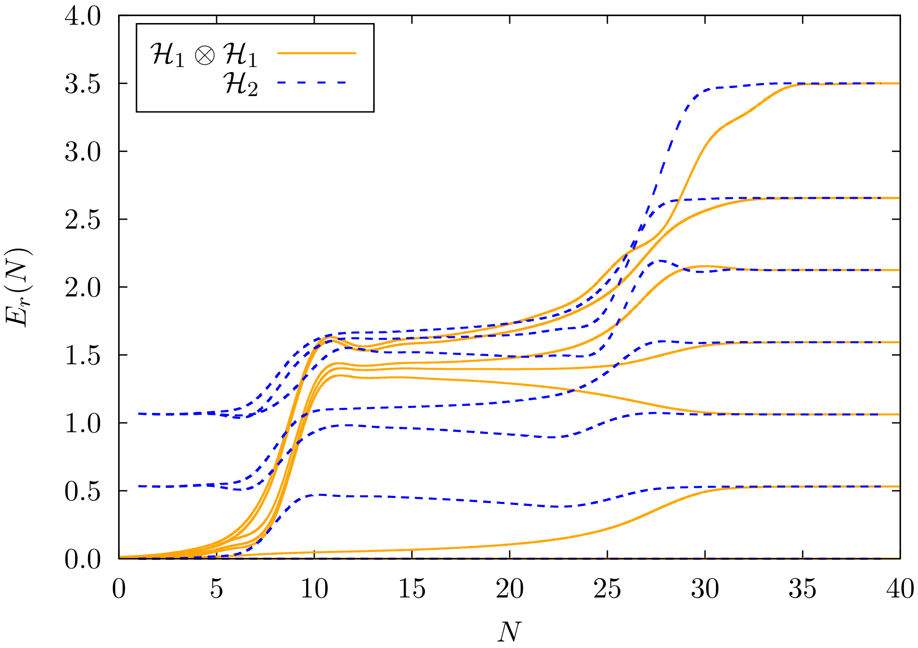

FIGURE 2.4: The RG flow of the lowest distinct energy eigenvalues of the 1IAM and 2IAM, whose Hilbert spaces are respectively denoted $\mathcal{H}_1$ and $\mathcal{H}_2$. The coupling constants in both models are equal, and all inter-impurity interactions in the 2IAM are switched off. We expect $\mathcal{H}_2 = \mathcal{H}_1 \otimes \mathcal{H}_1$, which holds at the stable FL RG FP (for $N > 32$). The RG flow for the models pass by the same 3 FPs, but the levels are different. This does not imply the models are different, just that the RG flows take different trajectories. The NRG parameters are $\epsilon = -0.0005$, $U = 0.001$, $V = 0.004$, $\Lambda = 6.0$ and $N_{\text{S}} = 4000$.

where $\bar{\beta} \sim 1$ (we take $\bar{\beta} = 1.04$). By exploiting this, we can calculate the thermodynamic properties of the impurity over all temperature scales reached in the NRG iteration. A more detailed discussion of these arguments is presented in [23]. The entropy and uniform spin susceptibility of the entire system, $S^{\mathrm{tot}}(T)$ and $\chi^{\mathrm{tot}}(T)$ respectively, are defined by

$$S^{\mathrm{tot}}(T) = \beta \left\langle\!\left\langle H \right\rangle\!\right\rangle + \ln\left(Z\right), \tag{2.3.2}$$

$$\chi^{\mathrm{tot}}(T) = \beta \left[\left\langle\!\left\langle {S_z}^2 \right\rangle\!\right\rangle - \left\langle\!\left\langle S_z \right\rangle\!\right\rangle^2 \right], \tag{2.3.3}$$

whilst the thermal trace $\langle\!\langle \mathcal{O} \rangle\!\rangle$ is

$$\left\langle\!\left\langle \mathcal{O} \right\rangle\!\right\rangle = \frac{1}{Z} \mathrm{Tr} \left(\mathrm{e}^{-\beta H} \mathcal{O} \right). \tag{2.3.4}$$

The partition function is given by $Z := \mathrm{Tr}\left(\mathrm{e}^{-\beta H}\right)$. The impurity contribution to these quantities is

$$S(T) = S^{\mathrm{tot}}(T) - S^0(T) \tag{2.3.5}$$

and

$$\chi(T) = \chi^{\mathrm{tot}}(T) - \chi^0(T), \tag{2.3.6}$$

respectively, where the superscript '0' denotes that the quantity corresponds to the free tight-binding chain without the impurity present. This definition of the thermodynamic quantities was introduced in [21]. For a given NRG iteration N, we approximate the thermal trace as

$$\left\langle\!\left\langle \mathcal{O} \right\rangle\!\right\rangle_N \simeq \frac{1}{Z_N} \sum_{Q_1,Q_2,S} \sum_r \left(2S+1\right) \mathrm{e}^{-\bar{\beta} E_{Q_1,Q_2,S,r}(N)} \left\langle Q_1, Q_2, S, r; N \right| \mathcal{O} \left| Q_1, Q_2, S, r; N \right\rangle \tag{2.3.7}$$

where we sum over reduced eigenstates and account for the spin degeneracy. Z_N is the partition function at temperature T_N, and given by

$$Z_N = \sum_{Q_1,Q_2,S} \sum_r \left(2S+1\right) \mathrm{e}^{-\bar{\beta} E_{Q_1,Q_2,S,r}(N)}. \tag{2.3.8}$$

It follows that the thermodynamic quantities corresponding to the entire system H can be calculated for all temperatures below the bare energy scale. The impurity contribution to $S(T)$ and $\chi(T)$ is determined by calculating these quantities for the 'no-impurity' Hamiltonian

$$H_N^0 = \sum_\alpha \sum_{n=0}^{N-1} \xi_n \Lambda^{(N-n-1)/2} \left[c^\dagger_{\alpha n \sigma} c_{\alpha (n+1) \sigma} + c^\dagger_{\alpha (n+1) \sigma} c_{\alpha n \sigma} \right] \tag{2.3.9}$$

and subtracting them from the total quantities. The thermodynamic quantities of this quadratic Hamiltonian are calculated in appendix C, where we specialise to the case N even and transform H_N^0 to have the form

$$H_N^0 = \sum_\alpha \eta_0^{\mathrm{E}} p_{\alpha 0\sigma}^\dagger p_{\alpha 0\sigma} + \sum_\alpha \sum_{n=1}^{N/2} \eta_n^{\mathrm{E}} \left[p_{\alpha n\sigma}^\dagger p_{\alpha n\sigma} + h_{\alpha n\sigma}^\dagger h_{\alpha n\sigma} \right]. \tag{2.3.10}$$

The single particle energies are denoted η_n^{E}, $n \geq 0$ and are equal for particle and hole excitations in channel α created respectively by $p_{\alpha n\sigma}^\dagger$ and $h_{\alpha n\sigma}^\dagger$. This is due to the p-h symmetry of the bulk. We derive the partition function of the conduction system as

$$\ln(Z_N^0) = 4 \ln\left(1 + \mathrm{e}^{-\bar{\beta}\eta_0^{\mathrm{E}}}\right) + 8 \sum_{n=1}^{N/2} \ln\left(1 + \mathrm{e}^{-\bar{\beta}\eta_n^{\mathrm{E}}}\right), \tag{2.3.11}$$

while we obtain the traces

$$\langle\langle H \rangle\rangle_N^0 = 4 \frac{\eta_0^{\mathrm{E}} \mathrm{e}^{-\bar{\beta}\eta_0^{\mathrm{E}}}}{\left(1 + \mathrm{e}^{-\bar{\beta}\eta_0^{\mathrm{E}}}\right)} + 8 \sum_{n=1}^{N/2} \frac{\eta_n^{\mathrm{E}} \mathrm{e}^{-\bar{\beta}\eta_n^{\mathrm{E}}}}{\left(1 + \mathrm{e}^{-\bar{\beta}\eta_n^{\mathrm{E}}}\right)} \tag{2.3.12}$$

and

$$\langle\langle S_z^2 \rangle\rangle_N^0 = \frac{\mathrm{e}^{-\bar{\beta}\eta_0^{\mathrm{E}}}}{\left(1 + \mathrm{e}^{-\bar{\beta}\eta_0^{\mathrm{E}}}\right)^2} + 2 \sum_{n=1}^{N/2} \frac{\mathrm{e}^{-\bar{\beta}\eta_n^{\mathrm{E}}}}{\left(1 + \mathrm{e}^{-\bar{\beta}\eta_n^{\mathrm{E}}}\right)^2}. \tag{2.3.13}$$

The trace over S_z vanishes when there is no magnetic field. We are thus able to compute $S^0(T_N)$ and $\chi^0(T_N)$ for any even N, and it follows that we are able to compute the impurity contributions $S(T)$ and $\chi(T)$ over all the energy scales reached by the NRG. As with the iterative diagonalisation routines, we validate our approach by studying the 2IAM with no inter-impurity coupling; the results for $S(T)$ and $\chi(T)$ are shown in figure 2.5. Using the Boltzmann entropy $S = \ln(\Omega)$, where Ω is the multiplicity of the system, we see that at high temperatures, the impurity system contributes 16 states to the total Hilbert space. This is due to each impurity site permitting the usual four states. However, as the temperature is lowered U becomes relatively large compared to the energy scale of the system, and the states $|0\rangle$ and $|\uparrow\downarrow\rangle$ (recall that these are degenerate for p-h symmetry) become unfavourable. These degrees of freedom are frozen out and each impurity becomes occupied by a single electron with spin degeneracy. The presence of a single electron is responsible for the emergence of a local moment FL regime in each impurity system, contributing 4 states. As T is further decreased, the local moment forms a tightly bound singlet with the adjacent s-waves (represented by

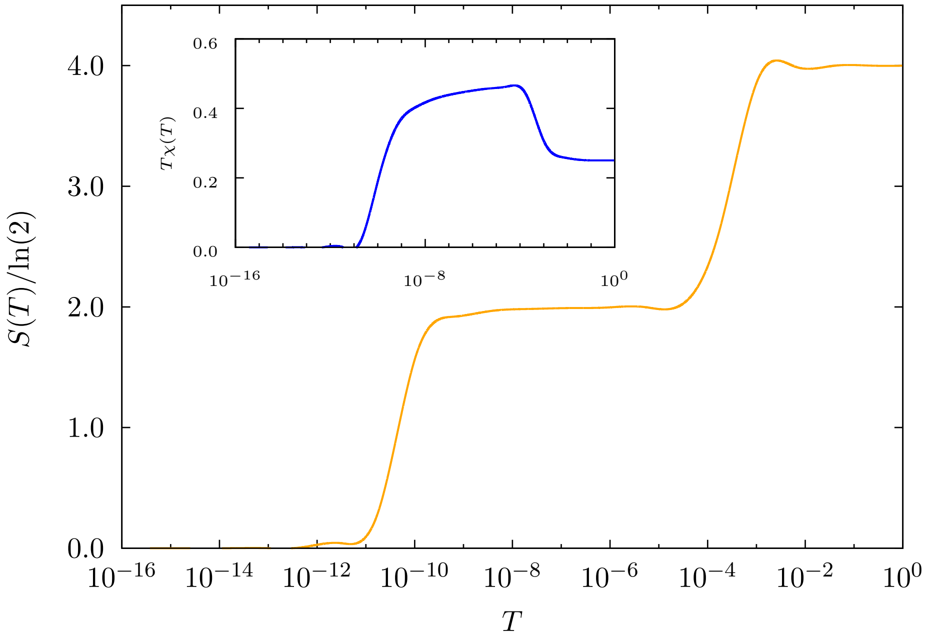

FIGURE 2.5: The entropy contribution $S(T)$ made by the impurity to the system of two uncoupled Anderson impurities as a function of temperature T. The inset shows the contributed uniform spin susceptibility $\chi(T)$. The NRG parameters are $\epsilon = -0.0005$, $U = 0.001$, $V = 0.004$, $\Lambda = 6.0$ and $N_{\mathrm{S}} = 4000$.

the first conduction site on the tight-binding chain), and becomes screened. In this FL regime the impurities are in a many-body singlet with the s-waves, and hence only contribute 1 state so that $S(T) = 0$. $\chi(T)$ varies accordingly as the system transitions between the FPs, in agreement with [24]. Our results agree with the established underlying physical picture of the 1IAM, and confirm our calculations.

2.4 Calculation of Dynamic Quantities

Originally, the NRG was used to just calculate static properties of the impurity system. In attempting to understand the process of excitation of a localised electron to the bulk via x-ray absorption, the NRG was generalised to calculate dynamic quantities [90]. Over the following two decades, the method evolved into what is now referred to as the 'conventional' method for calculation of dynamic response functions using the NRG [33, 34, 91, 31]. We outline our definitions, and the NRG calculations required, and will proceed to describe the conventional method, before expanding on the more sophisticated methods we use.

2.4.1 Green Function, Spectral Density and Susceptibility Definitions

All the dynamic quantities we calculate are related to the retarded Green function,

$$G_{AB}(t-t') = -i\Theta(t-t') \left\langle\!\left\langle \left[A(t), B(t')\right]_s \right\rangle\!\right\rangle \tag{2.4.1}$$

where we set $t' = 0$, and A and B are either Bosonic or Fermionic operators. The algebra is defined as $[A, B]_s = AB - sBA$, $s = 1$ if A and B are Fermionic, and $s = -1$ otherwise. We interpret $G_{AB}(t)$ as follows. At time $t' = 0$, the operator B acts on the vacuum to create some initial state, and at time t, A acts on this to create a final state (or vice versa). $G_{AB}(t)$ is the propagator between the initial and final states.

We are interested in the system response to some field which provides energy ω, and we thus perform a Laplace transformation to express (2.4.1) as

$$G_{AB}(z) = -i \int_0^{\infty} \mathrm{d}t \;\; \mathrm{e}^{izt} \, \mathrm{Tr}\left(\frac{\mathrm{e}^{-\beta H}}{Z} \left[A(t), B\right]_s \right) \tag{2.4.2}$$

where $\mathrm{Re}[z] = \omega$. Our correlation function between operators A and B is given by

$$\left\langle\!\left\langle A; B \right\rangle\!\right\rangle (\omega) = -\frac{1}{\pi} \lim_{\delta \to 0^+} G_{AB}(\omega + i\delta), \tag{2.4.3}$$

and the imaginary part of this is the spectral density, $\rho_{AB}(\omega) = \mathrm{Im}\,\langle\langle A; B\rangle\rangle\,(\omega)$. We now define the dynamic quantities we use throughout our investigations of the 2IAM. The local density of states[4] on impurity α is defined by

$$\rho_\alpha(\omega) = \mathrm{Im}\left\langle\left\langle d_{\alpha\sigma}; d^\dagger_{\alpha\sigma}\right\rangle\right\rangle(\omega) \tag{2.4.4}$$

and measures the amount of energy required to add (or remove) an electron to (or from) the impurity. Note that we assume that no magnetic field is present so σ may take any value without changing ρ_α. The 1-particle local spectral density on the first conduction site in channel α is denoted

$$\rho^{\mathrm{C}}_\alpha(\omega) = \mathrm{Im}\left\langle\left\langle c_{\alpha 0\sigma}; c^\dagger_{\alpha 0\sigma}\right\rangle\right\rangle(\omega). \tag{2.4.5}$$

We define the transverse spin susceptibility between impurities α and β as

$$\chi_{\alpha\beta}(\omega) = \left\langle\left\langle S^+_\alpha; S^-_\beta\right\rangle\right\rangle(\omega) \tag{2.4.6}$$

where $\alpha = \beta$ is permitted. We are particularly interested in the spin dynamics at a quantum critical point, discussed in chapter 5, where the total and staggered spin susceptibilities of the 2IAM are studied. These are respectively defined by

$$\begin{aligned}\chi_{\mathrm{tot}}(\omega) &= \langle\langle S^+_1 + S^+_2; S^-_1 + S^-_2\rangle\rangle\,(\omega)\\ &= \chi_{11}(\omega) + \chi_{12}(\omega) + \chi_{21}(\omega) + \chi_{22}(\omega)\end{aligned} \tag{2.4.7}$$

and

$$\begin{aligned}\chi_{\mathrm{stg}}(\omega) &= \langle\langle S^+_1 - S^+_2; S^-_1 - S^-_2\rangle\rangle\,(\omega)\\ &= \chi_{11}(\omega) - \chi_{12}(\omega) - \chi_{21}(\omega) + \chi_{22}(\omega).\end{aligned} \tag{2.4.8}$$

$\chi_{\mathrm{tot}}(\omega)$ measures the system response to a field which seeks to align the spins on each impurity, whilst $\chi_{\mathrm{stg}}(\omega)$ measures the response to a field seeking to oppositely align the spins. In our investigation of the critical point, we also study the response of the local singlet and triplet susceptibilities; these are defined by

$$\chi_{\mathrm{sng}}(\omega) = -\frac{1}{2}\left\langle\left\langle d^\dagger_{1\uparrow}d^\dagger_{2\downarrow} - d^\dagger_{1\downarrow}d^\dagger_{2\uparrow}; d_{2\downarrow}d_{1\uparrow} - d_{2\uparrow}d_{1\downarrow}\right\rangle\right\rangle(\omega) \tag{2.4.9}$$

and

$$\chi_{\mathrm{trp}}(\omega) = -\frac{1}{2}\left\langle\left\langle d^\dagger_{1\uparrow}d^\dagger_{2\downarrow} + d^\dagger_{1\downarrow}d^\dagger_{2\uparrow}; d_{2\downarrow}d_{1\uparrow} + d_{2\uparrow}d_{1\downarrow}\right\rangle\right\rangle(\omega). \tag{2.4.10}$$

They respectively measure the response of the system to a stimulus which creates or destroys a local singlet or triplet. The spectral density (2.4.3) satisfies certain

---

[4] Whenever we refer to spectral density without specifying any operators, we referring to $\rho_\alpha(\omega)$.

properties which we aim to reproduce in the NRG. In particular, the $T = 0$ spectral sum rule

$$\int_{-\infty}^{\infty} \mathrm{d}\omega \;\; \rho_{AB}(\omega) = \mathrm{Tr}\left[\rho\left[A, B\right]_s\right] \tag{2.4.11}$$

can be satisfied to machine precision, using the approaches in [36] and [37]. The local density of states satisfies $\int_{-\infty}^{\infty} \mathrm{d}\omega \rho_\alpha(\omega) = 1$, whilst the imaginary part of the spin susceptibilities satisfy

$$\int_{-\infty}^{\infty} \mathrm{d}\omega \;\; \mathrm{Im}\chi_{\alpha\beta}(\omega) = \frac{1}{Z}\mathrm{Tr}\left[\mathrm{e}^{-\beta H}\left[S_\alpha^+, S_\beta^-\right]\right] = \frac{2}{Z}\mathrm{Tr}\left[\mathrm{e}^{-\beta H} S_{\alpha z}\right]\delta_{\alpha\beta}. \tag{2.4.12}$$

In the absence of a magnetic field, $\int_{-\infty}^{\infty} \mathrm{d}\omega \mathrm{Im}\chi_{\alpha\beta}(\omega) = 0$ since positive and negative spin projections are degenerate. We also compute $\int_{-\infty}^{\infty} \mathrm{d}\omega \mathrm{Im}\chi_{\mathrm{sng}}(\omega) = \int_{-\infty}^{\infty} \mathrm{d}\omega \mathrm{Im}\chi_{\mathrm{trp}}(\omega) = {}^{n}\!/_{2} - 1$.

2.4.2 Conventional NRG Approach to Dynamic Quantities

We now outline the conventional approach to calculating dynamic quantities using the NRG. If we compute the trace in (2.4.2) using the retained states at some iteration N then, as in the calculation of thermodynamic quantities, we can gain insight into the system properties over some energy scale characterised by $\omega_N = \Lambda^{-(N-1)/2}$. Suppressing the various quantum numbers on our states, those retained at iteration N are denoted $|r; N\rangle$ and have energy $E_r(N)$. Since we are interested in calculating the dynamic properties of H, we need to use the unscaled energy eigenvalues, denoted $\epsilon_r(N) = \Lambda^{-(N-1)/2}E_r(N)$, which approximately satisfy

$$H\left|r; N\right\rangle = \epsilon_r(N)\left|r; N\right\rangle. \tag{2.4.13}$$

Adopting the Lehmann formulation of the Green function, we can write

$$G_{AB}(z) = \frac{1}{Z_N}\sum_{r_1 r_2} \frac{\left[\boldsymbol{A}^N\right]_{r_1 r_2}\left[\boldsymbol{B}^N\right]_{r_2 r_1}\left[\mathrm{e}^{-\beta\epsilon_{r_1}(N)} + \mathrm{e}^{-\beta\epsilon_{r_2}(N)}\right]}{z - \left[\epsilon_{r_2}(N) - \epsilon_{r_1}(N)\right]}, \tag{2.4.14}$$

where we define the local matrix elements

$$\begin{aligned} \left[\boldsymbol{A}^N\right]_{r_1 r_2} &= \left\langle r_1; N\right| A \left|r_2; N\right\rangle \\ \left[\boldsymbol{B}^N\right]_{r_1 r_2} &= \left\langle r_1; N\right| B \left|r_2; N\right\rangle \end{aligned} \tag{2.4.15}$$

which must be calculated during the NRG procedure (as described in detail in appendix D). Note that we now scale the energy levels rather than the temperature. The partition function Z_N is defined as usual by $Z_N = \sum_r \exp\left[-\beta\epsilon_r(N)\right]$, and for

$T = 0$ is equal to the degeneracy of the ground state. With the NRG, we only calculate the spectral densities. In our formalism these are

$$\rho_{AB}(\omega) = \frac{1}{Z_N} \sum_{r_1 r_2} \left[\boldsymbol{A}^N\right]_{r_1 r_2} \left[\boldsymbol{B}^N\right]_{r_2 r_1} \left[\mathrm{e}^{-\beta\epsilon_{r_1}(N)} + \mathrm{e}^{-\beta\epsilon_{r_2}(N)}\right] \delta\left(\omega - \Delta E\right) \tag{2.4.16}$$

where $\Delta E = \epsilon_{r_2}(N) - \epsilon_{r_1}(N)$. We thus obtain the spectral density, using the calculated properties for the system, at some iteration N. Since our system is discrete, the spectral density is comprised of a set of peaks. We argue (using separation of energy scales) that the spectral density is only really valid for energies $\Delta E \sim \omega_N$, and introduce a criterion that only peaks satisfying $\omega_{\mathrm{min}} < \Delta E < \omega_{\mathrm{max}}$ are retained. The boundary energies satisfy $(\omega_{\mathrm{min}}/\omega_N) \sim (\omega_{\mathrm{max}}/\omega_N) \sim \mathcal{O}(1)$. We obtain information for the spectral density on lower energy scales in the next NRG iteration. In this way we build the spectral density over the entire NRG by piecing together peaks from each iteration. It is important to note that the NRG is supposed to calculate the properties of the continuous model given by (2.1.1), but we see from (2.4.16) that we obtain a set of peaks rather than a continuous curve. To map the NRG spectral density back to the continuum model, we broaden the peaks into logarithmic Gaussians (which accounts for the fact the energy space has been logarithmically discretised). Namely, we make the replacement

$$\delta(\omega - \Delta E) \longrightarrow \begin{cases} \frac{\mathrm{e}^{-b^2/4}}{|\Delta E| b\sqrt{\pi}} \exp\left[-\left(\frac{\ln(\omega/\Delta E)}{b}\right)^2\right] & \mathrm{sgn}(\omega/\Delta E) = 1 \\ 0 & \text{otherwise} \end{cases} \tag{2.4.17}$$

which is normalised to preserve the area under the curve[5]. We call b the broadening factor. The value it should take depends on Λ and is somewhat ambiguous. We determine it by computing spectral densities for the uncoupled 2IAM, and find what value of b best satisfies the Friedel sum rule without introducing too many numerical artefacts (in practice, some oscillations in the spectra are unavoidable). We use $b = 1.25$ for $\Lambda = 6$. The conventional method is used to calculate $\rho_\alpha(\omega)$ for the channel symmetric uncoupled 2IAM and we compare this to the spectral density calculated for the 1IAM (with equal coupling constants) in figure 2.6. In principle, the results should be equal. However, the spectra differ in two key ways. The value of $\pi\Delta\rho_\alpha(0)$, fixed by the Friedel sum rule, is erroneously represented in

---

[5] As the NRG proceeds, we expect $\Delta E \sim \Lambda^{-N/2}$. It follows that ΔE will become close to zero, and given that we are using double precision, numerical issues can arise. For $\Delta E \lesssim 10^{-14}$, the factor of $1/\Delta E$ can blow up since small numerical errors in ΔE can cause large errors in $1/\Delta E$.

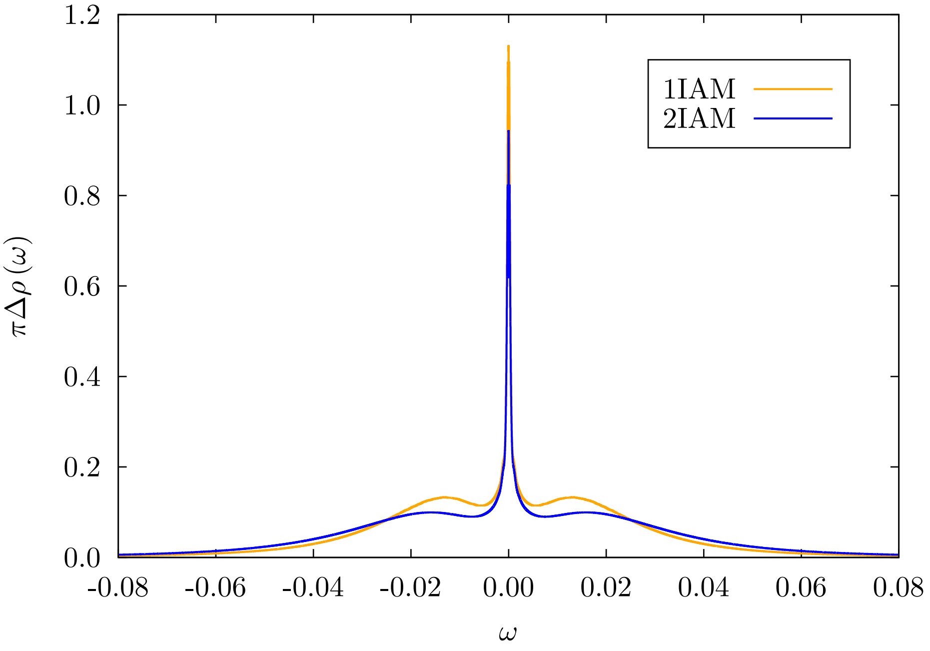

FIGURE 2.6: Comparison of the 1-particle spectral densities for the p-h symmetric 1IAM and uncoupled 2IAM as calculated using the conventional method. For the 1IAM we obtain $\pi\Delta\rho(0) = 1.12$ whilst for the 2IAM we find $\pi\Delta\rho(0) = 0.94$. The areas under the curves are respectively 0.95 and 0.92. We take $\omega_{\text{min}} = 1.3\omega_N$ and $\omega_{\text{max}} = 2.4\omega_N$.

each calculation, and the areas under the curves should satisfy $\int_{-\infty}^{\infty} \mathrm{d}\omega\ \rho_\alpha(\omega) = 1$. These observations underline several curable failings in the conventional method.

Firstly, the excitations of the system are computed with respect to only the levels of the iteration N. Therefore the ground state, as well as other excited states, is incorrectly identified. In order to get around this problem, we must allow the iterative diagonalisation to complete, and use the final ground state in our calculations. This approach proceeds by computing the density matrix for the full NRG chain, and reducing sequentially to obtain a reduced density matrix corresponding to the impurity. Secondly, the conventional method assumes that equation (2.4.14) is a faithful representation of (2.4.2). This is not true as the truncation necessarily results in an incomplete eigenspace. Finally, the spectra depend very strongly on the values of ω_{min} and ω_{max} that one chooses; these directly effect the area under the curves and the height of any peaks. These three shortcomings can be rectified through more formal calculation of the correlation functions. The authors of [92] and [93] identify a complete basis set generated by the NRG, which allows reliable computation of the trace [36, 37]. We also must identify the system ground state as the ground state of the final NRG iteration. We can then build a density matrix and calculate (2.4.2) much more accurately.

2.4.3 Anders-Schiller Complete NRG Basis

The established approach to the iterative diagonalisation of the NRG posits that one starts with an impurity system (coupled to a conduction electron site on each chain) and increases the length of the chains at each iteration. However, an alternative approach is to suppose that the length M of the chains is predetermined and constant for all iterations, and only the hopping matrix elements are changed. At iteration N, the hopping element $t_N = \Lambda^{-N/2}\xi_N$ is switched on, while all hopping elements $t_{N+1} \dots t_{M-1}$ remain zero. As in [36, 92, 93], we adopt the latter interpretation. Correspondingly, the energies of H_N acquire an additional degeneracy 16^{M-N}, which comes from taking the sites $N+1, N+2 \dots M$ for each bath as an environment (similar to Hofstetter's approach to calculating local Green functions [35]) as depicted in figure 2.7. We define the set of states corresponding to the

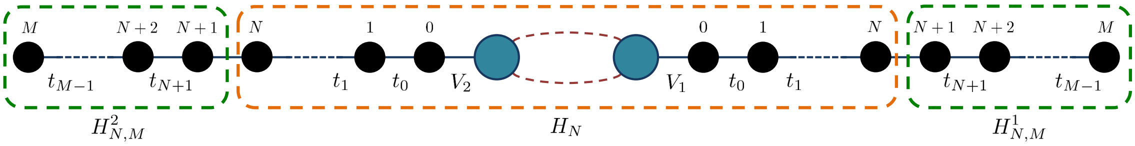

FIGURE 2.7: Illustration of the 2IAM at iteration N of a total M. An environment, described by $H^{\text{env}}_{N,M} = H^1_{N,M} + H^2_{N,M}$, is identified in which all the hopping amplitudes $t_N, t_{N+1} \ldots t_{M-1}$ are zero. The Hamiltonian H_N then acts on the entire model, with $M+1$ sites on each chain.

uncoupled site N on each channel to be

$$\{|\psi; N\rangle\} = \{|\phi; N\rangle_1 \otimes |\phi; N\rangle_2\} \quad \forall \quad |\phi; N\rangle_\alpha \in \Big\{ |0; N\rangle_\alpha , |\uparrow; N\rangle_\alpha , |\downarrow; N\rangle_\alpha , |\uparrow\downarrow; N\rangle_\alpha \Big\}. \tag{2.4.18}$$

It follows that the set of states

$$|r; N\rangle \bigotimes_{N'=N+1}^{M} \{|\psi; N'\rangle\} \tag{2.4.19}$$

are all eigenstates of H_N with eigenvalue $E_r(N)$; these encompass the additional energy degeneracies. We account for these by including an environment label e, which contains all possible configurations of the environment states. The eigenstates of H_N are thus denoted $|r, e; N\rangle$.

We denote N_{min} as the first iteration where states are truncated. In contrast to the conventional NRG, the truncated states are now retained (but not used to progress the NRG) and labelled as $|r, e; N_{\text{min}}\rangle_{\text{dis}}$, whilst the remaining states are labelled as $|r, e; N_{\text{min}}\rangle_{\text{kp}}$. We continue this process as depicted in figure 2.8, up until iteration M, where all states of H_M are to be regarded as truncated. Since this procedure keeps track of all the states generated from the NRG, which are initially complete, we are able to build from them a complete basis. After the NRG has reached iteration M, we may compile these states and observe

$$\mathbb{I} = \sum_{N=N_{\text{min}}}^{M} \sum_{r,e} |r, e; N\rangle_{\text{dis}} \, {}_{\text{dis}}\langle r, e; N| \tag{2.4.20}$$

where it is important to note that r and e are N-dependent. Since all the retained states at iteration N are used to compute the states at iteration $N+1$, there is a relationship between the states $|r, e; N\rangle_{\text{kp}}$ and all eigenstates of subsequent Hamiltonians. To visualise this, the identity operator may be divided into $\mathbb{I} = \mathbb{I}^-_N + \mathbb{I}^+_N$

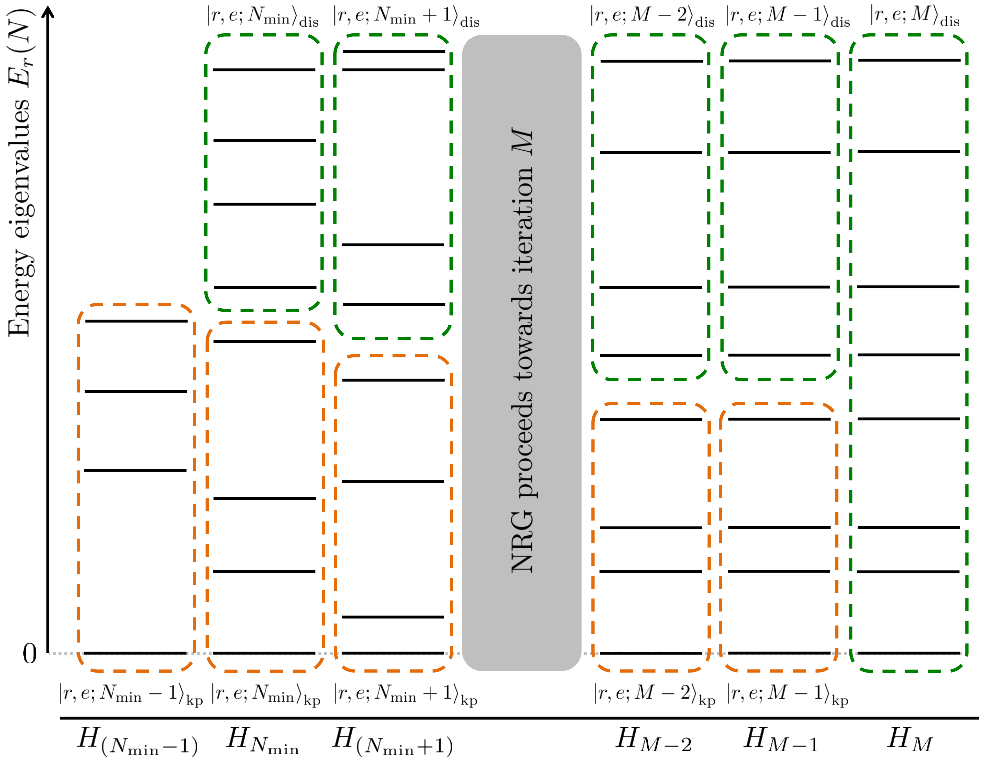

FIGURE 2.8: The construction of a complete basis from the iterative diagonalisation. Truncation first occurs at iteration $N = N_{\rm min}$, and from then onwards all truncated states (enclosed by the green boxes) at iteration N are stored as $|r,e;N\rangle_{\rm dis}$. Regarding the final set of states, corresponding to H_M, as truncated, the collection of truncated states is complete. We further note in the text a relationship between states $|r,e;N\rangle_{\rm kp}$ retained at iteration N (enclosed in the orange boxes) and all subsequent eigenstates.

where

$$\mathbb{I}_N^- = \sum_{N'=N_{\rm min}}^{N} \sum_{r,e} |r,e;N'\rangle_{\rm dis}\ {}_{\rm dis}\langle r,e;N'| \tag{2.4.21}$$

and

$$\mathbb{I}_N^+ = \sum_{N'=N+1}^{M} \sum_{r,e} |r,e;N'\rangle_{\rm dis}\ {}_{\rm dis}\langle r,e;N'|. \tag{2.4.22}$$

We see that $\mathbb{I}_N^-$ projects onto the subspace spanned by all truncated states up to iteration N, whilst $\mathbb{I}_N^+$ projects onto the subspace spanned by all subsequent eigenstates. However, one may argue that at iteration N, the collection of all truncated states and those retained is complete. Therefore the operator $\mathbb{I}_N^+$ must also project onto the subspace spanned by the retained states at iteration N, such that

$$\mathbb{I}_N^+ = \sum_{r,e} |r,e;N\rangle_{\text{kp}}\ {}_{\text{kp}}\langle r,e;N|. \tag{2.4.23}$$

We hence have a complete basis that may be constructed from any $N \leq M$, with which one may compute the Green function and spectral density.

2.4.4 Complete Fock Space Approach to $T = 0$ Green Functions

One of the failings of the conventional method for NRG calculation of dynamic quantities is its inability to identify the ground state. As argued in [35], a way around this is to allow the NRG to reach the final iteration M, and construct the density matrix using the final states. The density matrix is then to be reduced by tracing out the environment degrees of freedom. The iteration scheme for this procedure is derived in appendix E. Following the discussions in [36] and [37], we now demonstrate how calculation of the dynamic quantities using the NRG proceeds given the complete Anders-Schiller basis and reduced density matrix. Similar to the conventional method, we make the assumption that the complete basis is also an approximate eigenbasis of H_M, such that

$$H_M\,|r,e;N\rangle_{\text{dis}} \simeq E_r(N)\,|r,e;N\rangle_{\text{dis}}\,, \tag{2.4.24}$$

where $E_r(N)$ is the scaled energy. Equivalently, we assume that the complete basis satisfies $H\,|r,e;N\rangle_{\text{dis}} \simeq \epsilon_r(N)\,|r,e;N\rangle_{\text{dis}}$. These assumptions are validated by the notion that at iteration N we have a good sampling of energies on the scale ω_N. At this point, we distinguish between the approaches taken in [36] and [37]; the full density matrix, $\rho = \frac{1}{Z_M}\mathrm{e}^{-\beta H}$, is determined by the insertion of the identity (2.4.20) such that

$$\rho = \frac{1}{Z_M}\sum_{N=N_{\min}}^{M}\sum_{r,e}\mathrm{e}^{-\beta\epsilon_r(N)}\,|r,e;N\rangle_{\text{dis}}\ {}_{\text{dis}}\langle r,e;N| \tag{2.4.25}$$

as in [37]. However, we could approximate to $T \sim 0$ and argue that since each iteration H_N corresponds to a separate temperature scale, thermodynamic properties evaluated at that scale can be approximately described by the energies of H_N. Making this argument, the density matrix becomes

$$\rho \approx \frac{1}{Z_M}\sum_{r}\mathrm{e}^{-\beta E_r(M)}\,|r;M\rangle\,\langle r;M| \tag{2.4.26}$$

with $Z_M = \sum_r \mathrm{e}^{-\beta\epsilon_r(M)}$. This approximation is used in [36] and we shall adopt it in this work, but we stress that our results are only valid for $T = 0$. We also point out that the eigenstates $|r;M\rangle$ are elements of the complete basis, and are orthogonal to all $|r,e;N\rangle_{\text{dis}}$ for $N \neq M$. Given these precursors, we derive the full Green function (2.4.2) following the arguments of [36]. The result is

$$G_{AB}(z) = G^{\text{i}}_{AB}(z) + G^{\text{ii}}_{AB}(z) + G^{\text{iii}}_{AB}(z) \tag{2.4.27}$$

where

$$G^{\text{i}}_{AB}(z) = \frac{1}{Z_M} \sum_{l_1,l_2} \left[\boldsymbol{A}^M\right]_{l_1,l_2} \left[\boldsymbol{B}^M\right]_{l_2,l_1} \frac{\mathrm{e}^{-\beta\epsilon_{l_1}(M)} + s\mathrm{e}^{-\beta\epsilon_{l_2}(M)}}{z - \Big[\epsilon_{l_2}(M) - \epsilon_{l_1}(M)\Big]} \tag{2.4.28}$$

accounts for contributions from the final NRG iteration M, whilst

$$G^{\text{ii}}_{AB}(z) = \sum_{N=N_{\min}}^{M-1} \sum_{l} \sum_{k_1,k_2} \left[\boldsymbol{A}^N\right]_{l,k_1} \left[\boldsymbol{\rho}^N_{\text{red}}\right]_{k_1,k_2} \left[\boldsymbol{B}^N\right]_{k_2,l} \frac{s}{z - \Big[\epsilon_{k_2}(N) - \epsilon_l(N)\Big]} \tag{2.4.29}$$

and

$$G^{\text{iii}}_{AB}(z) = \sum_{N=N_{\min}}^{M-1} \sum_{l} \sum_{k_1,k_2} \left[\boldsymbol{B}^N\right]_{l,k_1} \left[\boldsymbol{\rho}^N_{\text{red}}\right]_{k_1,k_2} \left[\boldsymbol{A}^N\right]_{k_2,l} \frac{1}{z - \Big[\epsilon_l(N) - \epsilon_{k_2}(N)\Big]} \tag{2.4.30}$$

respectively account for the negative and positive frequency contributions. In the above expressions we follow [36] and define l to sum over the discarded states, and k to sum over the retained states. The reduced density matrix $\boldsymbol{\rho}^N_{\text{red}}$ is constructed as in Hofstetter's approach [35], and we apply the formalism to the 2IAM in appendix E. In addition, the matrix elements are defined as

$$\left[\boldsymbol{A}^N\right]_{l,k} = \langle l;N|\, A\, |k;N\rangle \tag{2.4.31}$$

with the expression of B being similar[6]. We choose a notation which illustrates that in the numerics, one may perform these calculations using matrix multiplication which, as we have discussed, gives rise to a boost in computational efficiency.

This formalism of the Green function contains no truncation errors due to the trace, and always satisfies the spectral sum rule[7] given in (2.4.11). Using this method,

---

[6] Provided the bra and ket states carry equal environment labels, the local matrix element is independent of them. Environment labels are thus suppressed, and local matrix elements can be calculated in exactly the same way as the conventional approach to spectral densities.

[7] This is true for $T = 0$, but for finite temperatures we must treat the density matrix more generally. See [37] for more details.

we compute the dynamic quantities listed in section 2.4.1. These quantities are discussed extensively throughout this work. It is important to note that the NRG still fails to satisfy $\pi\Delta\rho_\alpha(0) = 1$, instead we find $\pi\Delta\rho_\alpha(0) \approx 0.85$ representing a systematic 15% underestimation which should be taken into account whenever we require the value of $\rho_\alpha(0)$.

The origin of this error is in the discretisation of the model. In the formulation of the Wilson chain, one expands sections of the conduction band into a Fourier series, each term of which is labelled by an index p. The impurity only couples directly to the $p = 0$ term, which is then coupled to $p > 0$ terms. The strength of this latter coupling is characterised by $(1 - \Lambda^{-1})/2\pi$, and is therefore very weak for small Λ. The higher p terms are neglected, giving rise to the observed error, which increases as Λ increases. We use a considerably large Λ and as a result our errors are also reasonably large.

Since this error emerges from the value of Λ used (and also how we broaden the discrete spectra into a continuous one), there is no dependence on any other model quantities (such as coupling constants). We have tested this extensively, by comparing the value of $\rho_\alpha(0)$ to that obtained by means of RPT (see next chapter) and we find that the error is systematic. This is further evidenced by figure 5.21 in chapter 5 which shows that when this error is accounted for, the two methods agree very well, even when the low-energy FL regimes differ.

2.5 The Discrete vs Continuum Model

Under the NRG mapping and approximations outlined in section 2.1, we seek to understand the continuum model (2.1.1) by studying the discrete model (2.1.2). However, the physical quantities calculated for each model are progressively more inconsistent as Λ increases. For example, when one calculates the static spin susceptibility [25], or the bulk density of states [94], the results differ by a factor of

$$A_\Lambda = \frac{1}{2}\frac{\Lambda + 1}{\Lambda - 1}\ln(\Lambda). \tag{2.5.1}$$

As a result, for large Λ the results become increasingly less reliable. This can be prevented by accounting for the A_Λ factor by rescaling the hybridisation width in the discrete model. We define the hybridisation width of the continuum and discrete models respectively as Δ^{cont} and Δ^{dis}, and they are related by

$$\Delta^{\text{dis}} = A_\Lambda \Delta^{\text{cont}}. \tag{2.5.2}$$

All quantities calculated using the NRG for a quoted Δ^{cont} have a hybridisation width Δ^{dis}. We shall often use the value of $\rho_\alpha(0)$ to compare NRG results with RPT results, and also to calculate local occupancies via the Friedel sum rule. We therefore must establish the relation between the spectral densities in the continuum and discrete models, respectively denoted $\rho_\alpha^{\text{dis}}(\omega)$ and $\rho_\alpha^{\text{cont}}(\omega)$. We argue that local occupation should be equal in the discrete and continuum models which, by the Friedel sum rule, implies

$$\Delta^{\text{dis}} \rho_\alpha^{\text{dis}}(0) = \Delta^{\text{cont}} \rho_\alpha^{\text{cont}}(0). \tag{2.5.3}$$

We thus quote values of $\rho_\alpha^{\text{cont}}(0)$ given by

$$\rho_\alpha^{\text{cont}}(0) = A_\Lambda \rho_\alpha^{\text{dis}}(0). \tag{2.5.4}$$

Subject to the usual 15% systematic error, we consistently obtain good agreement with the Friedel sum rule. When we quote results in terms of Δ, we are referring to the continuum value Δ^{cont}, and likewise results for $\rho_\alpha(0)$.

Chapter 3

Renormalised Perturbation Theory: Parameters and Dynamic Quantities

The NRG, discussed in the previous chapter, provides a formalism which allows us to calculate static and dynamic quantities of the 2IAM, which remain valid over all energy scales reached by the iterative diagonalisation algorithm. However it provides no obvious insight into how the structure of the Hamiltonian changes with the energy scale, whether new types of interactions emerge, or the relevance of a quasiparticle picture. The RPT presumes a low-energy FL structure of the Hamiltonian, in terms of renormalised coupling constants and quasiparticles, and is applied in this chapter to calculate dynamic quantities (also in terms of the renormalised parameters). It is not immediately obvious how dynamic quantities in terms of unknown renormalised coupling constants will be useful in our investigations; however, these renormalised parameters may be calculated using the NRG. The combination of approaches is very powerful and provides quantitative insight into the low-energy structure, and any emergent symmetry, of the Hamiltonian. We make extensive use of the RPT in our analysis of the emergent SU(4) behaviour in chapter 4, as well as the quantum critical point we consider in chapter 5.

3.1 Calculation of Renormalised Parameters and the NRG

We are able to calculate the renormalised parameters using the NRG, by the approaches developed in [40, 95, 96]. The interaction terms are to be considered as a perturbation to the non-interacting NRG Hamiltonian (2.1.6). Suppose we consider the free Hamiltonian at iteration N for bath α, denoted $H^0_\alpha(N)$, such that each channel contains $N+2$ sites (including their respective impurities). We define a basis $|i\rangle = c^\dagger_{\alpha i\sigma}|0\rangle, (c^\dagger_{\alpha -1\sigma} = d^\dagger_{\alpha\sigma})$ for fixed σ so that we may build a spin-dependent matrix representation of the Hamiltonian and calculate the local Green function. It follows from the (2.1.6) that

$$H^0_\alpha(N) = \begin{pmatrix} \Lambda^{(N-1)/2}\epsilon_\alpha & -\Lambda^{(N-1)/2}V_\alpha & 0 & 0 & \cdots \\ -\Lambda^{(N-1)/2}V_\alpha & 0 & -\Lambda^{(N-1)/2}\xi_0 & 0 & \\ 0 & -\Lambda^{(N-1)/2}\xi_0 & 0 & -\Lambda^{(N-2)/2}\xi_1 & \\ 0 & 0 & -\Lambda^{(N-2)/2}\xi_1 & 0 & \\ \vdots & & & & \ddots \end{pmatrix}. \quad (3.1.1)$$

The indices i which label elements in the Hamiltonian are chosen to span $i \in \{-1, 0, 1 \dots N\}$ such that $i = -1$ corresponds to the impurity site. The local Green functions for the non-interacting system are the matrix elements of the resolvent, $\mathcal{R}_\alpha(\omega) = \left(\omega\mathbb{I} - H^0_\alpha(N)\right)^{-1}$ [87]. We hence define the non-interacting local impurity Green function $G^{(0)}_\alpha(\omega) = \langle -1| \mathcal{R}_\alpha(\omega) |-1\rangle$. Using the identity

$$\left(\begin{array}{c|c} A & B \\ \hline C & D \end{array}\right)^{-1} = \left(\begin{array}{c|c} \left(A - BD^{-1}C\right)^{-1} & \left(BD^{-1}C - A\right)^{-1} BD^{-1} \\ \hline D^{-1}C\left(BD^{-1}C - A\right)^{-1} & \left(D - CA^{-1}B\right)^{-1} \end{array}\right), \quad (3.1.2)$$

which assumes matrices A and D are invertible, we calculate $G^{(0)}_\alpha(\omega)$ recursively in terms of the local Green functions of the conduction sites as

$$G^{(0)}_\alpha(\omega) = \frac{1}{\omega - \Lambda^{(N-1)/2}\epsilon_\alpha - \Lambda^{N-1}V^2_\alpha g_{00}(\omega)}, \quad (3.1.3)$$

where $g_{00}(\omega) = \langle 0| \mathcal{R}_\alpha(\omega) |0\rangle$ is the local Green function corresponding to the first conduction site[1] given by

$$g_{00}(\omega) = \cfrac{1}{\omega - \cfrac{\xi_0^2 \Lambda^{N-1}}{\omega - \cfrac{\xi_1^2 \Lambda^{N-2}}{\ddots \cfrac{\Lambda \xi_{N-1}^2}{\omega - \cfrac{\xi_N^2}{\omega}}}}} \tag{3.1.4}$$

where the Green function on the final site in the NRG chain is given by

$$g_{NN}(\omega) = \frac{1}{\omega}. \tag{3.1.5}$$

Given the impurity Green function and following [40], we are able to calculate the renormalised parameters corresponding to the quadratic part of the Hamiltonian, using that the 1-particle excitations are given by the poles of the Green function, and also that the NRG provides the energy of these excitations. We therefore require

$$E - \Lambda^{(N-1)/2}\epsilon_\alpha - \Lambda^{N-1} V_\alpha^2 g_{00}(E) = 0 \tag{3.1.6}$$

for E denoting the energies of the 1-particle excitations, relative to the ground state. The NRG provides the excitation energies of the system in terms of quasiparticles, relative to a ground state $Q = 0$. The 1-particle excitation energies at iteration N, $E_{\mathrm{p}\alpha}(N)$ and $E_{\mathrm{h}\alpha}(N)$, for the 'particle' and 'hole' quasiparticles are given respectively by the lowest energies of the $Q_\alpha = 1, S_z = 1/2$ and $Q_\alpha = -1, S_z = -1/2$ sectors. Note that these energies may lie in any of the $S = 1/2, 3/2, 5/2 \ldots$ sectors. We hence obtain the equations

$$\begin{aligned} E_{\mathrm{p}\alpha}(N) - \Lambda^{(N-1)/2}\epsilon_\alpha(N) - \Lambda^{N-1} V_\alpha(N)^2 g_{00}(E_{\mathrm{p}\alpha}(N)) = 0 \\ -E_{\mathrm{h}\alpha}(N) - \Lambda^{(N-1)/2}\epsilon_\alpha(N) - \Lambda^{N-1} V_\alpha(N)^2 g_{00}(-E_{\mathrm{h}\alpha}(N)) = 0, \end{aligned} \tag{3.1.7}$$

where we have promoted the coupling constants ϵ_α and V_α to carry N-dependence. These equations may be solved simultaneously so that

$$\begin{aligned} \frac{\pi \epsilon_\alpha(N)}{2\Delta_\alpha(N)} &= \Lambda^{(N-1)/2} \frac{E_{\mathrm{h}\alpha}(N) g_{00}(E_{\mathrm{p}\alpha}(N)) + E_{\mathrm{p}\alpha}(N) g_{00}(-E_{\mathrm{h}\alpha}(N))}{E_{\mathrm{p}\alpha}(N) + E_{\mathrm{h}\alpha}(N)} \\ \frac{\pi}{2\Delta_\alpha(N)} &= \Lambda^{N-1} \frac{g_{00}(E_{\mathrm{p}\alpha}(N)) - g_{00}(-E_{\mathrm{h}\alpha}(N))}{E_{\mathrm{p}\alpha}(N) + E_{\mathrm{h}\alpha}(N)}, \end{aligned} \tag{3.1.8}$$

---

[1] In the model we consider, both Wilson chains are identical, so the conduction site Green functions do not carry the label α.

and we define our renormalised parameters by

$$\begin{aligned}\tilde{\epsilon}_\alpha &= \lim_{N\to\infty} \epsilon_\alpha(N) \\ \tilde{\Delta}_\alpha &= \lim_{N\to\infty} \Delta_\alpha(N).\end{aligned} \tag{3.1.9}$$

We now turn our attention to the calculation of interaction parameters; we may separate the Hamiltonian into a free part $H^0_\alpha(N)$, and an interaction term $H'(N)$. The free Hamiltonian may be diagonalised and written in terms of quasiparticle creation / annihilation operators. These are respectively $p_{\alpha r}$ and $h_{\alpha r}$, where r labels the energy of the excitation. We write

$$H^0_\alpha(N) = \sum_{r=0}^{N/2} E_{\mathrm{p}\alpha r}(N) p^\dagger_{\alpha r\sigma} p_{\alpha r\sigma} + E_{\mathrm{h}\alpha r}(N) h^\dagger_{\alpha r\sigma} h_{\alpha r\sigma} \tag{3.1.10}$$

where N is even and $E_{\mathrm{p}\alpha r}(N)$ is the energy of a $r+1$ particle excited state (similarly defined for hole states). The impurity site operators $d_{\alpha\sigma}$ may be written in terms of the particle and hole operators by means of a basis transformation;

$$d_{\alpha\sigma} = \sum_{r=0}^{N/2} \left(\psi_{\mathrm{p}\alpha r}(-1) p_{\alpha r\sigma} + \psi_{\mathrm{h}\alpha r}(-1) h^\dagger_{\alpha r\bar{\sigma}} \right) \tag{3.1.11}$$

with $\bar{\sigma} = -\sigma$. The impurity Green function at iteration N is then given by

$$G^{(0)}_\alpha(\omega) = \sum_r \frac{|\psi_{\mathrm{p}\alpha r}(-1)|^2}{\omega - E_{\mathrm{p}\alpha r}(N)} + \sum_r \frac{|\psi_{\mathrm{h}\alpha r}(-1)|^2}{\omega + E_{\mathrm{h}\alpha r}(N)}. \tag{3.1.12}$$

If one performs a Laurent expansion about a simple pole, corresponding to either $E_{\mathrm{p}\alpha}(N)$ or $E_{\mathrm{h}\alpha}(N)$, and (infinitesimally close to the pole) equates the result to the continued fraction above then one may show that

$$|\psi_{\mathrm{p}\alpha r}(-1)|^2 = \frac{1}{1 - \Lambda^{N-1} \tilde{V}^2_\alpha \partial_\omega g_{00}(E_{\mathrm{p}\alpha r})} \tag{3.1.13}$$

and

$$|\psi_{\mathrm{h}\alpha r}(-1)|^2 = \frac{1}{1 - \Lambda^{N-1} \tilde{V}^2_\alpha \partial_\omega g_{00}(-E_{\mathrm{h}\alpha r})}. \tag{3.1.14}$$

The calculation of these overlaps, and the expression of the impurity electron operators in terms of the quasiparticle operators, sets the stage for the application of perturbation theory. To compute the renormalised on-site Coulomb interaction, we consider a perturbative correction to the transformed Hamiltonian, denoted $H_{U\alpha}(N)$ and given by

$$H_{U\alpha}(N) = \tilde{U}_\alpha(N) \Lambda^{(N-1)/2} : d^\dagger_{\alpha\uparrow} d_{\alpha\uparrow} d^\dagger_{\alpha\downarrow} d_{\alpha\downarrow} :, \tag{3.1.15}$$

which is normally ordered to enforce the requirement that the Coulomb interaction takes place between 2 quasiparticles, and includes the factor $\Lambda^{(N-1)/2}$ to account for the rescaling [40, 95]. As $N \to \infty$, the interaction coupling constants tend to zero as the system becomes free. We therefore calculate only the first order corrections to the low lying states, and thus obtain an estimate of $\tilde{U}_\alpha$. In the Brillouin-Wigner perturbation theory, the first order approximation to the energy eigenvalues is the expectation value of the perturbative Hamiltonian in the corresponding unperturbed eigenstate. The lowest energy 2-particle state for bath α, $|\mathrm{pp};\alpha\rangle = p^\dagger_{\alpha 0\downarrow} p^\dagger_{\alpha 0\uparrow} |0\rangle$, gives a correction

$$\langle \mathrm{pp};\alpha| H_{U\alpha}(N) |\mathrm{pp};\alpha\rangle = \tilde{U}_{\mathrm{pp}\alpha}(N)\Lambda^{(N-1)/2} |\psi_{\mathrm{p}\alpha 0}(-1)|^2 |\psi_{\mathrm{p}\alpha 0}(-1)|^2 . \tag{3.1.16}$$

This may be computed directly from the NRG, and for the 2-particle state is given by

$$\langle \mathrm{pp};\alpha| H_{U\alpha}(N) |\mathrm{pp};\alpha\rangle = E_{\mathrm{pp}\alpha}(N) - 2E_{\mathrm{p}\alpha}(N) \tag{3.1.17}$$

where $E_{\mathrm{pp}\alpha}(N)$ is the lowest energy 2-particle state. We hence write the renormalised $U_{\mathrm{pp}\alpha}$ as

$$\tilde{U}_{\mathrm{pp}\alpha} = \lim_{N\to\infty} \Lambda^{-(N-1)/2} \frac{E_{\mathrm{pp}\alpha}(N) - 2E_{\mathrm{p}\alpha}(N)}{|\psi_{\mathrm{p}\alpha 0}(-1)|^2 |\psi_{\mathrm{p}\alpha 0}(-1)|^2}. \tag{3.1.18}$$

In the same way, one may compute the particle-hole and hole-hole on-site Coulomb interactions, $\tilde{U}_{\mathrm{ph}\alpha}$ and $\tilde{U}_{\mathrm{hh}\alpha}$ respectively. The inter-impurity Coulomb interaction is similarly calculated. We take a perturbative Hamiltonian

$$H_{U_{12}}(N) = \tilde{U}_{12}(N)\Lambda^{(N-1)/2} \sum_{\sigma\sigma'} : d^\dagger_{1\sigma} d_{1\sigma} d^\dagger_{2\sigma'} d_{2\sigma'} : \tag{3.1.19}$$

and we find that the inter-impurity Coulomb coupling constant splits into four variants, between a particle and hole in each channel. As before the renormalised interaction takes the form

$$\tilde{U}_{12\ \mathrm{p}_1\mathrm{p}_2} = \lim_{N\to\infty} \Lambda^{-(N-1)/2} \frac{E_{\mathrm{p}_1\mathrm{p}_2}(N) - E_{\mathrm{p}1}(N) - E_{\mathrm{p}2}(N)}{|\psi_{\mathrm{p}10}(-1)|^2 |\psi_{\mathrm{p}20}(-1)|^2}, \tag{3.1.20}$$

with the other variants taking similar forms. Finally, the renormalised inter-impurity magnetic interaction J is determined by considering the Hamiltonian

$$H_J(N) = 2\tilde{J}(N)\Lambda^{(N-1)/2} : \mathbf{S}_1 \cdot \mathbf{S}_2 : \tag{3.1.21}$$

which introduces an energy splitting between singlet and triplet states. We denote $E_{\mathrm{S}\ \mathrm{p}_1\mathrm{p}_2}$ the lowest energy singlet ($S = 0$) state for a system with one quasiparticle on each impurity, and $E_{\mathrm{T\ p_1p_2}}$ the lowest energy triplet ($S = 1$) state for the same system. We also define the matrix elements, evaluated respectively at the singlet and triplet energies as

$$|\psi_{\mathrm{S}\ \alpha\ \mathrm{p_1p_2}}|^2 = \frac{1}{1 - \Lambda^{N-1}\tilde{V}_\alpha^2 \partial_\omega g_{00}(E_{\mathrm{S\ p_1p_2}}/2)} \tag{3.1.22}$$

and

$$|\psi_{\mathrm{T}\ \alpha\ \mathrm{p_1p_2}}|^2 = \frac{1}{1 - \Lambda^{N-1}\tilde{V}_\alpha^2 \partial_\omega g_{00}(E_{\mathrm{T\ p_1p_2}}/2)}. \tag{3.1.23}$$

The renormalised J is then written as

$$2\tilde{J}_{p_1p_2} = \lim_{N\to\infty} \Lambda^{-(N-1)/2} \frac{E_{\mathrm{T\ p_1p_2}}(N) - E_{\mathrm{S\ p_1p_2}}(N)}{|\psi_{\mathrm{T\ 1\ p_1p_2}}|\,|\psi_{\mathrm{T\ 2\ p_1p_2}}|\,|\psi_{\mathrm{S\ 1\ p_1p_2}}|\,|\psi_{\mathrm{S\ 2\ p_1p_2}}|}, \tag{3.1.24}$$

and the interactions between other particle/hole variants are analogous [96, 95]. The renormalised parameters give insight into the low-energy behaviour of the system. The quasiparticle level $\tilde{\epsilon}_\alpha$ corresponds to the energy of the quasiparticle resonance. In a system with p-h symmetry in channel α, $\tilde{\epsilon}_\alpha = 0$ since the resonance forms at the Fermi level. The system enters the low-energy regime for temperatures of order T_{K}, which is set by the bare model parameters. If we have a reasonably large Λ (say $\Lambda = 6$) then we can reach this temperature scale in fewer NRG iterations than for smaller Λ. For $\Lambda = 6$ we find around 30 iterations to be sufficient for the parameters to plateau. Typically, the renormalised parameters plateau when they are equal to around 5 significant figures.

3.2 Renormalised Perturbation Theory and the Anderson Model

We now introduce the RPT for the 2IAM[2], following the methods outlined in [97, 98, 99, 54]. RPT takes the approach of rescaling our bare Fermionic fields and the coupling constants, in a manner achieved by expressing the Hamiltonian and Green function in a low-energy form. Furthermore, it relates the bare couplings to the renormalised couplings precisely. RPT differs from bare perturbation theory in the following sense: in bare perturbation theory, one calculates a series expansion in terms of the bare parameters. In the RPT, we perform a non-perturbative method to calculate the low-energy FP in terms of renormalised parameters. We then perturb the low-energy system and expand in these renormalised parameters.

---

[2] The formalism is analogously applied to the 1IAM.

Although we consider the model in the absence of a local magnetic field, certain dynamic quantities (ie spin susceptibility) require that we explicitly include one, which we label h_α. The localised d-level energy is then given by $\epsilon_{\alpha\sigma} = \epsilon_\alpha - \sigma h_\alpha$. In practice, we always set $h_\alpha = 0$. The 1-particle local Green function of the non-interacting impurity electrons of the 2IAM is given by

$$G^{(0)}_{\alpha\sigma}(\omega) = \frac{1}{\omega - \epsilon_{\alpha\sigma} + i\Delta_{\alpha\sigma}\mathrm{sgn}(\omega)} \tag{3.2.1}$$

as shown in [59]. The inclusion of interactions is accomplished by introduction of a self-energy $\Sigma_{\alpha\sigma}(\omega, h)$ [54]. This is defined in terms of the full (interacting) Green function $G_{\alpha\sigma}(\omega)$ by the Dyson equation

$$\Sigma_{\alpha\sigma}(\omega, h) = \left[G^{(0)}_{\alpha\sigma}(\omega)\right]^{-1} - \left[G_{\alpha\sigma}(\omega)\right]^{-1} \tag{3.2.2}$$

so that the interacting impurity Green function takes the form

$$G_{\alpha\sigma}(\omega) = \frac{1}{\omega - \epsilon_{\alpha\sigma} + i\Delta_{\alpha\sigma}\mathrm{sgn}(\omega) - \Sigma_{\alpha\sigma}(\omega, h)}. \tag{3.2.3}$$

In order to understand how the model behaves at low energies, which will correspond to the FPs of the RG, we assume that the FPs of the system are described by quasiparticles in a FL regime. FLs, which describe the low-temperature interactions of electrons in a typical metal, have a number of properties which are worth noting. Both the specific heat and entropy scale linearly with T, the resistivity as T^2, while the thermal conductivity coefficient goes as T^{-1}. The self energy satisfies $\mathrm{Im}\Sigma(\omega) \sim \omega^2$ for small ω. Good introductions to this theory are [100] and [101].

Since $\mathrm{Im}\Sigma(\omega) \sim \omega^2$, we expect the renormalised self-energy $\tilde{\Sigma}_{\alpha\sigma}(\omega, h)$ to vanish as $\omega \to 0$, and the renormalised Green function $\tilde{G}_{\alpha\sigma}(\omega)$ will describe a non-interacting system with renormalised coupling constants $\tilde{\epsilon}_{\alpha\sigma}$ and $\tilde{\Delta}_{\alpha\sigma}$. To acquire the desired form, we expand $\Sigma_{\alpha\sigma}(\omega, h)$ around $\omega = 0$;

$$\Sigma_{\alpha\sigma}(\omega, h) = \Sigma_{\alpha\sigma}(0, h) + \omega\partial_\omega\Sigma_{\alpha\sigma}(\omega, 0)\Big|_{\omega=0} + \Sigma^{\mathrm{rem}}_{\alpha\sigma}(\omega, h), \tag{3.2.4}$$

where we have defined the 'remainder' self-energy $\Sigma^{\mathrm{rem}}_{\alpha\sigma}(\omega, h) \sim \mathcal{O}\left(\omega^2\right)$. Upon insertion into the full Green function we obtain

$$G_{\alpha\sigma}(\omega) = \frac{1}{\left[1 - \partial_\omega\Sigma_{\alpha\sigma}(0, 0)\right]\omega - \left[\epsilon_{\alpha\sigma} + \Sigma_{\alpha\sigma}(0, h)\right] + i\Delta_{\alpha\sigma}\mathrm{sgn}(\omega) - \Sigma^{\mathrm{rem}}_{\alpha\sigma}(\omega, h)}, \tag{3.2.5}$$

from which we can define the renormalised Green function,

$$\tilde{G}_{\alpha\sigma}(\omega) = \frac{1}{\omega - \tilde{\epsilon}_{\alpha\sigma} + i\tilde{\Delta}_{\alpha\sigma}\mathrm{sgn}(\omega) - \tilde{\Sigma}_{\alpha\sigma}(\omega, h)} \tag{3.2.6}$$

in terms of renormalised parameters. These are given by

$$\begin{aligned} \tilde{\epsilon}_{\alpha\sigma} &= z_{\alpha\sigma}\left[\epsilon_{\alpha\sigma} + \Sigma_{\alpha\sigma}(0, h)\right] \\ \tilde{\Delta}_{\alpha\sigma} &= z_{\alpha\sigma}\Delta_{\alpha\sigma} \\ \tilde{\Sigma}_{\alpha\sigma}(\omega) &= z_{\alpha\sigma}\Sigma^{\mathrm{rem}}_{\alpha\sigma}(\omega, h), \end{aligned} \tag{3.2.7}$$

where the quasiparticle weight is defined as

$$z_{\alpha\sigma} = \frac{1}{1 - \partial_\omega \Sigma_{\alpha\sigma}(0, 0)} \tag{3.2.8}$$

and scales the bare particles into quasiparticles $\tilde{d}^\dagger_{\alpha\sigma} = d^\dagger_{\alpha\sigma}/\sqrt{z_{\alpha\sigma}}$. Note that $z_{\alpha\sigma}$ and $\tilde{\epsilon}_{\alpha\sigma}$ are real; this follows from the Luttinger theorem $\mathrm{Im}\left[\Sigma_{\alpha\sigma}(0, h)\right] = 0$ [102]. Furthermore, the renormalised self-energy $\tilde{\Sigma}_{\alpha\sigma}(\omega, h)$ scales as $\mathcal{O}(\omega^2)$ by construction, so that exactly at the low-energy FP, where $\omega^2 \sim 0$, the system is described by a free effective Hamiltonian $\tilde{H}_0$ similar to the original model, except with renormalised parameters and no quartic interaction terms;

$$\tilde{H}_0 = \sum_{\alpha\boldsymbol{k}} \epsilon_{\alpha\boldsymbol{k}} c^\dagger_{\alpha\boldsymbol{k}\sigma} c_{\alpha\boldsymbol{k}\sigma} + \sum_{\alpha\boldsymbol{k}} \tilde{V}_{\alpha\sigma}\left[c^\dagger_{\alpha\boldsymbol{k}\sigma}\tilde{d}_{\alpha\sigma} + \tilde{d}^\dagger_{\alpha\sigma} c_{\alpha\boldsymbol{k}\sigma}\right] + \sum_{\sigma} \tilde{\epsilon}_{\alpha\sigma}\tilde{d}^\dagger_{\alpha\sigma}\tilde{d}_{\alpha\sigma}. \tag{3.2.9}$$

The conduction electrons do not interact and therefore do not renormalise. It follows from (3.2.3) that the 1-quasiparticle Green function at the free FL FP is given by

$$\tilde{G}^{(0)}_{\alpha\sigma}(\omega) = \frac{1}{\omega - \tilde{\epsilon}_{\alpha\sigma} + i\tilde{\Delta}_{\alpha\sigma}\mathrm{sgn}(\omega)} \tag{3.2.10}$$

and the non-interacting quasiparticle density of states is

$$\tilde{\rho}^{(0)}_{\alpha\sigma}(\omega) = \frac{1}{\pi}\frac{\tilde{\Delta}_{\alpha\sigma}}{\left(\tilde{\epsilon}_{\alpha\sigma} - \omega\right)^2 + \tilde{\Delta}_{\alpha\sigma}{}^2}. \tag{3.2.11}$$

Hence the free model satisfies

$$\tilde{n}_{\alpha\sigma} = \frac{1}{2} - \frac{1}{\pi}\arctan\left(\frac{\tilde{\epsilon}_{\alpha\sigma}}{\tilde{\Delta}_{\alpha\sigma}}\right) \tag{3.2.12}$$

which is equivalent to the exact result due to Langreth [60] and we obtain $n_{\alpha\sigma} = \tilde{n}_{\alpha\sigma}$, which has been proved in [103]. From this equality, our assumption that the low-energy system is a Fermi liquid, and (1.3.8), we have that the quasiparticle spectral density and the bare spectral density are related by

$$\rho_\alpha(0) = z_\alpha\tilde{\rho}_\alpha(0). \tag{3.2.13}$$

For small ω, we can thus approximate $\rho_\alpha(\omega) \simeq z_\alpha \tilde{\rho}_\alpha(\omega)$. Away from the FL fixed point, we have interactions governed by the renormalised parameters $\tilde{U}_\alpha$, $\tilde{U}_{12}$ and $\tilde{J}$. To understand how they renormalise (and also to motivate the diagrammatic perturbation theory) we write the quartic terms of the bare Hamiltonian as

$$\begin{aligned} H^{(4)} = &\sum_\alpha \frac{U_\alpha}{2} d^\dagger_{\alpha\sigma} d^\dagger_{\alpha\sigma'} d_{\alpha\sigma'} d_{\alpha\sigma} + \frac{2U_{12} - J}{4} \sum_{\alpha\neq\alpha'} d^\dagger_{\alpha\sigma} d^\dagger_{\alpha'\sigma'} d_{\alpha'\sigma'} d_{\alpha\sigma} \\ &- \frac{J}{2} \sum_{\alpha\neq\alpha'} d^\dagger_{\alpha\sigma} d^\dagger_{\alpha'\sigma'} d_{\alpha\sigma'} d_{\alpha'\sigma}, \end{aligned} \tag{3.2.14}$$

which illustrates the terms, and their couplings, responsible for 2-particle inter- and intra-channel scattering. The renormalisation of the couplings can be defined in terms of the 4-point vertex function

$$\begin{aligned} &\Gamma^{\alpha_1\sigma_1;\alpha_2\sigma_2}_{\alpha_3\sigma_3;\alpha_4\sigma_4}(\omega_1, \omega_2, \omega_3, \omega_4) \\ &= \left(\prod_{j=1}^{4} \int_{-\infty}^{\infty} \frac{\mathrm{d}\tau_j}{2\pi} \mathrm{e}^{-i\omega_j\tau_j} \right) \left\langle \mathrm{T}_\tau d_{\alpha_1\sigma_1}(\tau_1)\, d_{\alpha_2\sigma_2}(\tau_2)\, d^\dagger_{\alpha_3\sigma_3}(\tau_3)\, d^\dagger_{\alpha_4\sigma_4}(\tau_4) \right\rangle, \end{aligned} \tag{3.2.15}$$

where T_τ denotes time ordering, which is scaled by the quasiparticle weights

$$\tilde{\Gamma}^{\alpha_1\sigma_1;\alpha_2\sigma_2}_{\alpha_3\sigma_3;\alpha_4\sigma_4}(0,0,0,0) = \sqrt{z_1 z_2 z_3 z_4}\, \Gamma^{\alpha_1\sigma_1;\alpha_2\sigma_2}_{\alpha_3\sigma_3;\alpha_4\sigma_4}(0,0,0,0). \tag{3.2.16}$$

The renormalised interaction strengths then satisfy

$$\begin{aligned} \tilde{\Gamma}^{\alpha_1\sigma_1;\alpha_2\sigma_2}_{\alpha_3\sigma_3;\alpha_4\sigma_4}(0,0,0,0) = &\tilde{U}_\alpha \delta^\alpha_{\alpha_1} \delta^\alpha_{\alpha_2} \delta^\alpha_{\alpha_3} \delta^\alpha_{\alpha_4} \left[\delta^{\sigma_1}_{\sigma_4} \delta^{\sigma_2}_{\sigma_3} - \delta^{\sigma_1}_{\sigma_3} \delta^{\sigma_2}_{\sigma_4} \right] \\ &+ \left(\tilde{U}_{12} - \frac{\tilde{J}}{2} \right) \left[\delta^{\alpha_1}_{\alpha_4} \delta^{\alpha_2}_{\alpha_3} \delta^{\sigma_1}_{\sigma_4} \delta^{\sigma_2}_{\sigma_3} - \delta^{\alpha_1}_{\alpha_3} \delta^{\alpha_2}_{\alpha_4} \delta^{\sigma_1}_{\sigma_3} \delta^{\sigma_2}_{\sigma_4} \right] \\ &- \tilde{J} \left[\delta^{\alpha_1}_{\alpha_3} \delta^{\alpha_2}_{\alpha_4} \delta^{\sigma_1}_{\sigma_4} \delta^{\sigma_2}_{\sigma_3} - \delta^{\alpha_1}_{\alpha_4} \delta^{\alpha_2}_{\alpha_3} \delta^{\sigma_1}_{\sigma_3} \delta^{\sigma_2}_{\sigma_4} \right], \end{aligned} \tag{3.2.17}$$

where we follow [104], and can be calculated individually by invoking their respective cases of the 4-point function.

3.3 The Kondo Temperature

We identify the Kondo temperature $T_{\mathrm{K}\,\alpha}$ as the energy scale below which the impurity system α enters its low-energy FL regime, however we note that it is only meaningful if this scale is universal (so that there is strong correlation). Otherwise $T_{\mathrm{K}\,\alpha}$ is simply the renormalised temperature scale. $T_{\mathrm{K}\,\alpha}$ is therefore related to the degree of renormalisation required to bring the system to the low-energy FP, which is characterised by the quasiparticle weight z_α. Throughout our work, we thus define the Kondo temperature by

$$T_{\mathrm{K}\,\alpha} = \frac{1}{4}\pi\tilde{\Delta}. \tag{3.3.1}$$

At p-h symmetry, when a single electron resides on each impurity, we may enter a Kondo regime in the limit of strong local Coulomb interactions compared to hybridisation amplitude. When this regime is reached we find $\tilde{U}_\alpha = \pi\tilde{\Delta}_\alpha$. We demonstrate the emergence of the Kondo regime in figure 3.1, and show that when we are in this regime, the system is exponentially renormalised with respect to U_α. This is characterised by $T_{\mathrm{K}\,\alpha} \sim \mathrm{e}^{-U_\alpha/\pi\Delta}$.

Since $T_{\mathrm{K}\,\alpha}$ corresponds to the energy scale of the low-energy FP, it is possible to probe an impurity system to measure it. On the low-energy scale we describe the system in terms of quasiparticles in a FL, and the energy scale where they emerge corresponds to a peak in the spectral density. $T_{\mathrm{K}\,\alpha}$ is therefore given (approximately) by the width of the quasi-particle peak in $\rho_\alpha(\omega)$. We note that when the low-energy FP does not correspond to a FL, our definition of $T_{\mathrm{K}\,\alpha}$ breaks down. In this case, relevant to our discussion in chapter 5, we can estimate $T_{\mathrm{K}\,\alpha}$ from the width of the low-energy resonance in $\rho_\alpha(\omega)$.

We also point out that there are several different definitions of T_{K}. As an extension of Kondo's perturbative treatment of the s-d model, [16] showed that the divergence characterising the failure of this treatment occurred at a temperature

$$T \sim D\mathrm{e}^{-1/2J\rho(0)}, \tag{3.3.2}$$

which one can also use as a definition of T_{K}. Through the inclusion of a magnetic field in the s-d model, [105] related the $T = 0$ spin susceptibility $\chi(0)$ to the Kondo temperature by

$$T_{\mathrm{K}} = \frac{(g\mu_{\mathrm{B}})^2}{4\chi(0)} \tag{3.3.3}$$

where g is the spin g-factor, and μ_{B} is the Bohr magneton. At p-h symmetry (where low-energy Kondo physics emerge), and in the strong correlation regime, our definition of T_{K} is equivalent to this, where we set $g\mu_{\mathrm{B}} = 1$.

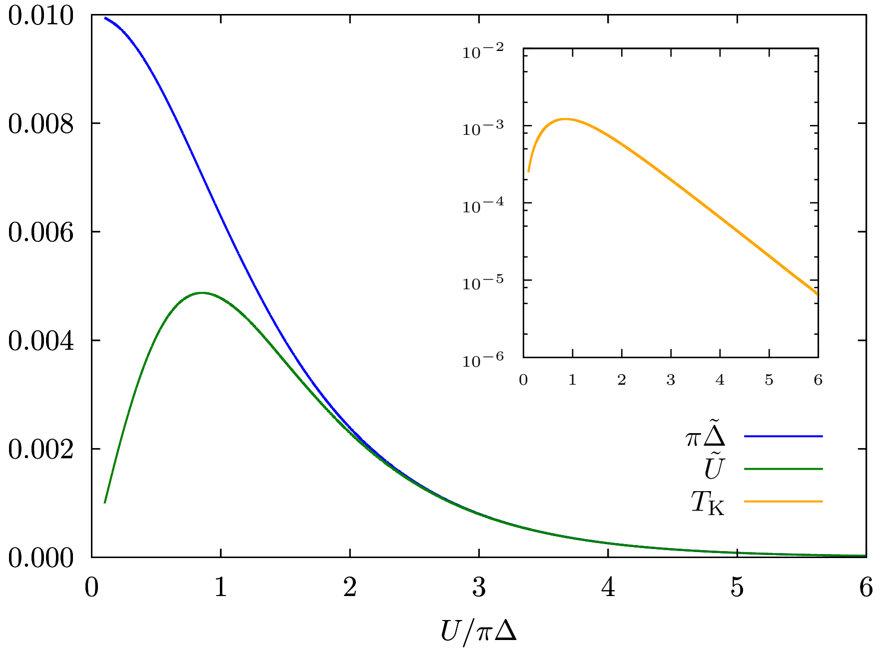

FIGURE 3.1: Renormalised parameters for the uncoupled channel symmetric, p-h symmetric 2IAM. For $U/\pi\Delta > 3$, we enter the strong correlation limit where $\tilde{U} \simeq \pi\tilde{\Delta}$ and the model is governed by Kondo physics. T_{K}, shown in the inset, exhibits logarithmic dependence on U in the strong correlation limit.

3.4 Counter-terms and Diagrammatic Perturbation Theory

The approach above allows one to very easily determine the renormalised parameters and quasiparticle density of states by making the assumption that the low-energy Hamiltonian is given by (3.2.9). However, the renormalised Hamiltonian $\tilde{H}$ is only valid over very small energy scales and therefore is clearly not equivalent to the full (bare) Hamiltonian H. The high-energy physics is contained in counter-terms; these are constraints which effectively cancel the divergences from the renormalised theory. We express the bare impurity system[3] as the Lagrangian

$$\begin{aligned}\mathcal{L} = &\sum_{\alpha\sigma} d^{\dagger}_{\alpha\sigma}(\tau)\left[\partial_{\tau} + \epsilon_{\alpha\sigma} - i\Delta_{\alpha\sigma}\right] d_{\alpha\sigma}(\tau) + \sum_{\alpha} U_{\alpha} n_{\alpha\uparrow}(\tau)\, n_{\alpha\downarrow}(\tau) \\ &+ U_{12}\sum_{\sigma\sigma'} n_{1\sigma}(\tau)\, n_{2\sigma'}(\tau) + 2J\boldsymbol{S}_1(\tau)\cdot\boldsymbol{S}_2(\tau),\end{aligned} \tag{3.4.1}$$

whilst the Lagrangian of the renormalised system is given by

$$\begin{aligned}\tilde{\mathcal{L}} = &\sum_{\alpha\sigma} \tilde{d}^{\dagger}_{\alpha\sigma}(\tau)\left[\partial_{\tau} + \tilde{\epsilon}_{\alpha\sigma} - i\tilde{\Delta}_{\alpha\sigma}\right] \tilde{d}_{\alpha\sigma}(\tau) + \sum_{\alpha} \tilde{U}_{\alpha} \tilde{n}_{\alpha\uparrow}(\tau)\, \tilde{n}_{\alpha\downarrow}(\tau) \\ &+ \tilde{U}_{12}\sum_{\sigma\sigma'} \tilde{n}_{1\sigma}(\tau)\, \tilde{n}_{2\sigma'}(\tau) + 2\tilde{J}\tilde{\boldsymbol{S}}_1(\tau)\cdot\tilde{\boldsymbol{S}}_2(\tau),\end{aligned} \tag{3.4.2}$$

and τ is used to denote imaginary-time. We construct a counter-term Lagrangian

$$\begin{aligned}\mathcal{L}_{\mathrm{CT}} = &\sum_{\alpha\sigma} \tilde{d}^{\dagger}_{\alpha\sigma}(\tau)\left[\lambda_{2,\alpha,\sigma}\partial_{\tau} + \lambda_{1,\alpha,\sigma}\right] \tilde{d}_{\alpha\sigma}(\tau) + \sum_{\alpha} \lambda_{3,\alpha} \tilde{n}_{\alpha\uparrow}(\tau)\, \tilde{n}_{\alpha\downarrow}(\tau) \\ &+ \lambda_4\sum_{\sigma\sigma'} \tilde{n}_{1\sigma}(\tau)\, \tilde{n}_{2\sigma'}(\tau) + \lambda_5\tilde{\boldsymbol{S}}_1(\tau)\cdot\tilde{\boldsymbol{S}}_2(\tau),\end{aligned} \tag{3.4.3}$$

and demand that it contains the high-energy behaviour of our system, so that

$$\mathcal{L} = \tilde{\mathcal{L}} + \mathcal{L}_{\mathrm{CT}}. \tag{3.4.4}$$

We thus obtain expressions for the counter-terms

$$\begin{aligned}\lambda_{1,\alpha,\sigma} &= -z_{\alpha}\Sigma_{\alpha\sigma}(0,h) \\ \lambda_{2,\alpha,\sigma} &= z_{\alpha} - 1 \\ \lambda_{3,\alpha} &= z_{\alpha}^2 U_{\alpha} - \tilde{U}_{\alpha} \\ \lambda_4 &= z_1 z_2 U_{12} - \tilde{U}_{12} \\ \lambda_5 &= 2z_1 z_2 J - 2\tilde{J}.\end{aligned} \tag{3.4.5}$$

---

[3] For simplicity, we leave out terms corresponding to the bulk as these play no role here.

Having formalised the difference between the renormalised and bare Hamiltonians, we now mention the difference between renormalised and bare quantities as pertaining to measurement in a laboratory. If an experiment takes place on some energy scale, then the quantities and couplings the experimentalist would measure are those which are renormalised to that scale. On higher energy scales the couplings would become more like the bare couplings, whilst on lower energy scales they tend towards those defined by the stable FP. As an example, if a 1IAM was cooled to temperatures below T_{K}, and an experimentalist attempted to measure the value of U, they would measure $\tilde{U}$.

Using the counter-terms, and our definitions of the renormalised parameters, we are able to perform diagrammatic perturbation theory on the low-energy system. The counter-terms are expanded in terms of the renormalised interaction parameters, with the coefficients being determined by the renormalisation conditions

$$\begin{aligned} \tilde{\Sigma}_\sigma(0,0) &= 0, \\ \partial_\omega \tilde{\Sigma}_\sigma(0,0) &= 0, \end{aligned} \tag{3.4.6}$$

and (3.2.17). These follow from the requirement that the low-energy FP is a FL. The reorganised renormalised Hamiltonian

$$\begin{aligned} \tilde{H} = &\sum_{\alpha\boldsymbol{k}} \epsilon_{\alpha\boldsymbol{k}} c^\dagger_{\alpha\boldsymbol{k}\sigma} c_{\alpha\boldsymbol{k}\sigma} + \sum_{\alpha\boldsymbol{k}} \tilde{V}_\alpha \left[c^\dagger_{\alpha\boldsymbol{k}\sigma} d_{\alpha\sigma} + d^\dagger_{\alpha\sigma} c_{\alpha\boldsymbol{k}\sigma} \right] + \sum_\alpha \tilde{\epsilon}_\alpha d^\dagger_{\alpha\sigma} d_{\alpha\sigma} \\ &+ \sum_\alpha \frac{\tilde{U}_\alpha}{2} d^\dagger_{\alpha\sigma} d^\dagger_{\alpha\sigma'} d_{\alpha\sigma'} d_{\alpha\sigma} + \frac{2\tilde{U}_{12} - \tilde{J}}{4} \sum_{\alpha\neq\alpha'} d^\dagger_{\alpha\sigma} d^\dagger_{\alpha'\sigma'} d_{\alpha'\sigma'} d_{\alpha\sigma} \\ &- \frac{\tilde{J}}{2} \sum_{\alpha\neq\alpha'} d^\dagger_{\alpha\sigma} d^\dagger_{\alpha'\sigma'} d_{\alpha\sigma'} d_{\alpha'\sigma}, \end{aligned} \tag{3.4.7}$$

gives rise to the interaction vertices shown in figure 3.2. The general Feynman rules, derived in [106] and [107], are adapted for our model and we list them as:

1. Vertices associated to the intra-impurity Coulomb interaction (figure 3.2a) on dot α contribute a factor of $-i\tilde{U}_\alpha$.

2. Vertices associated to the inter-impurity direct term (figure 3.2b) contribute a factor $-i(\tilde{U}_{12} - \tilde{J}/2)$.

3. Vertices associated to the inter-impurity exchange term (figure 3.2c) contribute a factor $+i\tilde{J}$.

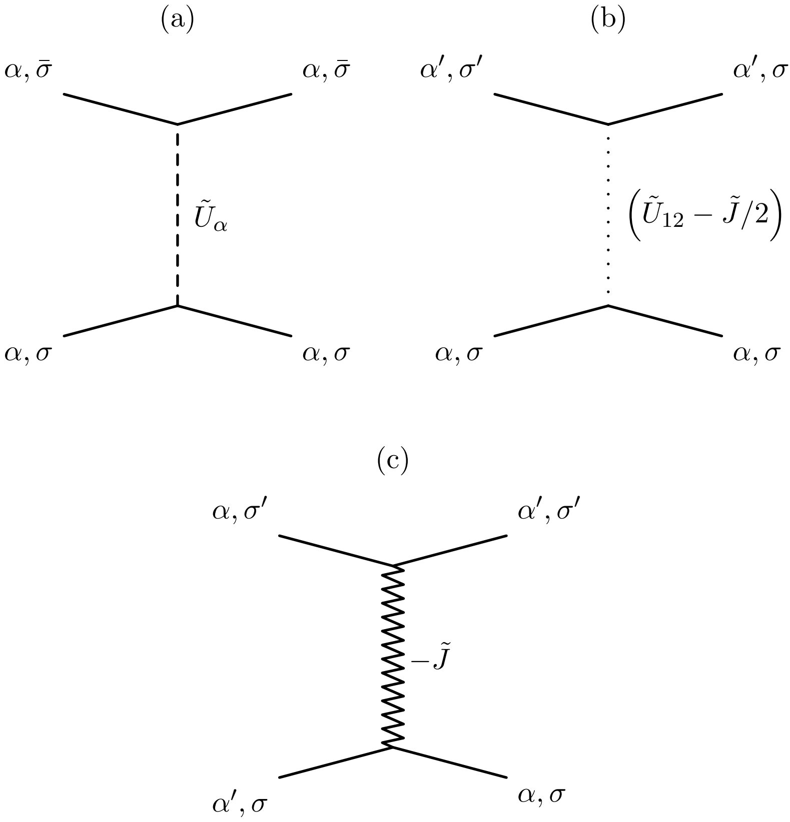

FIGURE 3.2: The scattering events, with their corresponding vertex factors, allowed by the renormalised Hamiltonian (3.4.7). We use the convention that $\alpha \neq \alpha'$. In (a), we see that scattering due to the local intra-impurity Coulomb term arises between opposite-spin electrons in the same channel. The direct, inter-impurity scattering shown in (b) scatters electrons in different channels, and does not depend on the spin. Meanwhile in (c), the exchange (Heisenberg) term scatters electrons into different channels.

4. Internal propagators of energy ω and spin σ in channel α contribute a factor $i\tilde{G}^{(0)}_{\alpha\sigma}(\omega)$. If evaluating a self-energy, there is an additional factor $\lim_{\delta\to 0^+}\exp(i\omega\delta)$ which restricts the contour integration.
5. Energy is conserved at every vertex, and any internal energy ω is integrated out by insertion of $\int_{-\infty}^{\infty} \mathrm{d}\omega/2\pi$.
6. Every Fermion loop contributes a factor of -1.
7. The resultant expression is to be multiplied by an overall factor i.
8. Interaction vertices must be adjusted according to the counter-terms.

The Feynman rules allow us to calculate, to certain order in the renormalised parameters, a number of different quantities. We focus on calculating these quantities at the Fermi level $\omega = 0$. To first order, we write $\tilde{\Sigma}_{\alpha\sigma}(0,h)$ as the sum of diagrams as in figure 3.3. The first diagram is given by the integral

$$I = -i(-i\tilde{U})\lim_{\delta\to 0^+}\int_{-\infty}^{\infty}\frac{\mathrm{d}\omega'}{2\pi} iG^{(0)}_{\alpha\bar{\sigma}}(\omega')\mathrm{e}^{i\delta\omega'} \tag{3.4.8}$$

where, as is usual for a self-energy diagram, the external legs are not included (they are only shown to illustrate that we are considering the self-energy in the channel α,σ). We calculate $I = \tilde{U}_\alpha \tilde{n}_{\alpha\bar{\sigma}}(h)$, with the other relevant diagrams evaluated similarly. Note that due to the absence of a Fermion loop in the oyster diagram, the result differs by a minus sign. The first order correction to the self-energy is therefore

$$\tilde{\Sigma}^{(1)}_{\alpha\sigma}(0,h) = \tilde{U}_\alpha \tilde{n}_{\alpha\bar{\sigma}}(h) + (\tilde{U}_{12} - \tilde{J}/2)\tilde{n}_{\alpha'\sigma}(h) + (\tilde{U}_{12} - \tilde{J}/2)\tilde{n}_{\alpha'\bar{\sigma}}(h) + \tilde{J}\tilde{n}_{\alpha'\sigma}(h), \tag{3.4.9}$$

and in order to satisfy the renormalisation conditions and counter-term rules, it is to be implied that we subtract the same expression with $h = 0$. We may use this expression to calculate both static and dynamic quantities. It is particularly useful in calculating 'longitudinal' dynamic quantities, which depend on the local occupation[4] $\langle \tilde{n}_{\alpha\sigma}(h)\rangle$; by the exact Friedel sum rule for a system of interacting quasiparticles, we have

$$\langle \tilde{n}_{\alpha\sigma}(h)\rangle = \frac{1}{2} - \frac{1}{\pi}\arctan\left[\frac{\tilde{\epsilon}_{\alpha\sigma} + \tilde{\Sigma}^{(1)}_{\alpha\sigma}(0,h)}{\tilde{\Delta}_\sigma}\right]. \tag{3.4.10}$$

---

[4] We use $\tilde{n}_{\alpha\sigma}(h)$ to denote the local channel occupation of the non-interacting FP quasiparticle system, while $\langle \tilde{n}_{\alpha\sigma}(h)\rangle$ represents the local occupation when interactions are present.

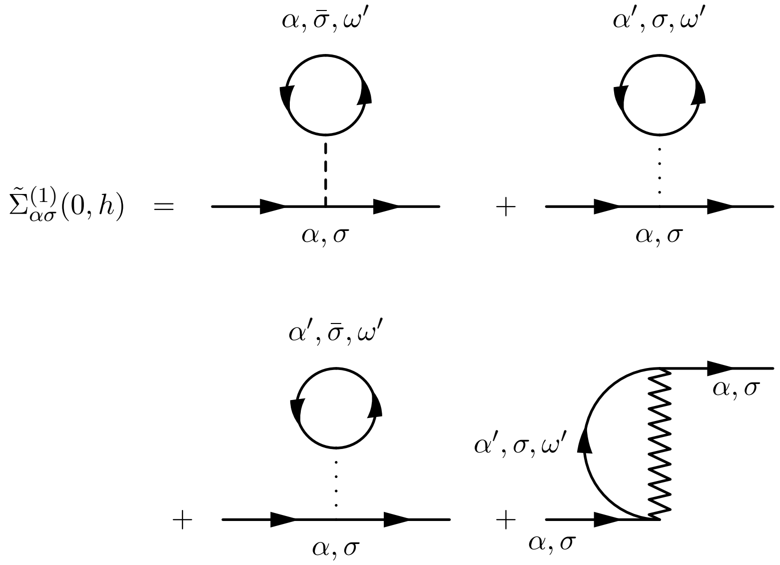

FIGURE 3.3: The allowed first order corrections to the renormalised self-energy.

3.5 Calculation of Dynamic Quantities

We now use the RPT to calculate the dynamic quantities that are relevant to our work presented here. We begin by calculation of $T = 0, \omega = 0$ longitudinal susceptibilities (we use these in our analysis of emergent SU(4) symmetry in chapter 4), before proceeding to calculate transverse susceptibilities (useful in understanding the quantum critical point we discuss in chapter 5). We also provide a brief description of how the formalism developed extends to finite frequency and temperature.

3.5.1 $\omega = 0$

The zero-frequency zero-temperature spin susceptibility

$$\chi_{\mathrm{S}} = \frac{1}{2}\sum_{\alpha} \partial_{h_\alpha} \left[\langle \tilde{n}_{\alpha\uparrow}(h_\alpha)\rangle - \langle \tilde{n}_{\alpha\downarrow}(h_\alpha)\rangle\right]\Big|_{h_\alpha=0}, \tag{3.5.1}$$

evaluated in the absence of a magnetic field, can be calculated by inserting (3.4.9) into (3.4.10) and differentiating as usual. We find

$$\chi_{\mathrm{S}} = \frac{1}{2}\sum_{\alpha} \tilde{\rho}^{(0)}_{\alpha}(0)\left[1 + \tilde{U}_{\alpha}\tilde{\rho}^{(0)}_{\alpha}(0) - \tilde{J}\tilde{\rho}^{(0)}_{\alpha'}(0)\right]. \tag{3.5.2}$$

The spin indices have been dropped since we set $h = 0$. Similarly, we define the charge susceptibility at $\omega = T = 0$ to be

$$\chi_{\mathrm{C}} = -4 \sum_{\alpha\sigma} \partial_{\tilde{\epsilon}} \left\langle \tilde{n}_{\alpha\sigma}(h_\alpha) \right\rangle \Big|_{h_\alpha = 0}, \tag{3.5.3}$$

where $\tilde{\epsilon} = \sum_{\alpha\sigma} \tilde{\epsilon}_{\alpha\sigma}$, which is calculated as

$$\chi_{\mathrm{C}} = \sum_{\alpha} 2\tilde{\rho}^{(0)}_{\alpha}(0) \left[1 - \tilde{U}_{\alpha} \tilde{\rho}^{(0)}_{\alpha}(0)\right] - 8\tilde{U}_{12} \tilde{\rho}^{(0)}_{1}(0) \tilde{\rho}^{(0)}_{2}(0). \tag{3.5.4}$$

Any difference between impurity levels ϵ_α can give rise to a ‘pseudospin’ field, where the occupation on impurity $\alpha = 1$ corresponds to an ‘up’ state and the occupation on impurity $\alpha = 2$ corresponds to a ‘down’ pseudospin. We define a pseudospin susceptibility

$$\chi_{\mathrm{PS}} = - \sum_{\alpha\sigma} \partial_{\tilde{\eta}} \left\langle \tilde{n}_{\alpha\sigma}(h_\alpha) \right\rangle \Big|_{h_\alpha = 0}, \tag{3.5.5}$$

where $\tilde{\eta} = \sum_{\sigma} \tilde{\epsilon}_{1\sigma} - \sum_{\sigma} \tilde{\epsilon}_{2\sigma}$. We evaluate this, again using (3.4.9), and find

$$\chi_{\mathrm{PS}} = \sum_{\alpha} \frac{1}{2} \tilde{\rho}^{(0)}_{\alpha}(0) \left[1 - \tilde{U}_{\alpha} \tilde{\rho}^{(0)}_{\alpha}(0)\right] + 2\tilde{U}_{12} \tilde{\rho}^{(0)}_{1}(0) \tilde{\rho}^{(0)}_{2}(0). \tag{3.5.6}$$

The constant factors in our definitions (3.5.1), (3.5.3) and (3.5.5) are present for convenience in our calculations throughout chapter 4. We define the Wilson Ratios, corresponding to each susceptibility, as

$$R_{\mathrm{S}} = \frac{2\chi_{\mathrm{S}}}{\tilde{\rho}^{(0)}_{1}(0) + \tilde{\rho}^{(0)}_{2}(0)} \tag{3.5.7}$$

$$R_{\mathrm{C}} = \frac{2\chi_{\mathrm{C}}}{\tilde{\rho}^{(0)}_{1}(0) + \tilde{\rho}^{(0)}_{2}(0)} \tag{3.5.8}$$

$$R_{\mathrm{PS}} = \frac{2\chi_{\mathrm{PS}}}{\tilde{\rho}^{(0)}_{1}(0) + \tilde{\rho}^{(0)}_{2}(0)}. \tag{3.5.9}$$

Heuristically, these ratios represent the interactions present in the system, with the total Wilson ratio in a non-interacting metal (ie Sommerfeld model) taking unit value. We use them in chapter 4 to formulate criteria for the emergence of an SU(4) Kondo regime, and to study systems which ‘nearly’ achieve such a regime.

In our analysis of the quantum critical point generated by the Heisenberg interaction in chapter 5, we use the NRG to calculate transverse dynamic quantities, and now seek to calculate these using the RPT. We cannot proceed as above, since our previous method relied on expressing the dynamic quantities in terms of local occupation. We thus sum the appropriate diagrams corresponding to the quantity at hand.

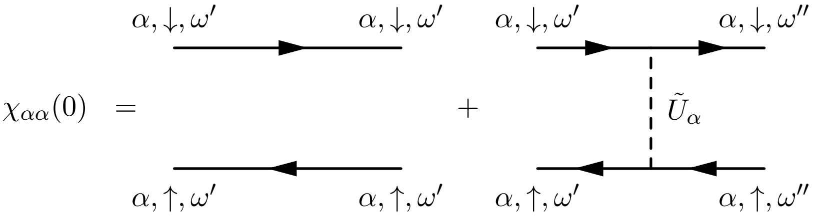

FIGURE 3.4: The transverse spin susceptibility, between equal impurities, expressed to first order.

The transverse spin susceptibility, between impurities α and β as defined in (2.4.6), is given by

$$\chi_{\alpha\beta}(\omega) = \left\langle\!\left\langle d^\dagger_{\alpha\uparrow} d_{\alpha\downarrow} ; d^\dagger_{\beta\downarrow} d_{\beta\uparrow} \right\rangle\!\right\rangle(\omega) \tag{3.5.10}$$

where we use $S^+_\alpha = d^\dagger_{\alpha\uparrow} d_{\alpha\downarrow}$ and $S^-_\alpha = d^\dagger_{\alpha\downarrow} d_{\alpha\uparrow}$. We initially specialise to the case $\alpha = \beta$ and interpret this as the Fourier transform of the propagator which at time $t = 0$, in channel α, creates a spin down particle and spin up hole, which are both annihilated at time $t = t$. To first order, $\chi_{\alpha\alpha}(0)$ is expressed as the sum of diagrams shown in figure 3.4. Using the Feynman rules, the diagrams respectively correspond to terms

$$-i \int_{-\infty}^{\infty} \frac{\mathrm{d}\omega'}{2\pi} \left[iG^{(0)}_{\alpha\bar{\sigma}}(\omega') \right]^2 \tag{3.5.11}$$

and

$$-i\left(-i\tilde{U}_\alpha\right) \int_{-\infty}^{\infty} \frac{\mathrm{d}\omega'}{2\pi} \frac{\mathrm{d}\omega''}{2\pi} \left[iG^{(0)}_{\alpha\bar{\sigma}}(\omega') \right]^2 \left[iG^{(0)}_{\alpha\bar{\sigma}}(\omega'') \right]^2, \tag{3.5.12}$$

where we note that both diagrams are in fact Fermion loops[5]. We find

$$\chi_{\alpha\alpha}(0) = \tilde{\rho}^{(0)}_\alpha(0) \left[1 + \tilde{U}_\alpha \tilde{\rho}^{(0)}_\alpha(0) \right]. \tag{3.5.13}$$

In the case $\beta = \alpha' \neq \alpha$, the only contributing diagram (to first order) is due to the exchange interaction, which maintains a particle's spin but changes its channel. The corresponding diagram is shown in figure 3.5, which we evaluate as

$$\chi_{\alpha\alpha'}(0) = -\tilde{J} \tilde{\rho}^{(0)}_\alpha(0) \tilde{\rho}^{(0)}_{\alpha'}(0). \tag{3.5.14}$$

---

[5] We do not close the loops at either end in our diagrams since this suggests that spin is not conserved.

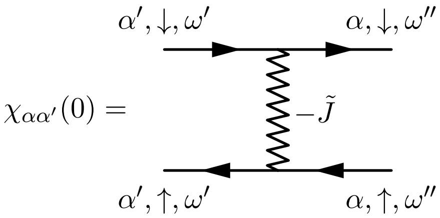

FIGURE 3.5: The transverse spin susceptibility, between different impurities ($\alpha \neq \alpha'$), expressed to first order.

Using (2.4.7) and (2.4.8) we hence arrive at expressions for the total and staggered transverse spin susceptibilities, respectively

$$\chi_{\text{tot}}(0) = \sum_{\alpha} \tilde{\rho}^{(0)}_{\alpha}(0) \left[1 + \tilde{U}_{\alpha} \tilde{\rho}^{(0)}_{\alpha}(0)\right] - 2\tilde{J} \tilde{\rho}^{(0)}_{1}(0) \tilde{\rho}^{(0)}_{2}(0) \tag{3.5.15}$$

and

$$\chi_{\text{stg}}(0) = \sum_{\alpha} \tilde{\rho}^{(0)}_{\alpha}(0) \left[1 + \tilde{U}_{\alpha} \tilde{\rho}^{(0)}_{\alpha}(0)\right] + 2\tilde{J} \tilde{\rho}^{(0)}_{1}(0) \tilde{\rho}^{(0)}_{2}(0). \tag{3.5.16}$$

We can also calculate the singlet and triplet susceptibilities using the RPT. We express them in terms of the 2-particle inter-impurity Green function

$$\Omega_{\sigma_1\sigma_2}(\omega) = \left\langle\!\!\left\langle d^{\dagger}_{1\sigma_1} d^{\dagger}_{2\bar{\sigma}_1} ; d_{2\sigma_2} d_{1\bar{\sigma}_2} \right\rangle\!\!\right\rangle(\omega), \tag{3.5.17}$$

so that

$$\chi_{\text{sng}}(\omega) = \frac{1}{2}\left[\Omega_{\uparrow\downarrow}(\omega) - \Omega_{\uparrow\uparrow}(\omega) - \Omega_{\downarrow\downarrow}(\omega) + \Omega_{\downarrow\uparrow}(\omega)\right] \tag{3.5.18}$$

and

$$\chi_{\text{trp}}(\omega) = \frac{1}{2}\left[\Omega_{\uparrow\downarrow}(\omega) + \Omega_{\uparrow\uparrow}(\omega) + \Omega_{\downarrow\downarrow}(\omega) + \Omega_{\downarrow\uparrow}(\omega)\right]. \tag{3.5.19}$$

To first order, the diagrammatic representations of $\Omega_{\sigma_1\sigma_2}(0)$ are shown in figure 3.6. The zeroth order term in figure 3.6a is given by

$$\begin{aligned} i\tilde{\Pi}(0) &:= \int_{-\infty}^{\infty} \frac{\mathrm{d}\omega'}{2\pi} \left[i\tilde{G}^{(0)}_{1}(\omega')\right] \left[i\tilde{G}^{(0)}_{2}(-\omega')\right] \\ &= -i \int_{-\infty}^{\infty} \frac{\mathrm{d}\omega'}{2\pi} \mathrm{sgn}(\omega') \frac{(\omega' + \tilde{\epsilon}_2)\,\tilde{\Delta}_1 + (\omega' - \tilde{\epsilon}_1)\,\tilde{\Delta}_2}{\left[(\omega' - \tilde{\epsilon}_1)^2 + \tilde{\Delta}_1\right]\left[(\omega' + \tilde{\epsilon}_2)^2 + \tilde{\Delta}_2\right]}. \end{aligned} \tag{3.5.20}$$

For the general case we do not calculate this expression explicitly (the result depends on the signs of the renormalised levels, and whether the model is p-h symmetric), but we note that in the case of channel symmetry, it is given by

$$\tilde{\Pi}(0) = -\frac{1}{\pi\tilde{\epsilon}} \arctan\left(\frac{\tilde{\epsilon}}{\tilde{\Delta}}\right). \tag{3.5.21}$$

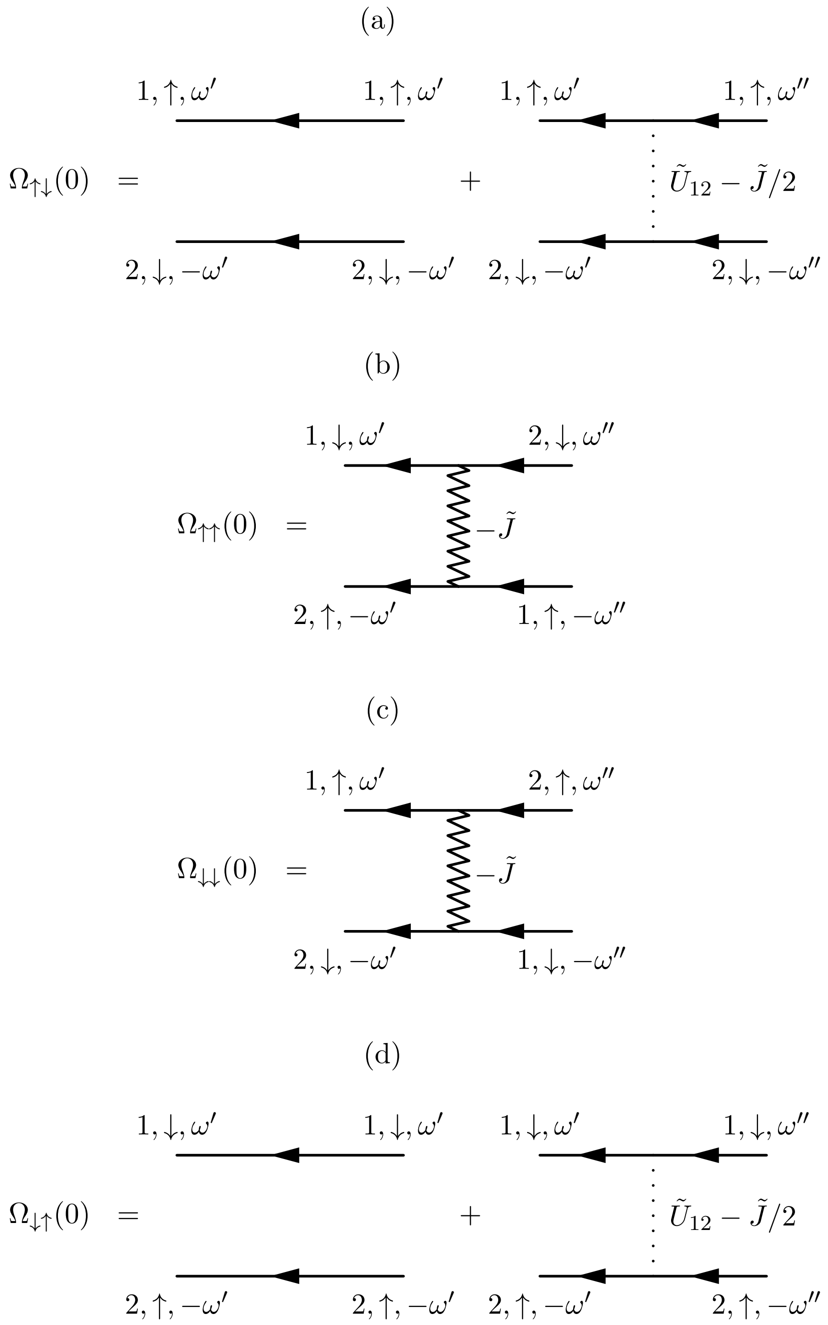

FIGURE 3.6: First order contributions to the various inter-impurity 2-particle Green functions useful to the calculation of the singlet and triplet pairing susceptibilities.

Evaluating the diagrams, we obtain

$$\Omega_{\uparrow\downarrow}(0) = \Omega_{\downarrow\uparrow}(0) = \Pi(0)\left[1 + \left(\tilde{U}_{12} - \frac{\tilde{J}}{2}\right)\Pi(0)\right], \tag{3.5.22}$$

$$\Omega_{\uparrow\uparrow}(0) = \Omega_{\downarrow\downarrow}(0) = \tilde{J}\Pi(0)^2, \tag{3.5.23}$$

where we note that the first order diagrams carry the same sign since

$$\int_{-\infty}^{\infty} \frac{\mathrm{d}\omega''}{2\pi}\left[i\tilde{G}_2^{(0)}(\omega'')\right]\left[i\tilde{G}_1^{(0)}(-\omega'')\right] = -i\tilde{\Pi}(0). \tag{3.5.24}$$

We hence calculate

$$\chi_{\mathrm{sng}}(0) = \Pi(0)\left[1 + \left(\tilde{U}_{12} - \frac{3\tilde{J}}{2}\right)\Pi(0)\right] \tag{3.5.25}$$

and

$$\chi_{\mathrm{trp}}(0) = \Pi(0)\left[1 + \left(\tilde{U}_{12} + \frac{\tilde{J}}{2}\right)\Pi(0)\right]. \tag{3.5.26}$$

3.5.2 $\omega \neq 0$

Our calculations of the dynamic quantities only provide insight into their values at the Fermi level, however it is possible to extend the approach to finite frequencies. In this regime, we must calculate terms to higher orders, where there is repeated scattering between the quasiparticles. To correctly account for the counter-terms, we perform the expansion in terms of the 'barred' couplings

$$\begin{aligned} \bar{U}_\alpha &= \tilde{U}_\alpha - \lambda_{3,\alpha} \\ \bar{U}_{12} &= \tilde{U}_{12} - \lambda_4 \\ \bar{J} &= \tilde{J} - \lambda_5. \end{aligned} \tag{3.5.27}$$

The sum over all distinct diagrams allows us to calculate the renormalised parameters from these. For example, the renormalised intra-impurity Coulomb interaction is given by the sum over all orders of the diagrams shown in figure 3.7 as $\tilde{U}_\alpha\left(\bar{U}_\alpha, \bar{J}\right)$. One may invert the resultant expression to find the barred couplings in terms of the renormalised ones: $\bar{U}_\alpha\left(\tilde{U}_\alpha, \tilde{J}\right)$. We perform the finite-frequency calculations similar to the zero-frequency case, using the barred couplings. By inserting expressions $\bar{U}_\alpha\left(\tilde{U}_\alpha, \tilde{J}\right)$, $\bar{U}_{12}\left(\tilde{U}_{12}, \tilde{J}\right)$ and $\bar{J}\left(\tilde{U}_{12}, \tilde{J}\right)$, the results of the perturbation theory may be interpreted using the usual renormalised couplings. We do not perform explicit calculations using this approach.

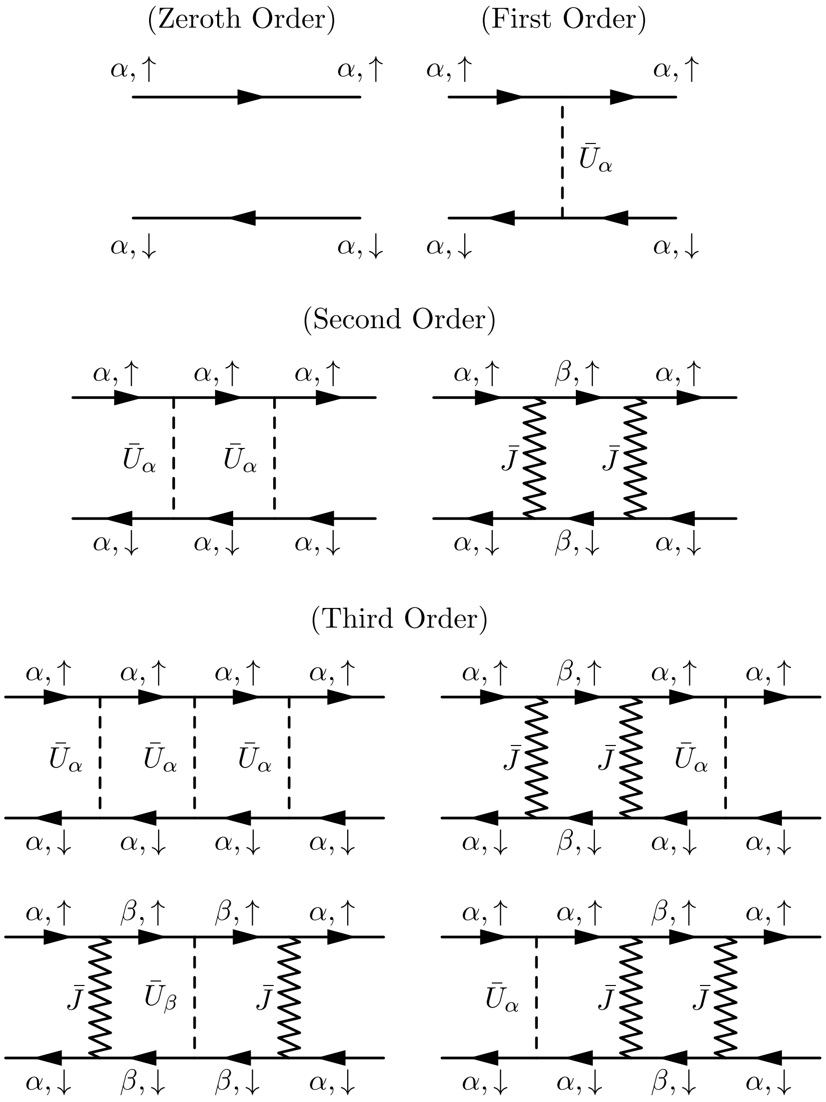

FIGURE 3.7: Contributions to the renormalised intra-impurity Coulomb interaction $\tilde{U}_\alpha$ due to repeated quasiparticle scattering. The perturbative expansion is in terms of couplings $\bar{U}_\alpha = \tilde{U}_\alpha - \lambda_{3,\alpha}$ and $\bar{J} = \tilde{J} - \lambda_5$. The sum over these diagrams (and those to higher order) gives the scattering amplitude $\tilde{U}_\alpha$.

3.5.3 1-Particle Spectral Density for the Low Temperature Regime

We finally seek to express to second order the 1-particle spectral density at finite ω and T, which we denote $\rho_\alpha(\omega,T)$. Away from the Fermi level, $\rho_\alpha(\omega,T)$ is deduced from the interacting Green function

$$G_\alpha(\omega,T) = \frac{z_\alpha}{\omega - \tilde{\epsilon}_\alpha + i\tilde{\Delta}_\alpha \mathrm{sgn}(\omega) - \tilde{\Sigma}_\alpha(\omega,T)}, \tag{3.5.28}$$

and evaluated as

$$\rho_\alpha(\omega,T) = \frac{z_\alpha}{\pi}\frac{\tilde{\Delta}_\alpha - \tilde{\Sigma}^{\mathrm{I}}_\alpha(\omega,T)}{\left[\omega - \tilde{\epsilon}_\alpha - \tilde{\Sigma}^{\mathrm{R}}_\alpha(\omega,T)\right]^2 + \left[\tilde{\Delta}_\alpha - \tilde{\Sigma}^{\mathrm{I}}_\alpha(\omega,T)\right]^2}, \tag{3.5.29}$$

where $\tilde{\Sigma}^{\mathrm{R}}_\alpha(\omega,T) = \mathrm{Re}\tilde{\Sigma}_\alpha(\omega,T)$ and $\tilde{\Sigma}^{\mathrm{I}}_\alpha(\omega,T) = \mathrm{Im}\tilde{\Sigma}_\alpha(\omega,T)$. Since we limit our discussion to consider only FL FPs, $\tilde{\Sigma}^{\mathrm{R}}_\alpha(\omega,T)$ and $\tilde{\Sigma}^{\mathrm{I}}_\alpha(\omega,T)$ both scale as ω^2 or T^2. Expanding $\rho_\alpha(\omega,T)$ to second order in ω and T, and using the standard series $(1-x)^{-1} = 1 + x + x^2 + \mathcal{O}(x^3)$, we obtain

$$\begin{aligned}\rho_\alpha(\omega,T) = \rho_\alpha(0,0)\Bigg[&1 + \frac{2\pi\tilde{\epsilon}_\alpha}{\tilde{\Delta}_\alpha}\tilde{\rho}_\alpha(0)\omega + \pi^2\tilde{\rho}_\alpha(0)^2\left(\frac{3\tilde{\epsilon}_\alpha^2}{\tilde{\Delta}_\alpha^2} - 1\right)\omega^2 \\ &- \frac{2\pi\tilde{\epsilon}_\alpha}{\tilde{\Delta}_\alpha}\tilde{\rho}_\alpha(0)\tilde{\Sigma}^{\mathrm{R}}_\alpha(\omega,T) + \pi\tilde{\rho}_\alpha(0)\left(1 - \frac{\tilde{\epsilon}_\alpha^2}{\tilde{\Delta}_\alpha^2}\right)\tilde{\Sigma}^{\mathrm{I}}_\alpha(\omega,T)\Bigg]\end{aligned} \tag{3.5.30}$$

which indicates that we require expressions for the real and imaginary parts of the renormalised self-energy. These have been calculated previously [108, 99, 97, 109], for the case $\tilde{J} = 0$, and we quote the results

$$\tilde{\Sigma}^{\mathrm{I}}_\alpha(\omega,T) = -\frac{\pi}{2}\left[\tilde{\rho}_\alpha(0)\right]^3\left[\tilde{U}_\alpha^2 + 2\tilde{U}_{12}^2\right]\left[\omega^2 + \pi^2T^2\right] \tag{3.5.31}$$

and

$$\begin{aligned}\tilde{\Sigma}^{\mathrm{R}}_\alpha(\omega,T) = &-\frac{\tilde{\epsilon}_\alpha}{3\tilde{\Delta}_\alpha}\left[\tilde{\rho}_\alpha(0)\right]^2\left[\tilde{U}_\alpha + 2\tilde{U}_{12}\right]\pi^3T^2 \\ &+ \frac{\tilde{\epsilon}_\alpha}{3\tilde{\Delta}_\alpha}\left[\tilde{\rho}_\alpha(0)\right]^3\left[\tilde{U}_\alpha + 2\tilde{U}_{12}\right]^2\pi^3T^2 \\ &+ \frac{\tilde{\epsilon}_\alpha}{3\tilde{\Delta}_\alpha}\left[\tilde{\rho}_\alpha(0)\right]^2\left[\tilde{U}_\alpha^2 + 2\tilde{U}_{12}^2\right]\left[\tilde{\rho}_\alpha(0) - \frac{1}{\pi\tilde{\epsilon}_\alpha}\arctan\left(\frac{\tilde{\epsilon}_\alpha}{\tilde{\Delta}_\alpha}\right)\right]\pi^3T^2.\end{aligned} \tag{3.5.32}$$

These expressions, combined with (3.5.30), allow us to determine the low-temperature behaviour of the 1-particle spectra. We will use this in chapter 4 to determine the temperature-dependence of the conductance between the impurity sites, and formulate an argument that specific properties of the conductance are indicative of a low-energy SU(4) symmetry.

Chapter 4

Emergent SU(4) Kondo Physics

In this chapter, we investigate whether an SU(4) Kondo regime, with unit total occupation, can arise on low energy scales in the 2IAM where there is no bare SU(4) symmetry, and the bare parameters resemble values attainable in a DQD experimental setup. We use the RPT to determine conditions on the renormalised parameters and Wilson ratios which are indicative of a low-energy Kondo regime that exhibits SU(4) symmetry. We test the parameter regimes where these conditions can be satisfied. Our study allows us to define a single T_{K}, and we then use the NRG to determine how this depends on U_{12}. We finalise our investigation by proposing a general property of the conductance which is indicative of an emergent SU(4) Kondo system with $n = 1$. Our work is geared towards experimental observation of this enhanced symmetry regime, and is likely to contribute to ongoing experimental work in the wider community.

4.1 Introduction

The usual Kondo effect, due to SU(2) spin degeneracy, has been accredited with explaining many different phenomena spanning the field of strongly correlated electrons. These include superconductivity [59], Kondo/topological insulators [110, 111] and the non-Fermi liquid (see chapter 5) properties associated with strange metals [112]. As we discuss in the chapter 1, the SU(2) Kondo effect has been well studied in gated quantum dot devices, in which certain model parameters may be tuned. In particular, the application of a bias voltage and subsequent measurement of the current has allowed detailed study of the Kondo many-body singlet, and its emergence [113, 114]. Given the importance of the Kondo effect in explaining several many-body problems, there is strong theoretical and experimental interest in more exotic Kondo states.

There has been a particular focus on understanding local models where there is an SU(2) psuedospin symmetry, due to the charge configuration, in addition to the usual SU(2) spin symmetry. These models are particularly relevant for carbon nanotube systems [115, 116, 117, 118] and DQD systems [119, 120, 121] where the total dot occupation is restricted to unity. We restrict our discussions to consider the DQD system only. The psuedospin symmetry in the DQD system is due to the occupation on each dot. We consider large inter-dot and intra-dot Coulomb repulsions so that the system prefers to contain a single electron, which is localised to one of the dots. The occupation on dot 1 corresponds to a pseudospin 'up' state, whilst the occupation on dot 2 corresponds to a 'down' state. The charge degrees of freedom hence give rise to the SU(2) pseudospin symmetry, and the total[1] charge symmetry has therefore been promoted from U(1) to U(2) $\cong$ U(1)$\otimes$SU(2). The model in this regime can give rise to an SU(4) 'spin' symmetry, but note that SU(4) $\geq$ SU(2)$\otimes$SU(2) $\cong$ SO(4). Correspondingly, in the 4-dimensional fundamental representation, there exist off-block-diagonal elements which couple the pseudospin and spin sectors, and in this sense the spin and charge degrees of freedom become entangled. A property of such a system is that, due to this entanglement, spin-polarised currents may be observed in the absence of a magnetic field [122]. This would have applications in the field of spintronics.

A detailed spectroscopic study of a DQD system, and a comparison with NRG calculations led to an initial claim that emergent SU(4) Kondo physics had been observed [123]. However, a study using the RPT concluded that due to the relative values of the inter- and intra-dot Coulomb coupling constants, the experimental system could not have been in an SU(4) Kondo regime [124]. In addition, tuning the couplings between the leads and dots in the DQD system is experimentally challenging, and an SU(4) symmetry requires that the couplings are precisely equal. This difficulty suggests that it may be more feasible to search for an SU(4) regime which

---

[1] To keep our notation compact, we discuss the total charge symmetry. This is invariance under a single U(1), rather than the usual U(1)$\otimes$U(1), which corresponds to conservation of the sum of particles in all charge and spin channels. One can easily check that channel charge (and in fact charge in each spin channel) is individually conserved in the SU(4) model.

emerges on lower energy scales, rather than fine tune the couplings to the leads. Through use of the non-crossing approximation, which assumes infinite inter- and intra-dot Coulomb repulsions, it has been shown that SU(4) may be restored on lower energy scales through adjustment of the gate voltages [125]. In effect, this tuning of the difference between the dot levels is equivalent to the application of pseudospin field. We seek to extend this work, using the RPT and NRG, to test whether SU(4) symmetry can emerge when the Coulomb repulsions are finite.

4.2 Relating the DQD System and 2IAM

Our investigation is heavily motivated by the experimental possibility of unambiguously observing emergent SU(4) Kondo physics. These experiments are carried out in engineered DQD structures, with a general schematic as shown in figure 1.4. We see that each dot has a source and drain lead, so that NRG studies of the system might appear to be prohibited due to the presence of 4 conduction baths. We show in this section that we can regard the equilibrium DQD system as the 2IAM. The DQD Hamiltonian is formulated as

$$\begin{aligned} H_{\text{DQD}} = &\sum_{\nu\alpha\boldsymbol{k}} \epsilon_{\nu\alpha\boldsymbol{k}} c^{\dagger}_{\nu\alpha\boldsymbol{k}\sigma} c_{\nu\alpha\boldsymbol{k}\sigma} + \sum_{\nu\alpha\boldsymbol{k}} V_{\nu\alpha\boldsymbol{k}} \left[c^{\dagger}_{\nu\alpha\boldsymbol{k}\sigma} d_{\alpha\sigma} + d^{\dagger}_{\alpha\sigma} c_{\nu\alpha\boldsymbol{k}\sigma} \right] \\ &+ \sum_{\alpha} \left[\epsilon_{\alpha} d^{\dagger}_{\alpha\sigma} d_{\alpha\sigma} + U_{\alpha} n_{\alpha\uparrow} n_{\alpha\downarrow} \right] + U_{12} \sum_{\sigma\sigma'} n_{1\sigma}\, n_{2\sigma'} \end{aligned} \tag{4.2.1}$$

where $\alpha \in \{1, 2\}$ sums over the dots as usual, and $\nu \in \{\text{S}, \text{D}\}$ sums over the source and drain leads connected to dot α. Throughout this chapter we switch off any inter-dot magnetic interaction. We define the Fermionic operators

$$\begin{aligned} b^{\dagger}_{\alpha\boldsymbol{k}\sigma} &= \frac{1}{\sqrt{|V_{\text{S}\alpha\boldsymbol{k}}|^2 + |V_{\text{D}\alpha\boldsymbol{k}}|^2}} \left[V_{\text{S}\alpha\boldsymbol{k}} c^{\dagger}_{\text{S}\alpha\boldsymbol{k}\sigma} + V_{\text{D}\alpha\boldsymbol{k}} c^{\dagger}_{\text{D}\alpha\boldsymbol{k}\sigma} \right] \\ \bar{b}^{\dagger}_{\alpha\boldsymbol{k}\sigma} &= \frac{1}{\sqrt{|V_{\text{S}\alpha\boldsymbol{k}}|^2 + |V_{\text{D}\alpha\boldsymbol{k}}|^2}} \left[V^{*}_{\text{D}\alpha\boldsymbol{k}} c^{\dagger}_{\text{S}\alpha\boldsymbol{k}\sigma} - V^{*}_{\text{S}\alpha\boldsymbol{k}} c^{\dagger}_{\text{D}\alpha\boldsymbol{k}\sigma}, \right] \end{aligned} \tag{4.2.2}$$

which satisfy the usual Dirac algebra, and enforce the equilibrium condition that $\mu_{\text{S}\alpha} = \mu_{\text{D}\alpha}$, or equivalently $\epsilon_{\text{S}\alpha\boldsymbol{k}} = \epsilon_{\text{D}\alpha\boldsymbol{k}} = \epsilon_{\alpha\boldsymbol{k}}$. The DQD Hamiltonian is then given by

$$\begin{aligned} H_{\text{DQD}} = &\sum_{\alpha\boldsymbol{k}} \epsilon_{\alpha\boldsymbol{k}} \bar{b}^{\dagger}_{\alpha\boldsymbol{k}\sigma} \bar{b}_{\alpha\boldsymbol{k}\sigma} + \sum_{\alpha\boldsymbol{k}} \epsilon_{\alpha\boldsymbol{k}} b^{\dagger}_{\alpha\boldsymbol{k}\sigma} b_{\alpha\boldsymbol{k}\sigma} + \sum_{\alpha\boldsymbol{k}} V_{\alpha\boldsymbol{k}} \left[b^{\dagger}_{\alpha\boldsymbol{k}\sigma} d_{\alpha\sigma} + d^{\dagger}_{\alpha\sigma} b_{\alpha\boldsymbol{k}\sigma} \right] \\ &+ \sum_{\alpha} \left[\epsilon_{\alpha} d^{\dagger}_{\alpha\sigma} d_{\alpha\sigma} + U_{\alpha} n_{\alpha\uparrow} n_{\alpha\downarrow} \right] + U_{12} \sum_{\sigma\sigma'} n_{1\sigma}\, n_{2\sigma'} \end{aligned} \tag{4.2.3}$$

where

$$V_{\alpha\boldsymbol{k}} = \sqrt{|V_{\mathrm{S}\alpha\boldsymbol{k}}|^2 + |V_{\mathrm{D}\alpha\boldsymbol{k}}|^2}, \tag{4.2.4}$$

and may therefore be decomposed into two subsystems. There is an uncoupled non-interacting Fermi gas of the $\bar{b}$ electrons which play no role in the dynamics of the dots, and the 2IAM which describes how the dots themselves are only coupled to the b electrons. We perform calculations for the equilibrium DQD system through use of the NRG and RPT as formulated for the 2IAM. We take the usual approximation that $V_{\alpha\boldsymbol{k}} = V_\alpha$ and assume that the system is isotropic. The hybridisation width on dot α is then given by $\Delta_\alpha = \Delta_{\mathrm{S}\alpha} + \Delta_{\mathrm{D}\alpha}$.

4.3 SU(4) on the Bare Scale

To manifest SU(4) in the 2IAM on the bare scale, the Hamiltonian must satisfy a number of conditions (these are to be used in the next section to specify the structure of the low-energy SU(4) effective Hamiltonian). We see that if $U_1 = U_2 = U_{12} := U$ and $\epsilon_1 = \epsilon_2 := \epsilon$ then the impurity Hamiltonian becomes

$$\begin{aligned} H_{\mathrm{imp}} &= \left(\epsilon + \frac{3U}{2}\right) n + \frac{U}{2}(n-2)^2 - 2U \\ &= \left(\epsilon - \frac{U}{2}\right) \sum_{\alpha\sigma} n_{\alpha\sigma} + \frac{U}{2} \sum_{\substack{\alpha_1\alpha_2 \\ \sigma_1\sigma_2}} n_{\alpha_1\sigma_1} n_{\alpha_2\sigma_2}. \end{aligned} \tag{4.3.1}$$

If we enforce the requirement that each bath has equal hybridisation, $V_1 = V_2 := V$ then we obtain the full Hamiltonian

$$\begin{aligned} H = &\sum_{\alpha\boldsymbol{k}} \epsilon_{\boldsymbol{k}} c^\dagger_{\alpha\boldsymbol{k}\sigma} c_{\alpha\boldsymbol{k}\sigma} + \sum_{\alpha\boldsymbol{k}} V \left[c^\dagger_{\alpha\boldsymbol{k}\sigma} d_{\alpha\sigma} + d^\dagger_{\alpha\sigma} c_{\alpha\boldsymbol{k}\sigma} \right] \\ &+ \left(\epsilon - \frac{U}{2}\right) \sum_{\alpha\sigma} n_{\alpha\sigma} + \frac{U}{2} \sum_{\substack{\alpha_1\alpha_2 \\ \sigma_1\sigma_2}} n_{\alpha_1\sigma_1} n_{\alpha_2\sigma_2}. \end{aligned} \tag{4.3.2}$$

This model exhibits the symmetry of interest. To make it manifest, we introduce the vectors

$$\boldsymbol{\Psi}_{\boldsymbol{k}} = \begin{pmatrix} c_{1\boldsymbol{k}\uparrow} \\ c_{1\boldsymbol{k}\downarrow} \\ c_{2\boldsymbol{k}\uparrow} \\ c_{2\boldsymbol{k}\downarrow} \end{pmatrix}, \quad \boldsymbol{\Phi} = \begin{pmatrix} d_{1\uparrow} \\ d_{1\downarrow} \\ d_{2\uparrow} \\ d_{2\downarrow} \end{pmatrix}, \tag{4.3.3}$$

which respectively encapsulate the degrees of freedom of the bulk and impurity systems. The Hamiltonian is then given by

$$H = \sum_{\boldsymbol{k}} \epsilon_{\boldsymbol{k}} \boldsymbol{\Psi}_{\boldsymbol{k}}^{\dagger} \boldsymbol{\Psi}_{\boldsymbol{k}} + \sum_{\boldsymbol{k}} V \left[\boldsymbol{\Psi}_{\boldsymbol{k}}^{\dagger} \boldsymbol{\Phi} + \boldsymbol{\Phi}^{\dagger} \boldsymbol{\Psi}_{\boldsymbol{k}} \right] + \left(\epsilon - \frac{5U}{2} \right) \boldsymbol{\Phi}^{\dagger} \boldsymbol{\Phi} + \frac{U}{2} \left(\boldsymbol{\Phi}^{\dagger} \boldsymbol{\Phi} \right) \left(\boldsymbol{\Phi}^{\dagger} \boldsymbol{\Phi} \right). \tag{4.3.4}$$

This is invariant under the coupled transformation

$$\begin{cases} \boldsymbol{\Psi}_{\boldsymbol{k}} & \to & \boldsymbol{U} \boldsymbol{\Psi}_{\boldsymbol{k}} \\ \boldsymbol{\Phi} & \to & \boldsymbol{U} \boldsymbol{\Phi} \end{cases}, \tag{4.3.5}$$

if $\boldsymbol{U}^{\dagger} \boldsymbol{U} = \boldsymbol{U} \boldsymbol{U}^{\dagger} = \mathbb{I}$, so the corresponding symmetry group is $\mathrm{U}(4) \cong \mathrm{SU}(4) \otimes \mathrm{U}(1)$. An observation of the Kondo effect, enhanced by the pseudospin degeneracy, in a DQD system [126] led the authors to estimate the coupling constants as $U_1 \simeq 1.2$meV, $U_2 \simeq 1.5$meV, $U_{12} \simeq 0.1$meV, $\Delta_1 \simeq \Delta_2 \simeq 0.005 - 0.020$meV. These motivate the need for our study; SU(4) symmetry does not (feasibly) exist on the bare scale, and if one hopes to observe it then it must emerge on lower energy scales.

4.4 Low-Energy Requirements for an $n = 1$ SU(4) Kondo Regime

We have established that the 2IAM is invariant under SU(4) if $U_1 = U_2 = U_{12}$, $\Delta_1 = \Delta_2$ and $\epsilon_1 = \epsilon_2$. These conditions must therefore be satisfied by the low energy Hamiltonian if SU(4) invariance is to emerge. We hence require

$$\tilde{U}_1 = \tilde{U}_2 = \tilde{U}_{12} := \tilde{U} \tag{4.4.1}$$

$$\tilde{\Delta}_1 = \tilde{\Delta}_2 := \tilde{\Delta} \tag{4.4.2}$$

$$\tilde{\epsilon}_1 = \tilde{\epsilon}_2 := \tilde{\epsilon}. \tag{4.4.3}$$

Due to the orbital degeneracy we also require that the electron has an equal probability of occupying either dot. We thus demand $\rho_1(\omega) = \rho_2(\omega) := \rho(\omega)$ for small ω. Since $\rho_\alpha(0) = z_\alpha \tilde{\rho}_\alpha(0)$, we hence arrive at the further condition

$$z_1 = z_2 := z. \tag{4.4.4}$$

The satisfaction of these constraints guarantees a low-energy emergent SU(4) symmetry, but does not guarantee an $n = 1$ Kondo regime. Using the renormalised form of the Friedel sum rule (3.2.12), the localisation of a single electron in the

DQD requires $\tilde{\epsilon} = \tilde{\Delta}$. Finally, to be in the Kondo regime the single d-electron must be totally localised to the dots such that the charge fluctuations are suppressed. We hence require $\chi_{\text{C}} = 0$, where χ_{C} is given in (3.5.3). It follows that $\tilde{U}\tilde{\rho}(0) = 1/3$. We condense all these requirements into 3 conditions:

1. $\rho_1(\omega) = \rho_2(\omega) = \rho(\omega)$ in the limit $\omega \to 0$,
2. $n = 1$,
3. $R_{\text{S}} = R_{\text{PS}} = 4/3$.

We use the satisfied conditions to identify the 'type' of low energy FP. If all conditions are satisfied, then we have an $n = 1$ SU(4) Kondo regime with a universal energy scale $T_{\text{K}}^{\text{SU}(4)} := 1/4\tilde{\rho}(0)$. If condition (1) is only satisfied at $\omega = 0$ and conditions (2) and (3) are satisfied, then we attribute the low energy FP with having restricted SU(4) symmetry. If only (1) and (2) are satisfied, but charge fluctuations are sufficiently suppressed so that $1 < R_{\text{PS}} \lesssim 4/3$ and $4/3 \lesssim R_{\text{PS}} < 2$, then we describe the FP has having approximate SU(4) symmetry.

An important observation is that if $\Delta_1 \neq \Delta_2$, we can not satisfy both conditions $\tilde{\Delta}_1 = \tilde{\Delta}_2$ and $z_1 = z_2$. Therefore in DQD systems with $\Delta_1 \neq \Delta_2$, we cannot have an emergent 'strict' SU(4) Kondo regime. However, we could still obtain a restricted SU(4) point in such a system.

4.5 Emergence of the SU(4), $n = 1$ Kondo Regime

Having established the criteria for a low-energy SU(4) Kondo system, we investigate whether the introduction of a pseudospin field can give rise to such a regime, in the case where U_1, U_2 and U_{12} are finite (this is possible in the case where U_1, U_2 and U_{12} are infinite [125]). We begin with the case $U_1 = U_2 = U_{12} = 0.5$, with $\pi\Delta_1 = 0.01$ and $\pi\Delta_2 = 0.007896$. We set $\epsilon_1 = -0.0933$ and tune ϵ_2 so that $n = 1$. Since the Coulomb repulsions are of the order of the bandwidth $D = 1$, and much larger than the hybridisation widths, we expect SU(4) symmetry to emerge on the lowest energy scales as the model has become more like those considered in [125]. Following their method, we introduce a pseudospin field $\delta\epsilon_{12} = \epsilon_1 - \epsilon_2$[2] and probe the resulting low-energy FL FPs, searching for an enhancement of χ_{PS}. The enhancement

---

[2] To maintain the total local occupation, we change both ϵ_1 and ϵ_2 as we vary $\delta\epsilon_{12}$ as $\epsilon_1 + \delta\epsilon_{12}/2$ and $\epsilon_2 - \delta\epsilon_{12}/2$.

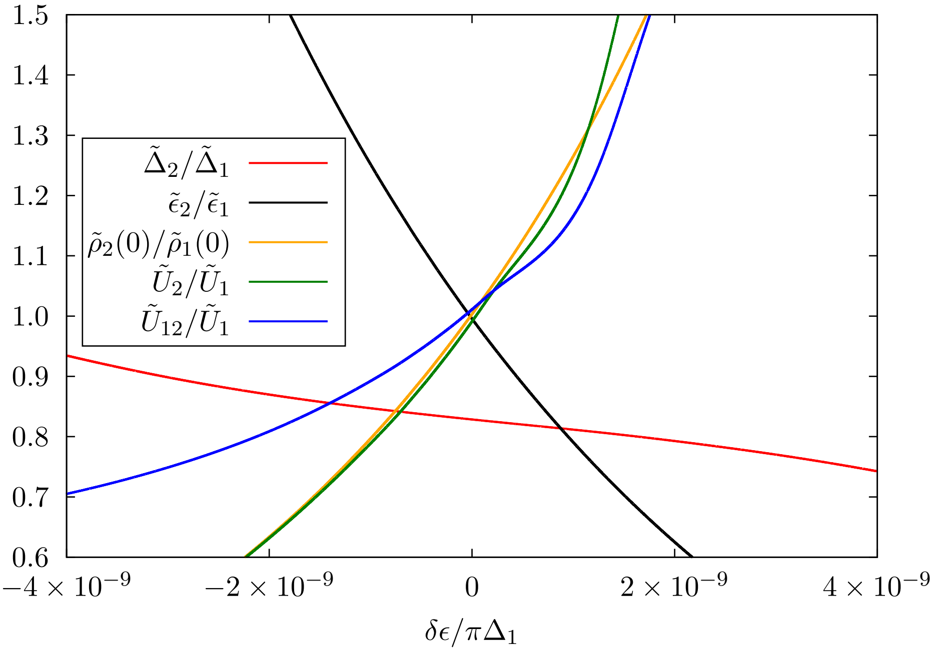

FIGURE 4.1: The ratios $\tilde{\Delta}_2/\tilde{\Delta}_1$, $\tilde{\epsilon}_2/\tilde{\epsilon}_1$, $\tilde{\rho}_2(0)/\tilde{\rho}_1(0)$, $\tilde{U}_2/\tilde{U}_1$, and $\tilde{U}_{12}/\tilde{U}_1$ for the model with $\pi\Delta_1 = 0.01$, $\pi\Delta_2 = 0.007896$, $U_1 = U_2 = U_{12} = 0.5$. For these parameters, $\delta_C = 2.960151343 \times 10^{-4}$ [109].

is maximal at $\delta\epsilon_{12} = \delta_C = 2.960151343 \times 10^{-4}$, and we define $\delta\epsilon = \delta\epsilon_{12} - \delta_C$ as a convenient measure of the deviation from this value. We plot in figure 4.1 the ratios $\tilde{\Delta}_2/\tilde{\Delta}_1$, $\tilde{\epsilon}_2/\tilde{\epsilon}_1$, $\tilde{\rho}_2(0)/\tilde{\rho}_1(0)$, $\tilde{U}_2/\tilde{U}_1$, and $\tilde{U}_{12}/\tilde{U}_1$. With the exception of $\tilde{\Delta}_2/\tilde{\Delta}_1$, these ratios cross at around unit value, so that we have a good approximation to emergent SU(4). However, we do not find $\tilde{\Delta}_1 = \tilde{\Delta}_2$. This is due to the aforementioned issue that if $\Delta_1 \neq \Delta_2$, we cannot obtain a strict SU(4) point. In this case $z_2/z_1 = 1.05$, so we obtain a restricted SU(4) symmetry. As discussed, the emergence of an SU(4) symmetry is not indicative of unit occupation or a Kondo regime. We show in figure 4.2a that $n = 1$ for all values of $\delta\epsilon_{12}$. Notice that the individual dot occupations cross at $\delta\epsilon \neq 0$. This is due to the Friedel sum rule; if $\rho_1(0) = \rho_2(0)$ and $\Delta_1 \neq \Delta_2$, then $n_1 \neq n_2$. Figure 4.2b shows that R_{PS} is enhanced to 4/3 (illustrated by the dashed line), while R_{S} is diminished to the same value and $R_{\mathrm{C}} = 0$. We therefore have that, at $\delta\epsilon = 0$, the system is in an $n = 1$ Kondo regime. There is a single emergent energy scale defined by the intersection of the $T_{\mathrm{K}\alpha}$ which we calculate as $T_{\mathrm{K}} \simeq 1.01 \times 10^{-10}$, as shown in figure 4.3. Noting from figure 3.1 that T_{K} decreases logarithmically with $U/\pi\Delta$ in the strong correlation regime, the small T_{K} is not

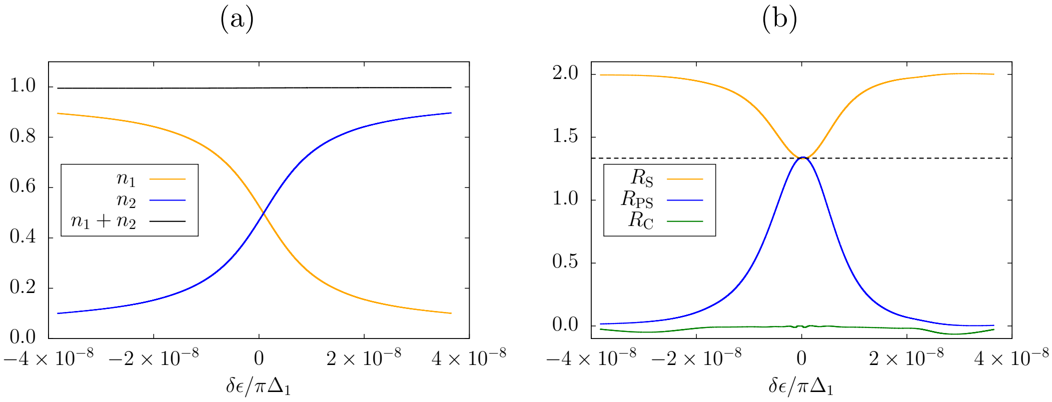

FIGURE 4.2: The individual and total occupations of each dot (a) and the spin and pseudospin Wilson ratios (b) for the same model as considered in figure 4.1.

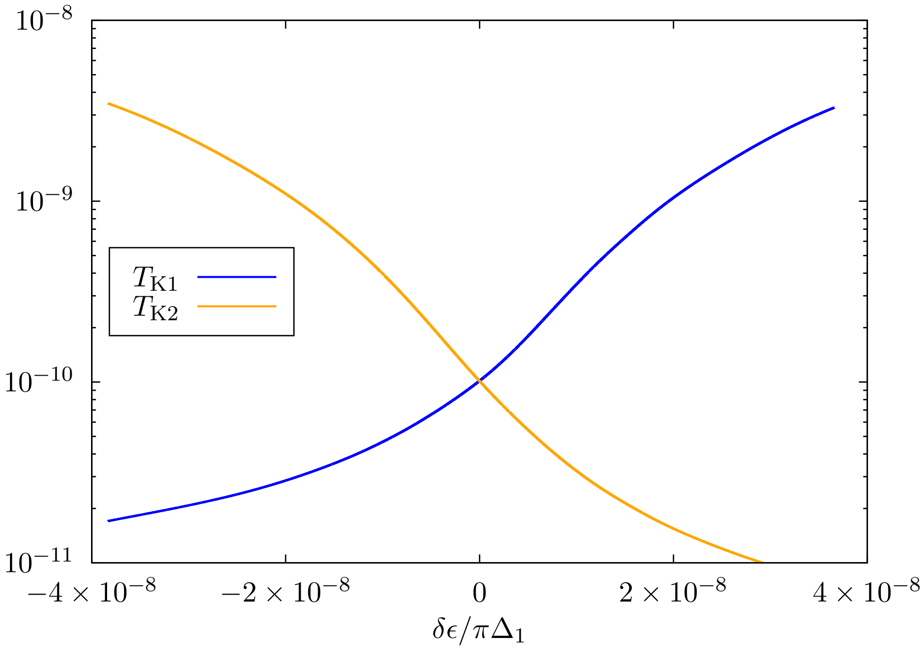

FIGURE 4.3: The values of $T_{K\alpha}$ for each dot as a function of the deviation from the point of maximal R_{PS}. The model parameters are the same as those in figure 4.1.

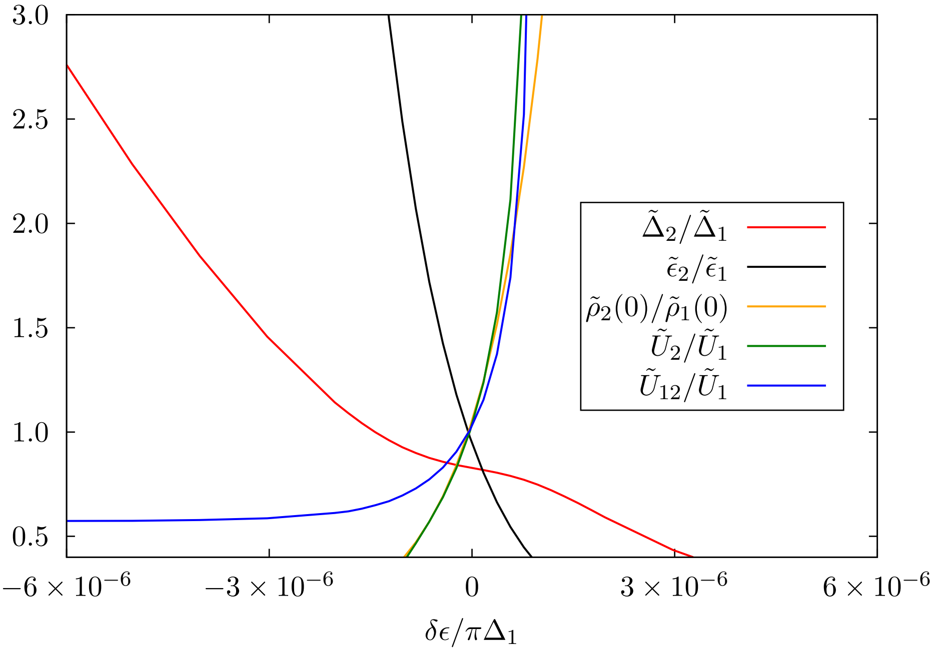

FIGURE 4.4: The ratios $\tilde{\Delta}_2/\tilde{\Delta}_1$, $\tilde{\epsilon}_2/\tilde{\epsilon}_1$, $\tilde{\rho}_2(0)/\tilde{\rho}_1(0)$, $\tilde{U}_2/\tilde{U}_1$, and $\tilde{U}_{12}/\tilde{U}_1$ for the model with $\pi\Delta_1 = 0.01$, $\pi\Delta_2 = 0.007896$, $U_1 = U_2 = 5$, $U_{12} = 3$. For these parameters, $\delta_{\mathrm{C}} = 6.113003 \times 10^{-4}$ [109].

surprising. We have performed a similar analysis of models with $U_1 = U_2 = U_{12}$ for smaller values of $U/\pi\Delta_1$, and find similar results, with a larger T_{K}. We thus conclude that in the model with $\Delta_1 \neq \Delta_2$ and $U_1 = U_2 = U_{12}$, it is possible to restore a restricted SU(4) symmetry[3], through application of a pseudospin field, and simultaneously achieve an $n = 1$ Kondo regime. This is in line with the conclusions of [125], which we have extended to the case of U finite and, furthermore, $U < D$.

We proceed to the more experimentally attainable system $U_1 = U_2 \neq U_{12}$. Initially we consider the case $U_1 = U_2 > D$ and $U_{12} > D$, and pick $U_1 = U_2 = 5$, $U_{12} = 3$. For this case we calculate $\delta_{\mathrm{C}} = 6.113003 \times 10^{-4}$. The ratios of the renormalised parameters are plotted in figure 4.4, and show that as in the previous cases, all ratios with the exception of $\tilde{\Delta}_2/\tilde{\Delta}_1$ become 1 at $\delta\epsilon = 0$. We thus have the possibility of a restricted SU(4) regime, and figure 4.5 confirms that this is the case. We have therefore shown that the conclusions of [125] also hold in this case.

---

[3] Since the SU(4) FP is restricted, we gain little information regarding the energy scales on which the symmetry persists. We therefore do not define a $T_{\mathrm{K}}^{\mathrm{SU}(4)}$.

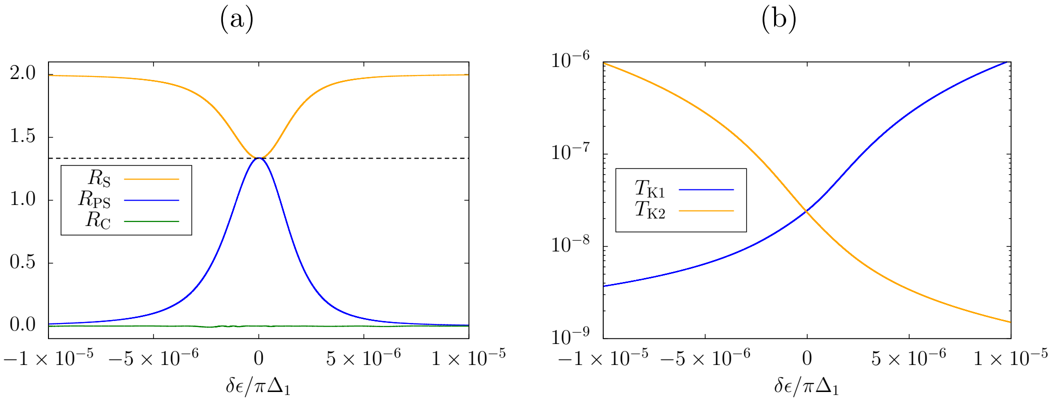

FIGURE 4.5: The relevant Wilson ratios (a) and the individual Kondo temperatures (b) as a function of $\delta\epsilon/\pi\Delta_1$ for the model parameters as given in the caption of figure 4.4.

Although it may appear that the difference between $U_1 = U_2$ and U_{12} plays little role, the Kondo temperature, given by $T_{\rm K} \simeq 2.4 \times 10^{-8}$, differs substantially from what we might expect - it is larger than the model with $U_1 = U_2 = U_{12} = 0.5$. The degree of renormalisation is thus drastically altered by U_{12}, and we shall discuss this later in the chapter.

We now bring down the Coulomb repulsions so that they are smaller than D, and choose $U_1 = U_2 = 0.05$, $U_{12} = 0.03$. We calculate $\delta_{\rm C} = -2.00 \times 10^{-5}$. Unlike the previous parameter sets, in this case the renormalised coupling constant ratios do not all reach 1. Figure 4.6 shows that $\tilde{U}_{12}/\tilde{U}_1$ only achieves the value of $\sim 1/2$ at $\delta\epsilon = 0$ so that there cannot be an SU(4) point in this model. Despite this, we still see an enhancement of $R_{\rm PS}$ shown in figure 4.7a. The model therefore reaches an approximate SU(4) FP. In line with the previous comments on the dependence of $T_{\rm K}$ on U_{12}, we have in this case $T_{\rm K} \simeq 1.35 \times 10^{-3}$, whereas for $U_1 = U_2 = U_{12} = 0.05$ we had found $T_{\rm K} \simeq 6.30 \times 10^{-4}$. It seems, as before, that a decrease of U_{12} results in an increase in $T_{\rm K}$. We also break the restriction $U_1 = U_2$ and find similar results.

Our calculations point to the conclusion that the application of a pseudospin field can restore a restricted SU(4) $n = 1$ Kondo regime if $U_1 = U_2 = U_{12}$, and in the case $U_1 > D$, $U_2 > D$ but only if $U_{12} > D$. Otherwise there is an enhancement of $\chi_{\rm PS}$ which leads to an approximate SU(4) point. This conclusion has direct signif-

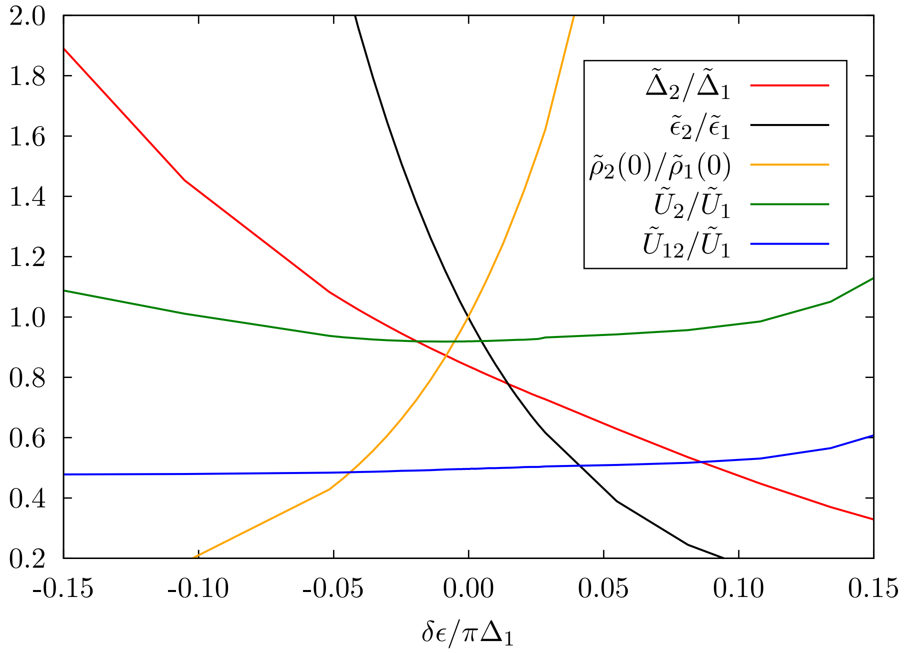

FIGURE 4.6: The ratios $\tilde{\Delta}_2/\tilde{\Delta}_1$, $\tilde{\epsilon}_2/\tilde{\epsilon}_1$, $\tilde{\rho}_2(0)/\tilde{\rho}_1(0)$, $\tilde{U}_2/\tilde{U}_1$, and $\tilde{U}_{12}/\tilde{U}_1$ for the model with $\pi\Delta_1 = 0.01$, $\pi\Delta_2 = 0.007896$, $U_1 = U_2 = 0.05$, $U_{12} = 0.03$. For these parameters, $\delta_{\mathrm{C}} = -2.00 \times 10^{-5}$ [109].

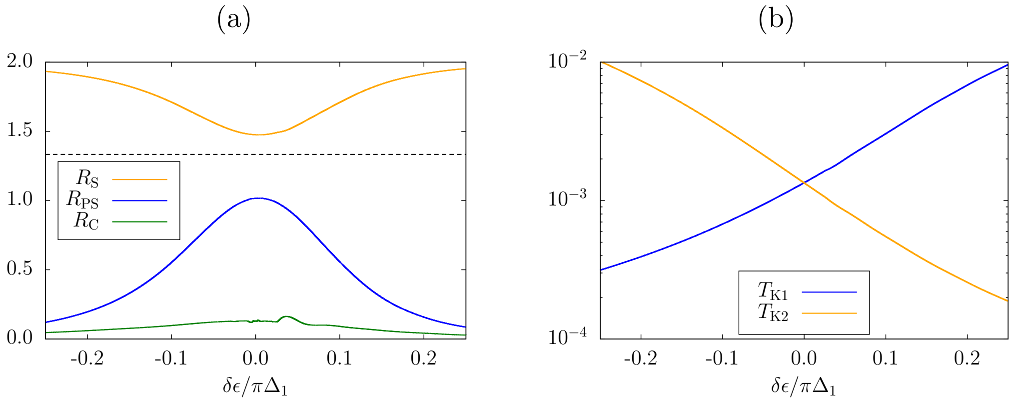

FIGURE 4.7: The relevant Wilson ratios (a) and the individual Kondo temperatures (b) as a function of $\delta\epsilon/\pi\Delta_1$ for the model parameters as given in the caption of figure 4.6.

icance to current experimental efforts towards observing emergent SU(4) in DQD systems. It is likely in such systems that $U_1, U_2 > D$ but the value of U_{12} will be much smaller [126]. If it is such that $U_{12} > D$, then the experimentalists will be able to obtain a restricted SU(4) point by varying the gate voltages, otherwise they will only obtain an approximate SU(4) point, but the changes in χ_{S} and χ_{PS} will provide experimental evidence that this regime has been reached.

4.6 Lingering Symmetry on Higher Energy Scales?

Our results point only towards an emergent restricted SU(4) symmetry in a typical DQD system. We now investigate, using the NRG to calculate spectral densities, the extent to which the restricted SU(4) symmetry survives on higher energy scales. To gain an idea over the range of ω one could expect the SU(4) symmetry to persist, we first consider the model with SU(4) symmetry on the bare and renormalised scales. We set $U_1 = U_2 = U_{12} = 0.05$, $\pi\Delta_1 = \pi\Delta_2 = 0.01$ and find that for unit occupation, we require $\epsilon_1 = \epsilon_2 = -0.021$. On the lowest energy scales, we calculate $\tilde{U}_1 = \tilde{U}_2 = \tilde{U}_{12} = 1.25 \times 10^{-3}$ and $\tilde{\epsilon}_1 = \tilde{\epsilon}_2 = \tilde{\Delta}_1 = \tilde{\Delta}_2 = 6.05 \times 10^{-4}$. The model is therefore in an SU(4) Kondo regime with $n = 1$. We plot in figure 4.8 the 1-particle spectral density of the d-electrons and quasiparticles (normalised to their values at the Fermi level to account for the systematic underestimation of this value in the NRG). It is clear that there is a region where the d-electron spectral density is very similar to the low energy quasiparticle model, which also exhibits the SU(4) symmetry. This region is approximately between $\omega = \pm T_{\mathrm{K}}^{\mathrm{SU(4)}}/2$, indicated by the vertical dashed lines. This scale corresponds to the energy scale where an $n = 1$ SU(4) Kondo regime persists.

We now seek to understand how this scale differs for a restricted SU(4) Kondo regime. We therefore modify our parameters to reintroduce an anisotropic difference between the hybridisations, and set $\pi\Delta_1 = 0.01$, $\pi\Delta_2 = 0.007896$ as before. In line with requirement (1), we now compare the spectral densities on each dot, rather than with the quasiparticle spectra. This gives us a measure of the energy range where the criterion is satisfied. We find $\rho_1(0) = \rho_2(0) = 38.0$ and compare the ratios $\rho_\alpha(\omega)/\rho_\alpha(0)$. These are plotted in figure 4.9. For these parameters, we have $T_{\mathrm{K}} = 6.3 \times 10^{-4}$ and we plot, as vertical dashed lines, the boundaries of the region where $|\omega| < T_{\mathrm{K}}/2$. The agreement between $\rho_1(\omega)$ and $\rho_2(\omega)$ is generally poor within

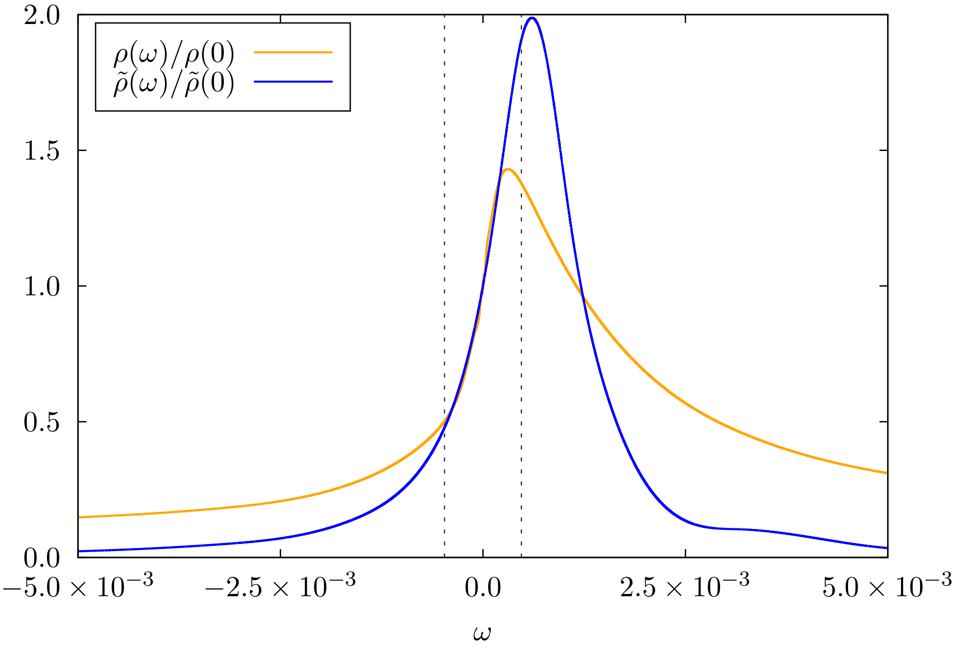

FIGURE 4.8: Comparison of the d-electron spectral density $\rho(\omega)$ and the non-interacting quasiparticle spectral density $\tilde{\rho}(\omega)$ for the model with $U_1 = U_2 = U_{12} = 0.05$, $\pi\Delta_1 = \pi\Delta_2 = 0.01$ and $\epsilon_1 = \epsilon_2 = -0.021$. The vertical dashed lines correspond to $\omega = \pm T_{\rm K}^{\rm SU(4)}/2$. We see that the width of the peak, which occurs at $\omega = \tilde{\epsilon}_1 = \tilde{\epsilon}_2$, is indicative of the Kondo temperature $T_{\rm K}^{\rm SU(4)}$.

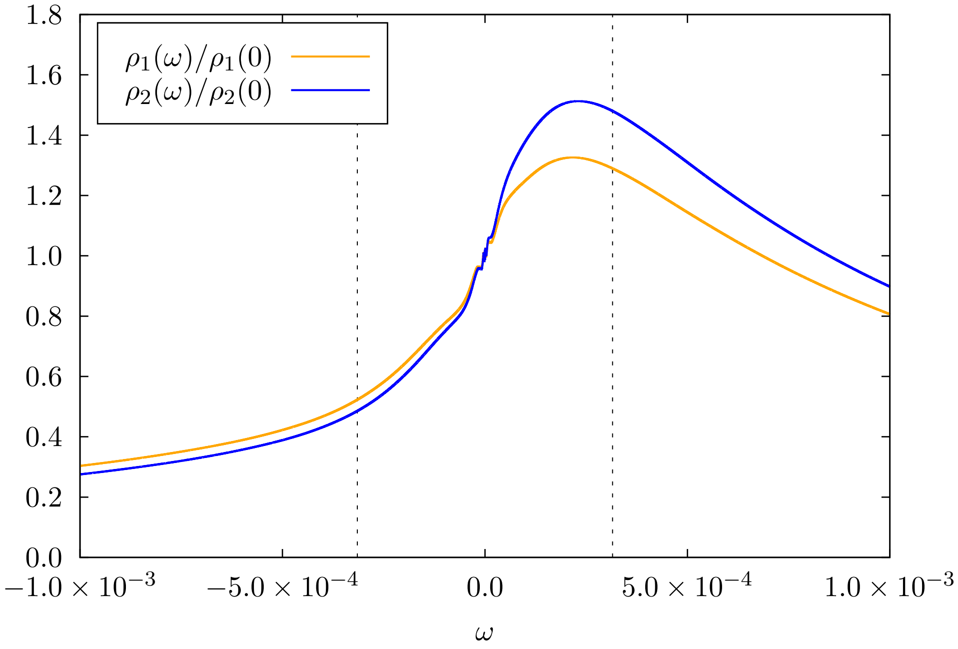

FIGURE 4.9: Comparison of $\rho_1(\omega)$ and $\rho_2(\omega)$ for the anisotropic model with $U_1 = U_2 = U_{12} = 0.05$, $\pi\Delta_1 = 0.01$, $\pi\Delta_2 = 0.007896$, $\epsilon_1 = -0.021$ and $\epsilon_2 = -0.0212022$. The vertical dashed lines correspond to $\omega = \pm T_{\mathrm{K}}/2$.

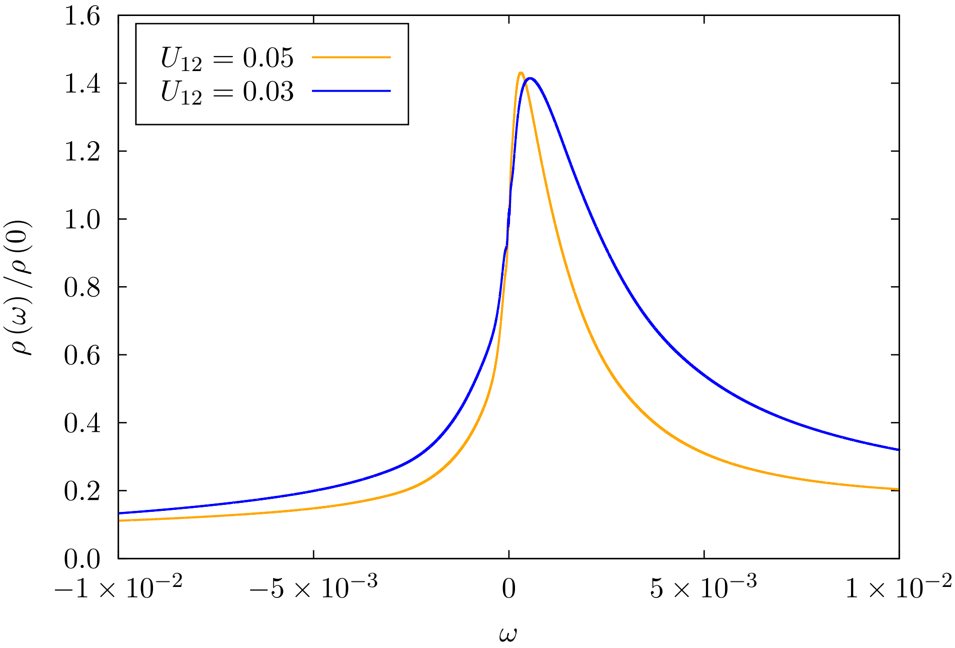

FIGURE 4.10: Plot of $\rho(\omega)$ for the channel symmetric model with $U_1 = U_2 = 0.05$ and $\pi\Delta_1 = \pi\Delta_2 = 0.01$. When $U_{12} = 0.05$, $\epsilon_1 = \epsilon_2 = -0.021$ and when $U_{12} = 0.03$, $\epsilon_1 = \epsilon_2 = -0.015$.

this region. We conclude that, in contrast to the case of a strict SU(4) $n = 1$ Kondo regime, the symmetry does not survive on energy scales governed by T_{K} when the system has a restricted SU(4) symmetry. It does, however, survive on much lower energy scales close to the Fermi level.

Finally we discuss how the spectral densities change when $U_1 = U_2 := U \neq U_{12}$, where $D > U$ and $U > U_{12}$. In this regime we only achieve an approximate SU(4) FP. We have already seen that the value of U_{12} appears significant in setting the degree of renormalisation. To investigate this, we take the parameters considered in figure 4.8, but set $U_{12} = 0.03$. In this model we find $\tilde{U}_1 = \tilde{U}_2 = 3.34 \times 10^{-3}$, $\tilde{U}_{12} = 1.64 \times 10^{-3}$, $\tilde{\epsilon}_1 = \tilde{\epsilon}_2 = \tilde{\Delta}_1 = \tilde{\Delta}_2 = 1.11 \times 10^{-3}$. We thus have $R_{\mathrm{S}} = 1.48$ and $R_{\mathrm{PS}} = 0.99$ and achieve an approximate SU(4) FP with $T_{\mathrm{K}} = 1.73 \times 10^{-3}$. We compare the spectral density of this model with the case $U_{12} = 0.05$ in figure 4.10. We see that, as predicted from the RPT analysis, T_{K}, which governs the width of the peaks, has increased as U_{12} decreased. However, if we compare to a model with $U, U_{12} > D$ a different picture emerges. The case with $U = 5$, $U_{12} = 3$ gives rise to a Kondo temperature $T_{\mathrm{K}} = 2.4 \times 10^{-8}$ whilst $U = U_{12} = 0.5$ gives a smaller value of $T_{\mathrm{K}} = 1.0 \times 10^{-10}$. One would expect that T_{K} would be smaller for the case with the larger U, but this is not the case. These results show that U_{12} plays a counter-intuitive role in setting this energy scale.

4.7 Inter-Dot and Intra-Dot Interactions and the Kondo Temperature

We now investigate how U_{12} effects the degree of renormalisation, characterised by T_{K}, and explore whether it restricts the possibility of emergent SU(4) symmetry. We set $\pi\Delta_1 = \pi\Delta_2 = 0.01$ and fix $U = U_1 = U_2$, varying U_{12} subject to the requirement $n_1 = n_2 = 1/2$. It follows that for all U_{12}, $\epsilon_1 = \epsilon_2$. We plot the ratios $\tilde{U}/2\pi\tilde{\Delta}$ and $\tilde{U}_{12}/2\pi\tilde{\Delta}$ as a function of U_{12}/U, for 2 values of U, in figure 4.11a. For a restricted, or strict, SU(4) point we require $\tilde{U}/2\pi\tilde{\Delta} = \tilde{U}_{12}/2\pi\tilde{\Delta}$. We see again that if $U, U_{12} < D$ then SU(4) symmetry may not be achieved unless $U = U_{12}$, which corresponds to a strict symmetry. The Wilson ratios R_{S} and R_{PS} are plotted against U_{12}/U for the same values of U in figure 4.11b. We see, in line with our previous conclusions, that it is possible to achieve only an approximate SU(4) point for all $U_{12} \neq U$. We show how the Kondo temperature varies for two different values of U in figure 4.11c. The change in T_{K} as one increases U_{12} is severe - for the lower value of U there is a general decline, but the values of T_{K} when $U_{12} = 0$ and when $U_{12} = U$ are similar in magnitude. For the larger value of U, the increase of $U_{12} \to U$ induces a change in T_{K} of 8 orders of magnitude. While it is not surprising that an increase in U_{12} causes a decrease in T_{K}, as it freezes out fluctuations between the $n = 0$ and $n = 1$ states, such a significant change is worth investigation. The different values of T_{K} for the 2 cases of U are apparent in the spectral densities, which we plot in figure 4.12. For $U = 0.05$, plotted in 4.12a, the quasiparticle peak of $\rho(\omega)$ shows a narrowing as U_{12} increases. In line with the change in T_{K} plotted in figure 4.11c, the widths of the quasiparticle peaks are all of similar orders. Conversely the spectral density peaks for the case $U = 0.5$, displayed in figure 4.12b, show a substantial narrowing of the quasiparticle peaks as U_{12} increases. There is also an emergence of atomic peaks at $\omega = \epsilon$ and $\omega = \epsilon + U_{12}$, which indicates that U_{12} plays a similar role to U in the 1IAM. We qualitatively relate the degree of renormalisation to the bare value of ϵ. This is plotted against U_{12}/U for the 2 cases of U in figure 4.13. We see that as U_{12} increases, the requirement $n_1 = n_2 = 1/2$ causes ϵ to be dragged further

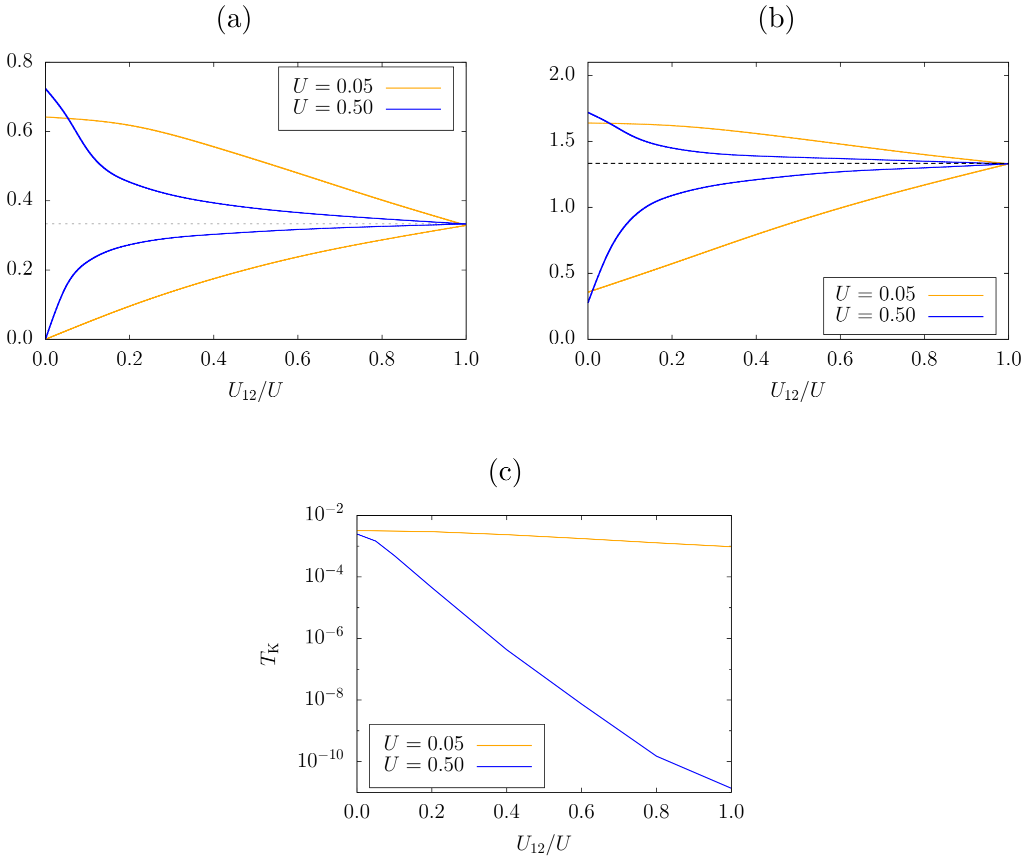

FIGURE 4.11: Results from [109] for the model with $U_1 = U_2 = U$, $\pi\Delta_1 = \pi\Delta_2 = 0.01$ where U_{12} is varied in the range $0 < U_{12} < U$. For each U_{12}, $\epsilon_1 = \epsilon_2$ is set so that $n_1 = n_2 = 1/2$. In (a) we plot of the ratio of renormalised parameters $\tilde{U}/2\pi\tilde{\Delta}$ and $\tilde{U}_{12}/2\pi\tilde{\Delta}$. The curves approaching the value of $1/3$ from above correspond to $\tilde{U}/2\pi\tilde{\Delta}$ and those approaching from below to $\tilde{U}_{12}/2\pi\tilde{\Delta}$. (b) is a plot of the Wilson ratios R_S and R_{PS}, where the curves approaching the value of $4/3$ from above correspond to R_S and those approaching from below to R_{PS}. (c) shows how T_K varies as U_{12} is switched on and approaches U.

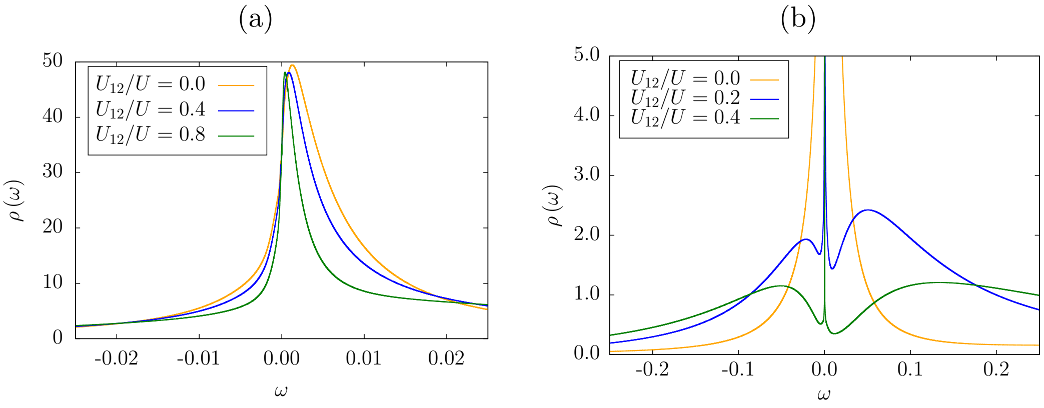

FIGURE 4.12: Spectral densities, and the impurity levels, for the model with $\pi\Delta_1 = \pi\Delta_2 = 0.01$ and varying values of U_{12}/U. (a) and (b) respectively show the spectral density for the model with $U = 0.05$ and $U = 0.5$.

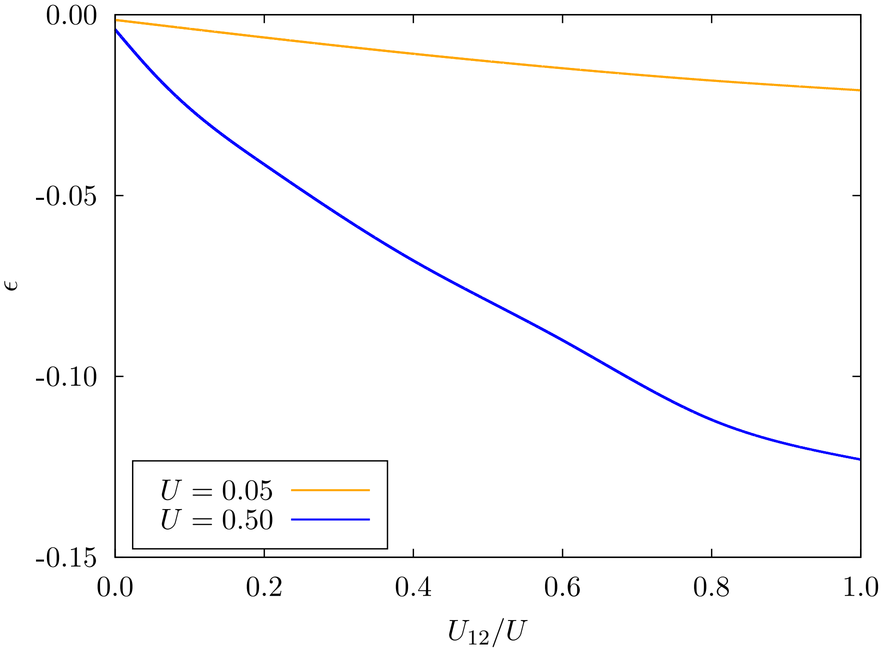

FIGURE 4.13: A plot showing how the value of ϵ changes with U_{12} for the different cases of U. The model parameters are the same as those in figure 4.12 [109].

below the Fermi level, and much more significantly so in the case $U = 0.5$. However, we require it to be rescaled to $\tilde{\epsilon} = \tilde{\Delta} > 0$. It follows that, since ϵ decreases much more quickly in the case of larger U, the degree of renormalisation should be much greater in this case. The qualitative agreement between figures 4.11c and 4.13 leads us to speculate that T_{K} is largely determined by ϵ, with $\ln(T_{\mathrm{K}}) \sim \epsilon$. In the strict SU(4) model under the limit $U, U_{12} \to \infty$ this dependence is well known [59, 125]. Our results suggest that it persists in an approximate SU(4) regime with $U \neq U_{12}$ and U, U_{12} finite.

We perform similar investigations for the $n = 2$ model, with the p-h symmetry condition (1.4.4) satisfied. If our assertion that, when $n = 1$, the degree of renormalisation is regulated by the requirement $\tilde{\epsilon} = \tilde{\Delta}$ then we should see dramatically different behaviour for $n = 2$ (where $\tilde{\epsilon} = 0$). In this case, at a universal SU(4) Kondo FP one should obtain $\tilde{U}\tilde{\rho}(0) = 1/3$ where $\tilde{\rho}(0) = 1/\pi\tilde{\Delta}$. We plot the ratios $\tilde{U}/\pi\tilde{\Delta}$ and $\tilde{U}_{12}/\pi\tilde{\Delta}$ as a function of U_{12}/U in figure 4.14a. For the $n = 1$ model the ratios continuously approach the universal value of 1/3 as $U_{12}/U \to 1$. In this case however, the ratios do not approach 1/3 until $U_{12} \simeq U$, when there is a rapid convergence to this value, representing a crossover from an SU(2) to SU(4) Kondo regime. This has been previously found in [96][4]. To demonstrate the impact of this rapid convergence to the value of 1/3, we plot the Wilson ratios R_{S} and R_{PS} against U_{12}/U for various values of U in figure 4.14b. We see that one may still obtain an approximate SU(4) FP, as in the $n = 1$ model, but only for U_{12} very close to U. Given that in DQD structures the value of U_{12} is determined by the distance between the dots, it may not be finely tuned. Hence any experimental observation of an $n = 2$ Kondo regime would be exceptionally challenging.

Again in contrast to the $n = 1$ model, the value of T_{K}, plotted against U_{12}/U in figure 4.14c, is largely invariant as U_{12} is increased, but increases significantly when $U_{12}/U \simeq 1$. We summarise the distinction between the 2 models as follows. When U_{12}/U corresponds to the regime of approximate SU(4) symmetry, and $U_{12} \to U$ from below, T_{K} decreases as $n = 1$, and increases for $n = 2$. The value of $\epsilon = -U/2 - U_{12}$ is largely unchanged throughout the region where T_{K} increases, implying that it no longer determines the degree of renormalisation. We also see the

---

[4] It was also found in [96] that as U_{12} is increased beyond U there is a QCP between two charge-ordered phases (originally seen in [127]). We do not observe such a QCP for $n = 1$.

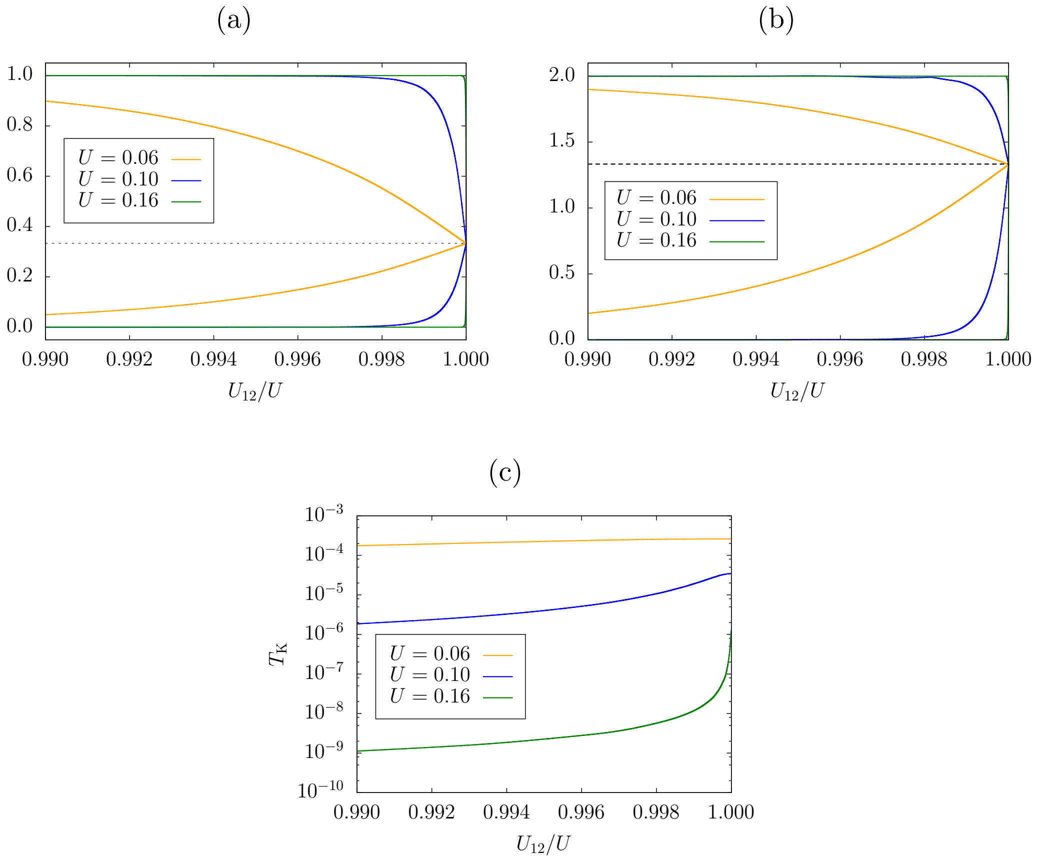

FIGURE 4.14: Results from [109] corresponding to the model with $U_1 = U_2 = U$, $\pi\Delta_1 = \pi\Delta_2 = 0.01$ and p-h symmetry. In (a) we plot of the ratio of renormalised parameters $\tilde{U}/\pi\tilde{\Delta}$ and $\tilde{U}_{12}/\pi\tilde{\Delta}$. The curves approaching the value of $1/3$ from above correspond to $\tilde{U}/\pi\tilde{\Delta}$ and those approaching from below to $\tilde{U}_{12}/\pi\tilde{\Delta}$. (b) shows the Wilson ratios R_{S} and R_{PS}, where the curves approaching the value of $4/3$ from above correspond to R_{S} and those approaching from below to R_{PS}. (c) is a plot of the Kondo temperature for the various values of U as a function of U_{12}/U.

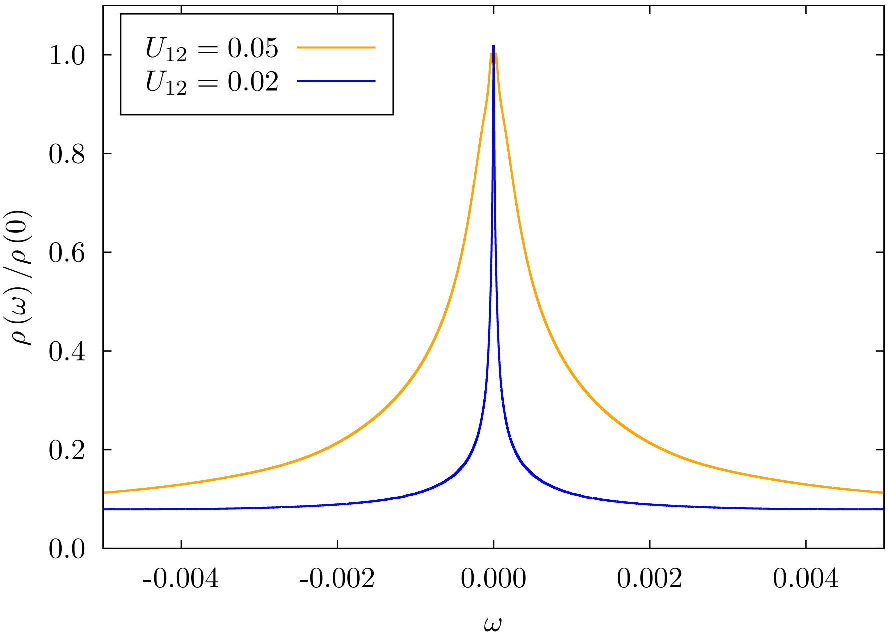

FIGURE 4.15: Plot of $\rho(\omega)/\rho(0)$ with parameters $U_1 = U_2 = 0.05$, $\pi\Delta_1 = \pi\Delta_2 = 0.01$ and p-h symmetry, for various values of U_{12}.

change in the values of T_{K} in the spectral density. We plot in figure 4.15 the spectra in the SU(2) case $U = 0.05$, $U_{12} = 0.02$ and the SU(4) model with $U = U_{12} = 0.05$. We see that the peak corresponding to an SU(4) $n = 2$ Kondo FP is much broader compared to the SU(2) peak.

Our investigation presented in this section confirms that in the channel-symmetric model with $U_1 = U_2 < D$, we cannot achieve a strict SU(4) Kondo regime, for $n = 1$ and $n = 2$, unless $U_{12} = U$. Otherwise, we may only achieve an approximate SU(4) FP. For the case $n = 1$, an approximate SU(4) FP is easily accessible, as an enhancement in χ_{PS} arises over a large range of U_{12}/U. When $n = 2$ this range is so narrow that experimental observation of any FP other than the usual SU(2) is unlikely. For $U_{12} \neq U$ the value of T_{K} differs in the $n = 1$ and $n = 2$ cases, and we speculate that in the $n = 1$ system the restriction $\tilde{\epsilon} = \tilde{\Delta}$ induces a very strong renormalisation. This is not observed in the $n = 2$ system where this restriction no longer applies.

4.8 Distinguishing the SU(2) and SU(4) Kondo Regimes

A powerful experimental technique for probing the many-body Kondo effect in detail is the study of the dot conductance [79, 128, 129]. The constraint $\tilde{\epsilon} = \tilde{\Delta}$ for an $n = 1$ SU(4) Kondo regime clearly implies a different many-body resonance in the spectral density as compared to the SU(2) and $n = 2$ SU(4) model. We now investigate how this changes the conductance and whether this is relevant to experiment. We consider the channel symmetric model $U_1 = U_2$ and $\Delta_1 = \Delta_2$ as in the previous section.

The current $I_\alpha(T, V_\alpha)$ at temperature T flowing through dot α, via source and drain baths with respective chemical potentials $\mu_{\mathrm{S}\alpha}$ and $\mu_{\mathrm{D}\alpha}$, which give rise to a voltage V_α, is calculated in [80] using a non-equilibrium Keldysh formalism, and perturbatively in [130]. The result is

$$I_\alpha(T, V_\alpha) = \frac{4\Delta_{\mathrm{S}\alpha}\Delta_{\mathrm{D}\alpha}}{\Delta_{\mathrm{S}\alpha} + \Delta_{\mathrm{D}\alpha}} \int_{-\infty}^{\infty} \mathrm{d}\omega \, (f_{\mathrm{S}\alpha}(\omega) - f_{\mathrm{D}\alpha}(\omega)) \left(-\frac{1}{\pi} \mathrm{Im} G_\alpha(\omega, T) \right), \quad (4.8.1)$$

where $f_{\nu\alpha}(\omega)$ is related to the Fermi function via $f_{\nu\alpha}(\omega) = f_{\mathrm{F}}(\omega - \mu_{\nu\alpha})$ and $G_\alpha(\omega, T)$ is the 1-particle local spectral density defined in (3.5.28). Following the arguments of [80], when the dot coupling to the source and drain is small we can consider the current as providing only a weak perturbation to the many-body correlated states, so that the current provides reliable information on these states. We limit our discussion to the equilibrium case $\mu_{\mathrm{S}\alpha} = \mu_{\mathrm{D}\alpha}$, which corresponds to the zero bias situation. In this case, the conductance of dot α is given by

$$G_\alpha(T) = -\frac{4\Delta_{\mathrm{S}\alpha}\Delta_{\mathrm{D}\alpha}}{\Delta_{\mathrm{S}\alpha} + \Delta_{\mathrm{D}\alpha}} \int_{-\infty}^{\infty} \mathrm{d}\omega \, \partial_\omega f_{\mathrm{F}}(\omega) \rho_\alpha(\omega, T) \quad (4.8.2)$$

and we use that $-\partial_\omega f_{\mathrm{F}}(\omega) = \beta \mathrm{e}^{\beta\omega} f_{\mathrm{F}}(\omega)^2$. We calculate $G_\alpha(T)$ to order T^2 using the RPT as in chapter 3. The finite-frequency finite-temperature spectral density $\rho_\alpha(\omega, T)$ is given in terms of renormalised parameters in (3.5.29), and the real and imaginary self-energies in (3.5.32) and (3.5.31) respectively.

For the SU(2) regime, we have $\tilde{U} = \pi\tilde{\Delta}$, $\tilde{\rho}(0) = 1/\pi\tilde{\Delta}$ and $\tilde{U}_{12} = \tilde{\epsilon} = 0$. In this case $\tilde{\Sigma}^{\mathrm{R}}_\alpha(\omega, T) = 0$. Expanding $\rho_\alpha(\omega, T)$ to order T^2, as in (3.5.30), and performing the integration, we obtain the expression

$$\left.\frac{G(T)}{G(0)}\right|_{\mathrm{SU}(2)} = 1 - \frac{\pi^4}{48}(1 + \phi) \left(\frac{T}{T_{\mathrm{K}}} \right)^2 + \mathcal{O}(T^4) \quad (4.8.3)$$

where the channel label has been dropped due to the assumed channel symmetry, and

$$\phi = \frac{2\tilde{U}^2 + 4\tilde{U}_{12}^2}{(\pi\tilde{\Delta})^2} \tag{4.8.4}$$

which takes the value $\phi = 2$. In the SU(4) $n = 1$ Kondo regime, we have the requirements $\tilde{\epsilon} = \tilde{\Delta}$, $\tilde{U} = \tilde{U}_{12}$, and $\tilde{\rho}(0) = 1/2\pi\tilde{\Delta}$. It follows that $\tilde{\Sigma}^{\mathrm{R}}_{\alpha}(\omega, T) \neq 0$ due to the finite $\tilde{\epsilon}$, and this changes the low-T behaviour of the conductance. We calculate

$$\left.\frac{G(T)}{G(0)}\right|_{\mathrm{SU}(4)} = 1 + \frac{\pi^4}{24}\left(1 - \psi\right)\left(\frac{T}{T_{\mathrm{K}}}\right)^2 + \mathcal{O}(T^4) \tag{4.8.5}$$

where we find $\psi \simeq -0.279$. This analysis has yielded a significant distinguishing feature between the $n = 2$ SU(2) and $n = 1$ SU(4) Kondo regimes; $G(T)$ shows an initial decrease for the SU(2) model, but an increase for the SU(4) model. The difference between the 2 models is related to the behaviour of the spectral density. When $n = 2$, $\rho(\omega)$ has a peak centred at $\omega = 0$ which decreases as ω increases from the Fermi level, whilst the peak structure for the SU(4) model is constrained by the requirement $n = 1$. In this model we have a narrow peak at $\omega = \tilde{\epsilon} > 0$ so that $\rho(\omega)$ increases as ω increases from 0. Differences between various physical quantities in SU(N) impurity models has been found before, and attributed to the peak structure of the spectral density [131].

The difference between $G(T)$ in the SU(2) and SU(4) models has been previously found in NRG calculations [123], and we have illustrated that this difference can be used to differentiate between the 2 regimes. Our result therefore should be useful to the experimental community seeking to observe an $n = 1$ SU(4) Kondo regime.

4.9 Conclusions

In this chapter we have investigated the possibility of emergent SU(4) Kondo regimes in DQD devices, and how these might be observed by an experimentalist. A common problem facing such an experimentalist is that fine control of the hybridisations and Coulomb interactions in DQD devices is currently not possible. We found that, in line with the conclusions of [125], if $U_1 = U_2 = U_{12}$ and $\Delta_1 \neq \Delta_2$, then the SU(4) Kondo regime may be restored on low energy scales by application of a pseudospin field $\epsilon_1 - \epsilon_2$. This is significant for experimentalists because the use of gate voltages in DQD systems allows fine control of the levels ϵ_α. However, the symmetry restoration is limited for such a model; one may only attain a restricted SU(4) symmetry. This regime only holds on very low energy scales (much lower than T_{K}).

When $U_1 = U_2 \neq U_{12}$, and the model is channel symmetric, we find that a restricted SU(4) Kondo regime may still be reached, but only when $U_1, U_2, U_{12} > D$. Otherwise, there is an emergent approximate SU(4) symmetry regime, where χ_{PS} is enhanced and χ_{S} is suppressed, but not sufficiently to achieve a strict, or restricted, SU(4) FP. For the $n = 1$ model, approximate SU(4) symmetry emerges over a broad range of U_{12}/U and a strict SU(4) point at $U_{12} = U$. However, in the case $n = 2$, approximate SU(4) symmetry only emergences for U_{12} very close to U, otherwise there is no enhancement of χ_{PS} and the system remains in an SU(2) Kondo state.

We have also studied how T_{K} depends on the bare parameters, and the role of U_{12} in governing the degree of renormalisation. We showed that U_{12} behaved similarly to U in the 1IAM, in that an increase in U_{12} caused a narrowing of the Kondo resonance, occurring at $\tilde{\epsilon}$ in the spectral density, and the emergence of atomic peaks. However, we found the degree of renormalisation is largely due to the bare value of ϵ, which had to be set such that $n = 1$. As U_{12} was increased, so ϵ decreased further below the Fermi level. To satisfy $n = 1$ we require $\tilde{\epsilon} = \tilde{\Delta} > 0$ so that as U_{12} increased so did the degree of renormalisation. The qualitative agreement between ϵ and T_{K} as a function of U_{12} led us to speculate that the relation $\ln(T_{\mathrm{K}}) \sim \epsilon$ holds in an approximate SU(4) regime in addition to the strict SU(4) model. Studies of the $n = 2$ model, where $\tilde{\epsilon} \neq \tilde{\Delta}$ did not show such a dependence. For similar $U/\pi\Delta$, T_{K} was many orders of magnitude larger in the $n = 2$ model as compared to $n = 1$.

We finally looked at the conductance of the dots, and showed that a way to distinguish between the SU(2) and SU(4) Kondo FPs is to study the temperature-dependence of $G(T)$. In the SU(4) system, $G(T)$ increases with T, whilst for the SU(2) model $G(T)$ decreases. This result relies only on the renormalised parameters satisfying their appropriate conditions for SU(4) or SU(2) symmetry, and does not rely on a universal energy scale. It should therefore be possible to observe it in a restricted SU(4) regime, which we have showed is experimentally attainable.

Chapter 5

Local Quantum Criticality and Majorana Fermions

In this chapter we study the Quantum Critical Point (QCP) which arises in the 2IAM when the impurities are coupled by a magnetic Heisenberg term. We calculate dynamic quantities of the model in various regimes, such as p-h asymmetry and channel asymmetry, and explicitly show the divergence of certain susceptibilities. We draw connections to the 2 Channel Kondo Model (2CKM) and an SO(7) invariant Majorana Fermion (MF) model, and discuss possible physical pictures of the mechanisms underlying the QCP. We begin by introducing the concept of QCPs and MFs, and show how the Anderson model can be related to an MF model. We then review the 2CKM (which has a QCP with similar properties to that of the 2IAM) and introduce an MF model which has been proposed to describe the 2CKM QCP. Afterwards, we proceed to present our results and interpretations.

5.1 Quantum Criticality

Inter-impurity interactions occurring in coupled impurity/quantum dot models often govern the critical behaviour of such systems. A critical point is best understood thermodynamically in terms of phase transitions. Let us suppose we have some system whose state or phase is entirely described by some thermodynamic quantity which we term the order parameter. A first order phase transition is a point in phase-space across which the order parameter changes discontinuously. At the transition, two distinct phases (each characterised by the order parameter) coexist in equilibrium. Often one can tune another thermodynamic quantity in a way that results in a line of first order transition points in phase-space; the phase equilibrium curve [132]. At the endpoint of this curve, the competing phases become one. This is a critical point, and it corresponds to a continuous, second-order phase transition.

Critical points appear in both quantum and classical models, but in each case they are governed by different physics. In a fully classical system, we can think of the state of matter as being described by the set of all momenta and positions of the atoms and electrons. For finite temperatures the momenta and positions follow from Boltzmann's distribution and, in equilibrium, the minimisation of the Gibbs free energy $F = U - TS$, where U and S are respectively the internal energy and entropy. In order to keep F minimal, there is competition between U and S, driven by the thermal fluctuations of the system. On approach to the critical point, the system decomposes into isolated 'chunks' of the different phases separated by the critical point, and the macroscopic properties begin to resemble a superposition of the two phases. Classically, the change in the two phases represents a reorganisation of the particles. For example, if one brings liquid water close to the liquid-vapour critical point then one can observe increased compressibility and decreased electrical conductance (as well as other changes), so that the system resembles vapour whilst retaining some 'liquid-like' characteristics [133]. At the critical point the chunks of each competing phase are more-or-less equally distributed throughout the system, with a divergent correlation length.

The description of a QCP differs from the classical case in the sense that, rather than looking for competing phases characterised by classical canonical variables, we look for competing regimes of the ground-state wavefunction of a many-body system [134]. A QCP therefore only resides at $T = 0$, unlike a classical critical point; this difference is ultimately responsible for the distinction between the two. At $T = 0$, there are no thermal fluctuations present, so the critical behaviour is a result of the quantum fluctuations in the system [135]. All finite temperature critical points may be described by the theory of classical phase transitions, even those with an underlying quantum mechanical description. We may think of (inverse) temperature as setting an (imaginary) time-scale. Since the QCP exists at $T = 0$, there is no timescale, so the time that the system requires to return to thermal equilibrium after a perturbation diverges on approach to the critical point. In addition to spatial scale invariance, at a QCP we acquire temporal scale invariance. This allows the quantum critical state to survive in finite (but low) temperature regimes, permitting experimental measurements to take place.

The merging of the phases at the QCP results in long-ranged critical phenomena which is due to a divergent correlation length and emergent scale invariance [136]. The QCP is therefore described by a FP of the RG, which exhibits the same characteristic scale invariance. Due to the large correlation length, the system at criticality becomes highly sensitive to certain changes in the environment; this results in a divergent susceptibility [47]. We study the low temperature behaviour of the 2IAM and when we change J we observe different low temperature RG FPs which represent distinct phases. If J is tuned correctly, we see the emergence of a QCP with unusual physical properties which are intimately linked to MF models.

5.2 Majorana Fermions and Overscreening

An important theme throughout this chapter is the notion of screening, and the emergence of MFs. These are a general type of particle which are their own antiparticle (and hence carry only half the degrees of freedom of 'normal' particles), and whose existence is permitted by the Dirac equation [137]. Across the discipline of physics, there are many important questions regarding MFs (such as whether the neutrino is Majorana or Dirac [138]). In our work we specialise to the 'condensed matter' picture of MFs, which could also be called Majorana bound states - these are combinations of particles and holes. We do not discuss real fundamental particles (like a neutrino), rather we discuss only low-energy quasiparticles satisfying the defining algebra of a MF.

MFs are of great interest to the condensed matter community because they give rise to non-Abelian statistics [139, 140] associated to some modes in the system. The statistics are determined by exchange of particles; in the typical case of Bosons and Fermions, the wavefunction is respectively symmetric and anti-symmetric under exchange. In 2 spacetime dimensions one can obtain particles which do not obey this simple exchange rule. Let us denote the group of exchange transformations in the usual Bosonic/Fermionic case $\mathbb{Z}_2 = \{-1, 1\}$. If we instead let our exchange group become some general non-Abelian group then, in some cases, behaviour useful to topological quantum computers emerges [139, 141, 142]. Specifically, these

2-dimensional quasiparticles with strange statistics, ‘non-Abelian anyons’, can be used to construct qubits which are stable with respect to perturbations, unlike the conventional trapped particle quantum computers, which are subject to severe decoherence. This stability is due to braiding, where the anyons world lines wrap around each other but are topologically protected from merging. MFs are examples of anyons, and it is therefore interesting to the condensed matter community that they arise at the QCP of certain impurity systems.

Whether MFs emerge in quantum impurity systems is determined by the mechanism employed to screen the impurity. We here distinguish between the ‘screened’, ‘underscreened’ and ‘overscreened’ cases. Suppose our impurity system of spin S is coupled to n channels, so that there are n different species of conduction electrons to couple to. If there are exactly enough conduction electrons to screen the impurity, $2S = n$, then the static spin may be screened, resulting in an SU$(2S + 1)$ Kondo regime. If there is an insufficient number of conduction electrons to fully screen the spin, $2S > n$, then the spin is underscreened. Conversely, if there are too many conduction species, $2S < n$, then the spin is overscreened [143]. In the unscreened cases, the residual interacting degrees of freedom determine the system behaviour. In the underscreened case, an effective, low-energy ferromagnetic interaction emerges, which logarithmically tends to zero on the lowest energy scales [144]. This reproduces a stable FL regime.

Conversely, in the overscreened case, where there is an antiferromagnetic effective coupling, a new ‘intermediate-coupling’ FP emerges, which is responsible for the low-energy behaviour [144, 145]. Various methods have been developed for understanding the properties of the low-energy FP in overscreened impurity models, including the Bethe Ansatz [146], Bosonisation [147, 148] and Boundary Conformal Field Theory (BCFT) [149, 20, 150, 151, 152]. These all show that this intermediate-coupling FP is of Non-Fermi Liquid (NFL) nature, and corresponds to a QCP. Curiously, the $T = 0$ impurity system contribution to the entropy is $\ln(2)/2$, implying that the multiplicity of the atomic states is non-integer. This property can be explained by the presence of a single uncoupled MF mode [148]. A local Dirac Fermion has 2 degrees of freedom (corresponding to spin up and down) and thus contributes an entropy of $\ln(2)$. A half-degree of freedom will contribute half this entropy. Clearly the 2IAM cannot be overscreened, as each impurity may support a spin $1/2$ and is coupled to its own bath, so one might question whether such anomalous properties can arise. At p-h symmetry, where we map to the 2 Impurity Kondo Model (2IKM), it has been shown that the NFL FPs of the 2-impurity and overscreened 2-channel models are equal, modulo potential scattering [153]. Therefore phenomena associated with overscreening can be achieved in 2-impurity models.

5.3 Majorana Fermions in the 2IAM

When p-h symmetry is enforced, we have claimed that the charge symmetry is promoted from U(1) to SU(2) in each channel. Unlike the SU(4) case, there is no coupling or entanglement between the spin and charge sectors, resulting in a global SO(4)⊗SO(4) symmetry (in the model with no-inter impurity interactions). The channels remain invariant under U(1), since SO(2) ≅ U(1) and SO(2) ≤ SO(4), but if we manifest the full SO(4) invariance, the model loses its manifest U(1) symmetry in each channel. We may describe the model in terms of two spin-like variables; spin (the usual) and isospin. An MF model emerges very naturally as we make explicit the SO(4) symmetry; they are linear superpositions of particle and hole excitations corresponding to each degree of freedom. In this section, we demonstrate the emergence of the symmetry, and motivate why this is useful for our analysis of the QCP. We define a total of 8 MF species, which are Hermitian, corresponding to the impurity sites,

$$\begin{aligned} d_0 &= \frac{1}{\sqrt{2}}\left[d^\dagger_{1,\uparrow} + d_{1,\uparrow}\right] & d_4 &= \frac{1}{\sqrt{2}}\left[d^\dagger_{2,\uparrow} + d_{2,\uparrow}\right] \\ d_1 &= -\frac{i}{\sqrt{2}}\left[d^\dagger_{1,\uparrow} - d_{1,\uparrow}\right] & d_5 &= -\frac{i}{\sqrt{2}}\left[d^\dagger_{2,\uparrow} - d_{2,\uparrow}\right] \\ d_2 &= -\frac{1}{\sqrt{2}}\left[d^\dagger_{1,\downarrow} + d_{1,\downarrow}\right] & d_6 &= -\frac{1}{\sqrt{2}}\left[d^\dagger_{2,\downarrow} + d_{2,\downarrow}\right] \\ d_3 &= -\frac{i}{\sqrt{2}}\left[d^\dagger_{1,\downarrow} - d_{1,\downarrow}\right] & d_7 &= -\frac{i}{\sqrt{2}}\left[d^\dagger_{2,\downarrow} - d_{2,\downarrow}\right] \end{aligned} \tag{5.3.1}$$

and a further 8 which are built from conduction electrons/holes,

$$\begin{aligned}
\chi_0(n) &= \frac{1}{\sqrt{2}}\mathrm{e}^{\frac{in\pi}{2}}\left[c^\dagger_{1,n,\uparrow}+(-1)^n c_{1,n,\uparrow}\right] & \chi_4(n) &= \frac{1}{\sqrt{2}}\mathrm{e}^{\frac{in\pi}{2}}\left[c^\dagger_{2,n,\uparrow}+(-1)^n c_{2,n,\uparrow}\right]\\
\chi_1(n) &= -\frac{i}{\sqrt{2}}\mathrm{e}^{\frac{in\pi}{2}}\left[c^\dagger_{1,n,\uparrow}-(-1)^n c_{1,n,\uparrow}\right] & \chi_5(n) &= -\frac{i}{\sqrt{2}}\mathrm{e}^{\frac{in\pi}{2}}\left[c^\dagger_{2,n,\uparrow}-(-1)^n c_{2,n,\uparrow}\right]\\
\chi_2(n) &= -\frac{1}{\sqrt{2}}\mathrm{e}^{\frac{in\pi}{2}}\left[c^\dagger_{1,n,\downarrow}+(-1)^n c_{1,n,\downarrow}\right] & \chi_6(n) &= -\frac{1}{\sqrt{2}}\mathrm{e}^{\frac{in\pi}{2}}\left[c^\dagger_{2,n,\downarrow}+(-1)^n c_{2,n,\downarrow}\right]\\
\chi_3(n) &= -\frac{i}{\sqrt{2}}\mathrm{e}^{\frac{in\pi}{2}}\left[c^\dagger_{1,n,\downarrow}-(-1)^n c_{1,n,\downarrow}\right] & \chi_7(n) &= -\frac{i}{\sqrt{2}}\mathrm{e}^{\frac{in\pi}{2}}\left[c^\dagger_{2,n,\downarrow}-(-1)^n c_{2,n,\downarrow}\right].
\end{aligned} \tag{5.3.2}$$

These obey the anticommutation relations

$$\left\{\chi_i(n)^\dagger,\chi_j(m)^\dagger\right\} = \left\{\chi_i(n)^\dagger,\chi_j(m)\right\} = \left\{\chi_i(n),\chi_j(m)\right\} = \delta_{ij}\delta_{mn} \tag{5.3.3}$$

and

$$\left\{d_i^\dagger,d_j^\dagger\right\} = \left\{d_i^\dagger,d_j\right\} = \left\{d_i,d_j\right\} = \delta_{ij}, \tag{5.3.4}$$

which we take to be the defining property of an MF. Neglecting inter-impurity interactions and enforcing p-h symmetry, the 2IAM Hamiltonian may be expressed as

$$\begin{aligned}
H = i\sum_{n=0}^{\infty}\sum_{i=0}^{3}\xi_n\Lambda^{-n/2}\chi_i(n+1)\chi_i(n) + iV_1\sum_{i=0}^{3}\chi_i(0)d_i + U_1 d_0d_1d_2d_3\\
+\, i\sum_{n=0}^{\infty}\sum_{i=4}^{7}\xi_n\Lambda^{-n/2}\chi_i(n+1)\chi_i(n) + iV_2\sum_{i=4}^{7}\chi_i(0)d_i + U_2 d_4d_5d_6d_7
\end{aligned} \tag{5.3.5}$$

where n labels the 2-body site on the tight-binding chain. Note that we express the NRG Hamiltonian, rather than the continuous one, in a basis of MFs for two reasons. Firstly, to illustrate the model with which previous NRG studies have been carried out, such as in [154]. Secondly, the NRG Hamiltonian is simply a tight-binding chain with strong similarities to the Kitaev model [142], which provides a simple representation of the MFs. To make manifest the symmetry, we define the vectors

$$\mathbf{\Omega}_1(n) = \begin{pmatrix}\chi_0(n)\\ \chi_1(n)\\ \chi_2(n)\\ \chi_3(n)\end{pmatrix}, \quad \mathbf{\Omega}_2(n) = \begin{pmatrix}\chi_4(n)\\ \chi_5(n)\\ \chi_6(n)\\ \chi_7(n)\end{pmatrix}, \quad \mathbf{\Pi}_1 = \begin{pmatrix}d_0\\ d_1\\ d_2\\ d_3\end{pmatrix}, \quad \mathbf{\Pi}_2 = \begin{pmatrix}d_4\\ d_5\\ d_6\\ d_7\end{pmatrix}, \tag{5.3.6}$$

so that the model is given by

$$H = i\sum_{n=0}^{\infty}\xi_n\Lambda^{-n/2}\boldsymbol{\Omega}_\alpha(n+1)^{\mathrm{T}}\boldsymbol{\Omega}_\alpha(n) + i\sum_{\alpha}V_\alpha\boldsymbol{\Omega}_\alpha(0)^{\mathrm{T}}\boldsymbol{\Pi}_\alpha + \sum_{\alpha}U_\alpha\det\left[\boldsymbol{\Pi}_\alpha^{\mathrm{T}}\mathbb{1}\right]. \tag{5.3.7}$$

This is invariant under the transformation

$$\begin{cases} \boldsymbol{\Omega}_\alpha(n) & \rightarrow & \boldsymbol{M}_\alpha\boldsymbol{\Omega}_\alpha(n) \\ \boldsymbol{\Pi}_\alpha & \rightarrow & \boldsymbol{M}_\alpha\boldsymbol{\Pi}_\alpha \end{cases}, \tag{5.3.8}$$

where $\boldsymbol{M}_\alpha$ is constrained by the Hermiticity of the MFs to contain only real entries, if $\boldsymbol{M}_\alpha^{\mathrm{T}}\boldsymbol{M}_\alpha = \boldsymbol{M}_\alpha\boldsymbol{M}_\alpha^{\mathrm{T}} = \mathbb{1}$ and $\det\boldsymbol{M}_\alpha = 1$. The uncoupled p-h symmetric 2IAM is thus invariant under SO(4)⊗SO(4). In the channel symmetric free model, the symmetry group expands to O(8). At the QCP we study, all the interaction terms renormalise to 0 [96] so that one might expect an emergent O(8) symmetry, in a basis spanned by MFs. However, there is the same $\ln(2)/2$ entropy contribution as in the overscreened models, which suggests that there is a free MF mode. This is supported by a BCFT argument that our model, at p-h symmetry, has an emergent O(7) symmetry [155]. There is a very close analogy to the 2CKM, whose QCP has very similar properties to the 2IAM, and for which an MF model has been developed [156].

5.4 Majorana Model for the 2CKM

In the 2CKM, where a static spin $S = 1/2$ is symmetrically coupled to two non-interacting electron baths, the bulk electrons try to screen the impurity spin at low temperatures. In this system, each conduction bath is competing to form a Kondo singlet with the static impurity spin. Since there is no way of a single half-integer spin being coupled to an even number of half-spin electrons such that there is no residual spin, the impurity system remains spinful and therefore, at zero temperature, contributes to the entropy. The impurity spin is overscreened and the low-temperature system is hence disordered. At this NFL FP, a property indicative of the presence of a free MF mode, $S(0) = \ln(2)/2$ arises [147, 148, 157, 158]. This entropy contribution accompanies a logarithmic divergence (with respect to temperature) of the uniform spin susceptibility and specific heat [23]. Although the entropy is seemingly unphysical, the associated NFL behaviour (divergence of thermodynamic quantities) has been observed in certain Cerium and Uranium systems, and this behaviour attributed to the overscreened Kondo effect [159, 160, 161, 162, 163, 164]. NFL behaviour associated to multi-channel Kondo systems has also been observed in QD devices [165].

One early approach[1] to understanding the 2CKM was the study of the σ-τ model [168] where, rather than two channels, there was only one channel but the impurity was coupled to both the channel spin and isospin. The σ-τ model has a NFL FP which displays some similar properties to that of the 2CKM, but does not explicitly demonstrate the presence of an uncoupled MF mode. The O(3)-symmetric Anderson model [169], becomes equivalent (at large U) to the σ-τ model by means of a Schrieffer-Wolff transformation. This model has the Hamiltonian

$$H_{\mathrm{O}(3)} = i\sum_{n=0}^{\infty}\sum_{i=0}^{3}\xi_n\Lambda^{-n/2}\chi_i(n+1)\chi_i(n) + iV\sum_{i=1}^{3}\chi_i(0)d_i + iV_0\chi_0(0)d_0 + Ud_0d_1d_2d_3 \tag{5.4.1}$$

with an explicit invariance under the transformation

$$\begin{pmatrix} \chi_1(n) \\ \chi_2(n) \\ \chi_3(n) \end{pmatrix} \to \boldsymbol{M}\begin{pmatrix} \chi_1(n) \\ \chi_2(n) \\ \chi_3(n) \end{pmatrix}, \qquad \begin{pmatrix} d_1 \\ d_2 \\ d_3 \end{pmatrix} \to \boldsymbol{M}\begin{pmatrix} d_1 \\ d_2 \\ d_3 \end{pmatrix} \tag{5.4.2}$$

for $\boldsymbol{M} \in \mathrm{SO}(3)$, and in the free case we have an O(3) symmetry. $H_{\mathrm{O}(3)}$ exhibits a critical point as $V_0 \to 0$, where the static NFL features of the 2CKM emerge, which has been shown explicitly using NRG calculations [154]. Interestingly, one sees that in the limit $V_0 \to 0$, the d_0 MF becomes totally decoupled from the bulk and gives rise to the anomalous entropy. Although the σ-τ and the O(3)-symmetric Anderson models show properties very similar to the NFL QCP of the 2CKM, the models are not equivalent (although certain dynamic quantities have been argued to be identical for both models, over all energy scales [170]). In particular, the σ-τ and the O(3) models do not permit overscreening of the impurity [23], since there is only 1 electron bath. Motivated by these models, the excitation spectra of the 2CKM was shown to be governed by 2 sectors of MFs [156], indicating that free MF modes govern the observable physics.

The MF model for the NFL FP of the 2CKM is built upon the idea that some

---

[1] We specialise to discussing literature which points towards an MF model for the 2CKM/2IKM, but it is worth noting that alternative approaches to understanding the NFL have also been relatively successful. These include Bethe Ansatz [146, 166], Bosonisation [147, 167] and BCFT [20, 152, 155].

Energy	Degeneracy
0	2
$1/8$	4
$1/2$	10
$5/8$	12
1	26
$9/8$	32
$3/2$	60
$13/8$	76

TABLE 5.1: The low-lying energy levels of the 2CKM at the NFL FP, calculated by BCFT [171]. The energies are in terms of a scale set by v_{F}. We also include the degeneracies, which arise from the quantum numbers associated to the spin and representation of SO(5).

MF modes are free. In the same way as for the 2IAM, the bulk degrees of freedom give rise to 8 species of non-local MFs. The authors of [156] superpose sets of 8 free MFs, of which some are connected to the impurity and the remainder disconnected. Motivated by the boundary conditions considered in the BCFT treatment of the multi-channel Kondo model, connected MFs are considered periodic, whilst disconnected MFs are antiperiodic. A single free MF, which lives on a chain of length N, is described by the Hamiltonian

$$H_{\mathrm{MF}} = it \sum_{n=0}^{N-1} \chi(n)\chi(n+1) \tag{5.4.3}$$

where the periodic MF modes satisfy $\chi(N) = \chi(0)$, and the antiperiodic $\chi(N) = -\chi(0)$. Assuming a linear dispersion,

$$\epsilon_k = \frac{\pi v_{\mathrm{F}}}{l} k, \tag{5.4.4}$$

where l sets the length scale and v_{F} is the Fermi velocity, one can diagonalise H_{MF} and calculate the spectra for the MFs. Periodic MFs have single-particle energies $0, 1, 2$, etc (in units of $\pi v_{\mathrm{F}}/l$) whilst antiperiodic MFs have single-particle energies $1/2, 3/2, 5/2$ etc. BCFT studies of the 2CKM has allowed calculation of the NFL levels at the QCP [171, 150], given in table 5.1, and have uncovered an emergent SO(5) symmetry. The free model, formulated as in section 5.3, has 8 different species of conduction MFs, and the low-energy model has an SO(5) symmetry. The construction of an MF model for the 2CKM therefore contained different combinations of

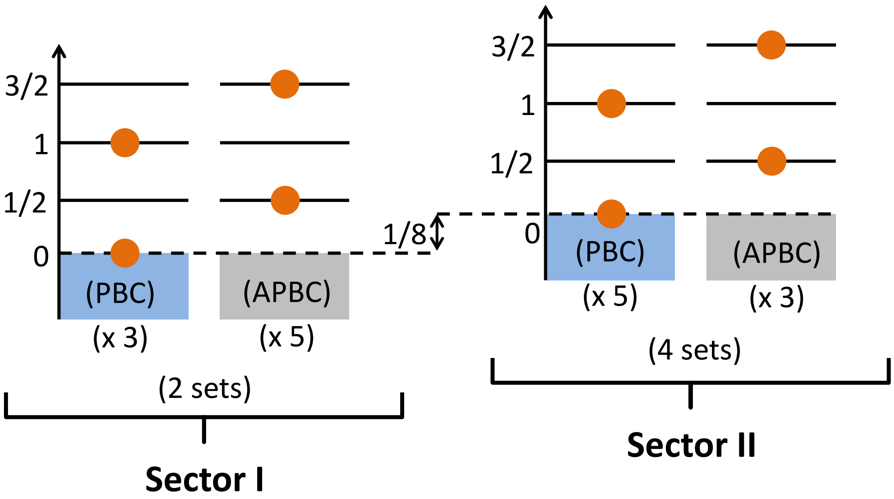

FIGURE 5.1: MF model of the 2CKM NFL FP, as proposed in [156]. Only energy levels with a circle may be occupied, and the 2 sectors act independently to describe the levels $0, {}^1\!/\!_2, 1$ etc (sector I) and ${}^1\!/\!_8, {}^5\!/\!_8, {}^9\!/\!_8$ etc (sector II). Energies are in units of $\pi v_{\mathrm{F}}/l$. PBC and APBC respectively indicate periodic and antiperiodic boundary conditions.

8 MFs, of which 5 would have different boundary conditions from the remaining 3. The successful model, formulated in [156], has 2 sectors, I and II, where the ground states of each sector are shifted by ${}^1\!/\!_8$. In sector I, there are 2 sets of 8 MFs, and each set has 3 MFs with periodic boundary conditions, and 5 with antiperiodic. Only one set may not be empty. Sector I gives us the 2CKM energies which are not shifted by ${}^1\!/\!_8$. There are 2 ground states, 1 corresponding to each set, where all 5 periodic MFs are not excited. As an example, to obtain an energy of ${}^3\!/\!_2$, we may excite any 5 MFs to ${}^3\!/\!_2$ (5 ways of doing this), excite a single periodic and antiperiodic MF (15 ways), or excite any 3 antiperiodic MFs to energy ${}^1\!/\!_2$ (10 ways). Noting we have 2 sets, the total degeneracy is therefore given by 60. The same approach is taken with sector II, which reproduces the energies shifted by ${}^1\!/\!_8$. This schema is illustrated in figure 5.1, and we show in table 5.2 how the many-body energies of the NFL can be constructed. This model gives a nice interpretation of both the emergent SO(5) symmetry, and the role of MFs, although it is somewhat mysterious why the sets and sectors come together as they do. A similar model has not been proposed for the 2IKM, however, which would be desirable because it also exhibits QCP with similar anomalous properties.

E_{NFL}	Sector	$\sum n_E[E]$	Degeneracy	Total Degeneracy
0	I	$3[0]$	1×2	2
$1/8$	II	$5[0]$	1×4	4
$1/2$	I	$1[1/2]$	5×2	10
$5/8$	II	$1[1/2]$	3×4	12
1	I	$1[1]$	3×2	
		$2[1/2]$	$\binom{5}{2} \times 2$	26
$9/8$	II	$1[1]$	5×4	
		$2[1/2]$	$\binom{3}{2} \times 4$	32
$3/2$	I	$1[3/2]$	5×2	
		$3[1/2]$	$\binom{5}{3} \times 2$	
		$1[1] + 1[1/2]$	$(3 \times 5) \times 2$	60
$13/8$	II	$1[3/2]$	3×4	
		$3[1/2]$	1×4	
		$1[1] + 1[1/2]$	$(5 \times 3) \times 4$	76

TABLE 5.2: The combinations of MFs which correspond to the 2CKM NFL FP energies.

5.5 2-Impurity Kondo Systems

In the 2IKM, one considers 2 distinct static impurity spins, $\boldsymbol{S}_1$ and $\boldsymbol{S}_2$, coupled to separated baths (labelled by $\alpha \in \{1,2\}$), with an antiferromagnetic Heisenberg interaction between the static spins. The Hamiltonian is given by

$$H_{\mathrm{2IKM}} = \sum_{\alpha} \left[\sum_{\boldsymbol{k}} \epsilon_{\alpha \boldsymbol{k}} c^{\dagger}_{\alpha \boldsymbol{k} \sigma} c_{\alpha \boldsymbol{k} \sigma} + 2J_{\alpha} \boldsymbol{S}_{\alpha}(0) \cdot \boldsymbol{S}_{\alpha} \right] + 2J \boldsymbol{S}_1 \cdot \boldsymbol{S}_2 \tag{5.5.1}$$

where $\boldsymbol{S}_{\alpha}(0)$ denotes the spin density of bath α local to impurity α. Like the 2CKM, the 2IKM exhibits a QCP governed by a NFL FP [172, 173], although the underlying physical picture differs. In the 2IKM, at the QCP, the system is competing between each of the baths screening their own impurity (for such a setup one could imagine $\tilde{J} \to 0$, while $\tilde{J}_1, \tilde{J}_2 \to \infty$) and the two impurity spins becoming so strongly coupled that they form a local singlet, and decouple from the rest of the system (now we would propose $\tilde{J} \to \infty$, while $\tilde{J}_1, \tilde{J}_2 \to 0$).

The total local spin susceptibility $\chi(\omega)$ quantifies the system response to a local field which seeks to fix the single impurity spin. In the 2CKM at the QCP, the inability of the baths to screen the static spin leads to long range correlations between the bulk electrons. As a result, the application of a local field to the impurity site leads to a divergence of $\chi(\omega)$ as $\omega \to 0$. In the 2IKM, it is the staggered spin susceptibility (measuring the response to a field which seeks to oppositely align the impurity spins) which diverges, whilst the total spin susceptibility (corresponding to the entire impurity system) remains finite [23].

Despite the differences in the underlying physical pictures and divergent quantities, the 2-channel and 2-impurity Kondo system QCPs both exhibit the anomalous entropy of $S(0) = \ln(2)/2$. This has been shown in the 2IKM analytically as well as numerically, through Bosonisation [174] and BCFT [155]. It is therefore suggested that an MF description is required for the 2-impurity case. It has been shown that the QCP of the 2CKM and 2IKM are identical with the exception of potential scattering [153], and therefore it seems probable that there are free MFs in the 2IKM. In our work, we consider the 2IAM, which is equivalent on low energy scales to the 2IKM when p-h symmetry is enforced. Our study of the QCP at p-h symmetry leads us to build an MF model for the 2IKM, although not for the 2IAM away from p-h symmetry.

5.6 Anderson Systems

At p-h symmetry, similar results to the 2CKM and 2IKM are obtained for the 2 Channel Anderson Model [175, 176] and the 2IAM [96, 108, 95]. As in the Kondo cases, there is an anomalous entropy contribution of $\ln(2)/2$ at the QCPs, and the total spin susceptibility diverges logarithmically for the 2CAM, whilst it is the staggered spin susceptibility which diverges in the 2IAM (with the total susceptibility remaining finite).

We study in detail the QCP of the 2IAM, through use of the NRG, and calculate dynamic quantities which show explicitly the divergences in certain correlation functions as well as properties of the density of states at the Fermi level. In addition, by calculating the imaginary part of the spin correlation functions, we explicitly show a logarithmic divergence of the relevant susceptibilities. An advantage of the NRG approach, compared to the Bethe Ansatz and BCFT approach, is that we can break symmetries in the bare model and investigate how the low-energy FP is affected. When we break p-h symmetry, we find that the anomalous properties persist, and study the dynamic quantities to gain a picture of the underlying physics. We also study how the QCP changes for the model with $U_1 \neq U_2$ and relate the p-h symmetric channel asymmetric case to the 2CKM, which is achieved when $U_1/\pi\Delta$ is large (strong correlation) and $U_2 = 0$.

Before we present our results and discussion, it is worth noting that this QCP is very well studied [26, 177, 178, 151, 155, 174], as are QCPs in similar models with modified symmetries [179]. However, there are shortages in the literature that we attempt to address. The QCP of the 2IKM/2IAM exhibits anomalous MF characteristics which have never been explained, and many of the methods which have been used to study the QCP assume p-h symmetry (eg Bethe ansatz, BCFT). However, the transition has been shown to exist when p-h symmetry is broken [96], and there have been few studies attempting to clarify the difference between the p-h symmetric and asymmetric transitions. Furthermore, the dynamics of the system have not been calculated before, and we use these to motivate a physical interpretation of the QCP.

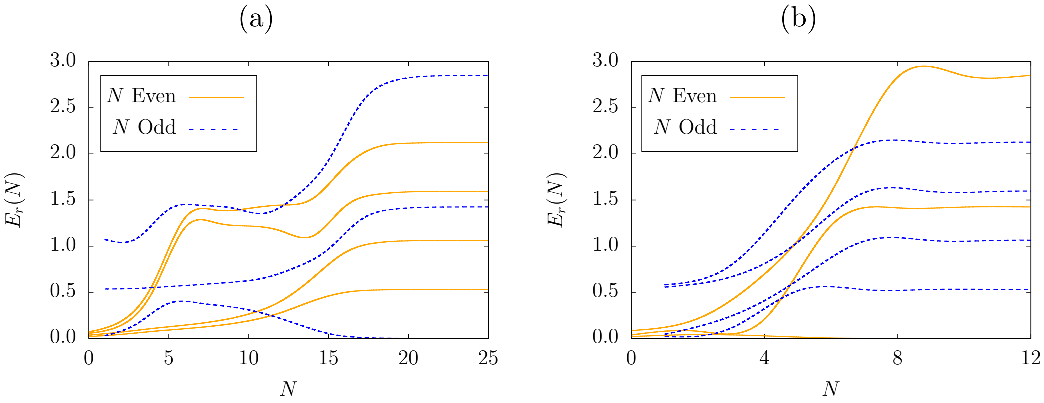

FIGURE 5.2: Comparison of the low-lying energy levels for the p-h symmetric model with $U/\pi\Delta = 6$, $\pi\Delta = 0.01$. In (a), we set $J = 0$ whilst in (b), $J/\pi\Delta = 1$.

5.7 Particle-Hole Symmetry

We begin by studying the 2IAM with p-h symmetry, and channel symmetry, whilst setting $U/\pi\Delta$ large (so that the system exhibits strong correlation). In this regime, the model is equivalent to the 2IKM on low-energy scales. We can therefore compare our results for the 2IAM to the previous studies on the 2IKM, and interpret the underlying physics similarly. We set $\pi\Delta = 0.01$, and $U/\pi\Delta = 6$. In figure 5.2 we plot the low-lying energy levels, as a function of the NRG iteration N, in the case $J = 0$ (a) and $J/\pi\Delta = 1$ (b). We see that the low energy eigenstate structure is totally changed and, in particular, the even and odd FPs of each case have swapped. It has been shown in [96] that for J above a critical value J_{C}, $\tilde{\Delta} = 0$, implying that the impurity sites have been totally decoupled from the baths. This corresponds to changing the number of coupled 2-body sites by 1, so that the odd and even FPs are exchanged. Our results support this picture.

We can calculate J_{C} by continuously partitioning a bracket $J_{\mathrm{L}} < J_{\mathrm{C}} < J_{\mathrm{U}}$ where J_{L} corresponds to the low energy regime where even/odd FPs have not been interchanged, and J_{U} to the regime where they have. For this model we calculate $J_{\mathrm{C}} = 8.8542371 \times 10^{-6}$, in agreement with [96] which states that, in the strong correlation regime, $J_{\mathrm{C}} = 1.378T_{\mathrm{K}}$, where T_{K} is defined by $T_{\mathrm{K}} = \pi\tilde{\Delta}(U,0)/4$ and $\tilde{\Delta}(U,J)$ is the renormalised hybridisation width in a model with bare parameters U and J. This ratio has also been found in [180, 178, 177], which study the 2IKM

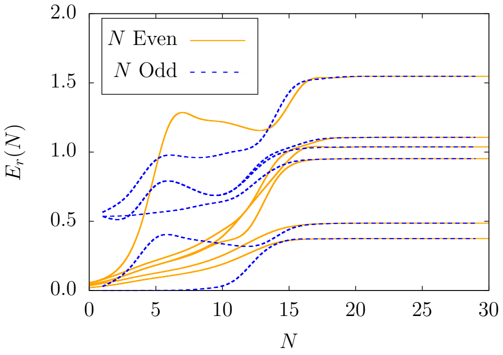

FIGURE 5.3: The RG flow of the lowest odd N and even N energy eigenvalues of the NRG Hamiltonians H_N. The model is channel symmetric and p-h symmetric, with $U/\pi\Delta = 6$. Some energies, which flow towards the illustrated levels have been omitted for clarity.

and we note that the authors use a different definition of T_K (so that the ratio is different, but a relevant substitution confirms equivalence). We plot in figure 5.3 the RG flow of the low-lying energies towards the unstable FP which emerges at $J = J_\mathrm{C}$. This FP is a QCP [96, 108]. Strikingly, the odd and even levels flow to the same FP, which suggests that we can build the levels from a superposition of the system with odd and even chain lengths. We build on this idea in section 5.10. The level structure is also of interest, as the degeneracies indicate that we are in a NFL regime [155]. We limit these levels to the continuum and compare with the BCFT analysis also in section 5.10. We cannot tune J precisely so that the RG flow ends exactly at the NFL FP, since it is unstable. The RG flow can, however, be brought arbitrarily close to the NFL FP, resulting in a ‘plateau’ of the levels, and to perform $T = 0$ calculations we simply claim that these levels correspond to the low-energy regime (since the NFL regime is a FP, this is true). For larger N, there is a crossover from the NFL to (even/odd) FL regime.

The NFL exhibits an anomalous impurity entropy contribution $\ln(2)/2$ as $T \to 0$, as shown in figure 5.4. As in the 2CKM and 2IKM, this is suggestive of the presence of a decoupled half degree of freedom (an MF mode). We also note that one must be very close to the value of J_C to see NFL behaviour - an accuracy of around 8 significant figures is required for an extended plateau. The renormalised parameters (a), and their ratios (b), on approach to the critical point ($J < J_\mathrm{C}$) are plotted in figure 5.5. We see that $\tilde{\Delta}$, $\tilde{U}$ and $\tilde{J}$ all vanish as $J \to J_\mathrm{C}$, but their ratios tend

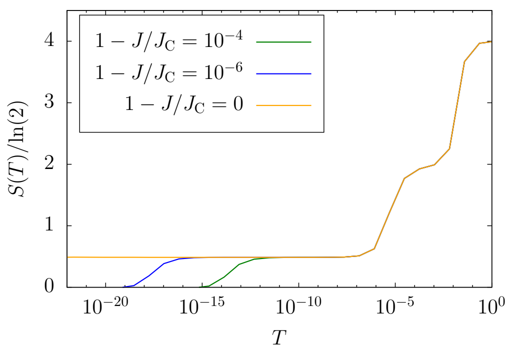

FIGURE 5.4: The entropy $S(T)$ as a function of T for the model with parameters as given in the caption of figure 5.3, and for varying values of J. The NFL plateau, where $S(T) = \ln(2)/2$ persists for $T < T_{\mathrm{K}}$.

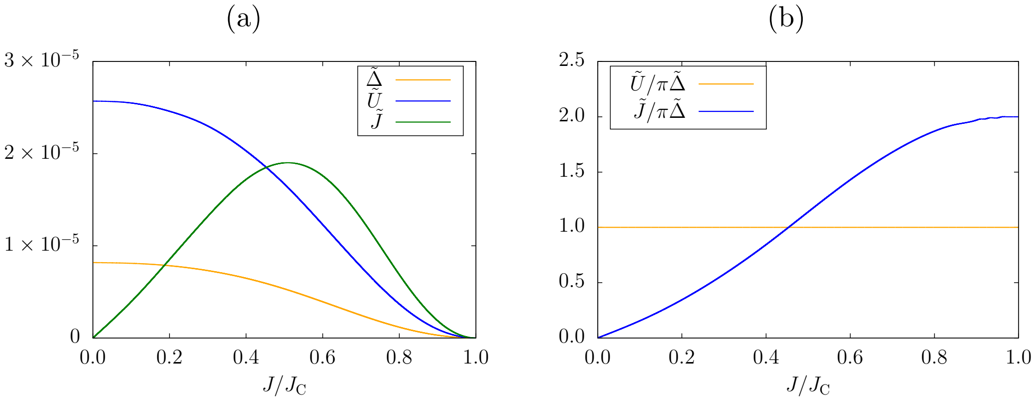

FIGURE 5.5: Plots of the renormalised parameters on approach to the NFL QCP from below. In (a) we plot $\tilde{\Delta}$, $\tilde{U}$ and $\tilde{J}$ against J/J_{C}, whilst the ratios $\tilde{U}/\pi\tilde{\Delta}$ and $\tilde{J}/\pi\tilde{\Delta}$ are plotted in (b). The model parameters are the same as those in figure 5.3.

to the constant values $\tilde{U}/\pi\tilde{\Delta} \to 1$ and $\tilde{J}/\pi\tilde{\Delta} \to 2$. There is hence an emergent single energy scale, T^*, which is defined by $\tilde{U} = \tilde{J}/2 = \pi\tilde{\Delta} = 4T^*$, and vanishes as $J \to J_{\mathrm{C}}$ (so that the system is conformally invariant). These results are in agreement with [96] and, using the RPT, the ratios provide insight into the behaviour of the dynamic quantities. Since $\tilde{\Delta} \to 0$ as $J \to J_{\mathrm{C}}$, we have $\tilde{\rho}(0) = 1/\pi\tilde{\Delta} \to \infty$ whilst $z \to 0$. Under channel symmetry, the total and staggered spin susceptibilities, given respectively in (3.5.15) and (3.5.16) become

$$\chi_{\mathrm{tot}}(0) = 2\tilde{\rho}(0)\left(1 + \tilde{U}\tilde{\rho}(0) - \tilde{J}\tilde{\rho}(0)\right) \tag{5.7.1}$$

and

$$\chi_{\mathrm{stg}}(0) = 2\tilde{\rho}(0)\left(1 + \tilde{U}\tilde{\rho}(0) + \tilde{J}\tilde{\rho}(0)\right). \tag{5.7.2}$$

Since $\tilde{U}\tilde{\rho}(0) \to 1$ and $\tilde{J}\tilde{\rho}(0) \to 2$, we can expect a divergence of the staggered spin susceptibility at $J = J_{\mathrm{C}}$, whilst $\chi_{\mathrm{tot}}(0)$ should not diverge. We can infer similar properties of the singlet and triplet susceptibilities. Defined in (3.5.20), the particle-particle scattering term, in the strong correlation limit with channel symmetry, becomes

$$\tilde{\Pi}(0) = -\frac{1}{\pi\tilde{\Delta}}, \tag{5.7.3}$$

so that we obtain

$$\chi_{\mathrm{sng}}(0) = -\frac{1}{\pi\tilde{\Delta}}\left(1 + \frac{3\tilde{J}}{2\pi\tilde{\Delta}}\right) \tag{5.7.4}$$

and

$$\chi_{\mathrm{trp}}(0) = -\frac{1}{\pi\tilde{\Delta}}\left(1 - \frac{\tilde{J}}{2\pi\tilde{\Delta}}\right) \tag{5.7.5}$$

where we use (3.5.25) and (3.5.26), and set $\tilde{U}_{12} = 0$. We can hence expect a divergence of the singlet susceptibility. The emergence of universality, and that we find $J_{\mathrm{C}} = 1.378T_{\mathrm{K}}$, implies that our calculations are consistent with the literature, and we now proceed to present NRG calculations of various dynamic quantities.

The underlying dynamics of the NFL FP are the same for all values of p-h and channel symmetry models we consider. We list the values of J_{C} for these models in table 5.3. We have found that the scaled levels $E_r(N)$ are identical for all of these models. This is because p-h symmetry constrains the low-energy FP. What is perhaps surprising is that the same universal ratios as before, $\tilde{U}/\pi\tilde{\Delta} \to 1$ and $\tilde{J}/\pi\tilde{\Delta} \to 2$, hold even in the weakly correlated model, with $U = 0$, implying emergent strong correlation [108]. We plot in figure 5.6a $\pi\Delta\rho(\omega)$ for the cases $J/J_{\mathrm{C}} = 0.5$

U	J_C
0.00	$5.07566704 \times 10^{-3}$
0.04	$8.89795460 \times 10^{-5}$
0.06	$8.85423711 \times 10^{-6}$
0.10	$7.86416000 \times 10^{-8}$

TABLE 5.3: The calculated values of J_C, to 9 significant figures, for the p-h and channel symmetric model with $\pi\Delta = 0.01$.

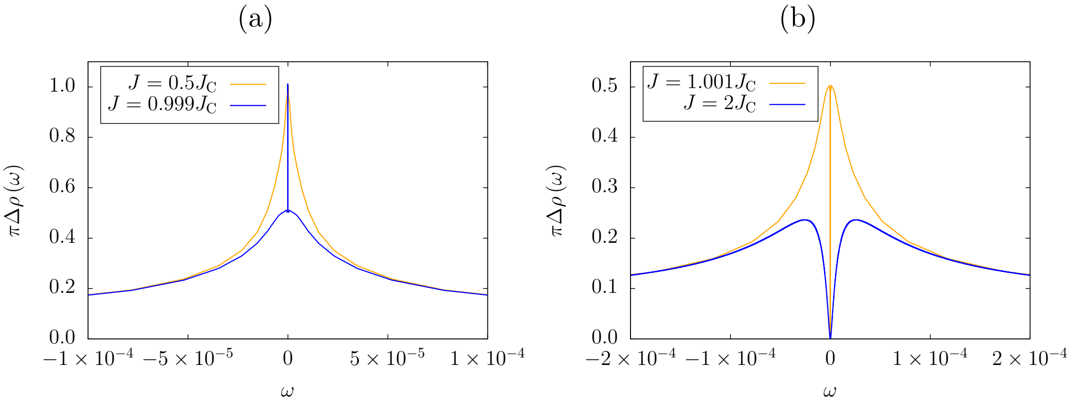
(a)

(b)

FIGURE 5.6: The spectral density below ($J < J_\mathrm{C}$) and above ($J > J_\mathrm{C}$) the transition corresponding to the parameters as given in the caption of figure 5.3. Note that the spectra have been scaled by the correction factor as discussed in chapter 2.

and $J/J_\mathrm{C} = 0.999$. We see that, in line with the usual $J = 0$ 2IAM at p-h symmetry, $\pi\Delta\rho(0) = 1$ due to the Friedel sum rule. However, the peak structure in the case $J/J_\mathrm{C} = 0.999$ is very different from that of $J/J_\mathrm{C} = 0.5$, which looks like a typical Kondo resonance. On the energy scales corresponding to the NFL FP, we see the emergence of a broad peak, of width characterised by T_K whose maximum appears to correspond to $\pi\Delta\rho(0) = 1/2$. When the RG flow heads away from the NFL FP, towards a stable FL FP, we obtain the usual result as constrained by the Friedel sum rule. However, the width of the Kondo peak is governed by $\tilde{\Delta}(U, J) \propto T^*$ where $T^* \to 0$ as $J \to J_\mathrm{C}$. When $J = J_\mathrm{C}/2$, the RG flow is not influenced by the NFL FP, so we obtain the usual Kondo peak, again of width $\tilde{\Delta}(U, J)$.

In contrast to this result, we plot $\pi\Delta\rho(\omega)$ for the cases $J/J_\mathrm{C} = 1.001$ and $J/J_\mathrm{C} = 2$ in figure 5.6b. We now obtain the unusual result $\pi\Delta\rho(0) = 0$, implying that the

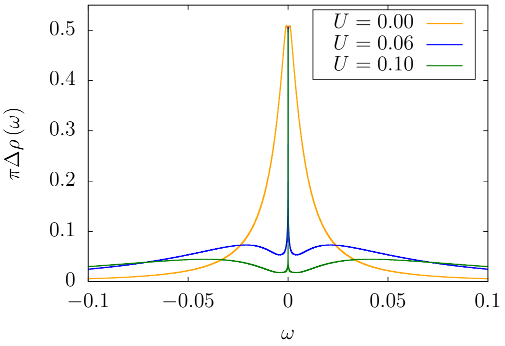

FIGURE 5.7: The 1-particle spectral density at $J = J_{\mathrm{C}}$ for various values of U. We take $\pi\Delta = 0.01$, and the values of J_{C} are given in table 5.3.

Kondo many-body singlet has been destroyed and adding or removing localised electrons now costs energy. The Kondo resonance has been bifurcated into 2 peaks above and below the Fermi level. When $J/J_{\mathrm{C}} = 1.001$, the RG flows close to the NFL FP, and on the energy scales where NFL behaviour manifests in the model (these are the energy scales where the anomalous entropy persists), we see that $\rho(\omega)$ again appears to be fixed to the value $\pi\Delta\rho(0) = 1/2$ similar to the $J < J_{\mathrm{C}}$ case. When the RG flow approaches the stable FP regime, we obtain $\pi\Delta\rho(0) = 0$. The model is said to be pseudogapped in this regime, which is consistent with the results of [96] where the authors found that for p-h symmetry, $\tilde{\Delta} = 0$ for $J > J_{\mathrm{C}}$. The discontinuous change in $\rho(0)$ as J crosses J_{C} corresponds to the $\pi/2$ phase shift, which is also observed in [96]. One might expect by (1.3.4) that this phase shift would change the local occupation, however this is not the case since p-h symmetry ensures $\rho(\omega)$ is symmetric about $\omega = 0$ so that the local occupation is always 1 on each impurity. We interpret the impurities to be so strongly bound that they are decoupled from the conduction electron baths, and the narrow peaks either side of the Fermi level to correspond to the energy required to add or remove an electron. We also plot $\pi\Delta\rho(\omega)$ for the case $J = J_{\mathrm{C}}$ in figure 5.7, where we consider several values of $U/\pi\Delta$. We see that a peak at the Fermi level persists, but only reaches the height $\pi\Delta\rho(0) = 1/2$, so that some spectral weight has been suddenly displaced. The value $\pi\Delta\rho(0) = 1/2$ appears to be universal in the model with p-h symmetry.

These observations alone do not paint a very clear picture of the underlying physics of the QCP. We interpret the case $J < J_{\mathrm{C}}$ as the system being in a Kondo regime,

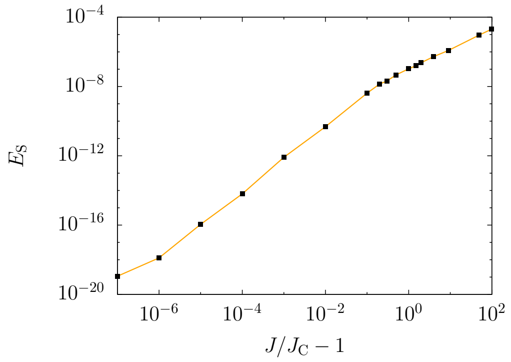

FIGURE 5.8: The binding energy E_S of the localised singlet that forms for $J > J_C$, as a function of $J/J_C - 1$. To a good approximation, the curve is linear (the correlation coefficient is given as $R^2 = 0.9915$) and is hence suggestive of the relationship $E_S = \alpha\,(J/J_C - 1)^{\beta}$. We calculate $\alpha = 5.8982 \times 10^{-8}$ and $\beta = 1.6836$ numerically using least-squared regression.

where the impurities each contain a single electron which forms a many-body singlet with the first conduction site. Conversely, we interpret $J > J_C$ as leading to the formation of a localised singlet. It follows that the addition or removal of a single electron to the impurity system will require the singlet to be broken, which costs energy. For this reason the spectral density has developed a pseudogap, with the distance between the peaks either side corresponding to the binding energy E_S of the singlet. Unsurprisingly, as one as increases J the binding energy increases, and the peaks either side of the Fermi level move apart. We plot this in figure 5.8, which shows that $E_S = \alpha\,(J/J_C - 1)^{\beta}$, where α and β are positive constants, with $\alpha \sim \mathcal{O}(T_K)$. We illustrate the 2 competing regimes in figure 5.9. The system at $J = J_C$ is interpreted as a superposition of these 2 regimes. The normalised superposition of $\rho(\omega)$ above and below the transition is very similar to the $\rho(\omega)$ at the transition, and supports the notion that here the system is in a superposition of each regime. Also in support of this notion is the fact that the even-odd oscillations disappear at the NFL FP. Since $\tilde{\Delta} = 0$ for $J > J_C$ the system in this regime would have an excitation spectra corresponding to an even chain length, whilst the system's excitation spectra for $J < J_C$ would be odd (or vice versa). Superposing an even and odd chain length would cause the even-odd oscillations to vanish.

Having formulated a picture of the NFL FP, we now test it using NRG calculations of various spin susceptibilities. With the NRG, we can only calculate the

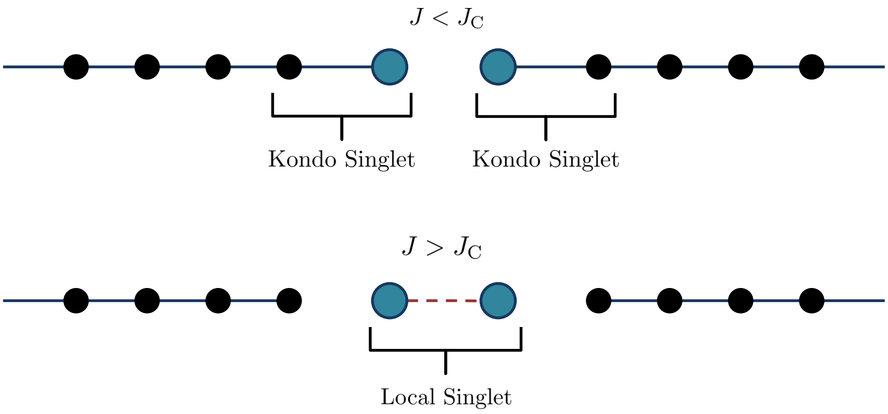

FIGURE 5.9: Schematic of the competing low energy regimes at the $J = J_\mathrm{C}$ QCP. The localised impurity sites are represented by the blue circles, whilst de-localised conduction sites are depicted by the black circles.

imaginary parts of the Green functions, but the real part may be determined by means of a Hilbert transform. However, the low-energy behaviour occurring on scales $\omega \sim \mathcal{O}(10^{-10})$ requires a logarithmic mesh close to $\omega = 0$. This makes the numerics of performing the Hilbert transform very challenging. For this reason we present only results for the imaginary part of the susceptibilities. In figures 5.10 and 5.11 respectively we plot $\mathrm{Im}\chi_\mathrm{tot}(\omega)$ and $\mathrm{Im}\chi_\mathrm{stg}(\omega)$ for the model with $U/\pi\Delta = 6$ at $J = J_\mathrm{C}$. We see that as $\omega \to 0$, $\mathrm{Im}\chi_\mathrm{tot}(\omega)$ approaches zero monotonically, and passes through it. Conversely, $\mathrm{Im}\chi_\mathrm{stg}(\omega)$ is discontinuous about $\omega = 0$. The real part of the susceptibility is given by

$$\mathrm{Re}\chi_\mathrm{stg}(\omega) = -\frac{1}{\pi}\lim_{\delta\to 0}\int_\delta^\infty \mathrm{d}\omega' \, \frac{\mathrm{Im}\chi_\mathrm{stg}(\omega+\omega') - \mathrm{Im}\chi_\mathrm{stg}(\omega-\omega')}{\omega'} \tag{5.7.6}$$

[181]. We see that if $\mathrm{Im}\chi_\mathrm{stg}(\omega)$ is discontinuous at $\omega = 0$ then there is a logarithmic divergence of $\mathrm{Re}\chi_\mathrm{stg}(\omega)$ at $\omega = 0$. In agreement with the RPT, we therefore have that the staggered spin susceptibility diverges at $J = J_\mathrm{C}$, whilst the total spin susceptibility remains finite. If the NFL FP represents the superposition of Kondo and local singlet regimes, then any perturbation which seeks to 'push' the system towards one of these regimes would result in long ranged behaviour and the corresponding susceptibility would therefore diverge. The total spin susceptibility measures the response to a field which seeks to arrange the spins on each impurity in parallel. In the Kondo regime this would have no effect (due to the local spin up and down states being degenerate), but in a local singlet regime this would result in a triplet

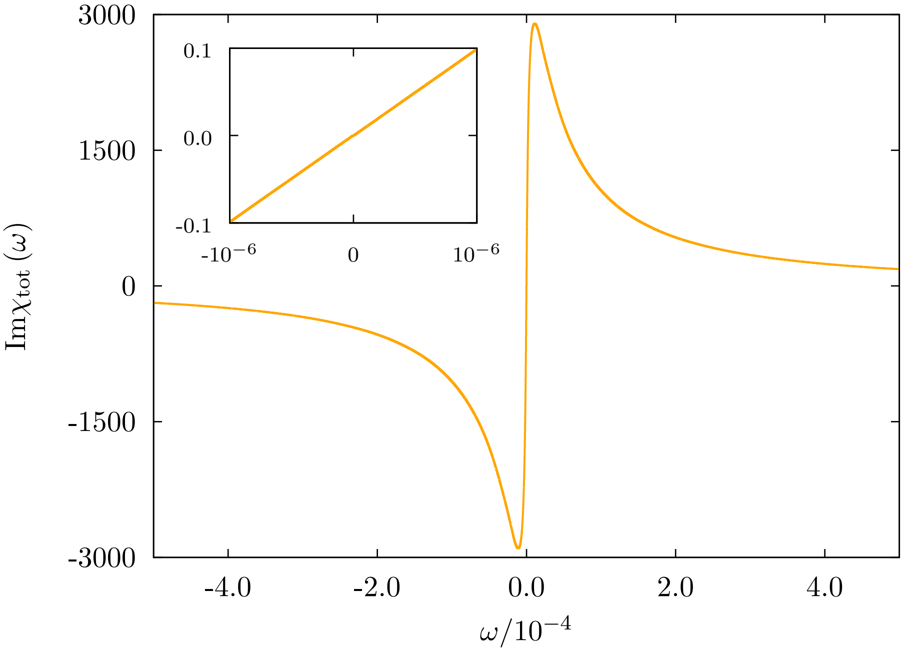

FIGURE 5.10: Plot of the imaginary part of the total spin susceptibility for the p-h and channel symmetric model with $U/\pi\Delta = 6$. The inset shows a close-up of the behaviour around the Fermi level.

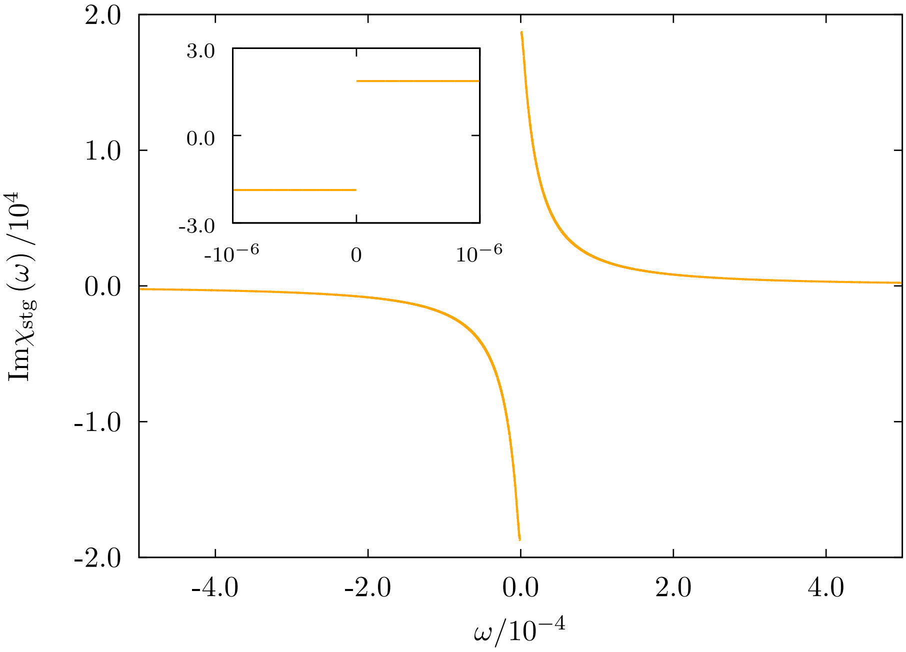

FIGURE 5.11: Plot of the imaginary part of the staggered spin susceptibility for the p-h and channel symmetric model with $U/\pi\Delta = 6$. The inset shows a close-up of the behaviour around the Fermi level.

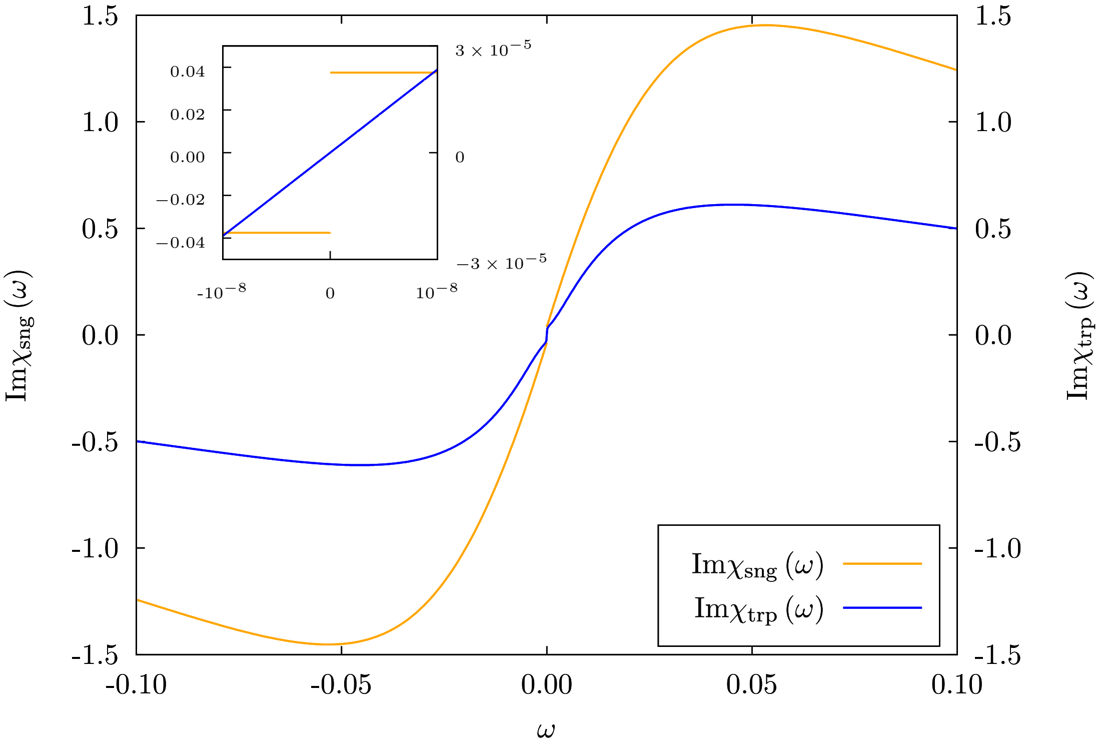

FIGURE 5.12: Plot of the imaginary part of the singlet (orange) and triplet (blue) pairing susceptibilities for the p-h and channel symmetric model with $U/\pi\Delta = 6$. The inset shows a close-up of the behaviour around the Fermi level. The triplet susceptibility is plotted against the axis on the right.

state forming. Whilst it would destroy the NFL ground state, this would cost energy so there is no divergence at the Fermi level. Arranging the spins oppositely, on the other hand, could result in the formation of a singlet. The system is highly sensitive to any field attempting to achieve such an arrangement, and we thus have that the staggered susceptibility diverges.

The singlet and triplet susceptibilities, measuring the system response to adding or removing a local singlet or triplet state, can also be calculated using the NRG. We plot these, again for the case $U/\pi\Delta = 6$ and $J = J_{\mathrm{C}}$, in figure 5.12. We see that the singlet susceptibility diverges (in the real part) whilst the triplet susceptibility remains finite. This is for the same reason that $\chi_{\mathrm{stg}}(\omega)$ diverges. Creating a singlet would collapse the ‘frustrated’ QCP ground state into the local singlet regime. When the system ceases to be in a superposition ($J \neq J_{\mathrm{C}}$), we find that all the divergences

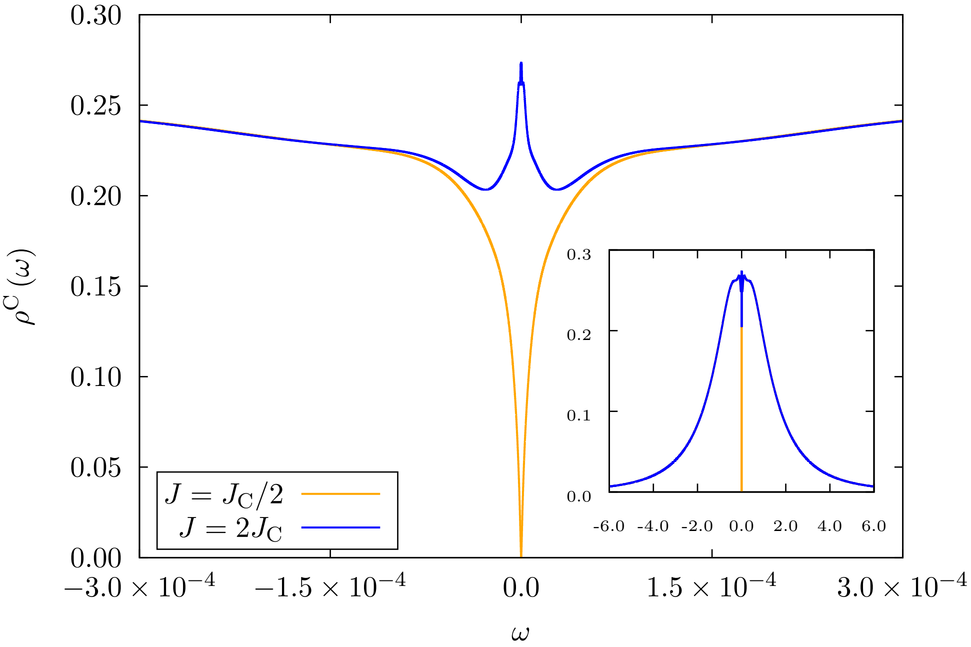

FIGURE 5.13: Plot of $\rho^{\mathrm{C}}(\omega)$ for the p-h symmetric model with $U/\pi\Delta = 6$ above and below the transition at J_{C}.

disappear, and close to the transition the susceptibilities are instead enhanced.

We also attempt to make sense of the observation in [96] that when $J > J_{\mathrm{C}}$, and the impurity sites are decoupled from the chains, the first conduction site becomes an 'effective' impurity. We also note from [96] that we may express the Green function of the first impurity site, $G^{\mathrm{C}}_{\alpha}(\omega)$, in terms of the local impurity Green function as

$$G^{\mathrm{C}}_{\alpha}(\omega) = -i\frac{\pi^2}{2}\left(1 - i\pi\Delta_{\alpha}G_{\alpha}(\omega)\right) \tag{5.7.7}$$

which leads to the sum rule

$$\pi D\rho^{\mathrm{C}}_{\alpha}(0) = 1 - \pi\Delta_{\alpha}\rho_{\alpha}(0). \tag{5.7.8}$$

We thus expect that when $\rho(0)$ is a minimum, $\rho^{\mathrm{C}}(0)$ is a maximum and vice versa[2]. We plot $\rho^{\mathrm{C}}(\omega)$ in figure 5.13 for the cases $J = 0.5J_{\mathrm{C}}$ (a) and $J = 2J_{\mathrm{C}}$ (b). We see that when $J < J_{\mathrm{C}}$, and $\rho(\omega)$ has a resonance at the Fermi level, $\rho^{\mathrm{C}}(\omega)$ has an 'anti-resonance' at the Fermi level, such that $\rho^{\mathrm{C}}(0) = 0$. The width is of the order

---

[2] This kind of structure appears to propagate down the Wilson chain, as can be seen from the continued fraction approach to calculating the conduction Green functions discussed in chapter 3.

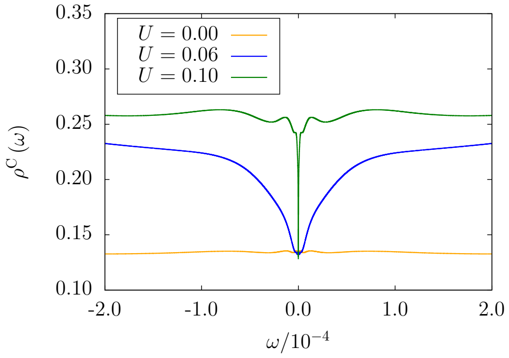

FIGURE 5.14: Plot of $\rho^{\mathrm{C}}(\omega)$ at $J = J_{\mathrm{C}}$ for various values of U. We take $\pi\Delta = 0.01$, and the values of J_{C} are given in table 5.3.

$\tilde{\Delta}(U, J) = 5.31 \times 10^{-6}$. Conversely, when $J > J_{\mathrm{C}}$, $\rho^{\mathrm{C}}(\omega)$ has a narrow resonance at the Fermi level, reaching the value $\rho^{\mathrm{C}}(0) = 0.272$, corresponding to $\pi D \rho^{\mathrm{C}}(0) = 1$. The values of $\rho^{\mathrm{C}}(0)$ are the same for the different values of U we consider. We interpret the renormalised parameters calculated in [96] as corresponding to this site, which behaves as an effective impurity. At $J = J_{\mathrm{C}}$, $\rho^{\mathrm{C}}(\omega)$ exhibits the same behaviour as $\rho(\omega)$ in that it appears to be a superposition of the cases $J < J_{\mathrm{C}}$ and $J > J_{\mathrm{C}}$, with $\rho^{\mathrm{C}}(0) = 0.136$, such that $\pi D \rho^{\mathrm{C}}(0) = 1/2$ (taking the midpoint of the cases $J < J_{\mathrm{C}}$ and $J > J_{\mathrm{C}}$). This is shown in figure 5.14 for various values of $U/\pi\Delta$, and like the value of $\pi\Delta\rho(0)$, it appears that $\rho^{\mathrm{C}}(0)$ is universal for the p-h symmetric model.

Our investigation of the p-h symmetric system around the NFL QCP provides evidence to suggest that the ground state of the QCP is a superposition of the local singlet and Kondo regimes. We have shown that the susceptibility to a field which could place the localised d-electrons in a singlet diverges at $J = J_{\mathrm{C}}$. We have also presented 1-particle spectral densities for the impurity and first conduction site in the regimes $J < J_{\mathrm{C}}$ and $J > J_{\mathrm{C}}$. It appears that at $J = J_{\mathrm{C}}$, the values of $\pi\Delta\rho(0)$ and $\rho^{\mathrm{C}}(0)$ are fixed regardless of the value of U. We find that for $J < J_{\mathrm{C}}$ the model is in a Kondo regime, whilst for $J > J_{\mathrm{C}}$ the system forms a local singlet, with the emergence of two peaks in the spectral density which replace the Kondo resonance. The separation between these peaks represents the binding energy of the singlet, and we have shown that as J increases above J_{C}, so the peaks move further apart. Finally, we have speculated that these two regimes correspond to a

ϵ	U	U_{12}	$J_{\rm C}$
-2.10×10^{-2}	5.00×10^{-2}	5.00×10^{-2}	$1.76290677 \times 10^{-2}$
-1.00×10^{-2}	0.00	0.00	$1.51263226 \times 10^{-2}$
1.59×10^{-3}	5.00×10^{-3}	0.00	$5.44017626 \times 10^{-3}$

TABLE 5.4: The calculated values of $J_{\rm C}$, to 9 significant figures, for the p-h asymmetric and channel symmetric model with $\pi\Delta = 0.01$.

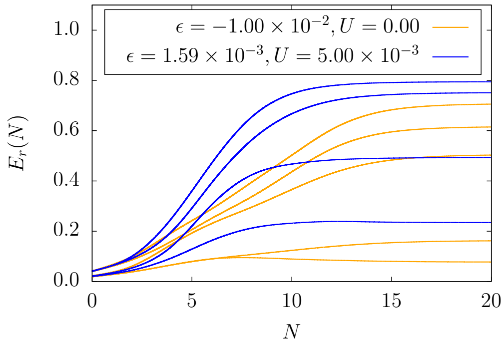

FIGURE 5.15: The RG flow of the distinct low-lying energies of the NRG Hamiltonian towards the NFL FP at $J = J_{\rm C}$, for two different models. We see that the structure of the levels is different for the two cases.

chain with even/odd (or vice versa) boundary conditions, so that the RG flow of the scaled NRG energies at $J = J_{\rm C}$ does not exhibit even/odd oscillations.

5.8 Particle-Hole Asymmetry

We now study the transition away from p-h symmetry. The structure of the NFL FP is no longer constrained, so for different bare parameters we obtain different levels. We calculate 3 different QCPs for p-h asymmetry, and give the corresponding parameters in table 5.4. We plot the RG flow of the low-lying energies at $J = J_{\rm C}$ in figure 5.15 where we see that the levels in the QCPs of the $\epsilon = 1.59 \times 10^{-3}, U = 5.00 \times 10^{-3}$ (a) and $\epsilon = -1.00 \times 10^{-2}, U = 0.00$ (b) models are significantly different. However, the odd/even oscillations still vanish at the NFL FP in the p-h asymmetric case, and the anomalous $\ln(2)/2$ entropy persists, as shown in figures 5.16a and 5.16b respectively. In addition, we find that the renormalised parameters all tend to zero as $J \to J_{\rm C}$ (figure 5.17a) and the relations $\tilde{U}\tilde{\rho}(0) \to 1$ and $\tilde{J}\tilde{\rho}(0) \to 2$ still hold. These are plotted against $J/J_{\rm C}$ in figure 5.17b. Therefore, despite the energy spectrum at

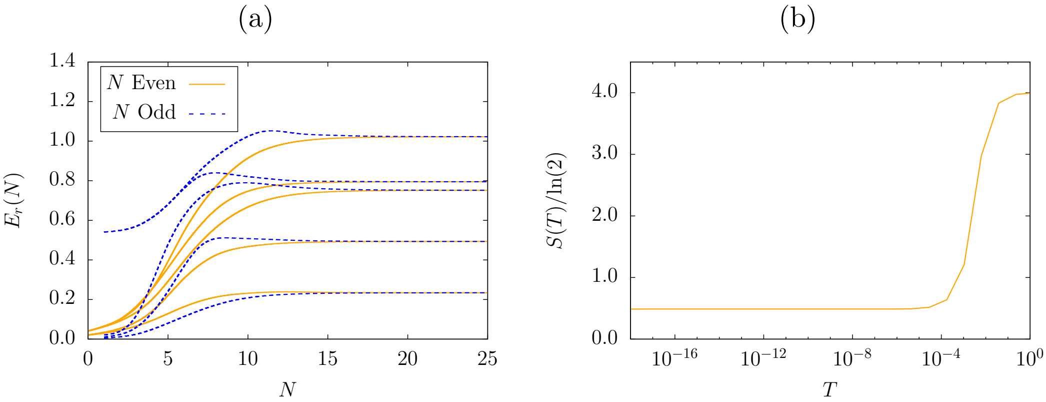

FIGURE 5.16: Plots of the low-lying NRG energy levels (a) and the entropy $S(T)$ (b) for the model with parameters $\epsilon = 1.59 \times 10^{-3}, U = 5.00 \times 10^{-3}$.

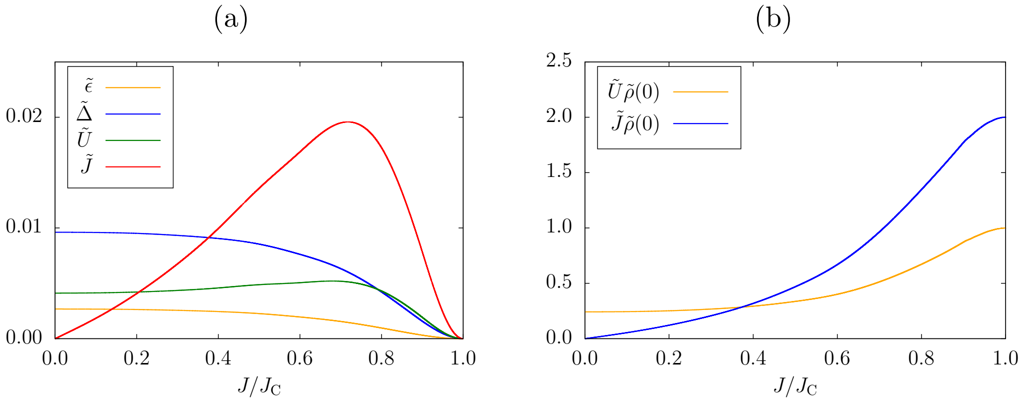

FIGURE 5.17: Plots of the renormalised parameters on approach to the NFL QCP from below. In (a) we plot $\tilde{\epsilon}$, $\tilde{\Delta}$, $\tilde{U}$ and $\tilde{J}$ against J/J_{C}, whilst the quantities $\tilde{U}\tilde{\rho}(0)$ and $\tilde{J}\tilde{\rho}(0)$ are plotted in (b). The model parameters are the same as those in figure 5.16.

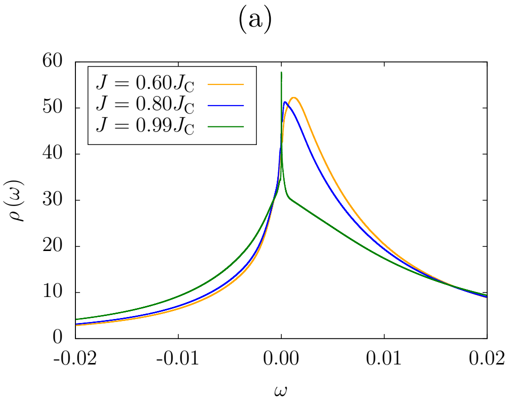

FIGURE 5.18: The 1-particle d-site spectral density for $J < J_{\mathrm{C}}$. The model in (a) has parameters $\epsilon = 1.59 \times 10^{-3}, U = 5.00 \times 10^{-3}$ whilst (b) corresponds to $\epsilon = -1.00 \times 10^{-2}, U = 0.00$. We set $\pi\Delta = 0.01$.

the NFL FP, we can expect a number of similarities with the p-h symmetric case and we investigate these in this section.

We first study the 1-particle functions. For the p-h symmetric model, we found $\pi\Delta\rho(0) = 1$ for $J < J_{\mathrm{C}}$, and $\pi\Delta\rho(0) = 0$ for $J > J_{\mathrm{C}}$. The former result is due to the Friedel sum rule and that $\tilde{\epsilon} = 0$. Away from p-h symmetry, when $\tilde{\epsilon} \neq 0$, it is unsurprising that these results do not persist. We plot $\rho(\omega)$ in figure 5.18, considering the cases $J/J_{\mathrm{C}} = 0.6, 0.8, 0.99$ for 2 separate p-h asymmetric models. We see that value of $\rho(0)$ increases as $J \to J_{\mathrm{C}}$, and the peaks narrow as $T^* \to 0$. In addition, we see that the peak shifts towards the Fermi level as $J \to J_{\mathrm{C}}$. We plot the spectra on the other side of the transition, $J > J_{\mathrm{C}}$, in figure 5.19, again for 2 different model parameters and several values of J/J_{C}. These plots show that there has been a sudden loss of spectral density at the Fermi level and that an anti-resonance has formed, but a pseudogap has not. The anti-resonance grows wider and deeper as J increases. As in the p-h symmetric model, the discontinuous change in $\rho(0)$ is due to a $\pi/2$ phase shift which does not change the local occupation of d-electrons. We also see that $\tilde{\epsilon}$ has crossed the Fermi level and as J increases moves further away from it. Correspondingly, a 2-(quasi)particle state is brought below the Fermi level (or liberated), but spectral weight has not been redistributed, since the width of the quasiparticle peak is infinitesimal just below and above the transition. We conjecture that this 2-quasiparticle state is a singlet. This localisation/liberation of 2 quasiparticles does

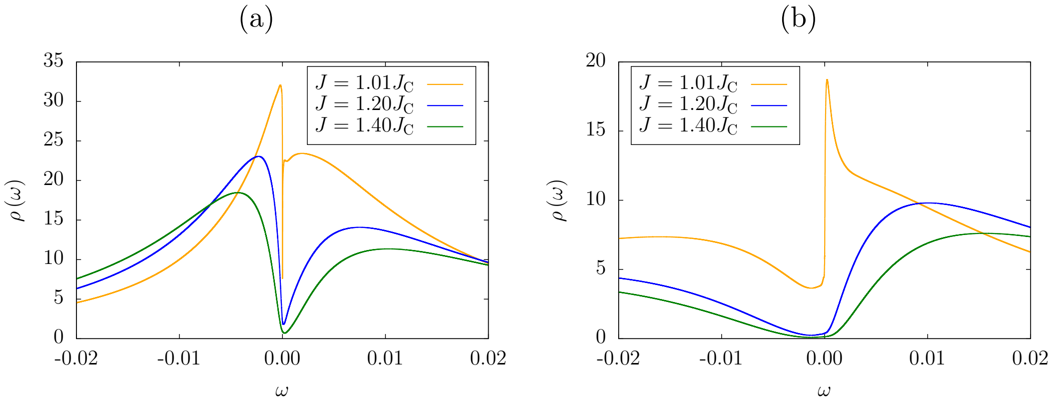

FIGURE 5.19: The 1-particle d-site spectral density for $J > J_{\mathrm{C}}$. The parameters corresponding to (a) and (b) are the same as those in figure 5.18.

not change the number of d-electrons. We plot n as a function of J/J_{C} in figure 5.20, as calculated by the NRG (integrating $\rho(\omega)$ up to the Fermi level) and RPT. We see that the RPT and NRG give different results for the occupation as J increases past J_{C}, but agree reasonably well for $J < J_{\mathrm{C}}$. The fact that $\tilde{\epsilon}$ has changed sign results in the localisation of a 2-particle state according to the RPT, but this is not reflected in the NRG. In the limit $J \to \infty$ the ground state is a local singlet, so that we expect $n \to 2$, which implies that RPT analysis must be modified to correctly calculate the occupation. We note from [96] that there is a phase shift of $\pi/2$ across the transition. We account for this phase shift by modifying the Friedel sum rule for the regime $J > J_{\mathrm{C}}$, where we make the substitution $\eta_{\alpha\sigma} \to \bar{\eta}_{\alpha\sigma} = \eta_{\alpha\sigma} + \phi$, for $\phi = \pm\pi/2$, and $\eta_{\alpha\sigma}$ given by

$$\eta_{\alpha\sigma} = \frac{\pi}{2} - \arctan\left(\frac{\tilde{\epsilon}_{\alpha\sigma}}{\tilde{\Delta}_\alpha}\right). \tag{5.8.1}$$

The phase of impurity α is given by $\bar{\eta}_\alpha = \sum_\sigma \bar{\eta}_{\alpha\sigma}$, and satisfies the modified relations

$$n_\alpha = \frac{\bar{\eta}_\alpha}{\pi} = \frac{\eta_\alpha}{\pi} + \frac{2\phi}{\pi} \tag{5.8.2}$$

and

$$\rho_\alpha(0) = \frac{1}{\pi\Delta_\alpha}\cos^2\left(\frac{\pi}{2}n_\alpha\right). \tag{5.8.3}$$

Note from (1.3.3) that since the phase is shifted by a constant, the form of the spectral density has not changed. The value of ϕ is determined by the value of ϵ; for $\epsilon \leq 0$, we take $\phi = \pi/2$, and $\phi = -\pi/2$ otherwise. This prescription also holds

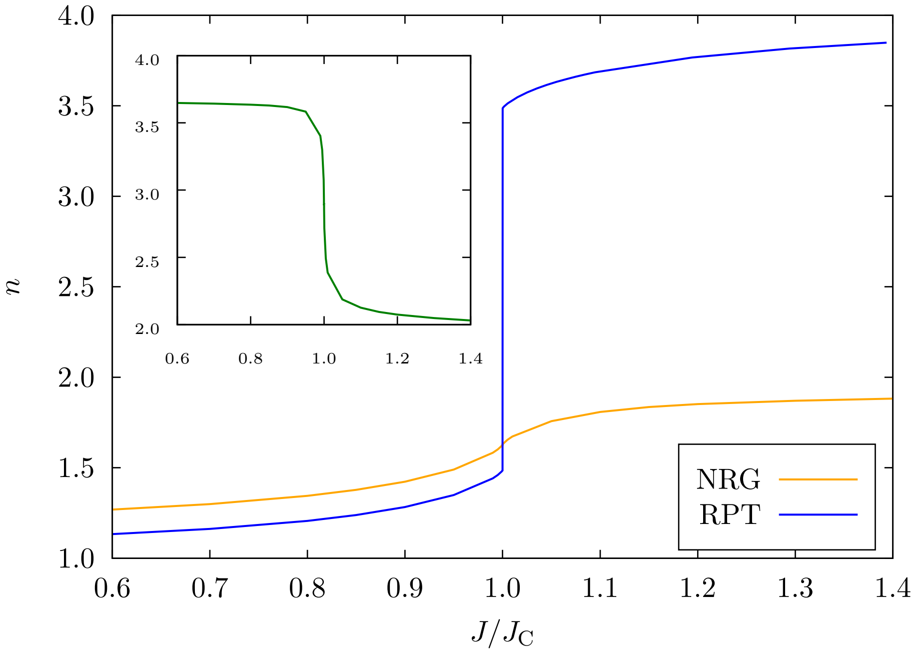

FIGURE 5.20: Plot of n as a function of J/J_{C} for the p-h asymmetric model with parameters $\epsilon = 1.59 \times 10^{-3}, U = 5.00 \times 10^{-3}$, as calculated by the NRG and RPT. Notice that for $J > J_{\mathrm{C}}$, the RPT results no longer agrees with the NRG. The inset corresponds to the model with parameters $\epsilon = -1.00 \times 10^{-2}, U = 0.00$ for which no renormalised parameters are available. The renormalised parameters for $J > J_{\mathrm{C}}$ were provided by the authors of [96].

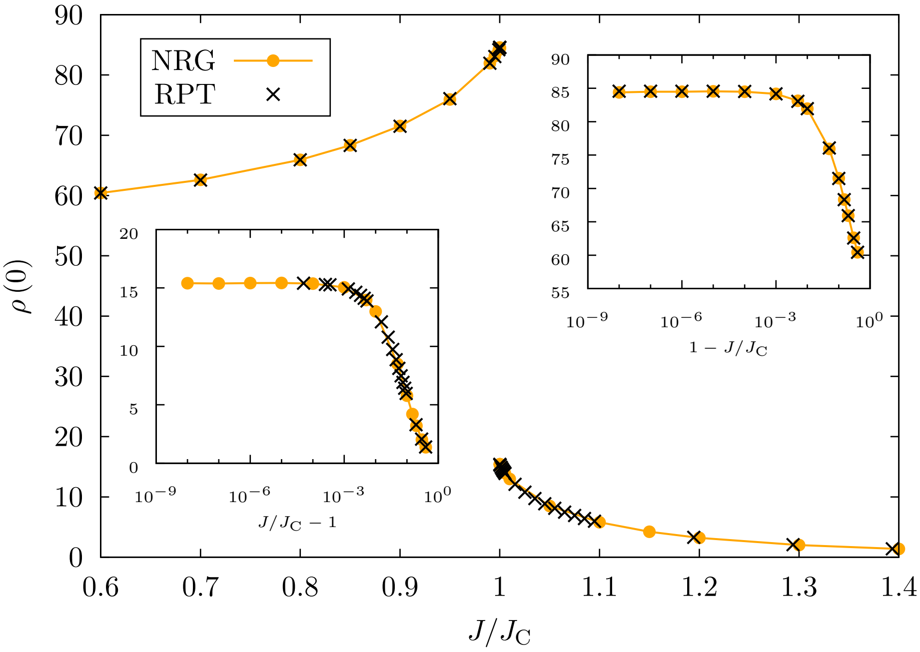

FIGURE 5.21: Plot of $\rho(0)$ as a function of J/J_C for the p-h asymmetric model with parameters $\epsilon = 1.59 \times 10^{-3}, U = 5.00 \times 10^{-3}$. The crosses show the values calculated using the RPT, $\rho(0) = z\tilde{\rho}(0)$. The insets show that $\rho(0)$ stabilises as we get very close to the transition. The renormalised parameters for $J > J_\mathrm{C}$ were provided by the authors of [96].

for p-h symmetry. An important consequence of the phase shift is the emergence of a difference between n_α and $\tilde{n}_\alpha = \eta_\alpha/\pi$. For the regime $J > J_\mathrm{C}$ we now have $\tilde{n}_\alpha = n_\alpha \pm 1$ such that as $J \to \infty$ and $n \to 2$, we have $\tilde{n} \to 0$ or $\tilde{n} \to 4$. This shift is reflected by $\tilde{\epsilon}$ crossing the Fermi level.

The authors of [96] found a discontinuous loss of spectral density at the Fermi level as J increases through J_C, and proposed a prescription for calculating the renormalised parameters in the regime $J > J_\mathrm{C}$. We confirm their results in figure 5.21, where we show explicitly the values of $\rho(0)$ calculated by the NRG and compare them to those they calculated using the RPT and presented in their paper. There is excellent agreement between the methods, and we see that sufficiently close to the transition, $|J/J_\mathrm{C} - 1| \lesssim 10^{-3}$, the value of $\rho(0)$ stabilises. Notice that the midpoint between the values of $\rho(0)$ above and below the transition corresponds to $\pi\Delta\rho(0) = 1/2$. If, at $J = J_\mathrm{C}$, the system is in a superposition of the $J < J_\mathrm{C}$ and

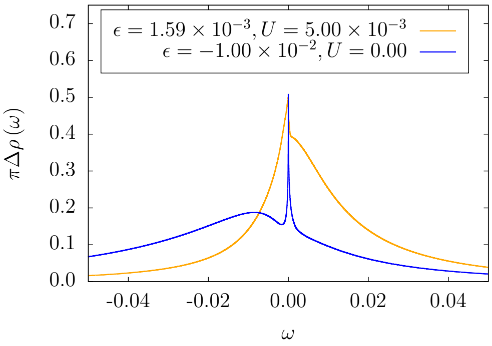

FIGURE 5.22: Plot of $\rho(\omega)$ at $J = J_\mathrm{C}$ for various p-h asymmetric models.

$J > J_\mathrm{C}$ regimes, then we might expect the corresponding value of $\rho(0)$ to be the midpoint of the $\rho(0)$ above and below the transition. We plot $\pi\Delta\rho(\omega)$ at $J = J_\mathrm{C}$ for two sets of p-h asymmetric parameters in figure 5.22. As we predict, and similar to the p-h symmetric model, we find $\pi\Delta\rho(0) = 1/2$, and posit that this value is universal to the magnetically induced QCP of the 2IAM. Interestingly, regardless of the bare parameters, the QCP appears to be constrained such that the midpoint of $\rho(0)$ above and below the transition is $1/2\pi\Delta$. In the p-h symmetric model, we saw a similar behaviour with $\rho^\mathrm{C}(0)$. In that case $\rho^\mathrm{C}(0)$ was equal for any $J < J_\mathrm{C}$ and for $J > J_\mathrm{C}$. Away from p-h symmetry this will no longer hold, as now the value of $\rho(0)$ varies with J. We therefore calculate $\rho^\mathrm{C}(\omega)$ very close to the transition, at $J/J_\mathrm{C} = 0.999999$ and $J/J_\mathrm{C} = 1.000001$. We plot these cases in figure 5.23a. On the lowest energy scales, $\omega < 10^{-12}$, the system crosses over from the NFL to FL regime, and we obtain an anti-resonance ($J < J_\mathrm{C}$) and resonance ($J > J_\mathrm{C}$). At the anti-resonance we obtain $\pi D\rho^\mathrm{C}(0) = 0.155$ whilst at the resonance $\pi D\rho^\mathrm{C}(0) = 0.854$. The midpoint of these two values, corresponding to $\pi D\rho^\mathrm{C}(0) = 1/2$, is equal to that found at $J = J_\mathrm{C}$ in the model with p-h symmetry. We plot $\rho^\mathrm{C}(\omega)$, at $J = J_\mathrm{C}$, in figure 5.23b for two p-h asymmetric models, and find that this value again appears to be universal. We point out that the values of $\pi\Delta\rho(0)$ and $\pi D\rho^\mathrm{C}(0)$ are interchanged either side of the transition. This suggests that the impurity spectral weight which is lost has 'jumped' to the next conduction site. We speculate that this may lead to a description of the first conduction site as an 'effective impurity' in the p-h asymmetric regime. This was conjectured in [96] for the case with p-h symmetry.

The 1-particle spectral functions suggest some similarities to the p-h symmetric

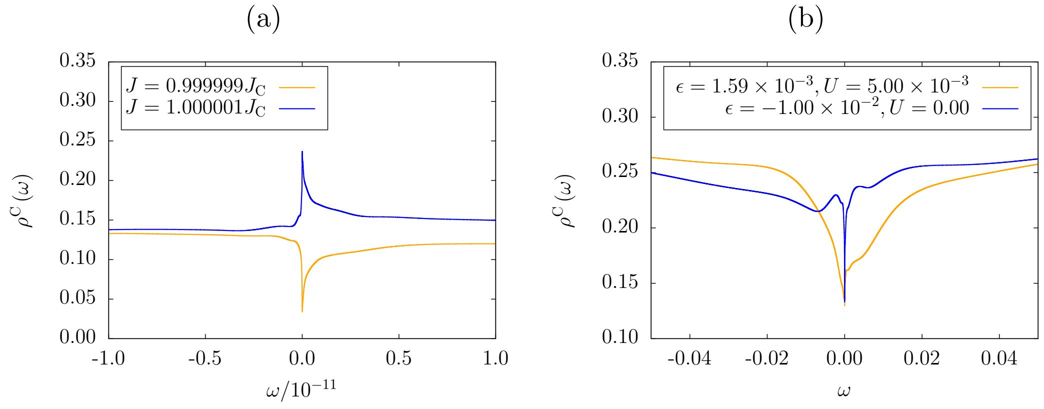

FIGURE 5.23: Plots of $\rho^{\mathrm{C}}(\omega)$ for various models. In (a) we plot $\rho^{\mathrm{C}}(\omega)$ just above and below the transition for the model with parameters $\epsilon = 1.59 \times 10^{-3}, U = 5.00 \times 10^{-3}$. In (b) we plot $\rho^{\mathrm{C}}(\omega)$ at the transition for 2 different models, showing that $\rho^{\mathrm{C}}(0)$ appears to be universal.

model. As J moves across J_{C}, we see a discontinuous loss of spectral density at the Fermi level. Although some spectral density persists at $\omega = 0$ for $J > J_{\mathrm{C}}$, this behaviour is similar to the p-h symmetric model. Interestingly, the behaviour of $\rho(0)$ around the transition is suggestive that the model tries (although fails) to restore the p-h symmetric condition $\rho(0) = 1/\pi\Delta$ when $J < J_{\mathrm{C}}$, as $\rho(0)$ increases as $J \to J_{\mathrm{C}}$. The result $\rho(0) = 0$ is only achieved in the limit $J \to \infty$. We also have that the NFL at $J = J_{\mathrm{C}}$ obeys very similar properties to the p-h symmetric case. We find that the value of $\rho(0)$ and $\rho^{\mathrm{C}}(0)$ take half their values just above and below the transition, and despite that fact that the energy levels differ at the NFL FP in p-h asymmetry, the results $\pi\Delta\rho(0) = {}^1\!/\!_2$ and $\rho^{\mathrm{C}}(0) = 0.137$ are equal to the p-h symmetric values. This suggests that these are universal.

The physics of the QCP, however, appears to be different in the cases of p-h symmetry or asymmetry. In p-h symmetry we had a competition between local singlet and Kondo singlet regimes. In both these regimes, each impurity is occupied by a single electron. The occupancy is fixed by p-h symmetry. Away from p-h symmetry, the occupancy changes ($n \to 2$ as $J \to \infty$). We find that the $\pi/2$ phase shift corresponds to a 2-quasiparticle state being pulled below or above the Fermi level, since $\tilde{\epsilon}$ changes sign. However, we do not find a discontinuous change in the d-electron occupancy across the transition. The d-electron and quasiparticle occupation num-

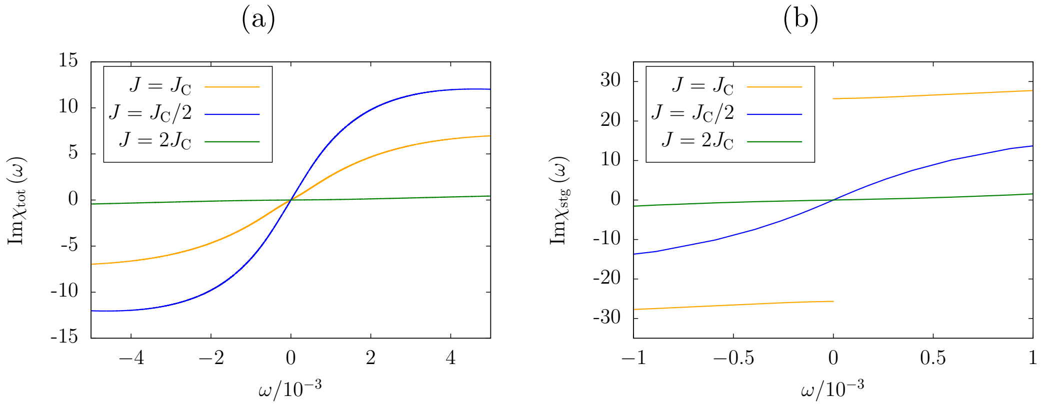

FIGURE 5.24: Plots focusing on the low-energy behaviour of $\mathrm{Im}\chi_\mathrm{tot}(\omega)$ (a) and $\mathrm{Im}\chi_\mathrm{stg}(\omega)$ (b) below, at, and above the transition $J = J_\mathrm{C}$. The model parameters are $\epsilon = 1.59 \times 10^{-3}, U = 5.00 \times 10^{-3}$.

bers are related by $\tilde{n} = n \pm 2$, so that across the transition 2 quasiparticles, bound in what we conjecture to be a singlet state, are localised or liberated. Despite the differing underlying physics, the $\pi/2$ phase shift is universal and the model in both p-h symmetric and asymmetric regimes satisfies the same modified Friedel sum rule.

We now present results for the 2-particle spectral functions, to attempt to clarify our picture of the QCP. We note from [96] that for $J > J_\mathrm{C}$, $\tilde{\Delta} > 0$, implying that z is finite. Since $\tilde{d} = d/\sqrt{z}$, the local susceptibilities in terms of d-electrons are proportional to the corresponding quasiparticle susceptibilities. In figure 5.24, we plot $\mathrm{Im}\chi_\mathrm{tot}(\omega)$ (a) and $\mathrm{Im}\chi_\mathrm{stg}(\omega)$ (b) for the cases $J/J_\mathrm{C} = 1/2, 1, 2$. Noting that the gradient at $\omega = 0$ determines the value of the real part at $\omega = 0$, we see that as J increases, χ_tot becomes suppressed. This is not surprising since, for a large J, the atomic system seeks to be in a singlet; a superposition of the system with oppositely aligned spins. As in the p-h symmetric case, $\chi_\mathrm{tot}(\omega)$ does not diverge at $J = J_\mathrm{C}$. Also in agreement with the p-h symmetric model, $\chi_\mathrm{stg}(\omega)$ diverges at $J = J_\mathrm{C}$, and not when $J \neq J_\mathrm{C}$. This suggests that one of the competing regimes at the QCP is comprised of oppositely aligned spins on the impurities. If our speculation that this 2-quasiparticle state, which rises or falls below the Fermi level, corresponds to the localisation or liberation of a singlet quasiparticle pair is true, then the NFL will be very sensitive to the addition of a singlet state, and the corresponding susceptibility will diverge. We plot in figure 5.25a and 5.25b the singlet and triplet susceptibilities.

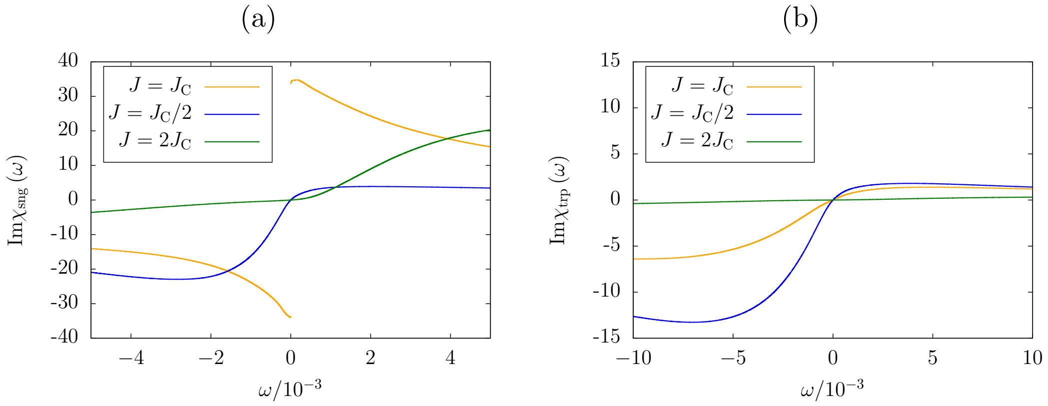

FIGURE 5.25: Plots focusing on the low-energy behaviour of $\mathrm{Im}\chi_\mathrm{sng}(\omega)$ (a) and $\mathrm{Im}\chi_\mathrm{trp}(\omega)$ (b) below, at, and above the transition $J = J_\mathrm{C}$. The model has the same parameters as is figure 5.24.

At $J = J_\mathrm{C}$, we see that $\chi_\mathrm{sng}(\omega)$ diverges, whilst away from J_C it remains finite. Note the very different forms of $\chi_\mathrm{sng}(\omega)$ for $J < J_\mathrm{C}$ and $J > J_\mathrm{C}$. This is due to the fact that the local occupation changes with J, and the area under $\chi_\mathrm{sng}(\omega)$ is equal to $n/2 - 1$. There is no divergence of $\chi_\mathrm{trp}(\omega)$, and above and below the transition the curves also change to reflect the different occupancies. It thus appears that a singlet pair is added or removed as J crosses J_C.

Our study of the QCP away from p-h symmetry has highlighted several similarities and differences to the p-h symmetric model. The NFL FP is described by different, non-universal levels which differ according to the bare parameters. However we recover the anomalous $\ln(2)/2$ entropy and the even-odd oscillations still vanish at the NFL FP. Close to the NFL FP, the levels stabilise (this corresponds to the region where $\rho(0)$ is unchanging) and we find that the odd and even FPs are exchanged above and below the transition. We had also observed this for p-h symmetry. Analysis of the dynamic quantities illustrates that the competing regimes at the QCP are slightly different in the p-h symmetric and asymmetric cases. At p-h symmetry, the values of $\rho(0)$ and $\rho^\mathrm{C}(0)$ were fixed above and below the transition. Away from p-h symmetry, however, these values change with J, and plateau only very close to $J = J_\mathrm{C}$. The discontinuous change in these quantities occurs in a similar manner in both cases, with their values at $J = J_\mathrm{C}$ being universal.

A 2-quasiparticle state is brought above or below the Fermi level. Our susceptibility calculations suggest that this 2-body state is in fact a quasiparticle singlet, and the QCP separates a system with and without this state. This is in contrast to the p-h symmetric model, where the competing regimes were argued to be a Kondo singlet and local singlet. We relate this to the renormalised hybridisation. As discussed in [96], when $J > J_{\mathrm{C}}$, $\tilde{\Delta} = 0$ for p-h symmetry whilst $\tilde{\Delta} \neq 0$ away from p-h symmetry. It follows that just above the transition, the d-site electrons are totally decoupled in the case of p-h symmetry, whilst for p-h asymmetry, there are d-electrons which are not in a singlet and retain the possibility of hopping into the bath. We interpret this as signifying that whilst there are 2 local quasiparticles/holes bound in a singlet, there are also free quasiparticles/holes which may hop into the bath. Further studies are required to fully clarify the underlying physics in this system.

5.9 Relation to the 2CKM

We have investigated the QCP at and away from p-h symmetry, and our results have provided some insight into the similarities and differences between the 2 cases. However, we have not developed any insight into the NFL FP structure, or the anomalous entropy. Recent work [153] has shown an intimate connection between the NFL FP of the 2IKM and 2CKM. Both of these models are well studied, and exact results using the BCFT approach provide the NFL levels/degeneracies. As we discussed in section 5.4, the NFL levels of the 2CKM have been explained by a MF model. We now study the correspondence between the 2IKM and 2CKM. In the next section we shall formulate an MF model for the 2IKM. We enforce p-h symmetry and strong correlation (to obtain a Kondo regime), and to achieve the 2CKM we set $U_2 = 0$. As usual, we take $\pi\Delta_1 = \pi\Delta_2 = \pi\Delta = 0.01$ and $U_{12} = 0$. We are therefore able to continuously move between the 2IKM and 2CKM, by adjusting the ratio U_2/U_1 from 1 to 0 (retaining p-h symmetry). We calculate QCPs for the model with $U_1/\pi\Delta = 10$ and $U_2/U_1 = 0, 0.1, 0.5, 0.9, 1.0$ and give their corresponding values of J_{C} table 5.5. We plot J_{C} against U_2/U_1 in figure 5.26a, and see that $J_{\mathrm{C}} \sim \mathrm{e}^{-U_2/U_1}$. Since J_{C} is indicative of T_{K}, the degree of renormalisation is determined by U_2, with the strongest renormalisation occurring in the channel symmetric model. We also find that the NFL levels and degeneracies are identical for all U_2, as shown in figure 5.26b. This may seem in contrast to the result that

U_1	U_2	J_C
0.10	0.00	$5.08205945 \times 10^{-4}$
0.10	0.01	$2.04835025 \times 10^{-4}$
0.10	0.05	$4.42970400 \times 10^{-6}$
0.10	0.09	$1.50967700 \times 10^{-7}$
0.10	0.10	$7.86416000 \times 10^{-8}$

TABLE 5.5: The calculated values of J_C, to 9 significant figures, for the p-h symmetric, channel asymmetric model with $\pi\Delta = 0.01$.

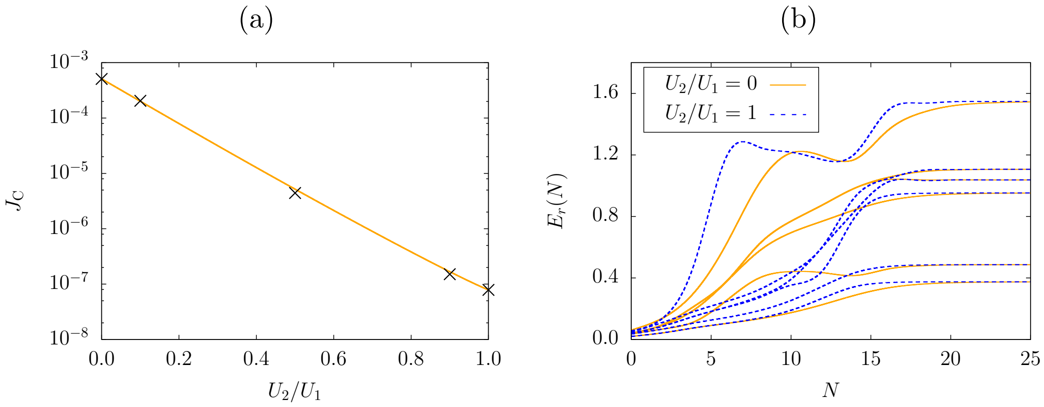

FIGURE 5.26: In (a) we plot J_C as a function of U_2/U_1 for the model where $U_1/\pi\Delta = 10$. (b) shows that the low-lying energy levels are the same for all NFL FPs regardless of the value of U_2. Note that in this plot we take $U_1/\pi\Delta = 6$, where the transition occurs at $J_\mathrm{C} = 9.03119710 \times 10^{-4}$.

the 2CKM model and 2IKM have different energy levels and degeneracies [155, 171], however we argue that the hybridisation between impurity 1 and it's neighbouring conduction electron constitutes a potential scattering. This is because we can have virtual processes involving electrons hopping off the impurity, whilst in the 2CKM, the coupling between these two sites is a Heisenberg one, so these types of processes are not permitted in the bare model. The authors of [153] show that the NFL FPs of the 2CKM, with the addition of potential scattering, and the 2IKM are the same. Our results are in agreement with their work.

We now present calculations of dynamic quantities for the 2IKM, and 2CKM, and initially focus on the 1-particle spectral densities. As we limit $U_2 \to 0$, we expect $T_{\mathrm{K}2}$

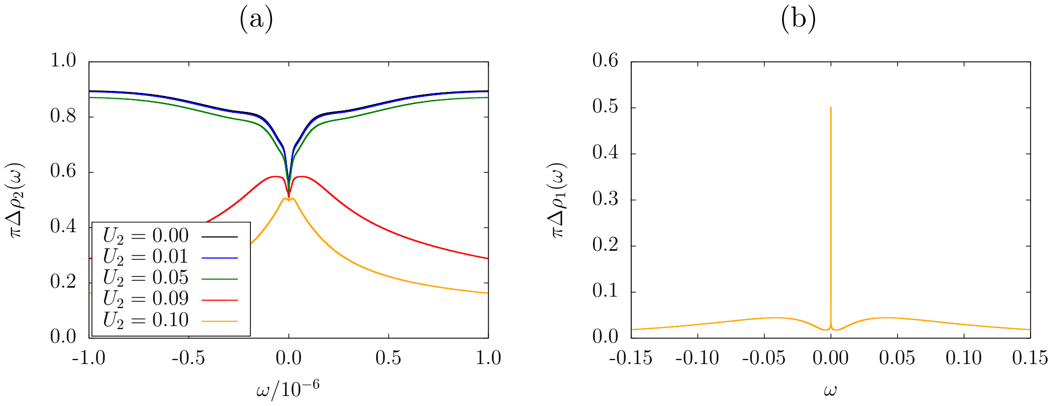

FIGURE 5.27: Plots of the non-interacting (a) and interacting (b) impurity site spectral densities at $J = J_{\mathrm{C}}$. In (a) we consider several values of U_2/U_1 to explicitly show that $\rho_2(0)$ becomes a local minimum for $U_2 \neq U_1$. In (b) we plot only the case $U_2 = 0$, as this spectral density changes very little with U_2.

to increase, since we are moving to the regime of weak correlation. Correspondingly, the peak of $\rho_2(\omega)$ will broaden. However, at $J = J_{\mathrm{C}}$, we expect that $\rho_2(0) = 1/2\pi\Delta$, as we found in all previous cases. This means that $\rho_2(\omega)$ will be dragged down at the Fermi level, such that $\rho_2(0)$ is a local minimum. We plot $\pi\Delta\rho_2(\omega)$, for $J = J_{\mathrm{C}}$, in figure 5.27a and see that when $U_2 = U_1$, where we have the 2IKM, the value of $\rho(0)$ is a local maximum but as soon as this equality is broken then $\rho(0)$ becomes a local minimum, and looks like a conduction site spectral density. Meanwhile, $\rho_1(\omega)$ changes very little with U_2, and we plot it for the case $U_2 = 0$ in figure 5.27b. We also analyse $\rho_1^{\mathrm{C}}(\omega)$ at $J = J_{\mathrm{C}}$, which we plot in figure 5.28. Similar to $\rho_2(\omega)$, there is a well defined local minimum at the Fermi level. The insets show the broad structure of $\rho_1^{\mathrm{C}}(\omega)$ and $\rho_2(\omega)$, clearly showing that they have the same features. We therefore assert that at $J = J_{\mathrm{C}}$, the interacting site has a resonance at the Fermi level, whilst its neighbouring sites have anti-resonances, meaning that we can interpret the system as a single Kondo site (impurity 1) coupled to two conduction baths. Our system thus corresponds to the 2CKM.

Away from $J = J_{\mathrm{C}}$, this peak structure breaks down. For $J < J_{\mathrm{C}}$, both $\rho_1(\omega)$ and $\rho_2(\omega)$ develop peaks at the Fermi level, whilst $\rho_1^{\mathrm{C}}(\omega)$ and $\rho_2^{\mathrm{C}}(\omega)$ are both gapped. We explain this as follows; on the lowest energy scales, the hybridisation V_1 becomes an effective antiferromagnetic Heisenberg coupling $J_{\mathrm{eff}} \sim -V_1^2/U_1$. The QCP

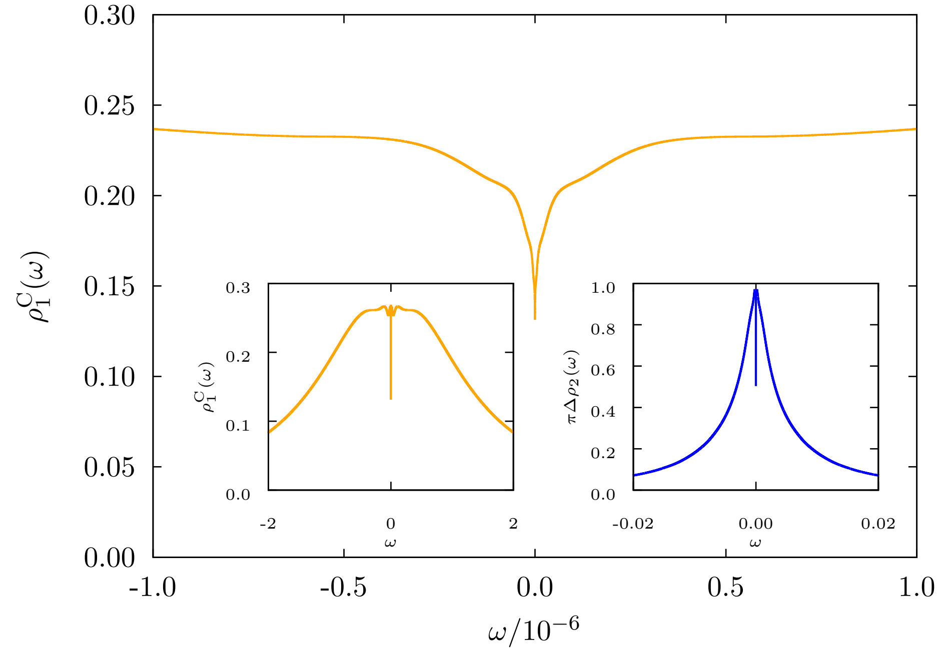

FIGURE 5.28: Plot of $\rho_1^{\mathrm{C}}(\omega)$ at $J = J_{\mathrm{C}}$, showing the formation of a local minimum at $\omega = 0$, where the universal value 0.13 is reached. The insets compare the spectral densities on sites adjacent to the interacting impurity site, showing that they have very similar features.

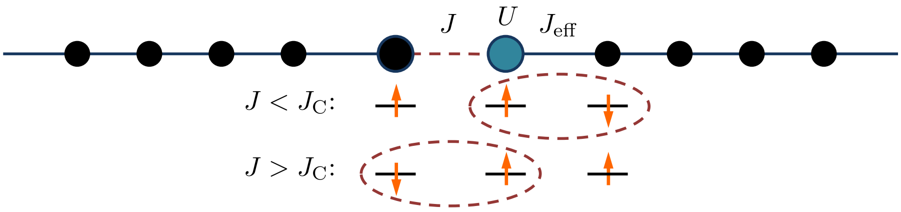

FIGURE 5.29: Schematic of the competing low energy regimes at the $J = J_{\text{C}}$ QCP of the 2IAM whose low energy regime corresponds to the 2CKM. The localised impurity sites are represented by the large circles, with the large black circle corresponding to the non-interacting impurity site. De-localised conduction sites are depicted by the black circles. The singly-occupied levels represent the low energy behaviour of the system, with the electrons enclosed in the red ellipse forming a singlet.

occurs due to the competition between J and J_{eff} resulting in an overscreening of the impurity. When $J < J_{\text{C}}$, the effective Heisenberg term wins, and the impurity forms a Kondo singlet with the first conduction site of the chain it is hybridised to. Therefore a Kondo peak develops in $\rho_1(\omega)$. The non-interacting impurity is then decoupled from the interacting impurity and is the first site in a tight-binding chain of free electrons. It therefore forms a (Lorentzian) peak centred on the Fermi level.

For $J > J_{\text{C}}$, the magnetic coupling between the interacting and non-interacting impurity wins over the hybridisation-induced effective magnetic coupling. We find in this case that both $\rho_1(\omega)$ and $\rho_2(\omega)$ become pseudogapped at the Fermi level whilst the $\rho_1^{\text{C}}(\omega)$ and $\rho_2^{\text{C}}(\omega)$ develop peaks. The impurity sites hence form a singlet, but our non-interacting impurity is a localised level. The singlet is therefore local and the 2 impurities decouple, as in the channel symmetric model considered above. The first conduction sites then develop peaks. We argue that since we have competition between a single interacting site forming a singlet with one of two adjacent conduction sites, as depicted in figure 5.29, our model corresponds to the 2CKM.

We now present 2-particle functions to support our arguments. Since the interacting impurity is overscreened at $J = J_{\text{C}}$, the spins on the chain sites are frustrated. Therefore if one attempts to align the non-interacting impurity sites spin, oppositely or in parallel, with the interacting impurity's spin, this will disrupt the entire spin chains and result in long ranged behaviour. In a departure from the 2IAM/2IKM results, we thus expect both the staggered and total spin susceptibil-

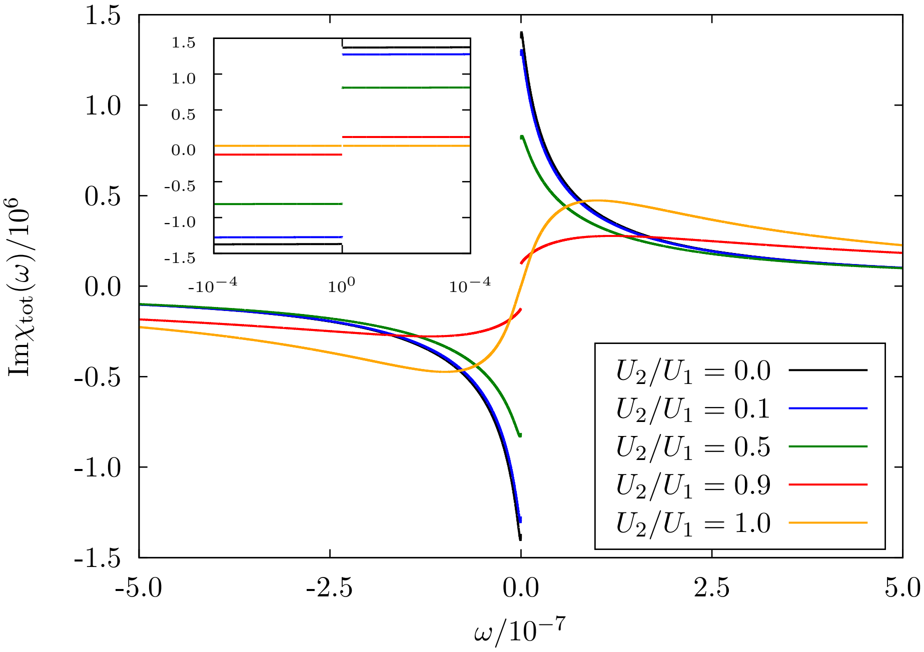

FIGURE 5.30: A plot of $\mathrm{Im}\chi_{\mathrm{tot}}(\omega)$ for models with $0 \leq U_2/U_1 \leq 1$, at the transition $J = J_{\mathrm{C}}$. The inset shows explicitly the low-energy discontinuities/divergences.

ities to diverge. We plot $\mathrm{Im}\chi_{\mathrm{tot}}(\omega)$ in figure 5.30, for several values of U_2/U_1, and see that in the channel symmetric case where $U_2/U_1 = 1$, $\mathrm{Im}\chi_{\mathrm{tot}}(\omega)$ passes smoothly through the Fermi level. However, as soon as $U_2 \neq U_1$ there emerges a discontinuity, implying a divergence in the real part. We note that the 'size' of the divergence, $\mathrm{Im}\chi_{\mathrm{tot}}(\delta^+)-\mathrm{Im}\chi_{\mathrm{tot}}(-\delta^+)$, where $\delta^+ \to 0, \delta > 0$, appears to be approximately proportional to $(U_2 - U_1)/U_1$. We also plot $\mathrm{Im}\chi_{\mathrm{stg}}(\omega)$, in figure 5.31, and see that this diverges for all values of U_2/U_1. Interestingly, the size of the discontinuity appears to increase suddenly when $U_2 = U_1$. These dynamic quantities are in line with our assertion that the NFL FP we are considering is that of the 2CKM. We also consider the singlet and triplet susceptibilities. Since the conduction site in channel 1 and the non-interacting impurity site are competing to form a singlet with the interacting impurity, we expect the singlet susceptibility to diverge. However the triplet susceptibility should not diverge since the formation of a triplet needn't change the spins on the sites, and because the system is not competing to be in a local triplet regime. We plot $\mathrm{Im}\chi_{\mathrm{sng}}(\omega)$ in figure 5.32 and $\mathrm{Im}\chi_{\mathrm{trp}}(\omega)$ in figure 5.33, and see that the singlet susceptibility diverges for all U_2/U_1 whilst the triplet susceptibility does not.

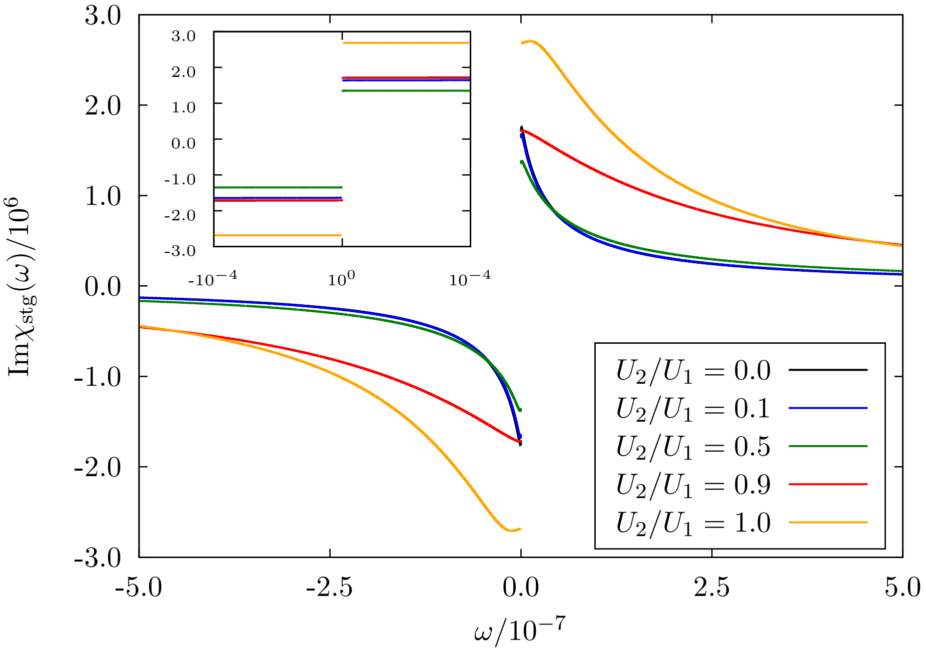

FIGURE 5.31: A plot of $\mathrm{Im}\chi_{\mathrm{stg}}(\omega)$ for models with $0 \leq U_2/U_1 \leq 1$, at the transition $J = J_{\mathrm{C}}$. The inset shows explicitly the low-energy discontinuities/divergences.

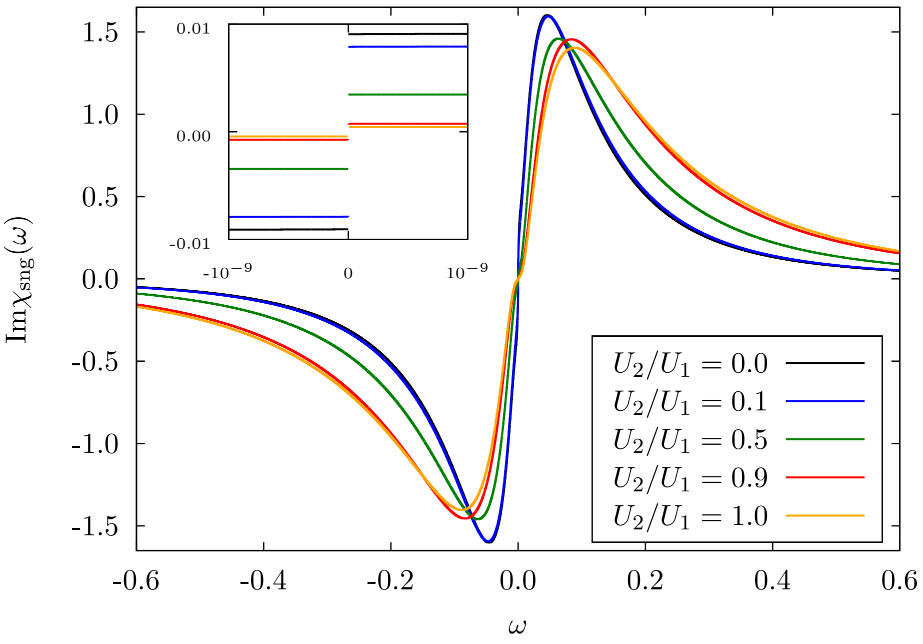

FIGURE 5.32: A plot of $\mathrm{Im}\chi_{\mathrm{sng}}(\omega)$ for models with $0 \leq U_2/U_1 \leq 1$, at the transition $J = J_{\mathrm{C}}$. The inset shows explicitly the low-energy discontinuities/divergences.

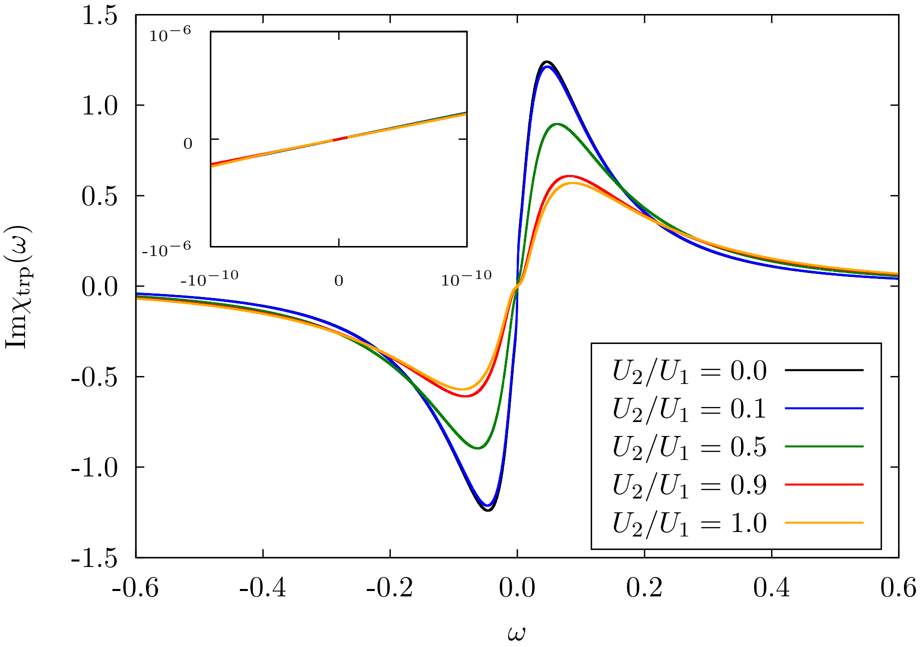

FIGURE 5.33: A plot of $\mathrm{Im}\chi_{\mathrm{trp}}(\omega)$ for models with $0 \leq U_2/U_1 \leq 1$, at the transition $J = J_{\mathrm{C}}$. The inset shows explicitly the low-energy discontinuities/divergences.

We have studied the 2IAM in the p-h symmetric case with $U_2 = 0$ and claimed that the low energy model is equivalent to that of the 2CKM, rather than the 2IKM. We have noted from [153] that the presence of a potential scattering term (in our case a hybridisation which plays the role of an antiferromagnetic exchange interaction on the low energy scale) implies equivalence between the NFL FPs of the 2 models. We have presented dynamic quantities which support this notion. At $J = J_{\mathrm{C}}$, the spectral densities on the sites neighbouring impurity 1 (with local interactions) look very similar, with an anti-resonance (but no gap) at the Fermi level, whilst the spectral density on the interacting impurity is peaked. This then looks like a single impurity hybridised with 2 conduction baths. In this case we would expect the total, staggered and singlet susceptibilities to diverge, and we have shown that this is the case.

Away from $J = J_{\mathrm{C}}$, we note significant differences between our model and the 2CKM. For $J < J_{\mathrm{C}}$, our interacting impurity forms a Kondo singlet with the first conduction electron site, resulting in a Kondo resonance in $\rho_1(\omega)$. The non-interacting impurity is decoupled and $\rho_2(\omega)$ takes a Lorentzian form. Meanwhile, for $J > J_C$, the impurities form a singlet. Here we have a departure from the 2CKM: Our non-interacting impurity is described by a localised level, so that the $J > J_C$ singlet decouples from the bulk (hence $\rho_1(0) = \rho_2(0) = 0$). In the 2CKM, we would expect a Kondo resonance as $\omega \to 0$. We argue that this difference comes down to our additional potential scattering [153]. As expected, away from the NFL FP, there are no divergences of dynamic quantities.

5.10 MF Model for the 2IKM QCP

We have provided evidence supporting the idea that we may obtain the 2CKM NFL FP by making one of the impurities of our p-h symmetric 2IAM/2IKM non-interacting. This is a significant result because there is a description, in terms of MFs, which accurately reproduces the NFL excitation levels and degeneracies of the 2CKM NFL FP [156], whilst such a description does not exist for the 2IKM. A model like this is desirable because the anomalous entropy suggests the presence of a free (or decoupled) MF. In this section we draw upon the MF description of the 2CKM to propose an MF model underlying the 2IKM NFL FP, or equivalently the NFL FP of the 2IAM at p-h symmetry.

We first establish that our results at p-h symmetry are consistent with the 2IKM. BCFT studies of the 2IKM QCP have provided the energy levels of the NFL FP [155], which we provide in table 5.6. The energies are in units of $\pi v_F/l$. We can establish equivalence with these values by limiting our NRG calculations to the continuum $\Lambda = 1$. In practice, we can only go down to $\Lambda = 2.5$ because the NFL FP is unstable, and as one decreases Λ, a larger number of states must be retained at each iteration of the NRG. We scale our energy levels such that the first level is equal to $^3/_8$. Higher energy levels should therefore be equal to the values in table 5.6 as $\Lambda \to 1$. We plot our scaled low-lying energies as a function of Λ in figure 5.34 for the p-h symmetric model. The energy levels approach the values given by the BCFT as we expect, and for $\Lambda = 2.5$ we also find agreement with the degeneracies from the NRG.

Given the agreement, we are in a position to propose an MF model for the 2IKM NFL FP. We note from [155] the emergence of an SO(7) symmetry, and from our discussions in section 5.3 that we expect a basis of 8 MFs. In the 2CKM, where

Energy	Degeneracy
0	1
$^3/_8$	8
$^1/_2$	7
$^7/_8$	8
1	22
$^{11}/_8$	56
$^3/_2$	49
$^{15}/_8$	64

TABLE 5.6: The low-lying energy levels of the 2IKM at the NFL FP, calculated by BCFT [155]. The energies are in terms of a scale set by the Fermi velocity. We also include the degeneracies, which arise from the quantum numbers associated to various species of spin and isospin. In the original work [155], the states are labelled by spin j and 2 flavours of isospin i_1, i_2, due to an SU(2)⊗SU(2)⊗SU(2) symmetry. The degeneracy of each state is given by $(2i_1 + 1)(2i_2 + 1)(2j + 1)$.

there is an SO(5) symmetry, the MF model was formulated by combining sets of 5 antiperiodic MFs with 3 periodic. We hence consider a set of 8 MFs, where 1 has periodic boundary conditions and the remaining 7 have anti-periodic boundary conditions. We name this system sector I, noting that the ground state degeneracy is correct. As with the 2CKM, we must construct a sector II, comprised of sets of 8 MFs where 7 are periodic and 1 is antiperiodic. These will correspond to the energies shifted by $^3/_8$, so the ground state is offset from the ground state of sector I by this amount. We note from table 5.6 that the degeneracy of the state with energy $^3/_8$ is 8, so we have 8 sets in sector II. The combination of these sectors is illustrated in figure 5.35, and we show in table 5.7 how we can build the NFL energy levels and degeneracies from this model. This MF model reproduces the correct spectrum, and we are now in a position to offer an interpretation of the anomalous $\ln(2)/2$ entropy, indicative of a single unhybridised MF, we see in the 2IKM.

Our calculations of dynamic quantities, in the case of the p-h symmetric 2IAM, indicate that at the QCP the system ground state is competing between 2 regimes. For $J < J_{\mathrm{C}}$, the ground state is 2 uncoupled many-body Kondo singlets, formed between the impurities and their adjacent baths. We denote this ground state $|\mathrm{KS}\rangle$. Meanwhile, for $J > J_{\mathrm{C}}$, the ground state is a local 2-body singlet, formed between

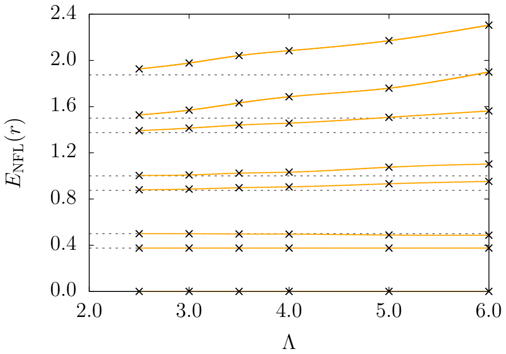

FIGURE 5.34: The levels at the NFL FP, denoted $E_{\mathrm{NFL}}(r)$, in the continuum limit $\Lambda \to 1$ of the 2IKM. The dashed lines represent the values obtained from a BCFT analysis [155], which are given with their degeneracies in table 5.6.

the impurities. This ground state is to be called $|\mathrm{LS}\rangle$. At $J = J_{\mathrm{C}}$, the ground state must be a combination of $|\mathrm{KS}\rangle$ and $|\mathrm{LS}\rangle$. We identify a possible excitation between these ground states as a Majorana zero mode

$$\chi = \frac{1}{\sqrt{2}} |\mathrm{LS}\rangle \langle\mathrm{KS}| + \frac{1}{\sqrt{2}} |\mathrm{KS}\rangle \langle\mathrm{LS}| \tag{5.10.1}$$

which is Hermitian and satisfies $\chi^2 = 1/2$. The excitations of the system are given by the eigenoperators of the Liouville operator $\mathcal{L}$, where $\mathcal{L}O = [H, O]$. We expect that $\mathcal{L}\chi = 0$, which would imply that χ is a zero mode excitation. This mode would be responsible for driving the system between the competing ground states, and gives rise to the residual entropy which is due to topological entanglement [182]. The entropy contribution associated with Majorana zero modes is well known to be $\ln(2)/2$ [183].

The Majorana zero mode occurring in the 2IKM is likely to be very similar to the mechanism which gives the anomalous entropy in other impurity systems. Away from p-h symmetry, we are currently unable to propose a MF model, but we speculate that a zero mode akin to χ is present in the system. This mode would drive excitations between a system with and without a localised quasiparticle singlet. Similarly, in the 2CKM model, the excitation would be between Kondo singlets formed with each channel.

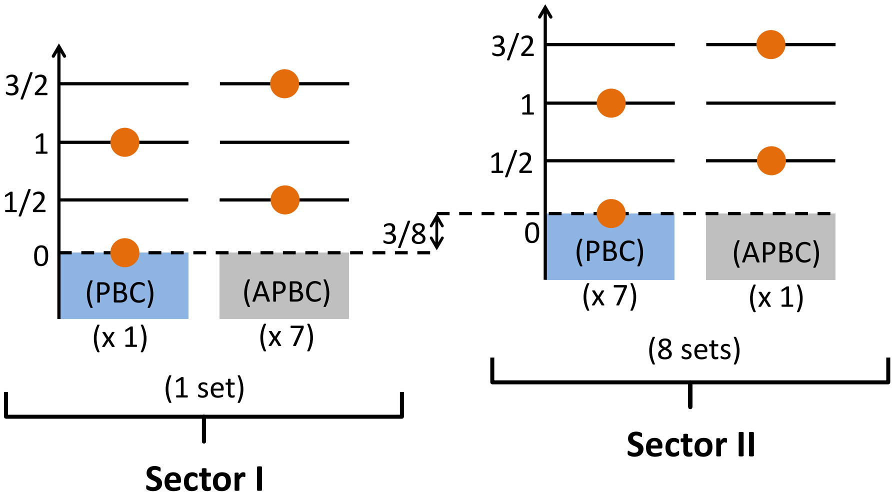

FIGURE 5.35: MF model of the 2IKM NFL FP. Only energy levels with a circle may be occupied, and the 2 sectors act independently to describe the levels $0, {}^1/_2, 1$ etc (sector I) and ${}^3/_8, {}^7/_8, {}^{11}/_8$ etc (sector II). Energies are in units of $\pi v_\mathrm{F}/l$.

E_NFL	Sector	$\sum n_E[E]$	Degeneracy	Total Degeneracy
0	I	$1[0]$	1	1
${}^3/_8$	II	$7[0]$	1×8	8
${}^1/_2$	I	$1[{}^1/_2]$	7	7
${}^7/_8$	II	$1[{}^1/_2]$	1×8	8
1	I	$1[1]$	1	
		$2[{}^1/_2]$	$\binom{7}{2}$	22
${}^{11}/_8$	II	$1[1]$	7×8	56
${}^3/_2$	I	$1[{}^3/_2]$	7	
		$3[{}^1/_2]$	$\binom{7}{3}$	
		$1[1] + 1[{}^1/_2]$	7	49
${}^{15}/_8$	II	$1[{}^3/_2]$	1×8	
		$1[1] + 1[{}^1/_2]$	7×8	64

TABLE 5.7: The combinations of MFs which correspond to the 2IKM NFL FP energies and degeneracies.

5.11 Conclusions

We have studied the NFL QCP of the 2IAM in regimes with and without various symmetries. We began our investigation with the channel symmetric and p-h symmetric model, which on low energy scales is equivalent to the 2IKM. In line with previous studies, we found a disappearance of the even/odd oscillations of the NRG levels at the NFL FP, which accompanied the emergence of a residual entropy contribution of $\ln(2)/2$. We calculated the 1-particle spectral densities of the impurity and conduction electrons. In the $J > J_{\mathrm{C}}$ regime $\rho(\omega)$ showed the formation of a 2-peak pseudogapped structure replacing the Kondo resonance for $J < J_{\mathrm{C}}$. We interpret the separation between the 2 peaks as the binding energy of a local singlet on the impurity sites. Meanwhile, $\rho^{\mathrm{C}}(\omega)$ developed a peak at the Fermi level, with $\pi D\rho^{\mathrm{C}}(0) = 1$. This is indicative of it becoming an 'effective impurity,' as was conjectured in [96]. The 1-particle functions give rise to the picture that the QCP separates a Kondo and local singlet regime. The 2-particle functions at $J = J_{\mathrm{C}}$ showed that the susceptibilities which could result in the formation of a singlet diverge, providing evidence for this picture. We also note the intriguing property that $\pi\Delta\rho(0) = \pi D\rho^{\mathrm{C}}(0) = 1/2$ at $J = J_{\mathrm{C}}$, which we suggest signifies the takeover of the conduction site as an effective impurity.

The picture away from p-h symmetry appears to be more complicated. We find the same disappearance of even/odd oscillations, exchange of odd and even FPs, and anomalous entropy as in the p-h symmetric model, but the key differences emerge from the fact that the local occupation is no longer constrained to 1 on each impurity. This is only achieved asymptotically in the limit $J \to \infty$. For $J > J_{\mathrm{C}}$ an antiresonance emerges close to the Fermi level in addition to a quasiparticle peak (which occurs on the other side of the Fermi level). This is similar to the p-h symmetric model, but there is no pseudogap (as $J \to \infty$ a pseudogap forms at the Fermi level). We find that $\tilde{\epsilon}$ changes sign across the transition, which signifies that a 2-quasiparticle state is localised or liberated. This change in quasiparticle occupation is not reflected in a redistribution of d-electron spectral weight, and is explained by a $\pi/2$ phase shift across the transition which results in a modified Friedel sum rule and implies that $\tilde{n} = n \pm 2$. The modified relations hold for both the p-h symmetric and asymmetric models. We conjecture that the 2-quasiparticle state is a singlet, and this is supported by the 2-particle functions we calculated. A significant similarity to the p-h symmetric model, however, is that $\pi\Delta\rho(0) = \pi D\rho^{\mathrm{C}}(0) = 1/2$ at $J = J_{\mathrm{C}}$, and either side of J_{C}, the lost spectral weight of $\rho(\omega)$ at the Fermi level has 'jumped' to the conduction site. In a departure to the observations of [96], but in a consistent manner with p-h symmetry, we thus conjecture that for $J > J_{\mathrm{C}}$ the conduction site acts as an effective impurity. The physical picture, in terms of d-electrons, is thus not clear. We know that there is a formation of a local singlet on one side of the transition, but there are not necessarily enough electrons to actually form it. Also, for $J > J_{\mathrm{C}}$, d-electrons remain hybridised to the bath, so the singlet may appear to be non-local. We conjecture that 2 quasiparticles/quasiholes are localised, while others, which are also present on the impurity sites, are hybridised. Further work is required to clarify this picture.

In the p-h symmetric model with channel anisotropy, we study the connection between the 2IKM and 2CKM. In agreement with [153] we find that the NFL FPs are equivalent as we tune U_2 from $U_2 = U_1$ (2IKM) to $U_2 = 0$ (2CKM). This is due to the potential scattering (hybridisation) present in our bare model. Our calculation of dynamic quantities shows that at $J = J_{\mathrm{C}}$, we obtain a peak structure in the spectral densities which indicates that our model corresponds to the 2CKM. In particular, the peaked interacting impurity is coupled to 2 sites with anti-resonances at the Fermi level. Moreover, we have shown a divergence in both the staggered and total spin susceptibilities which also agrees with the claim that the model is equivalent to the 2CKM.

The observation that we may obtain the 2CKM from the 2IKM is significant because there exists a model in terms of MFs which explains the NFL levels of the 2CKM [156]. The anomalous entropy, which is suggestive of a free MF mode, that emerges in several quantum impurity models has yet to be explained. A first step to understanding the entropy is to explain the NFL FP spectra of the models in terms of MFs. We construct such a model for the 2IKM, and conjecture that the $\ln(2)/2$ entropy is due to a Majorana zero mode. This would allow the system to 'jump' between the competing ground states with no energy, with a similar mechanism for the 2CKM and p-h asymmetric 2IAM.

There is much work to be done to find a unified picture of the QCP of the 2IAM/2IKM and 2CKM. We need to clarify the underlying physics away from p-h symmetry. It is likely that study of the p-h asymmetric 2 channel Anderson model would help in this goal, as this could be compared with the 2CKM. There are still open questions regarding the free MF mode which appears in our models. To explain the anomalous entropy we must show that the inter-ground-state excitation χ is a zero mode. It would also be interesting to understand the role of topology in the QCPs. The emergent fractional entropy indicates that topology is important, and the possible presence of Majorana zero modes leads one to ask whether coupled/overscreened impurities could be used to construct a topological quantum computer.

References

[1] A. Taraphder and P. Coleman (1991) **Phys. Rev. Lett.** **66**, 2814–2817.

[2] N. S. Vidhyadhiraja (2007) **Europhys. Lett.** **77(3)**, 36001.

[3] S. M. Cronenwett, T. H. Oosterkamp, and L. P. Kouwenhoven (1998) **Science** **281(5376)**, 540–544.

[4] T. Lobo, M. S. Figueira, and M. S. Ferreira (2006) **Braz. J. Phys.** **36**, 401 – 404.

[5] J. M. Maldacena and A. W. Ludwig (1997) **Nucl. Phys. B** **506(3)**, 565 – 588.

[6] S. D. Sarma, M. Freedman, and C. Nayak (2015) **Npj Quantum Information** **1**, 15001.

[7] W. de Haas, J. de Boer, and G. van den Berg (1934) **Physica** **1(7)**, 1115 – 1124.

[8] W. D. Haas and G. van den Berg (1937) **Physica** **4(8)**, 683 – 694.

[9] W. F. Giauque, J. W. Stout, and C. W. Clark (1937) **Phys. Rev.** **51**, 1108–1108.

[10] J. W. Stout and R. E. Barieau (1939) **J. Am. Chem. Soc.** **61(2)**, 238–241.

[11] D. MacDonald and I. Templeton (1951) **Philos. Mag.** **42(327)**, 432–434.

[12] M. P. Sarachik, E. Corenzwit, and L. D. Longinotti (1964) **Phys. Rev.** **135**, A1041–A1045.

[13] C. Zener (1951) **Phys. Rev.** **81**, 440–444.

[14] T. Kasuya (1956) **Prog. Theor. Phys.** **16(1)**, 45–57.

[15] J. Kondo (1964) **Prog. Theor. Phys.** **32(1)**, 37–49.

[16] A. A. Abrikosov (1965) **Physics** **2**, 5–20.

[17] P. W. Anderson (1970) **J. Phys. C: Solid State Phys.** **3(12)**, 2436.

[18] D. J. Gross and F. Wilczek (1973) **Phys. Rev. Lett.** **30**, 1343–1346.

[19] H. D. Politzer (1973) **Phys. Rev. Lett.** **30**, 1346–1349.

[20] I. Affleck and A. W. Ludwig (1991) **Nucl. Phys. B** **352(3)**, 849 – 862.

[21] K. G. Wilson (1975) **Rev. Mod. Phys.** **47**, 773–840.

[22] K. G. Wilson (1975) **Adv. Math.** **16(2)**, 170 – 186.

[23] R. Bulla, T. A. Costi, and T. Pruschke (2008) **Rev. Mod. Phys.** **80**, 395–450.

[24] H. R. Krishna-murthy, J. W. Wilkins, and K. G. Wilson (1980) **Phys. Rev. B** **21**, 1003–1043.

[25] H. R. Krishna-murthy, J. W. Wilkins, and K. G. Wilson (1980) **Phys. Rev. B** **21**, 1044–1083.

[26] B. A. Jones and C. M. Varma (1987) **Phys. Rev. Lett.** **58**, 843–846.

[27] C. A. Paula, M. F. Silva, and L. N. Oliveira (1999) **Phys. Rev. B** **59**, 85–88.

[28] D. M. Cragg, P. Lloyd, and P. Nozieres (1980) **J. Phys. C: Solid State Phys.** **13(5)**, 803.

[29] M. Koga and D. L. Cox (1999) **Phys. Rev. Lett.** **82**, 2575–2578.

[30] A. K. Mitchell, M. R. Galpin, S. Wilson-Fletcher, D. E. Logan, and R. Bulla (2014) **Phys. Rev. B** **89**, 121105.

[31] T. A. Costi and A. C. Hewson (1992) **Philos. Mag. B** **65(6)**, 1165–1170.

[32] T. A. Costi, A. C. Hewson, and V. Zlatic (1994) **J. Phys. Condens. Matter** **6(13)**, 2519.

[33] H. O. Frota and L. N. Oliveira (1986) **Phys. Rev. B** **33**, 7871–7874.

[34] O. Sakai, Y. Shimizu, and T. Kasuya (1989) **J. Phys. Soc. Jpn.** **58(10)**, 3666–3678.

[35] W. Hofstetter (2000) **Phys. Rev. Lett.** **85**, 1508–1511.

[36] R. Peters, T. Pruschke, and F. B. Anders (2006) **Phys. Rev. B** **74**, 245114.

[37] A. Weichselbaum and J. von Delft (2007) **Phys. Rev. Lett.** **99**, 076402.

[38] J. Ferreira, A. Ferreira, A. Leite, and V. Lbero (2012) **J. Magn. Magn. Mater.** **324(6)**, 1011 – 1016.

[39] S. Yotsuhashi and H. Maebashi (2002) **J. Phys. Soc. Jpn.** **71(7)**, 1705–1711.

[40] A. Hewson, A. Oguri, and D. Meyer (2004) **Eur. Phys. J. B** **40(2)**, 177–189.

[41] V. H. Tran, D. Kaczorowski, R. T. Khan, and E. Bauer (2011) **Phys. Rev. B** **83**, 064504.

[42] R. Žitko (2011) **Phys. Rev. B** **83**, 195137.

[43] K. G. Wilson (1971) **Phys. Rev. B** **4**, 3174–3183.

[44] K. G. Wilson (1971) **Phys. Rev. B** **4**, 3184–3205.

[45] K. G. Wilson and J. Kogut (1974) **Phys. Rep.** **12(2)**, 75 – 199.

[46] F. J. Wegner (1972) **Phys. Rev. B** **5**, 4529–4536.

[47] A. Altland and B. Simons (2006) Condensed Matter Field Theory, **Cambridge University Press** first edition.

[48] M. E. Fisher (1974) **Rev. Mod. Phys.** **46**, 597–616.

[49] J. Cardy (2008) **arXiv** (0807.3472).

[50] M. A. Continentino (2011) **Braz. J. Phys.** **41(2)**, 201–211.

[51] P. W. Anderson (1961) **Phys. Rev.** **124**, 41–53.

[52] J. R. Schrieffer and P. A. Wolff (1966) **Phys. Rev.** **149**, 491–492.

[53] R. Bulla, T. Pruschke, and A. Hewson (1997) **J. Phys. Condens. Matter** **9**, 10463–10474.

[54] A. C. Hewson (2001) **J. Phys. Condens. Matter 13(44)**, 10011.

[55] P. Wiegmann (1980) **Phys. Lett. A 80(2)**, 163 – 167.

[56] N. Kawakami and A. Okiji (1981) **Phys. Lett. A 86(9)**, 483 – 486.

[57] J. Friedel (1952) **Philos. Mag. 43(337)**, 153–189.

[58] J. Friedel (1956) **Can. J. Phys. 34(12A)**, 1190–1211.

[59] A. Hewson (1997) The Kondo Problem to Heavy Fermions, **Cambridge University Press** first (paperback) edition.

[60] D. C. Langreth (1966) **Phys. Rev. 150**, 516–518.

[61] E. Miranda (2003) **Braz. J. Phys. 33**, 3 – 35.

[62] I. Afflect (1995) **Acta Phys. Pol. B 26**, 1869–1932.

[63] D. L. Cox and A. Zawadowski (1998) **Adv. Phys. 47(5)**, 599–942.

[64] H. Grabert **Z. Phys. B: Condens. Matter 85(3)**, 319–325.

[65] M. H. Devoret and H. Grabert (1992) In: Single Charge Tunneling: Coulomb Blockade Phenomena In Nanostructures **Springer US** 1–19.

[66] Y. Nagamune, H. Sakaki, L. P. Kouwenhoven, L. C. Mur, C. J. P. M. Harmans, J. Motohisa, and H. Noge (1994) **App. Phys. Lett. 64(18)**, 2379–2381.

[67] P. Lafarge, H. Pothier, E. R. Williams, D. Esteve, C. Urbina, and M. H. Devoret (1991) **Z. Phys. B: Condens. Matter 85(3)**, 327–332.

[68] L. I. Glazman and R. I. Shekhter (1989) **J. Phys. Condens. Matter 1(33)**, 5811.

[69] D. Goldhaber-Gordon, H. Shtrikman, D. Mahalu, D. Abusch-Magder, U. Meirav, and M. A. Kastner (1998) **Nat. Phys. 391**, 156–159.

[70] P. Harrison (2010) Quantum Wells, Wires and Dots, **Wiley** 3 edition.

[71] O. B. Shchekin and D. G. Deppe (2002) **App. Phys. Lett. 80(18)**, 3277–3279.

[72] D. L. Huffaker, G. Park, Z. Zou, O. B. Shchekin, and D. G. Deppe (1998) **App. Phys. Lett. 73(18)**, 2564–2566.

[73] N. N. Ledentsov (2011) **Semicond. Sci. Technol.** **26(1)**, 014001.

[74] A. Nozik (2002) **Physica E** **14(12)**, 115 – 120.

[75] P. V. Kamat (2008) **J. Phys. Chem. C** **112(48)**, 18737–18753.

[76] D. E. Reiter, T. Kuhn, and V. M. Axt (2009) **Phys. Rev. Lett.** **102**, 177403.

[77] L. Zhuang, L. Guo, and S. Y. Chou (1998) **App. Phys. Lett.** **72(10)**, 1205–1207.

[78] L. Kouwenhoven and L. Glazman (2001) **Phys. World** **14(1)**, 33.

[79] K. Le Hur (2015) **Nat. Phys.** **526**, 203–204.

[80] Y. Meir and N. S. Wingreen (1992) **Phys. Rev. Lett.** **68**, 2512–2515.

[81] L. Kouwenhoven, C. Marcus, P. McEuen, S. Tarucha, R. Westervelt, and N. Wingreen (1997) In: Proceedings of the NATO Advanced Study Institute on Mesoscopic Electron Transport **Springer** 105–214.

[82] U. Wilhelm, J. Schmid, J. Weis, and K. v. Klitzing (2001) **Physica E** **9(4)**, 625 – 630.

[83] U. Wilhelm, J. Schmid, J. Weis, and K. Klitzing (2002) **Physica E** **14(4)**, 385 – 390.

[84] J. Bork, Y.-h. Zhang, L. Diekhoner, L. Borda, P. Simon, J. Kroha, P. Wahl, and K. Kern (2011) **Nat. Phys.** **7(11)**, 901–906.

[85] M. R. Galpin, D. E. Logan, and H. R. Krishnamurthy (2005) **Phys. Rev. Lett.** **94**, 186406.

[86] A. Hübel, K. Held, J. Weis, and K. v. Klitzing (2008) **Phys. Rev. Lett.** **101**, 186804.

[87] A. Messiah (1999) Quantum Mechanics, **Dover Publications** first (unabridged reprint) edition.

[88] E. U. Condon and G. H. Shortley (1935) The Theory of Atomic Spectra, **Cambridge University Press** first edition.

[89] H. B. Pang and D. L. Cox (1991) **Phys. Rev. B** **44**, 9454–9457.

[90] L. N. Oliveira and J. W. Wilkins (1981) **Phys. Rev. B** **24**, 4863–4866.

[91] R. Bulla, T. A. Costi, and D. Vollhardt (2001) **Phys. Rev. B** **64**, 045103.

[92] F. B. Anders and A. Schiller (2005) **Phys. Rev. Lett.** **95**, 196801.

[93] F. B. Anders and A. Schiller (2006) **Phys. Rev. B** **74**, 245113.

[94] V. L. Campo and L. N. Oliveira (2005) **Phys. Rev. B** **72**, 104432.

[95] D. J. G. Crow (2013) **Imperial College London** PhD thesis.

[96] Y. Nishikawa, D. J. G. Crow, and A. C. Hewson (2012) **Phys. Rev. B** **86**, 125134.

[97] Y. Nishikawa, D. J. G. Crow, and A. C. Hewson (2010) **Phys. Rev. B** **82**, 245109.

[98] Y. Nishikawa, D. J. G. Crow, and A. C. Hewson (2010) **Phys. Rev. B** **82**, 115123.

[99] A. C. Hewson (1993) **Phys. Rev. Lett.** **70**, 4007–4010.

[100] A. A. Abrikosov and I. M. Khalatnikov (1959) **Rep. Prog. Phys.** **22**, 329–367.

[101] L. Landau (1956) **J. Exp. Theor. Phys.** **3(6)**, 1058.

[102] J. M. Luttinger (1961) **Phys. Rev.** **121**, 942–949.

[103] H. Shiba (1975) **Prog. Theor. Phys.** **54(4)**, 967–981.

[104] A. Yoshimori (1976) **Prog. Theor. Phys.** **55(1)**, 67–80.

[105] H. Ishii and K. Yosida (1967) **Prog. Theor. Phys.** **38(1)**, 61–71.

[106] J. Bauer (2007) **Imperial College London** PhD thesis.

[107] R. Mattuck (1992) A Guide to Feynman Diagrams in the Many-body Problem, **Dover** second edition.

[108] Y. Nishikawa, D. J. G. Crow, and A. C. Hewson (2012) **Phys. Rev. Lett.** **108**, 056402.

[109] Y. Nishikawa, O. J. Curtin, A. C. Hewson, D. J. G. Crow, and J. Bauer (2016) **Phys. Rev. B** **93**, 235115.

[110] M. Dzero, K. Sun, V. Galitski, and P. Coleman (2010) **Phys. Rev. Lett.** **104**, 106408.

[111] D. J. Kim, J. Xia, and Z. Fisk (2014) **Nat. Mater.** **13(5)**, 466–470.

[112] Q. Si and S. Paschen (2013) **Phys. Status Solidi B** **250(3)**, online access.

[113] W. G. van der Wiel, S. D. Franceschi, T. Fujisawa, J. M. Elzerman, S. Tarucha, and L. P. Kouwenhoven (2000) **Science** **289(5487)**, 2105–2108.

[114] A. Kogan, S. Amasha, D. Goldhaber-Gordon, G. Granger, M. A. Kastner, and H. Shtrikman (2004) **Phys. Rev. Lett.** **93**, 166602.

[115] F. B. Anders, D. E. Logan, M. R. Galpin, and G. Finkelstein (2008) **Phys. Rev. Lett.** **100**, 086809.

[116] A. Makarovski, A. Zhukov, J. Liu, and G. Finkelstein (2007) **Phys. Rev. B** **75**, 241407.

[117] A. Makarovski, J. Liu, and G. Finkelstein (2007) **Phys. Rev. Lett.** **99**, 066801.

[118] P. Jarillo-Herrero, J. Kong, H. S. J. van der Zant, C. Dekker, L. P. Kouwenhoven, and S. De Franceschi (2005) **Nat. Phys.** **434(7032)**, 484–488.

[119] L. Borda, G. Zaránd, W. Hofstetter, B. I. Halperin, and J. von Delft (2003) **Phys. Rev. Lett.** **90**, 026602.

[120] K. Le Hur, P. Simon, and D. Loss (2007) **Phys. Rev. B** **75**, 035332.

[121] T. Sato and M. Eto (2005) **Physica E** **29(34)**, 652 – 655.

[122] C. A. Büsser, A. E. Feiguin, and G. B. Martins (2012) **Phys. Rev. B** **85**, 241310.

[123] A. J. Keller, S. Amasha, I. Weymann, C. P. Moca, I. G. Rau, J. A. Katine, H. Shtrikman, G. Zarand, and D. Goldhaber-Gordon (2014) **Nat. Phys.** **10(2)**, 145–150.

[124] Y. Nishikawa, A. C. Hewson, D. J. G. Crow, and J. Bauer (2013) **Phys. Rev. B** **88**, 245130.

[125] L. Tosi, P. Roura-Bas, and A. A. Aligia (2015) **J. Phys. Condens. Matter** **27(33)**, 335601.

[126] S. Amasha, A. J. Keller, I. G. Rau, A. Carmi, J. A. Katine, H. Shtrikman, Y. Oreg, and D. Goldhaber-Gordon (2013) **Phys. Rev. Lett.** **110**, 046604.

[127] M. R. Galpin, D. E. Logan, and H. R. Krishnamurthy (2006) **J. Phys. Condens. Matter** **18(29)**, 6545.

[128] Z. Iftikhar, S. Jezouin, A. Anthore, U. Gennser, F. D. Parmentier, A. Cavanna, and F. Pierre (2015) **Nat. Phys.** **526(7572)**, 233–236.

[129] A. J. Keller, L. Peeters, C. P. Moca, I. Weymann, D. Mahalu, V. Umansky, G. Zarand, and D. Goldhaber-Gordon (2015) **Nat. Phys.** **526(7572)**, 237–240.

[130] S. Hershfield, J. H. Davies, and J. W. Wilkins (1991) **Phys. Rev. Lett.** **67**, 3720–3723.

[131] V. T. Rajan (1983) **Phys. Rev. Lett.** **51**, 308–311.

[132] F. Mandl (1988) Statistical Physics, **Wiley** second edition.

[133] M. A. Anisimov, J. V. Sengers, and J. M. L. Sengers (2004) In: Aqueous Systems at Elevated Temperatures and Pressures **Academic Press** 29 – 71.

[134] S. Sachdev and B. Keimer (2011) **Phys. Today** **64**, 29.

[135] S. Sachdev (2011) Quantum Phase Transitions, **Cambridge University Press** first edition.

[136] M. E. Peskin and D. V. Schroeder (2005) An Introduction to Quantum Field Theory, **Levant Books** first indian edition.

[137] E. Majorana and L. Maiani (2006) In: Ettore Majorana Scientific Papers: On occasion of the centenary of his birth **Springer Berlin Heidelberg** 201–233.

[138] B. Kayser (2009) **arXiv** (0903.0899).

[139] J. Alicea, Y. Oreg, G. Refael, F. von Oppen, and M. P. A. Fisher (2011) **Nat. Phys.** **7(5)**, 412–417.

[140] J. Fröhlich and F. Gabbiani (1990) **Rev. Math. Phys.** **02(03)**, 251–353.

[141] A. Kitaev (2003) **Ann. Phys.** **303(1)**, 2 – 30.

[142] A. Y. Kitaev (2001) **Phys. Usp.** **44(10S)**, 131.

[143] A. C. Hewson and V. Zlatic (2003) Concepts in Electron Correlation, In: Nato Science **2(110)**, **Springer Netherlands**.

[144] P. Coleman (2015) Introduction to Many-Body Physics, **Cambridge University Press**.

[145] P. Nozières and A. Blandin (1980) **J. Phys.** **41(3)**, 193–211.

[146] N. Andrei and C. Destri (1984) **Phys. Rev. Lett.** **52**, 364–367.

[147] V. J. Emery and S. Kivelson (1992) **Phys. Rev. B** **46**, 10812–10817.

[148] A. M. Sengupta and A. Georges (1994) **Phys. Rev. B** **49**, 10020–10022.

[149] I. Affleck (1990) **Nucl. Phys. B** **336(3)**, 517 – 532.

[150] I. Affleck and A. W. Ludwig (1991) **Nucl. Phys. B** **360(2)**, 641 – 696.

[151] I. Affleck and A. W. W. Ludwig (1992) **Phys. Rev. Lett.** **68**, 1046–1049.

[152] A. W. Ludwig and I. Affleck (1994) **Nucl. Phys. B** **428(3)**, 545 – 611.

[153] A. K. Mitchell, E. Sela, and D. E. Logan (2012) **Phys. Rev. Lett.** **108**, 086405.

[154] R. Bulla and A. Hewson (1997) **Z. Phys. B: Condens. Matter** **104(2)**, 333–340.

[155] I. Affleck, A. W. W. Ludwig, and B. A. Jones (1995) **Phys. Rev. B** **52**, 9528–9546.

[156] R. Bulla, A. C. Hewson, and G.-M. Zhang (1997) **Phys. Rev. B** **56**, 11721–11740.

[157] A. W. Ludwig (1994) **Physica B** **199**, 406 – 408.

[158] I. Affleck and A. W. W. Ludwig (1991) **Phys. Rev. Lett.** **67**, 161–164.

[159] K Buschow, (ed.) (2005) Concise Encyclopedia of Magnetic and Superconducting Materials, **Elsevier** second edition.

[160] A. Yatskar, W. P. Beyermann, R. Movshovich, and P. C. Canfield (1996) **Phys. Rev. Lett.** **77**, 3637–3640.

[161] D. L. Cox (1987) **Phys. Rev. Lett.** **59**, 1240–1243.

[162] C. L. Seaman, M. B. Maple, B. W. Lee, S. Ghamaty, M. S. Torikachvili, J.-S. Kang, L. Z. Liu, J. W. Allen, and D. L. Cox (1991) **Phys. Rev. Lett.** **67**, 2882–2885.

[163] M. B. Maple, M. C. Andrade, J. Herrmann, Y. Dalichaouch, D. A. Gajewski, C. L. Seaman, R. Chau, R. Movshovich, M. C. Aronson, and R. Osborn **J. Low Temp. Phys.** **99(3)**, 223–249.

[164] H. v. Löhneysen, T. Pietrus, G. Portisch, H. G. Schlager, A. Schröder, M. Sieck, and T. Trappmann (1994) **Phys. Rev. Lett.** **72**, 3262–3265.

[165] R. M. Potok, I. G. Rau, H. Shtrikman, Y. Oreg, and D. Goldhaber-Gordon **Nat. Phys.** **446**, 267–171.

[166] A. M. Tsvelik and P. B. Wiegmann **Z. Phys. B: Condens. Matter** **54(3)**, 201–206.

[167] G. Zaránd and J. von Delft (2000) **Phys. Rev. B** **61**, 6918–6933.

[168] P. Coleman, L. B. Ioffe, and A. M. Tsvelik (1995) **Phys. Rev. B** **52**, 6611–6627.

[169] P. Coleman and A. J. Schofield (1995) **Phys. Rev. Lett.** **75**, 2184–2187.

[170] S. Bradley, R. Bulla, A. Hewson, and G.-M. Zhang (1999) **Eur. Phys. J. B** **11(4)**, 535–550.

[171] I. Affleck, A. W. W. Ludwig, H.-B. Pang, and D. L. Cox (1992) **Phys. Rev. B** **45**, 7918–7935.

[172] B. Jones and K. Ingersent (1994) **Physica B** **199**, 411 – 412.

[173] K. Ingersent, B. A. Jones, and J. W. Wilkins (1992) **Phys. Rev. Lett.** **69**, 2594–2597.

[174] J. Gan (1995) **Phys. Rev. B** **51**, 8287–8309.

[175] C. J. Bolech and N. Andrei (2002) **Phys. Rev. Lett.** **88**, 237206.

[176] H. Johannesson, N. Andrei, and C. J. Bolech (2003) **Phys. Rev. B** **68**, 075112.

[177] B. A. Jones and C. M. Varma (1989) **Phys. Rev. B** **40**, 324–329.

[178] C. Sire, C. M. Varma, and H. R. Krishnamurthy (1993) **Phys. Rev. B** **48**, 13833–13839.

[179] M. Fabrizio, A. F. Ho, L. D. Leo, and G. E. Santoro (2003) **Phys. Rev. Lett.** **91**, 246402.

[180] B. A. Jones, C. M. Varma, and J. W. Wilkins (1988) **Phys. Rev. Lett.** **61**, 125–128.

[181] A. Zygmund (1988) Trigonometric Series, **Cambridge University Press** second edition.

[182] A. Kitaev and J. Preskill (2006) **Phys. Rev. Lett.** **96**, 110404.

[183] C.-Y. Hou, K. Shtengel, G. Refael, and P. M. Goldbart (2012) **New J. Phys.** **14(10)**, 105005.

Acknowledgements

A PhD is a long, arduous and isolating endeavour, requiring support and assistance from many people. At the risk of being mawkish, I would like to give a mention to all those who helped me through.

Firstly, I am very grateful to my supervisors, Alex Hewson, Ortwin Hess and Derek Lee, for their assistance and encouragement over the last four years. I am especially indebted to Alex Hewson for his careful supervision and for sharing his phenomenal knowledge. He has offered continuous help and insight, as well as many interesting conversations over cake and tea.

I would also like to thank our collaborators, Dan Crow and Yunori Nishikawa, who have made massive contributions to the work I have presented. Their experience, knowledge, and assistance have been invaluable over the past few years.

Aside from the academic support, I have been helped through by my friends and family. My parents and brother, Jack, have been encouraging and supportive whenever I have needed to run from London and hide in amongst the fields, cliffs, and pubs of the countryside.

My friends and (ex)housemates, especially Savi, Jim, Noe, Anna and Ayisha have ensured that my life revolved around things other than physics, and I have had many awesome nights drinking beers, watching TV and talking with them. At some points during the PhD, these were the only things keeping me going.

My colleagues in the condensed matter group have provided many interesting and fun discussions over various tea breaks, and excursions to certain Polish and German bars. I would especially like to thank Doris for her friendship and many hours

of tea, cookies, and assortments of ghastly spirits. She and her husband Fabi have been super accommodating upon visiting their home in Germany, and these (usually nerdy) trips have been great fun.

A special mention is owed to members of the space and atmospherics group. In particular to Ruth, Josh, Jamie, Benoit and Amy. We have gone on numerous awesome adventures over the last three years, seeking out mountains and challenges throughout Europe. These trips have been amazing and long may they continue.

Finally, and most importantly, I am massively indebted to my partner Alex. His love, understanding, and support have kept me going through some very tough times. His parents, Orietta and Reinhard, have also been great. Their encouragement, accommodation, various treats and many finely cooked dinners have significantly helped me through this experience.

Appendix A

List of Clebsch-Gordan Coefficients

To derive the iterative diagonalisation scheme for the NRG, and calculate the local matrix elements, we need to combine angular momenta. In this appendix, we provide the relevant Clebsch-Gordan coefficients in the form most useful to us. These coefficients, and others, can be found in [88], and are presented here in a form more convenient to our calculations. We suppose that we have some spin system (S, S_z) which we seek to combine with a spin system (S_O, σ) to obtain (S', S'_z). We present the Clebsch-Gordan coefficients in the form

$$\langle S, S_z; S_O, \sigma | S', S'_z \rangle \, .$$

There are two useful cases in our work.

Case I: $S_O = {}^1\!/_2$

$$\begin{aligned}
\langle S - {}^1\!/_2, S_z - {}^1\!/_2; {}^1\!/_2, {}^1\!/_2 | S, S_z \rangle &= \sqrt{\frac{S + S_z}{2S}}, \\
\langle S - {}^1\!/_2, S_z + {}^1\!/_2; {}^1\!/_2, -{}^1\!/_2 | S, S_z \rangle &= \sqrt{\frac{S - S_z}{2S}}, \\
\langle S + {}^1\!/_2, S_z - {}^1\!/_2; {}^1\!/_2, {}^1\!/_2 | S, S_z \rangle &= -\sqrt{\frac{S - S_z + 1}{2S + 2}}, \\
\langle S + {}^1\!/_2, S_z + {}^1\!/_2; {}^1\!/_2, -{}^1\!/_2 | S, S_z \rangle &= \sqrt{\frac{S + S_z + 1}{2S + 2}}
\end{aligned}$$

Case II: $\boldsymbol{S_O = 1}$

$$\langle S-1, S_z-1; 1, 1|S, S_z\rangle = \sqrt{\frac{(S+S_z-1)\,(S+S_z)}{2S\,(2S-1)}},$$

$$\langle S-1, S_z; 1, 0|S, S_z\rangle = \sqrt{\frac{(S-S_z)\,(S+S_z)}{S\,(2S-1)}},$$

$$\langle S-1, S_z+1; 1, -1|S, S_z\rangle = \sqrt{\frac{(S-S_z-1)\,(S-S_z)}{2S(2S-1)}},$$

$$\langle S, S_z-1; 1, 1|S, S_z\rangle = -\sqrt{\frac{(S+S_z)\,(S-S_z+1)}{2S\,(S+1)}},$$

$$\langle S, S_z; 1, 0|S, S_z\rangle = \frac{S_z}{\sqrt{S(S+1)}},$$

$$\langle S, S_z+1; 1, -1|S, S_z\rangle = \sqrt{\frac{(S-S_z)\,(S+S_z+1)}{2S(S+1)}},$$

$$\langle S+1, S_z-1; 1, 1|S, S_z\rangle = \sqrt{\frac{(S-S_z+1)\,(S-S_z+2)}{(2S+2)(2S+3)}},$$

$$\langle S+1, S_z; 1, 0|S, S_z\rangle = -\sqrt{\frac{(S-S_z+1)\,(S+S_z+1)}{(S+1)\,(2S+3)}},$$

$$\langle S+1, S_z+1; 1, -1|S, S_z\rangle = \sqrt{\frac{(S+S_z+2)\,(S+S_z+1)}{(2S+2)(2S+3)}}.$$

Appendix B

Iterative Diagonalisation for the 2-Impurity NRG

The iteration diagonalisation executed in the NRG carries out the transformation $H_N \to H_{N+1}$. There are two key stages in this process. The first is the construction of the basis of H_{N+1} in terms of the eigenstates of H_N and the new site basis states. The second is the calculation of the matrix elements of H_{N+1} in this basis. In this appendix we provide the formulae required to carry out these calculations.

B.1 Basis States of H_{N+1}

In this section we apply the definitions of (2.2.3) and list the basis states of H_{N+1}. For clarity, we adopt the labelling convention $|i, j\rangle = |Q_1, Q_2, S, S_z, r, i, j; N\rangle$. The basis states are as follow.

$$|0,0\rangle = |0\rangle_1 \, |0\rangle_2 \, |Q_1+1, Q_2+1, S, S_z, r; N\rangle$$

$$\begin{aligned} |0,1\rangle = {} & \sqrt{\frac{S+S_z}{2S}} \, |0\rangle_1 \, |\uparrow\rangle_2 \, |Q_1+1, Q_2, S-{}^1\!/\!_2, S_z-{}^1\!/\!_2, r; N\rangle \\ & + \sqrt{\frac{S-S_z}{2S}} \, |0\rangle_1 \, |\downarrow\rangle_2 \, |Q_1+1, Q_2, S-{}^1\!/\!_2, S_z+{}^1\!/\!_2, r; N\rangle \end{aligned}$$

$$\begin{aligned} |0,2\rangle = {} & -\sqrt{\frac{S-S_z+1}{2S+2}} \, |0\rangle_1 \, |\uparrow\rangle_2 \, |Q_1+1, Q_2, S+{}^1\!/\!_2, S_z-{}^1\!/\!_2, r; N\rangle \\ & + \sqrt{\frac{S+S_z+1}{2S+2}} \, |0\rangle_1 \, |\downarrow\rangle_2 \, |Q_1+1, Q_2, S+{}^1\!/\!_2, S_z+{}^1\!/\!_2, r; N\rangle \end{aligned}$$

$$|0,3\rangle = |0\rangle_1 |{\uparrow\downarrow}\rangle_2 |Q_1+1, Q_2-1, S, S_z, r; N\rangle$$

$$\begin{aligned}|1,0\rangle = &\sqrt{\frac{S+S_z}{2S}}\,|{\uparrow}\rangle_1 |0\rangle_2 |Q_1, Q_2+1, S-{}^1\!/\!_2, S_z-{}^1\!/\!_2, r; N\rangle \\ &+\sqrt{\frac{S-S_z}{2S}}\,|{\downarrow}\rangle_1 |0\rangle_2 |Q_1, Q_2+1, S-{}^1\!/\!_2, S_z+{}^1\!/\!_2, r; N\rangle\end{aligned}$$

$$\begin{aligned}|1,1\rangle = &\sqrt{\frac{(S+S_z)(S+S_z-1)}{2S(2S-1)}}\,|{\uparrow}\rangle_1 |{\uparrow}\rangle_2 |Q_1, Q_2, S-1, S_z-1, r; N\rangle \\ &+\sqrt{\frac{(S+S_z)(S-S_z)}{2S(2S-1)}}\,|{\downarrow}\rangle_1 |{\uparrow}\rangle_2 |Q_1, Q_2, S-1, S_z, r; N\rangle \\ &+\sqrt{\frac{(S+S_z)(S-S_z)}{2S(2S-1)}}\,|{\uparrow}\rangle_1 |{\downarrow}\rangle_2 |Q_1, Q_2, S-1, S_z, r; N\rangle \\ &+\sqrt{\frac{(S-S_z)(S-S_z-1)}{2S(2S-1)}}\,|{\downarrow}\rangle_1 |{\downarrow}\rangle_2 |Q_1, Q_2, S-1, S_z+1, r; N\rangle\end{aligned}$$

$$\begin{aligned}|1,2\rangle = &-\sqrt{\frac{(S-S_z+1)(S+S_z)}{(2S+1)(2S+2)}}\,|{\uparrow}\rangle_1 |{\uparrow}\rangle_2 |Q_1, Q_2, S, S_z-1, r; N\rangle \\ &-\sqrt{\frac{(S-S_z+1)(S-S_z+1)}{(2S+1)(2S+2)}}\,|{\downarrow}\rangle_1 |{\uparrow}\rangle_2 |Q_1, Q_2, S, S_z, r; N\rangle \\ &+\sqrt{\frac{(S+S_z+1)(S+S_z+1)}{(2S+1)(2S+2)}}\,|{\uparrow}\rangle_1 |{\downarrow}\rangle_2 |Q_1, Q_2, S, S_z, r; N\rangle \\ &+\sqrt{\frac{(S+S_z+1)(S-S_z)}{(2S+1)(2S+2)}}\,|{\downarrow}\rangle_1 |{\downarrow}\rangle_2 |Q_1, Q_2, S, S_z+1, r; N\rangle\end{aligned}$$

$$\begin{aligned}|1,3\rangle = &\sqrt{\frac{S+S_z}{2S}}\,|{\uparrow}\rangle_1 |{\uparrow\downarrow}\rangle_2 |Q_1, Q_2-1, S-{}^1\!/\!_2, S_z-{}^1\!/\!_2, r; N\rangle \\ &+\sqrt{\frac{S-S_z}{2S}}\,|{\downarrow}\rangle_1 |{\uparrow\downarrow}\rangle_2 |Q_1, Q_2-1, S-{}^1\!/\!_2, S_z+{}^1\!/\!_2, r; N\rangle\end{aligned}$$

$$\begin{aligned}|2,0\rangle = &-\sqrt{\frac{S-S_z+1}{2S+2}}\,|{\uparrow}\rangle_1 |0\rangle_2 |Q_1, Q_2+1, S+{}^1\!/\!_2, S_z-{}^1\!/\!_2, r; N\rangle \\ &+\sqrt{\frac{S+S_z+1}{2S+2}}\,|{\downarrow}\rangle_1 |0\rangle_2 |Q_1, Q_2+1, S+{}^1\!/\!_2, S_z+{}^1\!/\!_2, r; N\rangle\end{aligned}$$

$$
\begin{aligned}
|2,1\rangle = &-\sqrt{\frac{(S+S_z)(S-S_z+1)}{2S(2S+1)}}\,|{\uparrow}\rangle_1\,|{\uparrow}\rangle_2\,|Q_1,Q_2,S,S_z-1,r;N\rangle\\
&+\sqrt{\frac{(S+S_z)(S+S_z)}{2S(2S+1)}}\,|{\downarrow}\rangle_1\,|{\uparrow}\rangle_2\,|Q_1,Q_2,S,S_z,r;N\rangle\\
&-\sqrt{\frac{(S-S_z)(S-S_z)}{2S(2S+1)}}\,|{\uparrow}\rangle_1\,|{\downarrow}\rangle_2\,|Q_1,Q_2,S,S_z,r;N\rangle\\
&+\sqrt{\frac{(S-S_z)(S+S_z+1)}{2S(2S+1)}}\,|{\downarrow}\rangle_1\,|{\downarrow}\rangle_2\,|Q_1,Q_2,S,S_z+1,r;N\rangle
\end{aligned}
$$

$$
\begin{aligned}
|2,2\rangle = &\sqrt{\frac{(S-S_z+1)(S-S_z+2)}{(2S+2)(2S+3)}}\,|{\uparrow}\rangle_1\,|{\uparrow}\rangle_2\,|Q_1,Q_2,S+1,S_z-1,r;N\rangle\\
&-\sqrt{\frac{(S-S_z+1)(S+S_z+1)}{(2S+2)(2S+3)}}\,|{\downarrow}\rangle_1\,|{\uparrow}\rangle_2\,|Q_1,Q_2,S+1,S_z,r;N\rangle\\
&-\sqrt{\frac{(S+S_z+1)(S-S_z+1)}{(2S+2)(2S+3)}}\,|{\uparrow}\rangle_1\,|{\downarrow}\rangle_2\,|Q_1,Q_2,S+1,S_z,r;N\rangle\\
&+\sqrt{\frac{(S+S_z+1)(S+S_z+2)}{(2S+2)(2S+3)}}\,|{\downarrow}\rangle_1\,|{\downarrow}\rangle_2\,|Q_1,Q_2,S+1,S_z+1,r;N\rangle
\end{aligned}
$$

$$
\begin{aligned}
|2,3\rangle = &-\sqrt{\frac{S-S_z+1}{2S+2}}\,|{\uparrow}\rangle_1\,|{\uparrow\downarrow}\rangle_2\,|Q_1,Q_2-1,S+1/2,S_z-1/2,r;N\rangle\\
&+\sqrt{\frac{S+S_z+1}{2S+2}}\,|{\downarrow}\rangle_1\,|{\uparrow\downarrow}\rangle_2\,|Q_1,Q_2-1,S+1/2,S_z+1/2,r;N\rangle
\end{aligned}
$$

$$
|3,0\rangle = |{\uparrow\downarrow}\rangle_1\,|0\rangle_2\,|Q_1-1,Q_2+1,S,S_z,r;N\rangle
$$

$$
\begin{aligned}
|3,1\rangle = &\sqrt{\frac{S+S_z}{2S}}\,|{\uparrow\downarrow}\rangle_1\,|{\uparrow}\rangle_2\,|Q_1-1,Q_2,S-1/2,S_z-1/2,r;N\rangle\\
&+\sqrt{\frac{S-S_z}{2S}}\,|{\uparrow\downarrow}\rangle_1\,|{\downarrow}\rangle_2\,|Q_1-1,Q_2,S-1/2,S_z+1/2,r;N\rangle
\end{aligned}
$$

$$
\begin{aligned}
|3,2\rangle = &-\sqrt{\frac{S-S_z+1}{2S+2}}\,|{\uparrow\downarrow}\rangle_1\,|{\uparrow}\rangle_2\,|Q_1-1,Q_2,S+1/2,S_z-1/2,r;N\rangle\\
&+\sqrt{\frac{S+S_z+1}{2S+2}}\,|{\uparrow\downarrow}\rangle_1\,|{\downarrow}\rangle_2\,|Q_1-1,Q_2,S+1/2,S_z+1/2,r;N\rangle
\end{aligned}
$$

$$|3,3\rangle = |{\uparrow\downarrow}\rangle_1 |{\uparrow\downarrow}\rangle_2 |Q_1-1, Q_2-1, S, S_z, r; N\rangle$$

B.2 Matrix Elements of H_{N+1}

Given these basis definitions, we can proceed to calculate the matrix elements of H_{N+1}. We have the definition

$$H_{N+1} = \Lambda^{1/2} H_N + \sum_\alpha \xi_N \left[c^\dagger_{\alpha N\sigma} c_{\alpha(N+1)\sigma} + c^\dagger_{\alpha(N+1)\sigma} c_{\alpha N\sigma} \right], \tag{B.1}$$

and it follows that the diagonal components of H_{N+1} are easy to calculate

$$\langle i,j| H_{N+1} |i,j\rangle = \Lambda^{1/2} E_{Q_1,Q_2,S,S_z,r}(N). \tag{B.2}$$

To compute the off-diagonal components, we define the Hamiltonian

$$H' = c^\dagger_{1N\sigma} c_{1(N+1)\sigma} + c^\dagger_{2N\sigma} c_{2(N+1)\sigma}, \tag{B.3}$$

such that

$$H_{N+1} = \Lambda^{1/2} H_N + \xi_N \left[H' + (H')^\dagger \right]. \tag{B.4}$$

We calculate only the matrix elements of H', and then symmetrise our Hamiltonian. This is numerically advantageous since we only need to calculate half the entries of the matrix representation of H_{N+1}. We compute these matrix elements in terms of reduced matrix elements

$$\langle Q_1', Q_2', S', r'; N || c^\dagger_N || Q_1, Q_2, S, r; N\rangle \tag{B.5}$$

defined by

$$\begin{aligned}\langle Q_1', Q_2', S', S_z', r'; N| c^\dagger_{N\sigma} |Q_1, Q_2, S, S_z, r; N\rangle \\ = \langle S, S_z; 1/2, \sigma | S', S_z'\rangle \langle Q_1', Q_2', S', r'; N || c^\dagger_N || Q_1, Q_2, S, r; N\rangle.\end{aligned} \tag{B.6}$$

Additionally, the reduced eigenstates decompose into a reduced eigenbasis in a way defined by

$$|Q_1, Q_2, S, r; N\rangle = \sum_{p,i,j} U_{Q_1Q_2S}(r; p, i, j; N) |Q_1, Q_2, S, p, i, j; N\rangle \tag{B.7}$$

where the label p is summed over all states in the H_{N-1} system. The off-diagonal matrix elements are given as follow.

$$\langle 0,0|\, H' \,|0,1\rangle = \langle Q_1+1.Q_2+1, S, r'; N||c^\dagger_{2\,N}||Q_1+1, Q_2, S-{}^1\!/_2, r; N\rangle$$

$$\langle 0,0|\, H' \,|0,2\rangle = \langle Q_1+1, Q_2+1, S, r'; N||c^\dagger_{2\,N}||Q_1+1, Q_2, S+{}^1\!/_2, r; N\rangle$$

$$\langle 0,1|\, H' \,|0,3\rangle = \sqrt{\frac{2S}{2S+1}}\,\langle Q_1+1, Q_2, S-{}^1\!/_2, r'; N||c^\dagger_{2\,N}||Q_1+1, Q_2-1, S, r; N\rangle$$

$$\langle 0,2|\, H' \,|0,3\rangle = -\sqrt{\frac{2S+2}{2S+1}}\,\langle Q_1+1, Q_2, S+{}^1\!/_2, r'; N||c^\dagger_{2\,N}||Q_1+1, Q_2-1, S, r; N\rangle$$

$$\langle 0,0|\, H' \,|1,0\rangle = \langle Q_1+1, Q_2+1, S, r'; N||c^\dagger_{1\,N}||Q_1, Q_2+1, S-{}^1\!/_2, r; N\rangle$$

$$\langle 0,1|\, H' \,|1,1\rangle = -\,\langle Q_1+1, Q_2, S-{}^1\!/_2, r'; N||c^\dagger_{1\,N}||Q_1, Q_2, S-1, r; N\rangle$$

$$\langle 1,0|\, H' \,|1,1\rangle = \langle Q_1, Q_2+1, S-{}^1\!/_2, r'; N||c^\dagger_{2\,N}||Q_1, Q_2, S-1, r; N\rangle$$

$$\langle 0,2|\, H' \,|1,2\rangle = -\,\langle Q_1+1, Q_2, S+{}^1\!/_2, r'; N||c^\dagger_{1\,N}||Q_1, Q_2, S, r; N\rangle$$

$$\langle 1,0|\, H' \,|1,2\rangle = \frac{\sqrt{2S(2S+2)}}{2S+1}\,\langle Q_1, Q_2+1, S-{}^1\!/_2, r'; N||c^\dagger_{2\,N}||Q_1, Q_2, S, r; N\rangle$$

$$\langle 2,0|\, H' \,|1,2\rangle = -\frac{1}{2S+1}\,\langle Q_1, Q_2+1, S+{}^1\!/_2, r'; N||c^\dagger_{2\,N}||Q_1, Q_2, S, r; N\rangle$$

$$\langle 0,3|\, H' \,|1,3\rangle = \langle Q_1+1, Q_2-1, S, r'; N || c^\dagger_{1\,N} || Q_1, Q_2-1, S-{}^1\!/\!{}_2, r; N\rangle$$

$$\langle 1,1|\, H' \,|1,3\rangle = \sqrt{\frac{2S-1}{2S}}\,\langle Q_1, Q_2, S-1, r'; N || c^\dagger_{2\,N} || Q_1, Q_2-1, S-{}^1\!/\!{}_2, r; N\rangle$$

$$\langle 1,2|\, H' \,|1,3\rangle = -\sqrt{\frac{2S+2}{2S+1}}\,\langle Q_1, Q_2, S, r'; N || c^\dagger_{2\,N} || Q_1, Q_2-1, S-{}^1\!/\!{}_2, r; N\rangle$$

$$\langle 2,1|\, H' \,|1,3\rangle = -\frac{1}{\sqrt{2S(2S+1)}}\,\langle Q_1, Q_2, S, r'; N || c^\dagger_{2\,N} || Q_1, Q_2-1, S-{}^1\!/\!{}_2, r; N\rangle$$

$$\langle 0,0|\, H' \,|2,0\rangle = \langle Q_1+1, Q_2+1, S, r'; N || c^\dagger_{1\,N} || Q_1, Q_2+1, S+{}^1\!/\!{}_2, r; N\rangle$$

$$\langle 0,1|\, H' \,|2,1\rangle = -\,\langle Q_1+1, Q_2, S-{}^1\!/\!{}_2, r'; N || c^\dagger_{1\,N} || Q_1, Q_2, S, r; N\rangle$$

$$\langle 1,0|\, H' \,|2,1\rangle = \frac{1}{2S+1}\,\langle Q_1, Q_2+1, S-{}^1\!/\!{}_2, r'; N || c^\dagger_{2\,N} || Q_1, Q_2, S, r; N\rangle$$

$$\langle 2,0|\, H' \,|2,1\rangle = \frac{\sqrt{2S(2S+2)}}{2S+1}\,\langle Q_1, Q_2+1, S+{}^1\!/\!{}_2, r'; N || c^\dagger_{2\,N} || Q_1, Q_2, S, r; N\rangle$$

$$\langle 0,2|\, H' \,|2,2\rangle = -\,\langle Q_1+1, Q_2, S+{}^1\!/\!{}_2, r'; N || c^\dagger_{1\,N} || Q_1, Q_2, S+1, r; N\rangle$$

$$\langle 2,0|\, H' \,|2,2\rangle = \langle Q_1, Q_2+1, S+{}^1\!/\!{}_2, r'; N || c^\dagger_{2\,N} || Q_1, Q_2, S+1, r; N\rangle$$

$$\langle 0,3|\, H' \,|2,3\rangle = \langle Q_1+1, Q_2-1, S, r'; N || c^\dagger_{1\,N} || Q_1, Q_2-1, S+{}^1\!/_2, r; N\rangle$$

$$\langle 1,2|\, H' \,|2,3\rangle = -\frac{1}{\sqrt{(2S+1)(2S+2)}}\, \langle Q_1, Q_2, S, r'; N || c^\dagger_{2\,N} || Q_1, Q_2-1, S+{}^1\!/_2, r; N\rangle$$

$$\langle 2,1|\, H' \,|2,3\rangle = \sqrt{\frac{2S}{2S+1}}\, \langle Q_1, Q_2, S, r'; N || c^\dagger_{2\,N} || Q_1, Q_2-1, S+{}^1\!/_2, r; N\rangle$$

$$\langle 2,2|\, H' \,|2,3\rangle = -\sqrt{\frac{2S+3}{2S+2}}\, \langle Q_1, Q_2, S+1, r'; N || c^\dagger_{2\,N} || Q_1, Q_2-1, S+{}^1\!/_2, r; N\rangle$$

$$\langle 1,0|\, H' \,|3,0\rangle = \sqrt{\frac{2S}{2S+1}}\, \langle Q_1, Q_2+1, S-{}^1\!/_2, r'; N || c^\dagger_{1\,N} || Q_1-1, Q_2+1, S, r; N\rangle$$

$$\langle 2,0|\, H' \,|3,0\rangle = -\sqrt{\frac{2S+2}{2S+1}}\, \langle Q_1, Q_2+1, S+{}^1\!/_2, r'; N || c^\dagger_{1\,N} || Q_1-1, Q_2+1, S, r; N\rangle$$

$$\langle 3,0|\, H' \,|3,1\rangle = \langle Q_1-1, Q_2+1, S, r'; N || c^\dagger_{2\,N} || Q_1-1, Q_2, S-{}^1\!/_2, r; N\rangle$$

$$\langle 1,1|\, H' \,|3,1\rangle = -\sqrt{\frac{2S-1}{2S}}\, \langle Q_1, Q_2, S-1, r'; N || c^\dagger_{1\,N} || Q_1-1, Q_2, S-{}^1\!/_2, r; N\rangle$$

$$\langle 2,1|\, H' \,|3,1\rangle = \sqrt{\frac{2S+1}{2S}}\, \langle Q_1, Q_2, S, r'; N || c^\dagger_{1\,N} || Q_1-1, Q_2, S-{}^1\!/_2, r; N\rangle$$

$$\langle 3,0|\, H' \,|3,2\rangle = \langle Q_1-1, Q_2+1, S, r'; N || c^\dagger_{2\,N} || Q_1-1, Q_2, S+{}^1\!/_2, r; N\rangle$$

$$\langle 1,2|\, H' \,|3,2\rangle = -\sqrt{\frac{2S+1}{2S+2}}\, \langle Q_1, Q_2, S, r'; N || c^{\dagger}_{1\,N} || Q_1 - 1, Q_2, S + {}^1\!/_2, r; N\rangle$$

$$\langle 2,2|\, H' \,|3,2\rangle = \sqrt{\frac{2S+3}{2S+2}}\, \langle Q_1, Q_2, S+1, r'; N || c^{\dagger}_{1\,N} || Q_1 - 1, Q_2, S + {}^1\!/_2, r; N\rangle$$

$$\langle 1,3|\, H' \,|3,3\rangle = \sqrt{\frac{2S}{2S+1}}\, \langle Q_1, Q_2 - 1, S - {}^1\!/_2, r'; N || c^{\dagger}_{1\,N} || Q_1 - 1, Q_2 - 1, S, r; N\rangle$$

$$\langle 2,3|\, H' \,|3,3\rangle = -\sqrt{\frac{2S+2}{2S+1}}\, \langle Q_1, Q_2 - 1, S + {}^1\!/_2, r'; N || c^{\dagger}_{1\,N} || Q_1 - 1, Q_2 - 1, S, r; N\rangle$$

$$\langle 3,1|\, H' \,|3,3\rangle = \sqrt{\frac{2S}{2S+1}}\, \langle Q_1 - 1, Q_2, S - {}^1\!/_2, r'; N || c^{\dagger}_{2\,N} || Q_1 - 1, Q_2 - 1, S, r; N\rangle$$

$$\langle 3,2|\, H' \,|3,3\rangle = -\sqrt{\frac{2S+2}{2S+1}}\, \langle Q_1 - 1, Q_2, S + {}^1\!/_2, r'; N || c^{\dagger}_{2\,N} || Q_1 - 1, Q_2 - 1, S, r; N\rangle$$

B.3 Computation of the Reduced Matrix Elements

We thus have all the matrix elements of H_{N+1} in terms of the reduced matrix elements of the site N operators. We must therefore express these matrix elements in terms of the eigenvector entries of the H_N system, which are stored as $U_{Q_1 Q_2 S}(r; p, i, j; N)$. As before, the generic reduced matrix element

$$\langle Q_1', Q_2', S', r'; N || c^{\dagger}_{N} || Q_1, Q_2, S, r; N\rangle \tag{B.1}$$

may be written in terms of matrix elements of the basis states as

$$
\begin{aligned}
&\langle Q_1', Q_2', S', r'; N || c_N^\dagger || Q_1, Q_2, S, r; N \rangle \\
&= \sum_{\substack{p,i,j \\ p',i',j'}} U_{Q_1' Q_2' S'}\left(r'; p', i', j'; N\right) U_{Q_1 Q_2 S}\left(r; p, i, j; N\right) \\
&\qquad \frac{\langle Q_1', Q_2', S', S_z', p', i', j'; N | c_{N\uparrow}^\dagger | Q_1, Q_2, S, S_z - 1/2, p, i, j; N \rangle}{\langle S, S_z - 1/2; 1/2, 1/2 | S', S_z' \rangle}
\end{aligned}
\tag{B.2}
$$

where we have used the Wigner-Eckart theorem. All of the Hamiltonian matrix elements may be written in terms of the four reduced matrix elements

$$
\begin{aligned}
&\langle Q_1 + 1, Q_2 + 1, S, r'; N || c_{1N}^\dagger || Q_1, Q_2 + 1, S - 1/2, r; N \rangle , \\
&\langle Q_1 + 1, Q_2 + 1, S, r'; N || c_{1N}^\dagger || Q_1, Q_2 + 1, S + 1/2, r; N \rangle , \\
&\langle Q_1 + 1, Q_2 + 1, S, r'; N || c_{2N}^\dagger || Q_1 + 1, Q_2, S - 1/2, r; N \rangle , \\
&\langle Q_1 + 1, Q_2 + 1, S, r'; N || c_{2N}^\dagger || Q_1 + 1, Q_2, S + 1/2, r; N \rangle
\end{aligned}
$$

which we compute as

$$
\begin{aligned}
&\langle Q_1 + 1, Q_2 + 1, S, r'; N || c_{1N}^\dagger || Q_1, Q_2 + 1, S - 1/2, r; N \rangle \\
&\quad = \sum_p \Gamma(1,0,0,0) \delta_{N-1}\left(Q_1 + 1, Q_2 + 2, S - 1/2\right) \\
&\quad + \Gamma(1,1,0,1) \delta_{N-1}\left(Q_1 + 1, Q_2 + 1, S - 1\right) \\
&\quad + \frac{\sqrt{2S(2S+2)}}{2S+1} \Gamma(1,2,0,2) \delta_{N-1}\left(Q_1 + 1, Q_2 + 1, S\right) \\
&\quad + \frac{1}{2S+1} \Gamma(2,1,0,2) \delta_{N-1}\left(Q_1 + 1, Q_2 + 1, S\right) \\
&\quad + \Gamma(1,3,0,3) \delta_{N-1}\left(Q_1 + 1, Q_2, S - 1/2\right) \\
&\quad - \frac{1}{\sqrt{2S(2S+1)}} \Gamma(3,1,1,2) \delta_{N-1}\left(Q_1, Q_2 + 1, S - 1/2\right) \\
&\quad + \sqrt{\frac{2S}{2S+1}} \Gamma(3,0,2,0) \delta_{N-1}\left(Q_1, Q_2 + 2, S\right) \\
&\quad + \sqrt{\frac{2S-1}{2S}} \Gamma(3,1,2,1) \delta_{N-1}\left(Q_1, Q_2 + 1, S - 1/2\right) \\
&\quad + \sqrt{\frac{2S}{2S+1}} \Gamma(3,2,2,2) \delta_{N-1}\left(Q_1, Q_2 + 1, S + 1/2\right) \\
&\quad + \sqrt{\frac{2S}{2S+1}} \Gamma(3,3,2,3) \delta_{N-1}\left(Q_1, Q_2, S\right) ,
\end{aligned}
$$

and

$$\langle Q_1+1, Q_2+1, S, r'; N||c_{1N}^{\dagger}||Q_1, Q_2+1, S+{}^1\!/\!_2, r; N\rangle$$

$$\begin{aligned}
&= \sum_p \Lambda(2,0,0,0)\delta_{N-1}\left(Q_1+1, Q_2+2, S+{}^1\!/\!_2\right) \\
&- \frac{1}{2S+1}\Lambda(1,2,0,1)\delta_{N-1}\left(Q_1+1, Q_2+1, S\right) \\
&+ \frac{\sqrt{2S(2S+2)}}{2S+1}\Lambda(2,1,0,1)\delta_{N-1}\left(Q_1+1, Q_2+1, S\right) \\
&+ \Lambda(2,2,0,2)\delta_{N-1}\left(Q_1+1, Q_2+1, S+1\right) \\
&+ \Lambda(2,3,0,3)\delta_{N-1}\left(Q_1+1, Q_2, S+{}^1\!/\!_2\right) \\
&- \sqrt{\frac{2S+2}{2S+1}}\Lambda(3,0,1,0)\delta_{N-1}\left(Q_1, Q_2+2, S\right) \\
&- \sqrt{\frac{2S+2}{2S+1}}\Lambda(3,1,1,1)\delta_{N-1}\left(Q_1, Q_2+1, S-{}^1\!/\!_2\right) \\
&- \sqrt{\frac{2S+3}{2S+2}}\Lambda(3,2,1,2)\delta_{N-1}\left(Q_1, Q_2+1, S+{}^1\!/\!_2\right) \\
&- \sqrt{\frac{2S+2}{2S+1}}\Lambda(3,3,1,3)\delta_{N-1}\left(Q_1, Q_2, S\right) \\
&- \frac{1}{\sqrt{(2S+1)(2S+2)}}\Lambda(3,2,2,1)\delta_{N-1}\left(Q_1, Q_2+1, S+{}^1\!/\!_2\right)
\end{aligned}$$

for channel 1, whilst for channel 2 we have

$$\langle Q_1+1, Q_2+1, S, r'; N || c^\dagger_{2N} || Q_1+1, Q_2, S-{}^1\!/\!_2, r; N\rangle$$

$$\begin{aligned}
&= \sum_p \Theta(0,1,0,0)\delta_{N-1}\left(Q_1+2, Q_2+1, S-{}^1\!/\!_2\right) \\
&+ \sqrt{\frac{2S}{2S+1}}\Theta(0,3,0,2)\delta_{N-1}\left(Q_1+2, Q_2, S\right) \\
&- \Theta(1,1,1,0)\delta_{N-1}\left(Q_1+1, Q_2+1, S-1\right) \\
&- \sqrt{\frac{2S}{2S+1}}\Theta(1,3,1,2)\delta_{N-1}\left(Q_1+1, Q_2, S-{}^1\!/\!_2\right) \\
&- \Theta(2,1,2,0)\delta_{N-1}\left(Q_1+1, Q_2+1, S\right) \\
&- \sqrt{\frac{2S}{2S+1}}\Theta(2,3,2,2)\delta_{N-1}\left(Q_1+1, Q_2, S+{}^1\!/\!_2\right) \\
&+ \Theta(3,1,3,0)\delta_{N-1}\left(Q_1, Q_2+1, S-{}^1\!/\!_2\right) \\
&+ \sqrt{\frac{2S}{2S+1}}\Theta(3,3,3,2)\delta_{N-1}\left(Q_1, Q_2, S\right)
\end{aligned}$$

and

$$\langle Q_1+1, Q_2+1, S, r'; N || c^\dagger_{2N} || Q_1+1, Q_2, S+{}^1\!/\!_2, r; N\rangle$$

$$\begin{aligned}
&= \sum_p \Pi(0,2,0,0)\delta_{N-1}\left(Q_1+2, Q_2+1, S+{}^1\!/\!_2\right) \\
&- \sqrt{\frac{2S+2}{2S+1}}\Pi(0,3,0,1)\delta_{N-1}\left(Q_1+2, Q_2, S\right) \\
&- \Pi(1,2,1,0)\delta_{N-1}\left(Q_1+1, Q_2+1, S\right) \\
&+ \sqrt{\frac{2S+2}{2S+1}}\Pi(1,3,1,1)\delta_{N-1}\left(Q_1+1, Q_2, S-{}^1\!/\!_2\right) \\
&- \Pi(2,2,2,0)\delta_{N-1}\left(Q_1+1, Q_2+1, S+1\right) \\
&+ \sqrt{\frac{2S+2}{2S+1}}\Pi(2,3,2,1)\delta_{N-1}\left(Q_1+1, Q_2, S+{}^1\!/\!_2\right) \\
&+ \Pi(3,2,3,0)\delta_{N-1}\left(Q_1, Q_2+1, S+{}^1\!/\!_2\right) \\
&- \sqrt{\frac{2S+2}{2S+1}}\Pi(3,3,3,1)\delta_{N-1}\left(Q_1, Q_2, S\right),
\end{aligned}$$

where we have defined

$$\begin{aligned}
\Gamma(i',j',i,j) &= U_{Q_1+1,\,Q_2+1,\,S}\big(r';p',i',j';N\big)\,U_{Q_1,\,Q_2+1,\,S-1/2}\big(r;p,i,j;N\big)\\
\Lambda(i',j',i,j) &= U_{Q_1+1,\,Q_2+1,\,S}\big(r';p',i',j';N\big)\,U_{Q_1,\,Q_2+1,\,S+1/2}\big(r;p,i,j;N\big)\\
\Theta(i',j',i,j) &= U_{Q_1+1,\,Q_2+1,\,S}\big(r';p',i',j';N\big)\,U_{Q_1+1,\,Q_2,\,S-1/2}\big(r;p,i,j;N\big)\\
\Pi(i',j',i,j) &= U_{Q_1+1,\,Q_2+1,\,S}\big(r';p',i',j';N\big)\,U_{Q_1+1,\,Q_2,\,S+1/2}\big(r;p,i,j;N\big).
\end{aligned}$$

The delta function

$$\delta_{N-1}(Q_1,Q_2,S)$$

takes value 1 if the sector (Q_1,Q_2,S) is allowed in the system described by H_{N-1}, and is otherwise 0.

Appendix C

Calculation of Thermodynamic Quantities of the Conduction Band

The impurity contribution to $S^{\text{tot}}(T)$ and $\chi^{\text{tot}}(T)$ is determined by calculating these quantities for the 'no-impurity' Hamiltonian

$$H_N^0 = \sum_{n=0}^{N-1} \xi_n \Lambda^{(N-n-1)/2} \left[c^\dagger_{n\sigma} c_{(n+1)\sigma} + c^\dagger_{(n+1)\sigma} c_{n\sigma} \right] \tag{C.1}$$

and subtracting them from the corresponding total quantities. We assume the conduction baths are identical, so drop the channel index. The thermodynamic quantities of this quadratic Hamiltonian may be determined exactly as follows. We define

$$\boldsymbol{V}^\dagger_\sigma = \left(c^\dagger_{0\sigma}, c^\dagger_{1\sigma} \dots c^\dagger_{N\sigma} \right) \tag{C.2}$$

so that

$$H_N^0 = \boldsymbol{V}^\dagger_\sigma \boldsymbol{\mathcal{M}} \boldsymbol{V}_\sigma \tag{C.3}$$

where the tri-diagonal matrix $\boldsymbol{\mathcal{M}}$ is given by

$$\boldsymbol{\mathcal{M}} = \Lambda^{(N-1)/2} \begin{pmatrix} 0 & \xi_0 & 0 & 0 & \cdots \\ \xi_0 & 0 & \Lambda^{-1/2}\xi_1 & 0 & \\ 0 & \Lambda^{-1/2}\xi_1 & 0 & \Lambda^{-1}\xi_2 & \\ 0 & 0 & \Lambda^{-1}\xi_2 & 0 & \\ \vdots & & & & \ddots \end{pmatrix}. \tag{C.4}$$

By virtue of the zero-diagonal and being symmetric, the matrix $\boldsymbol{\mathcal{M}}$ has an equal number of positive and negative eigenvalues (and if N is even, there is a single zero eigenvalue). Moreover, the eigenvalues are $\mathbb{Z}_2$ symmetric such that if λ is an eigenvalue, then so is $-\lambda$. We will denote the positive eigenvalues of $\boldsymbol{\mathcal{M}}$ as η_i^{O} and η_i^{E} for the cases N odd and N even, respectively. The labels i are given by

$$i \in \left\{1, 2, \ldots \frac{1}{2}(N+1)\right\} \tag{C.5}$$

for odd N and

$$i \in \left\{0, 1, 2, \ldots \frac{N}{2}\right\} \tag{C.6}$$

for even N (with $\eta_0^{\mathrm{E}} = 0$). Correspondingly, we can map the free Hamiltonian to a diagonal quasiparticle Hamiltonian, given by

$$H_N^0 = \sum_{n=1}^{(N+1)/2} \eta_n^{\mathrm{O}} \left[p_{n\sigma}^\dagger p_{n\sigma} + h_{n\sigma}^\dagger h_{n\sigma}\right] \tag{C.7}$$

for odd N and

$$H_N^0 = \eta_0^{\mathrm{E}} p_{0\sigma}^\dagger p_{0\sigma} + \sum_{n=1}^{N/2} \eta_n^{\mathrm{E}} \left[p_{n\sigma}^\dagger p_{n\sigma} + h_{n\sigma}^\dagger h_{n\sigma}\right] \tag{C.8}$$

for even N. The Bogoliubov quasiparticle operators p and h can be thought of as the scalar product of the eigenvectors of $\boldsymbol{\mathcal{M}}$ with the vector $\boldsymbol{V}_\sigma^\dagger$, and are respectively the ‘particle’ and ‘hole’ operators. The thermodynamic quantities of these Hamiltonians are simple to calculate; we illustrate this by considering a simplified case.

Suppose we have a Hamiltonian of the form

$$H^0 = \epsilon c_\sigma^\dagger c_\sigma, \tag{C.9}$$

where we can define an eigenbasis as $|00\rangle$, $|\uparrow 0\rangle$, $|0\downarrow\rangle$ and $|\uparrow\downarrow\rangle$. Using this basis, we may write

$$\begin{aligned} Z &= \left(1 + \mathrm{e}^{-\beta\epsilon}\right)^2 \\ \langle\!\langle S_z \rangle\!\rangle &= 0 \\ \langle\!\langle S_z{}^2 \rangle\!\rangle &= \frac{1}{2Z}\mathrm{e}^{-\beta\epsilon} \\ \langle\!\langle H^0 \rangle\!\rangle &= \frac{2\epsilon}{Z}\left(1 + \mathrm{e}^{-\beta\epsilon}\right)\mathrm{e}^{-\beta\epsilon} \\ \langle\!\langle (H^0)^2 \rangle\!\rangle &= \frac{2\epsilon^2}{Z}\left(1 + 2\mathrm{e}^{-\beta\epsilon}\right)\mathrm{e}^{-\beta\epsilon}, \end{aligned} \tag{C.10}$$

from which the thermodynamic quantities of interest trivially follow. Let us now suppose that we have the Hamiltonian

$$H^0 = \epsilon_1 a_\sigma^\dagger a_\sigma + \epsilon_2 b_\sigma^\dagger b_\sigma \tag{C.11}$$

and define

$$\begin{aligned} H_1 &= \epsilon_1 a_\sigma^\dagger a_\sigma \\ H_2 &= \epsilon_2 b_\sigma^\dagger b_\sigma. \end{aligned} \tag{C.12}$$

One can show the following properties:

$$Z = Z_1 Z_2$$

$$\begin{aligned} \langle\langle H^0 \rangle\rangle &= \langle\langle H_1 \rangle\rangle + \langle\langle H_2 \rangle\rangle \\ \langle\langle S_z \rangle\rangle &= \langle\langle S_{1z} \rangle\rangle + \langle\langle S_{2z} \rangle\rangle \end{aligned} \tag{C.13}$$

$$\begin{aligned} \langle\langle H_1 H_2 \rangle\rangle &= \langle\langle H_1 \rangle\rangle \langle\langle H_2 \rangle\rangle \\ \langle\langle S_{1z} S_{2z} \rangle\rangle &= \langle\langle S_{1z} \rangle\rangle \langle\langle S_{2z} \rangle\rangle . \end{aligned}$$

These imply that

$$\begin{aligned} S^0(T) &= S_1(T) + S_2(T) \\ \chi^0(T) &= \chi_1(T) + \chi_2(T). \end{aligned} \tag{C.14}$$

Extending this, we see that for a Hamiltonian given by

$$H^0 = \sum_i \epsilon_i c_{i\sigma}^\dagger c_{i\sigma} \tag{C.15}$$

we can write

$$\begin{aligned} S^0(T) &= \sum_i S_i(T) \\ \chi^0(T) &= \sum_i \chi_i(T). \end{aligned} \tag{C.16}$$

This formalism can be directly applied to the diagonalised free quasiparticle Hamiltonian to obtain the thermodynamic quantities for the conduction band. For simplicity, we only calculate $S^0(T)$ and $\chi^0(T)$ for even N, for which

$$\ln(Z_N^0) = 4 \ln\left(1 + \mathrm{e}^{-\bar{\beta}\eta_0^{\mathrm{E}}}\right) + 8 \sum_{n=1}^{N/2} \ln\left(1 + \mathrm{e}^{-\bar{\beta}\eta_n^{\mathrm{E}}}\right), \tag{C.17}$$

while we obtain the traces

$$\langle\langle H \rangle\rangle_N^0 = 4 \frac{\eta_0^{\mathrm{E}} \mathrm{e}^{-\bar{\beta}\eta_0^{\mathrm{E}}}}{\left(1 + \mathrm{e}^{-\bar{\beta}\eta_0^{\mathrm{E}}}\right)} + 8 \sum_{n=1}^{N/2} \frac{\eta_n^{\mathrm{E}} \mathrm{e}^{-\bar{\beta}\eta_n^{\mathrm{E}}}}{\left(1 + \mathrm{e}^{-\bar{\beta}\eta_n^{\mathrm{E}}}\right)} \tag{C.18}$$

and

$$\langle\!\langle {S_z}^2 \rangle\!\rangle_N^0 = \frac{\mathrm{e}^{-\bar{\beta}\eta_0^{\mathrm{E}}}}{\left(1+\mathrm{e}^{-\bar{\beta}\eta_0^{\mathrm{E}}}\right)^2} + 2\sum_{n=1}^{N/2} \frac{\mathrm{e}^{-\bar{\beta}\eta_n^{\mathrm{E}}}}{\left(1+\mathrm{e}^{-\bar{\beta}\eta_n^{\mathrm{E}}}\right)^2}. \tag{C.19}$$

Note that the extra factor of 2 arises to account for both baths. We are thus able to compute the impurity contribution to $S(T)$ and $\chi(T)$ over all the energy scales reached by the NRG.

Appendix D

Local Matrix Elements for NRG Calculations

We see from (2.4.2) that the calculation of Green functions requires the trace over the operators A and B. We will compute the trace in an eigenbasis, and therefore must discuss how we determine the matrix elements of the local operators in our NRG. Given the eigenstates of the atomic system, the calculation of the matrix elements is easy. In this appendix, we discuss how we can keep track of these matrix elements, which will be reduced using the Wigner-Eckart theorom, as the NRG progresses. The eigenbasis at iteration N is the set of states

$$|Q_1, Q_2, S, S_z, r; N\rangle = \sum_{i,j,p} U_{Q_1Q_2S}(r; p, i, j; N)\, |Q_1, Q_2, S, S_z, p, i, j; N-1\rangle \tag{D.1}$$

but the calculations involve the reduced eigenbasis populated by

$$|Q_1, Q_2, S, r; N\rangle = \sum_{i,j,p} U_{Q_1Q_2S}(r; p, i, j; N)\, |Q_1, Q_2, S, p, i, j; N-1\rangle\,. \tag{D.2}$$

Reduced matrix elements of the form

$$\langle Q_1', Q_2', S', r'; N||O||Q_1, Q_2, S, r; N\rangle \tag{D.3}$$

are therefore required, where O is some operator. Let us suppose that the action of O creates some spin eigenstate of spin S_O and changes S_z by σ. The reduced matrix elements are thus given by

$$\begin{aligned}
&\langle Q_1, Q_2, S, r; N+1 || O || Q_1', Q_2', S', r'; N+1\rangle \\
&= \sum_{\substack{i,j,p \\ i',j',p'}} U_{Q_1 Q_2 S}\left(r\,; i, j\,, r; N+1\right) U_{Q_1' Q_2' S'}\left(r'; i', j', r'; N+1\right) \\
&\qquad \langle Q_1, Q_2, S, p\,, i, j; N || O || Q_1', Q_2', S', p', i', j'; N\rangle
\end{aligned} \tag{D.4}$$

where, by the Wigner-Eckart theorem (2.2.9), we have

$$\begin{aligned}
&\langle Q_1, Q_2, S, r, i, j; N || O || Q_1', Q_2', S', r', i, j; N\rangle \\
&\qquad = \frac{\langle Q_1, Q_2, S, S_z, r\,, i, j; N|\, O\, |Q_1', Q_2', S', S_z - \sigma, r_N', i', j'; N\rangle}{\langle S', S_z - \sigma; S_O, \sigma | S, S_z\rangle}.
\end{aligned} \tag{D.5}$$

These reduced matrix elements can be calculated using the corresponding Clebsch-Gordan coefficients. Since there is no magnetic field, only operator total spin S_O is important. We consider 3 cases in the work presented. $S_O = 0$ corresponds to calculating matrix elements of the singlet state, $S_O = 1/2$ corresponds to 1-particle matrix elements. $S_O = 1$ is required to calculate triplet and spin raising/lowering matrix elements.

Let us suppose that the operator O maps from charge Q to Q' (ie it creates $(Q' - Q)$ electrons). We also suppose it acts on a system of spin S' such that the final spin of the system is S. S can take values $S = S' + S_O, S' + S_O - 1, S' + S_O - 2, \ldots S' - S_O$. We provide the local matrix elements

$$\langle Q_1, Q_2, S, r, i, j; N || O || Q_1', Q_2', S', r', i', j'; N\rangle \tag{D.6}$$

in terms of the matrix elements

$$\langle Q_1, Q_2, S, r; N || O || Q_1', Q_2', S', r'; N\rangle \tag{D.7}$$

to establish an iteration procedure. Note that the N label is omitted to make the matrix elements appear (slightly) less confusing.

D.1 $S_O = 0$

$$\begin{aligned}
&\langle Q_1, Q_2, S, r, 0, 0 || \hat{O} || Q_1', Q_2', S, r', 0, 0\rangle \\
&\qquad\qquad = \langle Q_1 + 1, Q_2 + 1, S, r || \hat{O} || Q_1' + 1, Q_2' + 1, S, r'\rangle
\end{aligned}$$

$$\begin{aligned}&\langle Q_1, Q_2, S, r, 0, 1||\hat{O}||Q_1', Q_2', S, r', 0, 1\rangle \\ &\qquad = \langle Q_1+1, Q_2, S-{}^1\!/_2, r||\hat{O}||Q_1'+1, Q_2', S-{}^1\!/_2, r'\rangle\end{aligned}$$

$$\begin{aligned}&\langle Q_1, Q_2, S, r, 0, 2||\hat{O}||Q_1', Q_2', S, r', 0, 2\rangle \\ &\qquad = \langle Q_1, Q_2+1, S+{}^1\!/_2, r||\hat{O}||Q_1', Q_2'+1, S+{}^1\!/_2, r'\rangle\end{aligned}$$

$$\begin{aligned}&\langle Q_1, Q_2, S, r, 0, 3||\hat{O}||Q_1', Q_2', S, r', 0, 3\rangle \\ &\qquad = \langle Q_1+1, Q_2-1, S, r||\hat{O}||Q_1'+1, Q_2'-1, S, r'\rangle\end{aligned}$$

$$\begin{aligned}&\langle Q_1, Q_2, S, r, 1, 0||\hat{O}||Q_1', Q_2', S, r', 1, 0\rangle \\ &\qquad = \langle Q_1, Q_2+1, S-{}^1\!/_2, r||\hat{O}||Q_1', Q_2'-1, S-{}^1\!/_2, r'\rangle\end{aligned}$$

$$\begin{aligned}&\langle Q_1, Q_2, S, r, 1, 1||\hat{O}||Q_1', Q_2', S, r', 1, 1\rangle \\ &\qquad = \langle Q_1, Q_2, S-1, r||\hat{O}||Q_1', Q_2', S-1, r'\rangle\end{aligned}$$

$$\begin{aligned}&\langle Q_1, Q_2, S, r, 1, 2||\hat{O}||Q_1', Q_2', S, r', 1, 2\rangle \\ &\qquad = \langle Q_1, Q_2, S, r||\hat{O}||Q_1', Q_2', S, r'\rangle\end{aligned}$$

$$\begin{aligned}&\langle Q_1, Q_2, S, r, 1, 3||\hat{O}||Q_1', Q_2', S, r', 1, 3\rangle \\ &\qquad = \langle Q_1, Q_2-1, S-{}^1\!/_2, r||\hat{O}||Q_1', Q_2'-1, S-{}^1\!/_2, r'\rangle\end{aligned}$$

$$\begin{aligned}&\langle Q_1, Q_2, S, r, 2, 0||\hat{O}||Q_1', Q_2', S, r', 2, 0\rangle \\ &\qquad = \langle Q_1, Q_2+1, S+{}^1\!/_2, r||\hat{O}||Q_1', Q_2'+1, S+{}^1\!/_2, r'\rangle\end{aligned}$$

$$\begin{aligned}&\langle Q_1, Q_2, S, r, 2, 1||\hat{O}||Q_1', Q_2', S, r', 2, 1\rangle \\ &\qquad = \langle Q_1, Q_2, S, r||\hat{O}||Q_1', Q_2', S, r'\rangle\end{aligned}$$

$$\begin{aligned}&\langle Q_1, Q_2, S, r, 2, 2||\hat{O}||Q_1', Q_2', S, r', 2, 2\rangle \\ &\qquad = \langle Q_1, Q_2, S+1, r||\hat{O}||Q_1', Q_2', S+1, r'\rangle\end{aligned}$$

$$\begin{aligned}&\langle Q_1, Q_2, S, r, 2, 3||\hat{O}||Q_1', Q_2', S, r', 2, 3\rangle \\ &\qquad = \langle Q_1, Q_2-1, S+{}^1\!/_2, r||\hat{O}||Q_1', Q_2'-1, S+{}^1\!/_2, r'\rangle\end{aligned}$$

$$\begin{aligned}&\langle Q_1, Q_2, S, r, 3, 0||\hat{O}||Q_1', Q_2', S, r', 3, 0\rangle \\ &\qquad = \langle Q_1 - 1, Q_2 + 1, S, r||\hat{O}||Q_1' - 1, Q_2' + 1, S, r'\rangle\end{aligned}$$

$$\begin{aligned}&\langle Q_1, Q_2, S, r, 3, 1||\hat{O}||Q_1', Q_2', S, r', 3, 1\rangle \\ &\qquad = \langle Q_1 - 1, Q_2, S - 1/2, r||\hat{O}||Q_1' - 1, Q_2', S - 1/2, r'\rangle\end{aligned}$$

$$\begin{aligned}&\langle Q_1, Q_2, S, r, 3, 2||\hat{O}||Q_1', Q_2', S, r', 3, 2\rangle \\ &\qquad = \langle Q_1 - 1, Q_2, S + 1/2, r||\hat{O}||Q_1' - 1, Q_2', S + 1/2, r'\rangle\end{aligned}$$

$$\begin{aligned}&\langle Q_1, Q_2, S, r, 3, 3||\hat{O}||Q_1', Q_2', S, r', 3, 3\rangle \\ &\qquad = \langle Q_1 - 1, Q_2 - 1, S, r||\hat{O}||Q_1' - 1, Q_2' - 1, S, r'\rangle\end{aligned}$$

D.2 $S_O = 1/2$

D.2.1 $S' = S - 1/2$

$$\begin{aligned}&\langle Q_1, Q_2, S, r, 0, 0||\hat{O}||Q_1', Q_2', S - 1/2, r', 0, 0\rangle \\ &\qquad = \langle Q_1 + 1, Q_2 + 1, S, r||\hat{O}||Q_1' + 1, Q_2' + 1, S - 1/2, r'\rangle\end{aligned}$$

$$\begin{aligned}&\langle Q_1, Q_2, S, r, 0, 1||\hat{O}||Q_1', Q_2', S - 1/2, r', 0, 1\rangle \\ &\qquad = -\langle Q_1 + 1, Q_2, S - 1/2, r||\hat{O}||Q_1' + 1, Q_2', S - 1, r'\rangle\end{aligned}$$

$$\begin{aligned}&\langle Q_1, Q_2, S, r, 0, 1||\hat{O}||Q_1', Q_2', S - 1/2, r', 0, 2\rangle \\ &\qquad = -\frac{1}{2S+1}\langle Q_1 + 1, Q_2, S - 1/2, r||\hat{O}||Q_1' + 1, Q_2', S, r'\rangle\end{aligned}$$

$$\begin{aligned}&\langle Q_1, Q_2, S, r, 0, 2||\hat{O}||Q_1', Q_2', S - 1/2, r', 0, 2\rangle \\ &\qquad = -\frac{2\sqrt{S(S+1)}}{2S+1}\langle Q_1 + 1, Q_2, S + 1/2, r||\hat{O}||Q_1' + 1, Q_2', S, r'\rangle\end{aligned}$$

$$\begin{aligned}&\langle Q_1, Q_2, S, r, 0, 3||\hat{O}||Q_1', Q_2', S - 1/2, r', 0, 3\rangle \\ &\qquad = \langle Q_1 + 1, Q_2 - 1, S, r||\hat{O}||Q_1' + 1, Q_2' - 1, S - 1/2, r'\rangle\end{aligned}$$

$$\begin{aligned}&\langle Q_1, Q_2, S, r, 1, 0||\hat{O}||Q_1', Q_2', S - 1/2, r', 1, 0\rangle \\ &\qquad = -\langle Q_1, Q_2 + 1, S - 1/2, r||\hat{O}||Q_1', Q_2' + 1, S - 1, r'\rangle\end{aligned}$$

$$\langle Q_1, Q_2, S, r, 1, 0||\hat{O}||Q_1', Q_2', S - {}^1\!/\!_2, r', 2, 0\rangle = -\frac{1}{2S+1}\langle Q_1, Q_2+1, S-{}^1\!/\!_2, r||\hat{O}||Q_1'+1, Q_2', S, r'\rangle$$

$$\langle Q_1, Q_2, S, r, 1, 1||\hat{O}||Q_1', Q_2', S - {}^1\!/\!_2, r', 1, 1\rangle = \langle Q_1, Q_2, S-1, r||\hat{O}||Q_1', Q_2', S-{}^3\!/\!_2, r'\rangle$$

$$\langle Q_1, Q_2, S, r, 1, 1||\hat{O}||Q_1', Q_2', S - {}^1\!/\!_2, r', 1, 2\rangle = \frac{1}{2S}\sqrt{\frac{2S-1}{2S+1}}\langle Q_1, Q_2, S-1, r||\hat{O}||Q_1', Q_2', S-{}^1\!/\!_2, r'\rangle$$

$$\langle Q_1, Q_2, S, r, 1, 1||\hat{O}||Q_1', Q_2', S - {}^1\!/\!_2, r', 2, 1\rangle = \frac{1}{2S}\langle Q_1, Q_2, S-1, r||\hat{O}||Q_1', Q_2', S-{}^1\!/\!_2, r'\rangle$$

$$\langle Q_1, Q_2, S, r, 1, 2||\hat{O}||Q_1', Q_2', S - {}^1\!/\!_2, r', 1, 2\rangle = \frac{2\sqrt{S(S+1)}}{2S+1}\langle Q_1, Q_2, S, r||\hat{O}||Q_1', Q_2', S-{}^1\!/\!_2, r'\rangle$$

$$\langle Q_1, Q_2, S, r, 1, 2||\hat{O}||Q_1', Q_2', S - {}^1\!/\!_2, r', 2, 2\rangle = \frac{1}{2S+1}\sqrt{\frac{S}{S+1}}\langle Q_1, Q_2, S, r||\hat{O}||Q_1', Q_2', S+{}^1\!/\!_2, r'\rangle$$

$$\langle Q_1, Q_2, S, r, 1, 3||\hat{O}||Q_1', Q_2', S - {}^1\!/\!_2, r', 1, 3\rangle = -\langle Q_1, Q_2-1, S-{}^1\!/\!_2, r||\hat{O}||Q_1', Q_2'-1, S-1, r'\rangle$$

$$\langle Q_1, Q_2, S, r, 1, 3||\hat{O}||Q_1', Q_2', S - {}^1\!/\!_2, r', 2, 3\rangle = -\frac{1}{2S+1}\langle Q_1, Q_2-1, S-{}^1\!/\!_2, r||\hat{O}||Q_1', Q_2'-1, S, r'\rangle$$

$$\langle Q_1, Q_2, S, r, 2, 0||\hat{O}||Q_1', Q_2', S - {}^1\!/\!_2, r', 2, 0\rangle = -\frac{2\sqrt{S(S+1)}}{2S+1}\langle Q_1, Q_2+1, S+{}^1\!/\!_2, r||\hat{O}||Q_1', Q_2'+1, S, r'\rangle$$

$$\langle Q_1, Q_2, S, r, 2, 1||\hat{O}||Q_1', Q_2', S - {}^1\!/\!_2, r', 1, 2\rangle = -\frac{1}{2S(2S+1)}\langle Q_1, Q_2, S, r||\hat{O}||Q_1', Q_2', S-{}^1\!/\!_2, r'\rangle$$

$$\begin{aligned}&\langle Q_1, Q_2, S, r, 2, 1||\hat{O}||Q_1', Q_2', S - {}^1\!/\!_2, r', 2, 1\rangle\\&\qquad = \frac{\sqrt{(2S+1)(2S-1)}}{2S}\,\langle Q_1, Q_2, S, r||\hat{O}||Q_1', Q_2', S - {}^1\!/\!_2, r'\rangle\end{aligned}$$

$$\begin{aligned}&\langle Q_1, Q_2, S, r, 2, 1||\hat{O}||Q_1', Q_2', S - {}^1\!/\!_2, r', 2, 2\rangle\\&\qquad = \frac{1}{2S+1}\,\langle Q_1, Q_2, S, r||\hat{O}||Q_1', Q_2', S + {}^1\!/\!_2, r'\rangle\end{aligned}$$

$$\begin{aligned}&\langle Q_1, Q_2, S, r, 2, 2||\hat{O}||Q_1', Q_2', S - {}^1\!/\!_2, r', 2, 2\rangle\\&\qquad = \sqrt{\frac{S(2S+3)}{(S+1)(2S+1)}}\,\langle Q_1, Q_2, S+1, r||\hat{O}||Q_1', Q_2', S + {}^1\!/\!_2, r'\rangle\end{aligned}$$

$$\begin{aligned}&\langle Q_1, Q_2, S, r, 2, 3||\hat{O}||Q_1', Q_2', S - {}^1\!/\!_2, r', 2, 3\rangle\\&\qquad = -\frac{2\sqrt{S(S+1)}}{2S+1}\,\langle Q_1, Q_2 - 1, S + {}^1\!/\!_2, r||\hat{O}||Q_1', Q_2' - 1, S, r'\rangle\end{aligned}$$

$$\begin{aligned}&\langle Q_1, Q_2, S, r, 3, 0||\hat{O}||Q_1', Q_2', S - {}^1\!/\!_2, r', 3, 0\rangle\\&\qquad = \langle Q_1 - 1, Q_2 + 1, S, r||\hat{O}||Q_1' - 1, Q_2' + 1, S - {}^1\!/\!_2, r'\rangle\end{aligned}$$

$$\begin{aligned}&\langle Q_1, Q_2, S, r, 3, 1||\hat{O}||Q_1', Q_2', S - {}^1\!/\!_2, r', 3, 1\rangle\\&\qquad = -\,\langle Q_1 - 1, Q_2, S - {}^1\!/\!_2, r||\hat{O}||Q_1' - 1, Q_2', S - 1, r'\rangle\end{aligned}$$

$$\begin{aligned}&\langle Q_1, Q_2, S, r, 3, 1||\hat{O}||Q_1', Q_2', S - {}^1\!/\!_2, r', 3, 2\rangle\\&\qquad = -\frac{1}{2S+1}\,\langle Q_1 - 1, Q_2, S - {}^1\!/\!_2, r||\hat{O}||Q_1' - 1, Q_2', S, r'\rangle\end{aligned}$$

$$\begin{aligned}&\langle Q_1, Q_2, S, r, 3, 2||\hat{O}||Q_1', Q_2', S - {}^1\!/\!_2, r', 3, 2\rangle\\&\qquad = -\frac{2\sqrt{S(S+1)}}{2S+1}\,\langle Q_1 - 1, Q_2, S + {}^1\!/\!_2, r||\hat{O}||Q_1' - 1, Q_2', S, r'\rangle\end{aligned}$$

$$\begin{aligned}&\langle Q_1, Q_2, S, r, 3, 3||\hat{O}||Q_1', Q_2', S - {}^1\!/\!_2, r', 3, 3\rangle\\&\qquad = \langle Q_1 - 1, Q_2 - 1, S, r||\hat{O}||Q_1' - 1, Q_2' - 1, S - {}^1\!/\!_2, r'\rangle\end{aligned}$$

D.2.2 $S' = S + 1/2$

$$\langle Q_1, Q_2, S, r, 0, 0||\hat{O}||Q_1', Q_2', S + 1/2, r', 0, 0\rangle = \langle Q_1 + 1, Q_2 + 1, S, r||\hat{O}||Q_1' + 1, Q_2' + 1, S + 1/2, r'\rangle$$

$$\langle Q_1, Q_2, S, r, 0, 1||\hat{O}||Q_1', Q_2', S + 1/2, r', 0, 1\rangle = -\frac{2\sqrt{S(S+1)}}{2S+1}\langle Q_1 + 1, Q_2, S - 1/2, r||\hat{O}||Q_1' + 1, Q_2', S, r'\rangle$$

$$\langle Q_1, Q_2, S, r, 0, 2||\hat{O}||Q_1', Q_2', S + 1/2, r', 0, 1\rangle = \frac{1}{2S+1}\langle Q_1 + 1, Q_2, S + 1/2, r||\hat{O}||Q_1' + 1, Q_2', S, r'\rangle$$

$$\langle Q_1, Q_2, S, r, 0, 2||\hat{O}||Q_1', Q_2', S + 1/2, r', 0, 2\rangle = -\langle Q_1 + 1, Q_2, S + 1/2, r||\hat{O}||Q_1' + 1, Q_2', S + 1, r'\rangle$$

$$\langle Q_1, Q_2, S, r, 0, 3||\hat{O}||Q_1', Q_2', S + 1/2, r', 0, 3\rangle = \langle Q_1 + 1, Q_2 - 1, S, r||\hat{O}||Q_1' + 1, Q_2' - 1, S + 1/2, r'\rangle$$

$$\langle Q_1, Q_2, S, r, 1, 0||\hat{O}||Q_1', Q_2', S + 1/2, r', 1, 0\rangle = -\frac{2\sqrt{S(S+1)}}{2S+1}\langle Q_1, Q_2 + 1, S - 1/2, r||\hat{O}||Q_1', Q_2' + 1, S, r'\rangle$$

$$\langle Q_1, Q_2, S, r, 1, 1||\hat{O}||Q_1', Q_2', S + 1/2, r', 1, 1\rangle = \sqrt{\frac{(2S-1)(S+1)}{S(2S+1)}}\langle Q_1, Q_2, S - 1, r||\hat{O}||Q_1', Q_2', S - 1/2, r'\rangle$$

$$\langle Q_1, Q_2, S, r, 1, 2||\hat{O}||Q_1', Q_2', S + 1/2, r', 1, 1\rangle = -\frac{1}{2S+1}\langle Q_1, Q_2, S, r||\hat{O}||Q_1', Q_2', S - 1/2, r'\rangle$$

$$\langle Q_1, Q_2, S, r, 1, 2||\hat{O}||Q_1', Q_2', S + 1/2, r', 1, 2\rangle = \frac{\sqrt{(2S+3)(2S+1)}}{2(S+1)}\langle Q_1, Q_2, S, r||\hat{O}||Q_1', Q_2', S + 1/2, r'\rangle$$

$$\begin{aligned}&\langle Q_1, Q_2, S, r, 1, 2||\hat{O}||Q_1', Q_2', S+{}^1\!/\!_2, r', 2, 1\rangle \\ &\qquad = -\frac{1}{(2S+1)(2S+2)}\,\langle Q_1, Q_2, S, r||\hat{O}||Q_1', Q_2', S+{}^1\!/\!_2, r'\rangle\end{aligned}$$

$$\begin{aligned}&\langle Q_1, Q_2, S, r, 1, 3||\hat{O}||Q_1', Q_2', S+{}^1\!/\!_2, r', 1, 3\rangle \\ &\qquad = -\frac{2\sqrt{S(S+1)}}{2S+1}\,\langle Q_1, Q_2-1, S-{}^1\!/\!_2, r||\hat{O}||Q_1', Q_2'-1, S, r'\rangle\end{aligned}$$

$$\begin{aligned}&\langle Q_1, Q_2, S, r, 2, 0||\hat{O}||Q_1', Q_2', S+{}^1\!/\!_2, r', 1, 0\rangle \\ &\qquad = \frac{1}{2S+1}\,\langle Q_1, Q_2+1, S+{}^1\!/\!_2, r||\hat{O}||Q_1', Q_2'+1, S, r'\rangle\end{aligned}$$

$$\begin{aligned}&\langle Q_1, Q_2, S, r, 2, 0||\hat{O}||Q_1', Q_2', S+{}^1\!/\!_2, r', 2, 0\rangle \\ &\qquad = -\,\langle Q_1, Q_2+1, S+{}^1\!/\!_2, r||\hat{O}||Q_1', Q_2'+1, S+1, r'\rangle\end{aligned}$$

$$\begin{aligned}&\langle Q_1, Q_2, S, r, 2, 1||\hat{O}||Q_1', Q_2', S+{}^1\!/\!_2, r', 1, 1\rangle \\ &\qquad = -\frac{1}{2S+1}\sqrt{\frac{S+1}{S}}\,\langle Q_1, Q_2, S, r||\hat{O}||Q_1', Q_2', S-{}^1\!/\!_2, r'\rangle\end{aligned}$$

$$\begin{aligned}&\langle Q_1, Q_2, S, r, 2, 1||\hat{O}||Q_1', Q_2', S+{}^1\!/\!_2, r', 2, 1\rangle \\ &\qquad = \frac{2\sqrt{S(S+1)}}{2S+1}\,\langle Q_1, Q_2, S, r||\hat{O}||Q_1', Q_2', S+{}^1\!/\!_2, r'\rangle\end{aligned}$$

$$\begin{aligned}&\langle Q_1, Q_2, S, r, 2, 2||\hat{O}||Q_1', Q_2', S+{}^1\!/\!_2, r', 1, 2\rangle \\ &\qquad = -\frac{1}{2S+2}\,\langle Q_1, Q_2, S+1, r||\hat{O}||Q_1', Q_2', S+{}^1\!/\!_2, r'\rangle\end{aligned}$$

$$\begin{aligned}&\langle Q_1, Q_2, S, r, 2, 2||\hat{O}||Q_1', Q_2', S+{}^1\!/\!_2, r', 2, 1\rangle \\ &\qquad = -\frac{1}{2S+2}\sqrt{\frac{2S+3}{2S+1}}\,\langle Q_1, Q_2, S+1, r||\hat{O}||Q_1', Q_2', S+{}^1\!/\!_2, r'\rangle\end{aligned}$$

$$\begin{aligned}&\langle Q_1, Q_2, S, r, 2, 2||\hat{O}||Q_1', Q_2', S+{}^1\!/\!_2, r', 2, 2\rangle \\ &\qquad = \langle Q_1, Q_2, S+1, r||\hat{O}||Q_1', Q_2', S+{}^3\!/\!_2, r'\rangle\end{aligned}$$

$$\langle Q_1, Q_2, S, r, 2, 3||\hat{O}||Q_1', Q_2', S + {}^1\!/_2, r', 1, 3\rangle \\ = \frac{1}{2S+1}\langle Q_1, Q_2 - 1, S + {}^1\!/_2, r||\hat{O}||Q_1', Q_2' - 1, S, r'\rangle$$

$$\langle Q_1, Q_2, S, r, 2, 3||\hat{O}||Q_1', Q_2', S + {}^1\!/_2, r', 2, 3\rangle \\ = -\langle Q_1, Q_2 - 1, S + {}^1\!/_2, r||\hat{O}||Q_1', Q_2' - 1, S + 1, r'\rangle$$

$$\langle Q_1, Q_2, S, r, 3, 0||\hat{O}||Q_1', Q_2', S + {}^1\!/_2, r', 3, 0\rangle \\ = \langle Q_1 - 1, Q_2 + 1, S, r||\hat{O}||Q_1' - 1, Q_2' + 1, S + {}^1\!/_2, r'\rangle$$

$$\langle Q_1, Q_2, S, r, 3, 1||\hat{O}||Q_1', Q_2', S + {}^1\!/_2, r', 3, 1\rangle \\ = -\frac{2\sqrt{S(S+1)}}{2S+1}\langle Q_1 - 1, Q_2, S - {}^1\!/_2, r||\hat{O}||Q_1' - 1, Q_2', S, r'\rangle$$

$$\langle Q_1, Q_2, S, r, 3, 2||\hat{O}||Q_1', Q_2', S + {}^1\!/_2, r', 3, 1\rangle \\ = \frac{1}{2S+1}\langle Q_1 - 1, Q_2, S + {}^1\!/_2, r||\hat{O}||Q_1' - 1, Q_2', S, r'\rangle$$

$$\langle Q_1, Q_2, S, r, 3, 2||\hat{O}||Q_1', Q_2', S + {}^1\!/_2, r', 3, 2\rangle \\ = -\langle Q_1 - 1, Q_2, S + {}^1\!/_2, r||\hat{O}||Q_1' - 1, Q_2', S + 1, r'\rangle$$

$$\langle Q_1, Q_2, S, r, 3, 3||\hat{O}||Q_1', Q_2', S + {}^1\!/_2, r', 3, 3\rangle \\ = \langle Q_1 - 1, Q_2 - 1, S, r||\hat{O}||Q_1' - 1, Q_2' - 1, S + {}^1\!/_2, r'\rangle$$

D.3 $S_O = 1$

D.3.1 $S' = S - 1$

$$\langle Q_1, Q_2, S, r, 0, 0||\hat{O}||Q_1', Q_2', S - 1, r', 0, 0\rangle \\ = \langle Q_1 + 1, Q_2 + 1, S, r||\hat{O}||Q_1' + 1, Q_2' + 1, S - 1, r'\rangle$$

$$\langle Q_1, Q_2, S, r, 0, 1||\hat{O}||Q_1', Q_2', S - 1, r', 0, 1\rangle \\ = \langle Q_1 + 1, Q_2, S - {}^1\!/_2, r||\hat{O}||Q_1' + 1, Q_2', S - {}^3\!/_2, r'\rangle$$

$$\begin{aligned}&\langle Q_1, Q_2, S, r, 0, 1||\hat{O}||Q_1', Q_2', S-1, r', 0, 2\rangle \\ &\qquad = \frac{1}{\sqrt{S(2S+1)}}\,\langle Q_1+1, Q_2, S-{}^1\!/\!{}_2, r||\hat{O}||Q_1'+1, Q_2', S-{}^1\!/\!{}_2, r'\rangle\end{aligned}$$

$$\begin{aligned}&\langle Q_1, Q_2, S, r, 0, 2||\hat{O}||Q_1', Q_2', S-1, r', 0, 2\rangle \\ &\qquad = \sqrt{\frac{(S+1)(2S-1)}{S(2S+1)}}\,\langle Q_1+1, Q_2, S+{}^1\!/\!{}_2, r||\hat{O}||Q_1'+1, Q_2', S-{}^1\!/\!{}_2, r'\rangle\end{aligned}$$

$$\begin{aligned}&\langle Q_1, Q_2, S, r, 0, 3||\hat{O}||Q_1', Q_2', S-1, r', 0, 3\rangle \\ &\qquad = \langle Q_1+1, Q_2-1, S, r||\hat{O}||Q_1'+1, Q_2'-1, S-1, r'\rangle\end{aligned}$$

$$\begin{aligned}&\langle Q_1, Q_2, S, r, 1, 0||\hat{O}||Q_1', Q_2', S-1, r', 1, 0\rangle \\ &\qquad = \langle Q_1, Q_2+1, S-{}^1\!/\!{}_2, r||\hat{O}||Q_1', Q_2'+1, S-{}^3\!/\!{}_2, r'\rangle\end{aligned}$$

$$\begin{aligned}&\langle Q_1, Q_2, S, r, 1, 0||\hat{O}||Q_1', Q_2', S-1, r', 2, 0\rangle \\ &\qquad = \frac{1}{\sqrt{S(2S+1)}}\,\langle Q_1, Q_2+1, S-{}^1\!/\!{}_2, r||\hat{O}||Q_1', Q_2'+1, S-{}^1\!/\!{}_2, r'\rangle\end{aligned}$$

$$\begin{aligned}&\langle Q_1, Q_2, S, r, 1, 1||\hat{O}||Q_1', Q_2', S-1, r', 1, 1\rangle \\ &\qquad = \langle Q_1, Q_2, S-1, r||\hat{O}||Q_1', Q_2', S-2, r'\rangle\end{aligned}$$

$$\begin{aligned}&\langle Q_1, Q_2, S, r, 1, 1||\hat{O}||Q_1', Q_2', S-1, r', 1, 2\rangle \\ &\qquad = \frac{1}{S}\sqrt{\frac{S-1}{2S-1}}\,\langle Q_1, Q_2, S-1, r||\hat{O}||Q_1', Q_2', S-1, r'\rangle\end{aligned}$$

$$\begin{aligned}&\langle Q_1, Q_2, S, r, 1, 1||\hat{O}||Q_1', Q_2', S-1, r', 2, 1\rangle \\ &\qquad = \frac{1}{\sqrt{S(2S-1)}}\,\langle Q_1, Q_2, S-1, r||\hat{O}||Q_1', Q_2', S-1, r'\rangle\end{aligned}$$

$$\begin{aligned}&\langle Q_1, Q_2, S, r, 1, 1||\hat{O}||Q_1', Q_2', S-1, r', 2, 2\rangle \\ &\qquad = \frac{1}{S(2S+1)}\,\langle Q_1, Q_2, S-1, r||\hat{O}||Q_1', Q_2', S, r'\rangle\end{aligned}$$

$$\begin{aligned}&\langle Q_1, Q_2, S, r, 1, 2||\hat{O}||Q_1', Q_2', S-1, r', 1, 2\rangle\\&\qquad = \sqrt{\frac{(S+1)(2S-1)}{S(2S+1)}}\,\langle Q_1, Q_2, S, r||\hat{O}||Q_1', Q_2', S-1, r'\rangle\end{aligned}$$

$$\begin{aligned}&\langle Q_1, Q_2, S, r, 1, 2||\hat{O}||Q_1', Q_2', S-1, r', 2, 2\rangle\\&\qquad = \frac{1}{2S+1}\sqrt{\frac{2S-1}{S}}\,\langle Q_1, Q_2, S, r||\hat{O}||Q_1', Q_2', S, r'\rangle\end{aligned}$$

$$\begin{aligned}&\langle Q_1, Q_2, S, r, 1, 3||\hat{O}||Q_1', Q_2', S-1, r', 1, 3\rangle\\&\qquad = \langle Q_1, Q_2-1, S-1/2, r||\hat{O}||Q_1', Q_2'-1, S-3/2, r'\rangle\end{aligned}$$

$$\begin{aligned}&\langle Q_1, Q_2, S, r, 1, 3||\hat{O}||Q_1', Q_2', S-1, r', 2, 3\rangle\\&\qquad = \frac{1}{\sqrt{S(2S+1)}}\,\langle Q_1, Q_2-1, S-1/2, r||\hat{O}||Q_1', Q_2'-1, S-1/2, r'\rangle\end{aligned}$$

$$\begin{aligned}&\langle Q_1, Q_2, S, r, 2, 0||\hat{O}||Q_1', Q_2', S-1, r', 2, 0\rangle\\&\qquad = \sqrt{\frac{(S+1)(2S-1)}{S(2S+1)}}\,\langle Q_1, Q_2+1, S+1/2, r||\hat{O}||Q_1', Q_2'+1, S-1/2, r'\rangle\end{aligned}$$

$$\begin{aligned}&\langle Q_1, Q_2, S, r, 2, 1||\hat{O}||Q_1', Q_2', S-1, r', 1, 2\rangle\\&\qquad = -\frac{1}{S\sqrt{(2S-1)(2S+1)}}\,\langle Q_1, Q_2, S, r||\hat{O}||Q_1', Q_2', S-1, r'\rangle\end{aligned}$$

$$\begin{aligned}&\langle Q_1, Q_2, S, r, 2, 1||\hat{O}||Q_1', Q_2', S-1, r', 2, 1\rangle\\&\qquad = \sqrt{\frac{(S-1)(2S+1)}{S(2S-1)}}\,\langle Q_1, Q_2, S, r||\hat{O}||Q_1', Q_2', S-1, r'\rangle\end{aligned}$$

$$\begin{aligned}&\langle Q_1, Q_2, S, r, 2, 1||\hat{O}||Q_1', Q_2', S-1, r', 2, 2\rangle\\&\qquad = \frac{\sqrt{(S+1)(2S-1)}}{S(2S+1)}\,\langle Q_1, Q_2, S, r||\hat{O}||Q_1', Q_2', S, r'\rangle\end{aligned}$$

$$\begin{aligned}&\langle Q_1, Q_2, S, r, 2, 2||\hat{O}||Q_1', Q_2', S-1, r', 2, 2\rangle\\&\qquad = \frac{\sqrt{(2S-1)(2S+3)}}{2S+1}\,\langle Q_1, Q_2, S+1, r||\hat{O}||Q_1', Q_2', S, r'\rangle\end{aligned}$$

$$\langle Q_1, Q_2, S, r, 2, 3||\hat{O}||Q_1', Q_2', S-1, r', 2, 3\rangle$$
$$= \sqrt{\frac{(S+1)(2S-1)}{S(2S+1)}}\,\langle Q_1, Q_2-1, S+{}^1\!/\!_2, r||\hat{O}||Q_1', Q_2'-1, S-{}^1\!/\!_2, r'\rangle$$

$$\langle Q_1, Q_2, S, r, 3, 0||\hat{O}||Q_1', Q_2', S-1, r', 3, 0\rangle$$
$$= \langle Q_1-1, Q_2+1, S, r||\hat{O}||Q_1'-1, Q_2'+1, S-1, r'\rangle$$

$$\langle Q_1, Q_2, S, r, 3, 1||\hat{O}||Q_1', Q_2', S-1, r', 3, 1\rangle$$
$$= \langle Q_1-1, Q_2, S-{}^1\!/\!_2, r||\hat{O}||Q_1'-1, Q_2', S-{}^3\!/\!_2, r'\rangle$$

$$\langle Q_1, Q_2, S, r, 3, 1||\hat{O}||Q_1', Q_2', S-1, r', 3, 2\rangle$$
$$= \frac{1}{\sqrt{S(2S+1)}}\,\langle Q_1-1, Q_2, S-{}^1\!/\!_2, r||\hat{O}||Q_1'-1, Q_2', S-{}^1\!/\!_2, r'\rangle$$

$$\langle Q_1, Q_2, S, r, 3, 2||\hat{O}||Q_1', Q_2', S-1, r', 3, 2\rangle$$
$$= \sqrt{\frac{(S+1)(2S-1)}{S(2S+1)}}\,\langle Q_1-1, Q_2, S+{}^1\!/\!_2, r||\hat{O}||Q_1'-1, Q_2', S-{}^1\!/\!_2, r'\rangle$$

$$\langle Q_1, Q_2, S, r, 3, 3||\hat{O}||Q_1', Q_2', S-1, r', 3, 3\rangle$$
$$= \langle Q_1-1, Q_2-1, S, r||\hat{O}||Q_1'-1, Q_2'-1, S-1, r'\rangle$$

D.3.2 $S' = S$

$$\langle Q_1, Q_2, S, r, 0, 0||\hat{O}||Q_1', Q_2', S, r', 0, 0\rangle$$
$$= \langle Q_1+1, Q_2+1, S, r||\hat{O}||Q_1'+1, Q_2'+1, S, r'\rangle$$

$$\langle Q_1, Q_2, S, r, 0, 1||\hat{O}||Q_1', Q_2', S, r', 0, 1\rangle$$
$$= \sqrt{\frac{(S+1)(2S-1)}{S(2S+1)}}\,\langle Q_1+1, Q_2, S-{}^1\!/\!_2, r||\hat{O}||Q_1'+1, Q_2', S-{}^1\!/\!_2, r'\rangle$$

$$\langle Q_1, Q_2, S, r, 0, 1||\hat{O}||Q_1', Q_2', S, r', 0, 2\rangle$$
$$= \frac{1}{\sqrt{(S+1)(2S+1)}}\,\langle Q_1+1, Q_2, S-{}^1\!/\!_2, r||\hat{O}||Q_1'+1, Q_2', S+{}^1\!/\!_2, r'\rangle$$

$$\langle Q_1, Q_2, S, r, 0, 2||\hat{O}||Q_1', Q_2', S, r', 0, 1\rangle$$
$$= -\frac{1}{\sqrt{S(2S+1)}}\,\langle Q_1+1, Q_2, S+{}^1\!/\!{}_2, r||\hat{O}||Q_1'+1, Q_2', S-{}^1\!/\!{}_2, r'\rangle$$

$$\langle Q_1, Q_2, S, r, 0, 2||\hat{O}||Q_1', Q_2', S, r', 0, 2\rangle$$
$$= \sqrt{\frac{S(2S+3)}{(S+1)(2S+1)}}\,\langle Q_1+1, Q_2, S+{}^1\!/\!{}_2, r||\hat{O}||Q_1'+1, Q_2', S+{}^1\!/\!{}_2, r'\rangle$$

$$\langle Q_1, Q_2, S, r, 0, 3||\hat{O}||Q_1', Q_2', S, r', 0, 3\rangle$$
$$= \langle Q_1+1, Q_2-1, S, r||\hat{O}||Q_1'+1, Q_2'-1, S, r'\rangle$$

$$\langle Q_1, Q_2, S, r, 1, 0||\hat{O}||Q_1', Q_2', S, r', 1, 0\rangle$$
$$= \sqrt{\frac{(S+1)(2S-1)}{S(2S+1)}}\,\langle Q_1, Q_2+1, S-{}^1\!/\!{}_2, r||\hat{O}||Q_1', Q_2'+1, S-{}^1\!/\!{}_2, r'\rangle$$

$$\langle Q_1, Q_2, S, r, 1, 0||\hat{O}||Q_1', Q_2', S, r', 2, 0\rangle$$
$$= \frac{1}{\sqrt{(S+1)(2S+1)}}\,\langle Q_1, Q_2+1, S-{}^1\!/\!{}_2, r||\hat{O}||Q_1', Q_2'+1, S+{}^1\!/\!{}_2, r'\rangle$$

$$\langle Q_1, Q_2, S, r, 1, 1||\hat{O}||Q_1', Q_2', S, r', 1, 1\rangle$$
$$= \frac{\sqrt{(S-1)(S+1)}}{S}\,\langle Q_1, Q_2, S-1, r||\hat{O}||Q_1', Q_2', S-1, r'\rangle$$

$$\langle Q_1, Q_2, S, r, 1, 1||\hat{O}||Q_1', Q_2', S, r', 1, 2\rangle$$
$$= \frac{1}{2S+1}\sqrt{\frac{2S-1}{S}}\,\langle Q_1, Q_2, S-1, r||\hat{O}||Q_1', Q_2', S, r'\rangle$$

$$\langle Q_1, Q_2, S, r, 1, 1||\hat{O}||Q_1', Q_2', S, r', 2, 1\rangle$$
$$= \frac{\sqrt{(S+1)(2S-1)}}{S(2S+1)}\,\langle Q_1, Q_2, S-1, r||\hat{O}||Q_1', Q_2', S, r'\rangle$$

$$\langle Q_1, Q_2, S, r, 1, 2||\hat{O}||Q_1', Q_2', S, r', 1, 1\rangle$$
$$= -\frac{1}{\sqrt{S(2S+1)}}\,\langle Q_1, Q_2, S, r||\hat{O}||Q_1', Q_2', S-1, r'\rangle$$

$$\langle Q_1,Q_2,S,r,1,2||\hat{O}||Q_1',Q_2',S,r',1,2\rangle \\ = \frac{S(2S+3)}{(S+1)(2S+1)}\,\langle Q_1,Q_2,S,r||\hat{O}||Q_1',Q_2',S,r'\rangle$$

$$\langle Q_1,Q_2,S,r,1,2||\hat{O}||Q_1',Q_2',S,r',2,1\rangle \\ = -\frac{1}{(2S+1)\sqrt{S(S+1)}}\,\langle Q_1,Q_2,S,r||\hat{O}||Q_1',Q_2',S,r'\rangle$$

$$\langle Q_1,Q_2,S,r,1,2||\hat{O}||Q_1',Q_2',S,r',2,2\rangle \\ = \frac{1}{S+1}\sqrt{\frac{S}{2S+1}}\,\langle Q_1,Q_2,S,r||\hat{O}||Q_1',Q_2',S+1,r'\rangle$$

$$\langle Q_1,Q_2,S,r,1,3||\hat{O}||Q_1',Q_2',S,r',1,3\rangle \\ = \sqrt{\frac{(S+1)(2S-1)}{S(2S+1)}}\,\langle Q_1,Q_2-1,S-{}^1\!/\!_2,r||\hat{O}||Q_1',Q_2'-1,S-{}^1\!/\!_2,r'\rangle$$

$$\langle Q_1,Q_2,S,r,1,3||\hat{O}||Q_1',Q_2',S,r',2,3\rangle \\ = \frac{1}{\sqrt{(S+1)(2S+1)}}\,\langle Q_1,Q_2-1,S-{}^1\!/\!_2,r||\hat{O}||Q_1',Q_2'-1,S+{}^1\!/\!_2,r'\rangle$$

$$\langle Q_1,Q_2,S,r,2,0||\hat{O}||Q_1',Q_2',S,r',1,0\rangle \\ = -\frac{1}{\sqrt{S(2S+1)}}\,\langle Q_1,Q_2+1,S+{}^1\!/\!_2,r||\hat{O}||Q_1',Q_2'+1,S-{}^1\!/\!_2,r'\rangle$$

$$\langle Q_1,Q_2,S,r,2,0||\hat{O}||Q_1',Q_2',S,r',2,0\rangle \\ = \sqrt{\frac{S(2S+3)}{(S+1)(2S+1)}}\,\langle Q_1,Q_2+1,S+{}^1\!/\!_2,r||\hat{O}||Q_1',Q_2'+1,S+{}^1\!/\!_2,r'\rangle$$

$$\langle Q_1,Q_2,S,r,2,1||\hat{O}||Q_1',Q_2',S,r',1,1\rangle \\ = -\frac{1}{S}\sqrt{\frac{S+1}{2S+1}}\,\langle Q_1,Q_2,S,r||\hat{O}||Q_1',Q_2',S-1,r'\rangle$$

$$\langle Q_1,Q_2,S,r,2,1||\hat{O}||Q_1',Q_2',S,r',1,2\rangle \\ = -\frac{1}{(2S+1)\sqrt{S(S+1)}}\,\langle Q_1,Q_2,S,r||\hat{O}||Q_1',Q_2',S,r'\rangle$$

$$\begin{aligned}&\langle Q_1, Q_2, S, r, 2, 1||\hat{O}||Q_1', Q_2', S, r', 2, 1\rangle \\ &\qquad = \frac{(S+1)(2S-1)}{S(2S+1)} \langle Q_1, Q_2, S, r||\hat{O}||Q_1', Q_2', S, r'\rangle\end{aligned}$$

$$\begin{aligned}&\langle Q_1, Q_2, S, r, 2, 1||\hat{O}||Q_1', Q_2', S, r', 2, 2\rangle \\ &\qquad = \frac{1}{\sqrt{(S+1)(2S+1)}} \langle Q_1, Q_2, S, r||\hat{O}||Q_1', Q_2', S+1, r'\rangle\end{aligned}$$

$$\begin{aligned}&\langle Q_1, Q_2, S, r, 2, 2||\hat{O}||Q_1', Q_2', S, r', 1, 2\rangle \\ &\qquad = -\frac{\sqrt{S(2S+3)}}{(S+1)(2S+1)} \langle Q_1, Q_2, S+1, r||\hat{O}||Q_1', Q_2', S, r'\rangle\end{aligned}$$

$$\begin{aligned}&\langle Q_1, Q_2, S, r, 2, 2||\hat{O}||Q_1', Q_2', S, r', 2, 1\rangle \\ &\qquad = -\frac{1}{2S+1}\sqrt{\frac{2S+3}{S+1}} \langle Q_1, Q_2, S+1, r||\hat{O}||Q_1', Q_2', S, r'\rangle\end{aligned}$$

$$\begin{aligned}&\langle Q_1, Q_2, S, r, 2, 2||\hat{O}||Q_1', Q_2', S, r', 2, 2\rangle \\ &\qquad = \frac{\sqrt{S(S+2)}}{S+1} \langle Q_1, Q_2, S+1, r||\hat{O}||Q_1', Q_2', S+1, r'\rangle\end{aligned}$$

$$\begin{aligned}&\langle Q_1, Q_2, S, r, 2, 3||\hat{O}||Q_1', Q_2', S, r', 1, 3\rangle \\ &\qquad = -\frac{1}{\sqrt{S(2S+1)}} \langle Q_1, Q_2-1, S+{}^1\!/_2, r||\hat{O}||Q_1', Q_2'-1, S-{}^1\!/_2, r'\rangle\end{aligned}$$

$$\begin{aligned}&\langle Q_1, Q_2, S, r, 2, 3||\hat{O}||Q_1', Q_2', S, r', 2, 3\rangle \\ &\qquad = \sqrt{\frac{S(2S+3)}{(S+1)(2S+1)}} \langle Q_1, Q_2-1, S+{}^1\!/_2, r||\hat{O}||Q_1', Q_2'-1, S+{}^1\!/_2, r'\rangle\end{aligned}$$

$$\begin{aligned}&\langle Q_1, Q_2, S, r, 3, 0||\hat{O}||Q_1', Q_2', S, r', 3, 0\rangle \\ &\qquad = \langle Q_1-1, Q_2+1, S, r||\hat{O}||Q_1'-1, Q_2'+1, S, r'\rangle\end{aligned}$$

$$\begin{aligned}&\langle Q_1, Q_2, S, r, 3, 1||\hat{O}||Q_1', Q_2', S, r', 3, 1\rangle \\ &\qquad = \sqrt{\frac{(S+1)(2S-1)}{S(2S+1)}} \langle Q_1-1, Q_2, S-{}^1\!/_2, r||\hat{O}||Q_1'-1, Q_2', S-{}^1\!/_2, r'\rangle\end{aligned}$$

$$\begin{aligned}&\langle Q_1, Q_2, S, r, 3, 1||\hat{O}||Q_1', Q_2', S, r', 3, 2\rangle \\ &\qquad = \frac{1}{\sqrt{(S+1)(2S+1)}}\,\langle Q_1-1, Q_2, S-{}^1\!/\!_2, r||\hat{O}||Q_1'-1, Q_2', S+{}^1\!/\!_2, r'\rangle\end{aligned}$$

$$\begin{aligned}&\langle Q_1, Q_2, S, r, 3, 2||\hat{O}||Q_1', Q_2', S, r', 3, 1\rangle \\ &\qquad = -\frac{1}{\sqrt{S(2S+1)}}\,\langle Q_1-1, Q_2, S+{}^1\!/\!_2, r||\hat{O}||Q_1'-1, Q_2', S-{}^1\!/\!_2, r'\rangle\end{aligned}$$

$$\begin{aligned}&\langle Q_1, Q_2, S, r, 3, 2||\hat{O}||Q_1', Q_2', S, r', 3, 2\rangle \\ &\qquad = \sqrt{\frac{S(2S+3)}{(S+1)(2S+1)}}\,\langle Q_1-1, Q_2, S+{}^1\!/\!_2, r||\hat{O}||Q_1'-1, Q_2', S+{}^1\!/\!_2, r'\rangle\end{aligned}$$

$$\begin{aligned}&\langle Q_1, Q_2, S, r, 3, 3||\hat{O}||Q_1', Q_2', S, r', 3, 3\rangle \\ &\qquad = \langle Q_1-1, Q_2-1, S, r||\hat{O}||Q_1'-1, Q_2'-1, S, r'\rangle\end{aligned}$$

D.3.3 $S' = S + 1$

$$\begin{aligned}&\langle Q_1, Q_2, S, r, 0, 0||\hat{O}||Q_1', Q_2', S+1, r', 0, 0\rangle \\ &\qquad = \langle Q_1+1, Q_2+1, S, r||\hat{O}||Q_1'+1, Q_2'+1, S+1, r'\rangle\end{aligned}$$

$$\begin{aligned}&\langle Q_1, Q_2, S, r, 0, 1||\hat{O}||Q_1', Q_2', S+1, r', 0, 1\rangle \\ &\qquad = \sqrt{\frac{S(2S+3)}{(S+1)(2S+1)}}\,\langle Q_1+1, Q_2, S-{}^1\!/\!_2, r||\hat{O}||Q_1'+1, Q_2', S+{}^1\!/\!_2, r'\rangle\end{aligned}$$

$$\begin{aligned}&\langle Q_1, Q_2, S, r, 0, 2||\hat{O}||Q_1', Q_2', S+1, r', 0, 1\rangle \\ &\qquad = -\frac{1}{\sqrt{(S+1)(2S+1)}}\,\langle Q_1+1, Q_2, S+{}^1\!/\!_2, r||\hat{O}||Q_1'+1, Q_2', S+{}^1\!/\!_2, r'\rangle\end{aligned}$$

$$\begin{aligned}&\langle Q_1, Q_2, S, r, 0, 2||\hat{O}||Q_1', Q_2', S+1, r', 0, 2\rangle \\ &\qquad = \langle Q_1+1, Q_2, S+{}^1\!/\!_2, r||\hat{O}||Q_1'+1, Q_2', S+{}^3\!/\!_2, r'\rangle\end{aligned}$$

$$\begin{aligned}&\langle Q_1, Q_2, S, r, 0, 3||\hat{O}||Q_1', Q_2', S+1, r', 0, 3\rangle \\ &\qquad = \langle Q_1+1, Q_2-1, S, r||\hat{O}||Q_1'+1, Q_2'-1, S+1, r'\rangle\end{aligned}$$

$$\begin{aligned}&\langle Q_1, Q_2, S, r, 1, 0||\hat{O}||Q_1', Q_2', S+1, r', 1, 0\rangle \\ &\qquad = \sqrt{\frac{S(2S+3)}{(S+1)(2S+1)}}\,\langle Q_1, Q_2+1, S-{}^1\!/\!_2, r||\hat{O}||Q_1', Q_2'+1, S+{}^1\!/\!_2, r'\rangle\end{aligned}$$

$$\begin{aligned}&\langle Q_1, Q_2, S, r, 1, 1||\hat{O}||Q_1', Q_2', S+1, r', 1, 1\rangle \\ &\qquad = \frac{\sqrt{(2S-1)(2S+3)}}{2S+1}\,\langle Q_1, Q_2, S-1, r||\hat{O}||Q_1', Q_2', S, r'\rangle\end{aligned}$$

$$\begin{aligned}&\langle Q_1, Q_2, S, r, 1, 2||\hat{O}||Q_1', Q_2', S+1, r', 1, 1\rangle \\ &\qquad = -\frac{\sqrt{S(2S+3)}}{(S+1)(2S+1)}\,\langle Q_1, Q_2, S, r||\hat{O}||Q_1', Q_2', S, r'\rangle\end{aligned}$$

$$\begin{aligned}&\langle Q_1, Q_2, S, r, 1, 2||\hat{O}||Q_1', Q_2', S+1, r', 1, 2\rangle \\ &\qquad = \sqrt{\frac{(S+2)(2S+1)}{(S+1)(2S+3)}}\,\langle Q_1, Q_2, S, r||\hat{O}||Q_1', Q_2', S+1, r'\rangle\end{aligned}$$

$$\begin{aligned}&\langle Q_1, Q_2, S, r, 1, 2||\hat{O}||Q_1', Q_2', S+1, r', 2, 1\rangle \\ &\qquad = -\frac{1}{(S+1)\sqrt{(2S+1)(2S+3)}}\,\langle Q_1, Q_2, S, r||\hat{O}||Q_1', Q_2', S+1, r'\rangle\end{aligned}$$

$$\begin{aligned}&\langle Q_1, Q_2, S, r, 1, 3||\hat{O}||Q_1', Q_2', S+1, r', 1, 3\rangle \\ &\qquad = \sqrt{\frac{S(2S+3)}{(S+1)(2S+1)}}\,\langle Q_1, Q_2-1, S-{}^1\!/\!_2, r||\hat{O}||Q_1', Q_2'-1, S+{}^1\!/\!_2, r'\rangle\end{aligned}$$

$$\begin{aligned}&\langle Q_1, Q_2, S, r, 2, 0||\hat{O}||Q_1', Q_2', S+1, r', 1, 0\rangle \\ &\qquad = -\frac{1}{\sqrt{(S+1)(2S+1)}}\,\langle Q_1, Q_2+1, S+{}^1\!/\!_2, r||\hat{O}||Q_1', Q_2'+1, S+{}^1\!/\!_2, r'\rangle\end{aligned}$$

$$\begin{aligned}&\langle Q_1, Q_2, S, r, 2, 0||\hat{O}||Q_1', Q_2', S+1, r', 2, 0\rangle \\ &\qquad = \langle Q_1, Q_2+1, S+{}^1\!/\!_2, r||\hat{O}||Q_1', Q_2'+1, S+{}^3\!/\!_2, r'\rangle\end{aligned}$$

$$\begin{aligned}&\langle Q_1, Q_2, S, r, 2, 1||\hat{O}||Q_1', Q_2', S+1, r', 1, 1\rangle \\ &\qquad = -\frac{1}{2S+1}\sqrt{\frac{2S+3}{S+1}}\,\langle Q_1, Q_2, S, r||\hat{O}||Q_1', Q_2', S, r'\rangle\end{aligned}$$

$$\begin{aligned}&\langle Q_1, Q_2, S, r, 2, 1||\hat{O}||Q_1', Q_2', S+1, r', 2, 1\rangle \\ &\qquad = \sqrt{\frac{S(2S+3)}{(S+1)(2S+1)}}\,\langle Q_1, Q_2, S, r||\hat{O}||Q_1', Q_2', S+1, r'\rangle\end{aligned}$$

$$\begin{aligned}&\langle Q_1, Q_2, S, r, 2, 2||\hat{O}||Q_1', Q_2', S+1, r', 1, 1\rangle \\ &\qquad = \frac{1}{(S+1)(2S+1)}\,\langle Q_1, Q_2, S+1, r||\hat{O}||Q_1', Q_2', S, r'\rangle\end{aligned}$$

$$\begin{aligned}&\langle Q_1, Q_2, S, r, 2, 2||\hat{O}||Q_1', Q_2', S+1, r', 1, 2\rangle \\ &\qquad = -\frac{1}{\sqrt{(S+1)(2S+3)}}\,\langle Q_1, Q_2, S+1, r||\hat{O}||Q_1', Q_2', S+1, r'\rangle\end{aligned}$$

$$\begin{aligned}&\langle Q_1, Q_2, S, r, 2, 2||\hat{O}||Q_1', Q_2', S+1, r', 2, 1\rangle \\ &\qquad = -\frac{1}{S+1}\sqrt{\frac{S+2}{2S+3}}\,\langle Q_1, Q_2, S+1, r||\hat{O}||Q_1', Q_2', S+1, r'\rangle\end{aligned}$$

$$\begin{aligned}&\langle Q_1, Q_2, S, r, 2, 2||\hat{O}||Q_1', Q_2', S+1, r', 2, 2\rangle \\ &\qquad = \langle Q_1, Q_2, S+1, r||\hat{O}||Q_1', Q_2', S+2, r'\rangle\end{aligned}$$

$$\begin{aligned}&\langle Q_1, Q_2, S, r, 2, 3||\hat{O}||Q_1', Q_2', S+1, r', 1, 3\rangle \\ &\qquad = -\frac{1}{\sqrt{(S+1)(2S+1)}}\,\langle Q_1, Q_2-1, S+1/2, r||\hat{O}||Q_1', Q_2'-1, S+1/2, r'\rangle\end{aligned}$$

$$\begin{aligned}&\langle Q_1, Q_2, S, r, 2, 3||\hat{O}||Q_1', Q_2', S+1, r', 2, 3\rangle \\ &\qquad = \langle Q_1, Q_2-1, S+1/2, r||\hat{O}||Q_1', Q_2'-1, S+3/2, r'\rangle\end{aligned}$$

$$\begin{aligned}&\langle Q_1, Q_2, S, r, 3, 0||\hat{O}||Q_1', Q_2', S+1, r', 3, 0\rangle \\ &\qquad = \langle Q_1-1, Q_2+1, S, r||\hat{O}||Q_1'-1, Q_2'+1, S+1, r'\rangle\end{aligned}$$

$$\begin{aligned}&\langle Q_1, Q_2, S, r, 3, 1||\hat{O}||Q_1', Q_2', S+1, r', 3, 1\rangle \\ &\qquad = \sqrt{\frac{S(2S+3)}{(S+1)(2S+1)}}\,\langle Q_1-1, Q_2, S-1/2, r||\hat{O}||Q_1'-1, Q_2', S+1/2, r'\rangle\end{aligned}$$

$$\begin{aligned}&\langle Q_1, Q_2, S, r, 3, 2||\hat{O}||Q_1', Q_2', S+1, r', 3, 1\rangle \\ &\qquad = -\frac{1}{\sqrt{(S+1)(2S+1)}}\,\langle Q_1 - 1, Q_2, S + {}^1\!/_2, r||\hat{O}||Q_1' - 1, Q_2', S + {}^1\!/_2, r'\rangle\end{aligned}$$

$$\begin{aligned}&\langle Q_1, Q_2, S, r, 3, 2||\hat{O}||Q_1', Q_2', S+1, r', 3, 2\rangle \\ &\qquad = \langle Q_1 - 1, Q_2, S + {}^1\!/_2, r||\hat{O}||Q_1' - 1, Q_2', S + {}^3\!/_2, r'\rangle\end{aligned}$$

$$\begin{aligned}&\langle Q_1, Q_2, S, r, 3, 3||\hat{O}||Q_1', Q_2', S+1, r', 3, 3\rangle \\ &\qquad = \langle Q_1 - 1, Q_2 - 1, S, r||\hat{O}||Q_1' - 1, Q_2' - 1, S+1, r'\rangle\end{aligned}$$

Appendix E

Reduction of the Density Matrix in the NRG

One of the failings of the conventional method for NRG calculation of dynamic quantities is its inability to identify the ground state. As argued in [35], a way around this is to allow the NRG to reach the final iteration M, and construct the density matrix using the final states. The density matrix is then to be reduced by tracing out the environment states. At iteration M we will assume that the density matrix $\boldsymbol{\rho}^M$ is diagonal and given by

$$\begin{aligned}\boldsymbol{\rho}^M = \sum_{\substack{Q_1,Q_2\\ S,S_z,r,r'}} & \frac{\mathrm{e}^{-\beta\epsilon_{Q_1,Q_2,S,r}(M)}}{Z_M} \\ & \left|Q_1,Q_2,S,S_z,r';M\right\rangle W_M(Q_1,Q_2,S,r',r)\left\langle Q_1,Q_2,S,S_z,r;M\right| \end{aligned} \tag{E.1}$$

where

$$\epsilon_{Q_1,Q_2,S,r}(M) = \Lambda^{-(M-1)/2}E_{Q_1,Q_2,S,r}(M) \tag{E.2}$$

is the unscaled energy of the approximated Anderson Hamiltonian. This assumption is valid for low temperatures, as it assumes that the final NRG states (corresponding to the lowest energy scales reached) are the only important ones for describing the dynamics of the system. For $T = 0$, $W_M(Q_1,Q_2,S,r'_M,r_M) = 0$ unless the arguments correspond to the ground state. We define the reduced density matrix at iteration N as

$$\boldsymbol{\rho}^N_{\text{red}} = \sum_{\substack{Q_1,Q_2,S,S_z\\ r',r}} \left|Q_1,Q_2,S,S_z,r';N\right\rangle W_N(Q_1,Q_2,S,r',r)\left\langle Q_1,Q_2,S,S_z,r;N\right|, \tag{E.3}$$

and suppose that we have $\boldsymbol{\rho}_{\text{red}}^{N}$, and seek $\boldsymbol{\rho}_{\text{red}}^{N-1}$. This is determined by tracing out the degrees of freedom in the N-length chain which are not present in the $(N-1)$-length NRG chain;

$$\boldsymbol{\rho}_{\text{red}}^{N-1} = \sum_{\sigma_1,\sigma_2} \langle\sigma_2;N|\,\langle\sigma_1;N|\,\boldsymbol{\rho}_{\text{red}}^{N}\,|\sigma_1;N\rangle\,|\sigma_2;N\rangle \tag{E.4}$$

where $|\sigma_\alpha;N\rangle \in \{|0;N\rangle_\alpha, |\uparrow;N\rangle_\alpha, |\downarrow;N\rangle_\alpha, |\uparrow\downarrow;N\rangle_\alpha\}$. We proceed by means of the unitary basis decomposition

$$|Q_1,Q_2,S,S_z,r;N\rangle = \sum_{i,j,p} U_{Q_1Q_2S}(r;p,i,j;N)\,|Q_1,Q_2,S,S_z,r,i,j;N-1\rangle \tag{E.5}$$

to write

$$\begin{aligned}\boldsymbol{\rho}_{\text{red}}^{N} = \sum_{\substack{Q_1,Q_2,S,S_z\\ r',r}} \sum_{\substack{i,j,p\\ i',j',p'}} &|Q_1,Q_2,S,S_z,p',i',j';N-1\rangle\,\langle Q_1,Q_2,S,S_z,p,i,j;N-1| \\ &U_{Q_1Q_2S}(r';p',i',j';N)W_N(Q_1,Q_2,S,r',r)U_{Q_1Q_2S}(r;p,i,j;N).\end{aligned} \tag{E.6}$$

Through use of our basis definitions, we calculate explicitly

$$
\begin{aligned}
&W_{N-1}(Q_1, Q_2, S, p', p\ ) \\
&= \sum_{r,r'} \chi_N(Q_1 - 1, Q_2 - 1, S, r', p', r\ , p\ , 0, 0) \\
&+ \frac{2S+2}{2S+1} \chi_N(Q_1 - 1, Q_2, S + 1/2, r', p', r\ , p\ , 0, 1) \\
&+ \frac{2S}{2S+1} \chi_N(Q_1 - 1, Q_2, S - 1/2, r', p', r\ , p\ , 0, 2) \\
&+ \chi_N(Q_1 - 1, Q_2 + 1, S, r', p', r\ , p\ , 0, 3) \\
&+ \frac{2S+2}{2S+1} \chi_N(Q_1, Q_2 - 1, S + 1/2, r', p', r\ , p\ , 1, 0) \\
&+ \frac{2S+3}{2S+1} \chi_N(Q_1, Q_2, S + 1, r', p', r\ , p\ , 1, 1) \\
&+ \chi_N(Q_1, Q_2, S, r', p', r\ , p\ , 1, 2) \\
&+ \frac{2S+2}{2S+1} \chi_N(Q_1, Q_2 + 1, S + 1/2, r', p', r\ , p\ , 1, 3) \\
&+ \frac{2S}{2S+1} \chi_N(Q_1, Q_2 - 1, S - 1/2, r', p', r\ , p\ , 2, 0) \\
&+ \chi_N(Q_1, Q_2, S, r', p', r\ , p\ , 2, 1) \\
&+ \frac{2S-1}{2S+1} \chi_N(Q_1, Q_2, S - 1, r', p', r\ , p\ , 2, 2) \\
&+ \frac{2S}{2S+1} \chi_N(Q_1, Q_2 + 1, S - 1/2, r', p', r\ , p\ , 2, 3) \\
&+ \chi_N(Q_1 + 1, Q_2 - 1, S, r', p', r\ , p\ , 3, 0) \\
&+ \frac{2S+2}{2S+1} \chi_N(Q_1 + 1, Q_2, S + 1/2, r', p', r\ , p\ , 3, 1) \\
&+ \frac{2S}{2S+1} \chi_N(Q_1 + 1, Q_2, S - 1/2, r', p', r\ , p\ , 3, 2) \\
&+ \chi_N(Q_1 + 1, Q_2 + 1, S, r', p', r\ , p\ , 3, 3)
\end{aligned}
\tag{E.7}
$$

where we define

$$
\begin{aligned}
&\chi_N(Q_1, Q_2, S, r', p', r\ , p\ , i, j) \\
&\qquad = U_{Q_1,Q_2,S}(r'; p', i, j; N) W_N(Q_1, Q_2, S, r', r\ ) U_{Q_1,Q_2,S}(r; p, i, j; N).
\end{aligned}
\tag{E.8}
$$

We are hence able to iteratively reduce $\boldsymbol{\rho}_M$ and obtain correlation functions which correctly identify the ground state. Note that this expression can be written as multiplication of matrices, and hence can be implemented efficiently on a computer.